Numerical Analysis of Swirl Decay Dynamics and Heat Transfer Performance Enhancement in Double-Pipe Heat Exchanger Systems

by

Mohannad Eslam Ahmed Eid Shahin

M.Eng.

Thesis Submitted for the Degree of

Doctor of Philosophy

Department of Mechanical, Materials and Manufacturing Engineering

In the Faculty of Science and Engineering

University of Nottingham

Abstract

Heat transfer enhancement in double-pipe heat exchangers remains critical for industrial energy efficiency, yet swirl flow decay—a phenomenon where rotational momentum diminishes axially—presents a key challenge in maintaining optimal thermal performance. This study investigates swirl decay dynamics and its implications for heat transfer in annular flows using three-dimensional computational fluid dynamics (CFD) simulations in ANSYS Fluent, employing k-ε RNG-swirl modified turbulence model and finite volume discretization. The swirl decay was induced by inlet annular swirlers with vane angles of 30°, 45° and 60°. Three objectives guide the work: (1) quantifying the impact of decaying swirl on annular heat transfer, (2) developing a universal model correlating swirl number decay rate with friction factor under heated/unheated conditions, and (3) assessing the thermal benefits of sustaining a minimum swirl intensity. Simulations reveal that axial and tangential velocity profiles exhibit a radial outward bias (shift away from the inner pipe), amplified by larger swirl angles but reduced by higher Reynolds numbers. Swirl decay induces oscillating velocity peaks, particularly in regions of weakened rotational momentum, while thermal effects in heated flows accelerate decay and alter recirculation zones, notably extending the central vortex beyond the swirler. Local Nusselt number peaks near the swirler exit, attributed to thermal boundary layer thinning, inform a novel correlation linking swirl decay rate (quantified via the swirl number, a dimensionless measure of rotational momentum) to friction factor, valid across both adiabatic and heated cases. To enable practical design, the Decay Percentage, a new parameter defining allowable swirl loss over the exchanger length, is introduced, facilitating optimised configurations that balance compactness (2%–69% size reduction) and efficiency (139%–242% heat transfer gain). These findings advance passive enhancement strategies for heat exchangers in energy systems, offering a framework for performance tuning through controlled swirl decay.

Keywords:

- Computational Fluid Dynamics
- Concentric Annulus
- Decay Percentage
- Discontinuous Swirlers
- Double-Pipe Heat Exchanger
- Flow Boundary Layer
- Heat Transfer Augmentation
- Inlet Swirler
- Passive Heat Transfer Enhancement
- Rate of Decay
- Swirl Decay Dynamics
- Swirl Flow Dynamics
- Thermal Boundary Layer

Acknowledgement

The author expresses his sincere gratitude to his tutor and main supervisor at the University of Nottingham Malaysia (UNM), Professor Yousif Abdalla Abakr. Prof. Abakr's profound knowledge and experience in heat transfer and fluid mechanics have been instrumental in broadening the author's horizons and inspiring a passion for research. His constant encouragement and guidance have been invaluable throughout this journey.

Special thanks are extended to Dr. Khameel Bayo Mustapha for his unwavering support and insightful comments. His open-door policy and willingness to provide guidance were crucial in refining this thesis.

The author also wishes to acknowledge the invaluable contributions of his main supervisor in China, Dr. Chen Baiman at Dongguan University of Technology (DGUT). Dr. Chen's expertise and ideas have been essential in developing research that addresses important and previously unanswered questions. Dr. Lim Zi-Yian's role in facilitating communication and bridging the language barrier between the UNM and DGUT teams has been pivotal in fostering a constructive research collaboration.

Furthermore, the author is grateful to Dr. Kelvin Hoo, a former student of Prof. Yousif, for serving as an inspiration and demonstrating the rewards of hard work and dedication.

The author would also like to acknowledge the contributions of Ahmed Haytham Tajalsir Ahmed, a mechanical engineering alumnus at UNM, whose internship work shed light on important past research. Additionally, the author extends his sincere thanks to Nadine Atef Doushy, who holds a master’s degree in international relations and Fiancé, for her assistance with the writing structure and proofreading of the thesis.

Finally, the author extends his deepest appreciation to his family for their unwavering support, prayers, and encouragement throughout this endeavour. Their love and belief in him have been his constant source of strength.

This thesis is dedicated to the cherished memory of my late grandfather, Farid Mohamed Barakat, Undersecretary of the Ministry of Industry. He held a dream close to his heart – to witness me walk towards him, proudly holding my Doctorate degree. Though he is no longer with us to share this moment, his unwavering belief in me and his enduring love continue to inspire me. May this accomplishment serve as a tribute to his memory and the dreams he held for his family.

Nomenclature

Symbols

A	Area, $[\mathrm{m}^2]$
G	Axial flux of the momentum
z	Axial Location, [m]
D	Diameter of the Pipe or Annulus, [m]
d	Diameter of the Swirlers, [m]
$\bar{x}$	Dimensionless Axial Distance
Z^*	Dimensionless Axial Parameter
$\bar{r}$	Dimensionless Radial Distance
f	Friction Factor
Gz	Graetz Number
g	Gravitational Acceleration, $[\mathrm{m} \cdot \mathrm{s}^{-2}]$
h	Heat Transfer Coefficient, $[\mathrm{W} \cdot \mathrm{m}^{-2} \cdot \mathrm{K}^{-1}]$
H	Height of the Vanes, [m]
L	Length of the Heat Exchanger, [m]
l	Length of the Swirler, [m]
$\dot{m}$	Mass Flow Rate, $[\mathrm{kg} \cdot \mathrm{s}^{-1}]$
N	Number of Blades
Nu	Nusselt Number
Pr	Prandtl Number
P	Pressure, [Pa]
r	Radial Location in Annulus, [m]
r^*	Radius Ratio
Re	Reynolds Number
S	Source Term
c	Specific Heat Capacity, $[\mathrm{J} \cdot \mathrm{kg}^{-1} \cdot \mathrm{K}^{-1}]$

SN	Swirl Number
T	Temperature, [°C]
k	Thermal Conductivity, $[\mathrm{W} \cdot \mathrm{m}^{-1} \cdot \mathrm{K}^{-1}]$
u	Velocity, $[\mathrm{m} \cdot \mathrm{s}^{-1}]$

Greek Symbols

ζ	Annular Hydraulic Diameter Correction Term
θ	Circumferential Location, [m]
ρ	Density of the Fluid, $[\mathrm{kg} \cdot \mathrm{m}^{-3}]$
Δ	Difference
μ	Dynamic Viscosity of the Fluid, $[\mathrm{kg} \cdot \mathrm{m}^{-1} \cdot \mathrm{s}^{-1}]$
ϵ	Rate of Turbulent Dissipation
ω	Specific Rate of Turbulent Dissipation
δ	Thickness of Vanes, [m]

Subscripts

a	Annular
p	At Constant Pressure
m	Film
aug	Augmented
avg	Average
z	Axial Component
c	Cold
cond	Conductive
conv	Convective
cs	Cross-Sectional
D	Developing
FD	Fully Developed
h	Hot
hd	Hydraulic
sw	In terms of swirler
helix	In terms of the Helix of the Vanes
inlet	Inlet Boundary Surface
i	Inner Annular Wall
l	Local
max	Maximum
min	Minimum
o	Outer Annular Wall
outlet	Outlet Boundary Surface
0	Plain
r	Radial Component
s	Solid

surf	Surface
θ	Tangential Component
t	Tubular

Abbreviations

CFD	Computational Fluid Dynamics
CAD	Computer Aided Design
DP	Decay Percentage
DNS	Direct Numerical Simulation
DPHE	Double Pipe Heat Exchanger
LES	Large Eddy Simulation
PEC	Performance Enhancement Criteria
RNG	Re-Normalisation Group
RANS	Reynolds Averaged Navier-Stokes
RSM	Reynolds Stress Model
SST	Shear Stress Transport
SN	Swirl Number

Table of Contents

List of Figures

List of Tables

Chapter 1: Introduction

1.1 Background

Swirling flow, characterised by an axial flow with an azimuthal velocity component, is often generated by twisted tapes, swirl generators, or geometrical modifications in channels. This swirling motion significantly enhances the transport properties in heat transfer and other applications such as heat recovery systems, air conditioning, cyclone separators, swirl atomizers, static mixers and swirl combustors. However, swirling flow decays when not continuously induced due to viscous friction between the channel walls and the fluid. Eventually, the flow loses its swirling feature and recovers its axial structure along the pipe. The rate of this decay depends on the initial swirling intensity and the inlet velocity of the fluid.

Multiple heat transfer enhancement techniques have been developed over time. These techniques are listed in Table 1.1 and can be broadly classified based on their construction. Active techniques require an external power source, such as rotating propellers, jet impingements, or stirring of the fluid. In contrast, passive techniques do not require external power and include geometrical modifications of the channel (e.g., changing surface area or adding roughness) and the use of swirl generator devices like twisted tapes and helical coils.

Table 1.1: Different categories of thermal enhancement techniques applied in heat exchangers.

Active Techniques	**Passive Techniques**
Mechanical Aid	Modified Surface
Electrohydrodynamic	Vortex Generators
Magnetohydrodynamic	Swirl Devices
Pulsating Flow	

1.1.1 Active Techniques

Active heat transfer enhancement techniques rely on external energy inputs such as mechanical, electrical, or magnetic forces. While effective, their practical limitations, particularly in industrial settings, motivate the exploration of passive alternatives. Examples of these techniques include:

- **Mechanical Aids**

  Inducing rotations or vibrations as presented by Hosseinian et al. [1] who achieved 97% heat transfer improvement in a vibrating double pipe heat exchanger (DPHE) by disrupting the boundary layers. However, such methods require continuous mechanical power, increasing operational costs.

- **Electrohydrodynamic (EHD) Methods**

  Feng et al. [2] demonstrated enhanced flow boiling in mini-channels using electric fields, but dependency on dielectric fluids limits applicability to specialised systems.

- **Magnetohydrodynamics (MHD)**

  Goharkhah et al. [3] showed ferrofluids under alternating magnetic fields improve heat transfer by 31.4% yet nanoparticle suspensions pose challenges in large-scale flow systems.

- **Pulsating Flow**

  Yang et al. [4] reported superior thermal performance in ribbed channels with pulsating flows, but resonance effects complicate control at industrial scales.

These active techniques demand sustained energy inputs, complex hardware, or specialised fluids, limiting their cost-effectiveness and scalability. This underscores the need for passive methods, such as swirl flow in double pipe heat exchangers (DPHEs), that enhance heat transfer without external power.

1.1.2 Passive Techniques

Passive techniques enhance heat transfer without external energy inputs but often incur significant pressure drops, limiting their practicality. While diverse, their application in DPHEs faces challenges in balancing efficiency and pumping costs. Key methods and limitations include:

- **Modified Surfaces**
  - **Rough surfaces** (e.g., ribs and dimples) disrupt boundary layers but amplify friction losses. For example, Navickaitė et al. [5] achieved 25% heat transfer gains in shell-and-tube heat exchangers using corrugated tubes, but similar geometries in DPHEs risk probative pressure drops [6].
  - **Extended Surfaces** (e.g., fins and baffles) increase heat transfer area but worsen flow resistance. Kim [7] found branched fins ineffective in annular domains, highlighting geometry-specific limitations.
- **Vortex Generators**

  Perforated rings or helical turbulators, like those investigated by Sheikholeslami et al. [8], [9], enhance mixing but obstruct flow, complicating scalability in compact DPHEs.
- **Swirl Devices**

  Twisted tapes, helical fins, or vanes induce rotational flow, but uncontrolled swirl decay limits their effectiveness. For instance, Sivalakshmi [10] reported 35% effectiveness gains with helical fins but noted diminishing returns due to axial swirl decay.

Existing passive methods prioritise heat transfer gains without systematically addressing swirl decay dynamics or optimising the trade-off between thermal performance and friction. This limits their adaptability to industrial DPHEs, where compactness and controlled swirl longevity are critical.

1.1.3 ***Compound Techniques***

Compound techniques combine multiple heat transfer enhancement methods to exploit synergistic effects, yet their application in DPHEs often neglects swirl decay dynamics, a critical factor in sustained thermal performance. For example:

- Combing twisted tapes with rough surfaces [11] amplifies initial heat transfer but fails to address axial decay of swirl intensity, leading to diminishing returns.
- Pulsating flows paired with baffles [12] improve mixing but introduce resonance risks and unmanageable pressure drops in compact systems.

While such techniques achieve higher Nusselt numbers (Nu) through turbulence generation, their trade-offs, particularly in DPHEs, remain poorly quantified:

- **Swirl Decay:**

  Most studies assume sustained rotational momentum, overlooking axial decay (e.g., [13], [14]).
- **Friction Penalty:**

  Synergistic methods like helical fins combined with vortex generators [15] increase friction factors disproportionately, negating thermal gains.

Existing compound techniques prioritise short-term heat transfer peaks over controlled swirl longevity, limiting their adaptability to industrial DPHEs where compactness and steady performance are paramount. Despite their potential, existing compound techniques lack a systematic framework to manage swirl decay in DPHEs, a gap this study addresses through numerical analysis of decay dynamics and the novel Decay Percentage parameter.

1.2 Problem Statements and Motivation

Applications of heat exchangers are widespread in numerous industries. Enhancing their performance in terms of mass and heat transfer is an everlasting objective of the researchers worldwide. Forcing the working fluid into a swirling flow is a common practice among most research. However, the literature can be split into two categories: 1) Research focused on the breakdown of the flow characteristics and behaviour under different operating conditions such as fluid instabilities. 2) Research focused on finding optimal design of swirling devices. This type of research is usually aimed to reducing the pressure drop due to the obstruction caused by the walls of these devices while producing the maximum possible amount of heat or mass transfer through different mediums.

Limitations found using passive techniques were:

- **Fixed swirl intensity:** The swirl intensity generated by passive devices is often fixed and cannot be easily adjusted to varying flow conditions.
- **Limited control:** Passive methods offer limited control over the specific characteristics of the swirl flow, such as the swirl angle or axial velocity distribution.

The current research addresses these limitations by contributing a novel approach in placing discontinuous swirlers of different swirl angles at different locations based on the operating conditions offering a significantly better control over the swirl intensities and the desired flow characteristics.

1.3 Research Questions

This study addresses the following questions:

1. How do Reynolds number, swirl angle, and thermal effects influence velocity/temperature profiles and swirl decay in annular flows?
2. What is the relationship between swirl decay rate and friction factor under heated or unheated conditions?

3. Can maintaining a minimal swirl intensity along the heat exchanger length optimise thermal performance without excessive pressure penalties?

1.4 Hypotheses

The following hypotheses guide this study:

1. Swirl decay dynamics are governed by initial swirl intensity and Reynolds number, with higher angles (30°) amplifying heat transfer but accelerating decay.
2. A correlation exists between swirl number decay rate and friction factor, with heated flows exhibiting stronger coupling due to thermal boundary layer effects.
3. Maintaining high initial swirl intensity via discontinuous swirlers will improve thermal performance while limiting the friction losses.

1.5 Research Objectives

The study aims to advance the understanding of swirl decay dynamics in double pipe heat exchangers through numerical analysis with the following key objectives:

1) Analyse velocity and temperature profiles in annular swirl decaying flows evaluating the effects of:
    - Reynolds number (300-4000),
    - Swirl angle (30°, 45°, 60°),
    - Heated vs. unheated conditions.
2) Develop a correlation between swirl number decay rate and friction factor, validating its applicability under both heated and unheated flows.
3) Quantify the thermal performance impact of maintaining a minimal swirl intensity (e.g., 50% and 70% of maximum swirl number) along the entire length of the heat exchanger.

1.6 Scope of the Research

The research methodology is purely numerical, relying on computational fluid dynamics (CFD) simulations. While CFD offers robust predictive capabilities, it is important to acknowledge certain limitations:

- The use of Reynolds-Averaged Navier-Stokes (RANS) equations might have limitations in capturing mixed flow behaviour at low Reynolds numbers.
- The evaluation of Reynolds number at the annular inlet, irrespective of swirler geometry, might neglect the impact of jet effects on local flow regimes.
- The use of rounded values for Reynolds numbers might not precisely capture the laminar-to-turbulent flow transition point (i.e. critical Reynolds number).
- The extraction of velocity and temperature profiles along radial iso-planar lines might overlook local variations at specific radial and circumferential locations.

Despite these limitations, this research aims to contribute significantly to the understanding of swirl flow in DPHEs and to propose a novel approach to enhance their thermal performance. By investigating the interplay between swirl flow characteristics, heat transfer, and pressure drop, this study seeks to inform the design of more efficient and compact heat exchangers.

1.7 Significance of the Study

This research holds significant promise for advancing the design and application of double pipe heat exchangers. By investigating novel swirling flow control methods, our findings can contribute to:

- *Enhanced understanding of swirling flows*: This research provides a deeper scientific understanding of swirling flow behaviour within the DPHE annulus. This knowledge can inform the development of more accurate flow prediction models.
- *Decay rate correlation development*: Development of the model predicting the decay rate of the swirl number as the flow progresses axially is shown. This contributes to this field of research by expanding the current circle of knowledge adding a new model for one of the most popular designs swirl generators. This data can lead to developing a more generalised and accurate model that can predict a wider range of applications and swirl numbers.
- *Improved heat exchanger efficiency*: The developed methods, particularly Full Swirling Configuration, have the potential to significantly improve heat transfer performance in the heat exchangers. This translates to more compact exchangers for achieving the same level of cooling or heating, leading to cost savings in industries like oil and gas where exchanger size is a critical factor.

Overall, this research contributes to the development of next-generation heat exchangers that are more efficient, compact, and cost-effective. This can lead to significant benefits in various industrial applications that rely on heat transfer processes such as the oil and gas industries.

1.8 Thesis Structure

This thesis comprises of six chapters that systematically address swirl decay dynamics and thermal enhancement in double-pipe heat exchangers. Chapter 1 (Introduction) establishes the research context by reviewing swirl flow applications, limitations of existing enhancement techniques, and the critical gaps in controlled swirl decay flows. It formulates specific research questions, hypotheses, and objectives guiding the study.

Chapter 2 (Literature Review) critically evaluates prior research on swirl flow dynamics and passive heat transfer enhancement in double pipe heat exchangers. By synthesising methodologies, findings, and limitations from key studies, the review identifies unresolved challenges, particularly in managing swirl decay and optimising thermal performance. These gaps directly inform the formulation of research questions guiding this thesis.

Chapter 3 (Performance Evaluation Parameters) includes important parameters that are derived from the literature are defined in this chapter. These parameters are distinguished by their importance in evaluating the performance of the heat exchanger with and without the augmentation techniques. These universally realised parameters allow a fair comparison of performance among passive techniques.

Chapter 4 (Methodology) displays the way that the research objectives will be achieved. This will be in the form of presenting the different setups and dimensions of the geometries that are used in the investigations. The governing parameters that define the boundary and operating conditions of the numerical simulations. Validation of the numerical models and verification of the experiments are shown here as well.

Chapter 5 (Single and Full Swirling Configurations) presents the breakdown of the different characteristics defining the forced swirling flow are presented in this chapter. The evaluation of the swirl intensity produced by various operating conditions are shown. Modelling of the decay of the swirl number is demonstrated here. The utilisation of these results in assembling the full swirling configuration is demonstrated and the impact of such configuration on the thermal performance of the heat exchanger is analysed.

Chapter 6 (Conclusion and Future Recommendations) summarises findings and deductions found in the results are summarised and presented in this chapter. Also, future developments and continuance of this research are suggested to define objectives of future research in order to add on where this thesis has ended.

Chapter 2: Literature Review

This chapter synthesizes foundational and contemporary research on swirl flow dynamics, focusing on its application in double-pipe heat exchangers. The review begins with a historical overview of swirl flow recognition (Section 2.1), followed by passive techniques for swirl induction (Section 2.2), decay correlations (Section 2.3), and turbulence modelling (Section 2.6). Critical gaps in annular swirl decay quantification, discontinuous swirler optimisation, and turbulence model limitations are identified to contextualise this thesis's contributions.

2.1 The Birth of Swirl Flow: A Phenomenon in the Making

The recognition of swirl flows as a distinct phenomenon with unique properties emerged gradually throughout history, drawing from observations, scientific inquiry, and practical applications. Early civilizations documented swirling motions in nature, such as whirlpools and tornadoes, laying the groundwork for later scientific exploration. Leonardo da Vinci's sketches and notes depicting vortices in water and air exemplify this early recognition [16].

In parallel, 19th-century research in fluid mechanics, with contributions from Helmholtz and Kelvin on vortex motion, established theoretical frameworks for swirl dynamics [17]. The early 20th century marked a turning point, as swirl flows found practical applications. Max Jakob's extensive studies on swirl flows in heat exchangers and combustion chambers demonstrated their heat transfer enhancement potential [18]. Moody's work on friction factors [19] further quantified swirl's hydrodynamic impacts. The development of cyclone separators highlighted industrial relevance [20].

By the mid-20th century, swirl flows had firmly established themselves as a distinct and significant phenomenon. This evolution, from empirical observation to quantitative analysis, enabled modern applications in energy systems and heat exchangers.

2.2 Techniques of Swirl Flow Induction

Passive techniques for inducing swirl flow rely on the inherent energy of the fluid itself, without external power sources or moving parts. These methods use geometric modifications to the flow path, creating swirl through the interaction of the fluid with the altered geometry.

The examples presented in Section 1.1.2 highlight several key advantages of passive techniques:

- **Simplicity:** Passive devices are often simpler in design and construction compared to active methods, making them easier to implement and maintain.
- **Reliability:** The absence of moving parts reduces the risk of mechanical failure, enhancing the reliability and longevity of passive swirl generators.
- **Cost-effectiveness:** Passive techniques generally have lower manufacturing and operating costs compared to active methods, making them attractive for a wide range of applications.

Passive swirl flow induction techniques have found widespread use in various fields due to its advantages. Among these techniques, twisted tapes, helical inserts, tangential injectors, and guide vanes have emerged as prominent methods for generating swirl flow.

2.2.1 Twisted Tapes

Twisted tapes, flat strips of material twisted along their length, augment heat transfer by disrupting boundary layers. Key studies include:

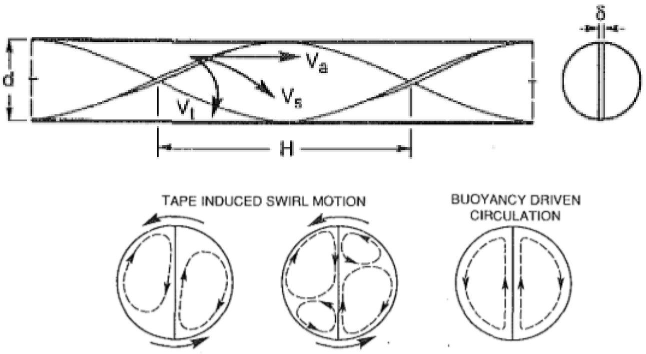

Figure 2.1: Top: Twisted tape in a tube. Bottom: Various secondary flow patterns under different conditions. [21]

- Manglik and Bergles [21], [22] conducted a comprehensive investigation into the effects of twist ratio, width-to-height ratio, and Reynolds number on the thermal-hydraulic performance of twisted tapes. Their findings revealed that twisted tapes significantly augment heat transfer, albeit with an associated pressure drop penalty.

- Subsequent research by Hong and Bergles [23] explored the impact of multiple twisted tapes with varying spacing and arrangement, further refining the understanding of their performance.

Further advancements in twisted tape design have led to the development of alternate-axis twisted tapes [24], [25], square-cut twisted tapes [26], and V-cut twisted tapes [27]. These modifications aim to optimize the heat transfer enhancement while mitigating the pressure drop penalty, thus improving the overall thermal-hydraulic performance. While twisted tapes excel in turbulent flows, helical inserts offer superior performance in laminar regimes, as discussed next.

2.2.2 Helical Inserts

Helical inserts, characterised by their spiral geometry, enhance heat transfer by including rotational flow and secondary vortices. Figure 2.2 compares common helical insert designs.

- García et al. [28] analysed helix angle, pitch length, and Reynolds number effects on the Nusselt number and friction factor of helical inserts in laminar flow. Their findings highlighted the significant heat transfer enhancement of eight times and friction factor increment of about 40% was achievable with helical inserts, particularly in laminar flow regimes.

Subsequent innovations have explored various helical insert configurations, including wire-coil inserts [29], [30], loose-fit and tight-fit inserts [31], multiple inserts with different arrangements [32], and trapezoidal-cut inserts [33]. Furthermore, twisted tapes can be part of compound techniques such as [34]. These studies have collectively contributed to a deeper understanding of the design parameters influencing the performance of helical inserts, paving the way for their optimization in various applications. While helical inserts excel in enclosed channels, tangential injectors leverage angular momentum injection for applications like combustion chambers, as discussed next.

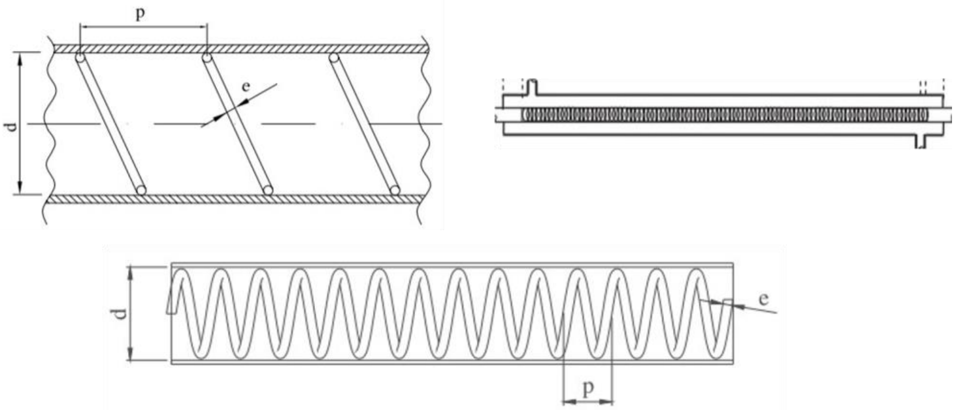

Figure 2.2: Schematic of various helical insert configurations. [28], [29], [30]

2.2.3 Tangential Injectors

Tangential injectors introduce fluid at an angle to the main flow generating swirl through angular momentum transfer. Figure 2.3 illustrates their application in combustion chambers.

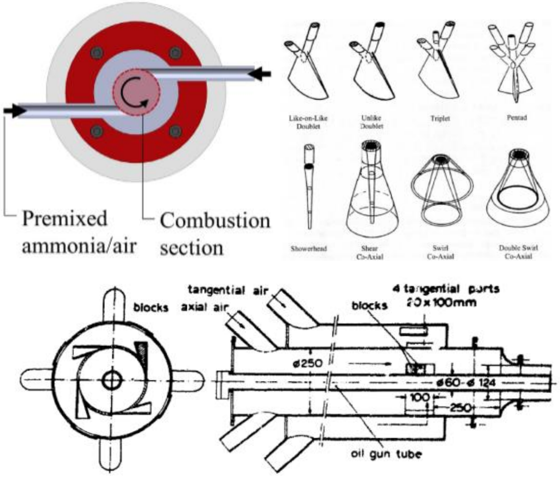

Figure 2.3: Tangential injector designs in combustion chambers. [35], [36], [37]

- Lee et al. [35] investigated tangential injection in gas turbine combustors. Their research highlighted optimal configuration in terms of flame stability at low equivalence and velocity conditions.

The seminal work of Staschus et al. [36] provides a comprehensive overview of tangential injection in various applications, while Syred and Beer [37] delved into the swirling flow patterns and mixing characteristics in a cyclone combustor with tangential injection. More recent studies have explored the use of tangential injection for heat transfer enhancement in circular tubes [38] and solar receivers [39], showcasing its versatility in different engineering systems. While tangential injectors stand out in open systems, inlet swirl generators offer localised control for confined flows, as discussed in the next section.

2.2.4 Inlet Swirl Generators

Inlet swirl generators induce rotational motion at pipe entrances enhancing heat transfer and mixing. Figure 2.4 presents different inlet swirl generator designs.

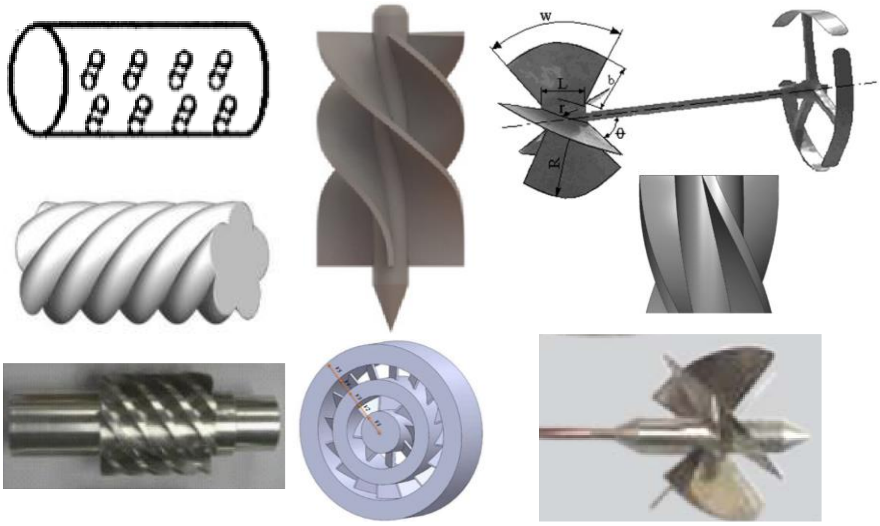

Figure 2.4: Inlet swirl generator designs including perforated swirlers [41], twisted lobes [50] and axial vanes [43], [95], [128], [162], [163], [164]

- Durmus [40] designed snail-like swirl generator with five angles. It was found that Nusselt number was improved by the 200% with a pressure drop of 160%. However, swirl decay was not observed due to high inlet flow rates, masking long-term performance trade-offs.
- Akpinar et al. [41] proposed swirl generators with zig-zag and straight holes with different number of holes and hole diameters. It was deduced that Nusselt number was increased by 140% with smaller holes, but the overall performance was reduced due to the increased pressure drop. Even though larger holes achieved less thermal enhancement, but the overall performance was found to be better in comparison to the former.

- Baiman and Kelvin [42], [43], [44], [45], [46] experimentally and numerically investigated annular swirl flow using axial vanes (30°, 45°, 60°) under laminar and turbulent regimes. Their investigations included:
    - Swirl intensity decayed exponentially downstream, with higher vane angles exhibiting faster decay due to increased viscous dissipation.
    - Laminar flow showed velocity profiles skewed toward the outer wall, while turbulent flows were Reynolds number independent.
    - Modified Kays [47] and Shah-Bhatti [48] correlations to account for annular swirl decay in laminar flow. However, no universal model was found for transitional regimes (1500<Re<3000).
- Jafari et. al. [49], [50] proposed innovative four and five-lobe swirl generators for turbulent flow. These designs achieved a Nusselt number enhancement of 40% with a pressure drop of 15% in comparison to other designs mentioned in their paper. Nevertheless, a significant drop in overall performance was noticed in the case of laminar flow.

While these techniques enhance short-term thermal performance, their long-term viability hinges on managing swirl decay – a challenge unresolved in current literature. The following section evaluates predictive correlations for swirl decay dynamics to address this gap.

2.3 Swirl Decay Correlation

Swirl decay, the axial reduction of rotational momentum, is critical for designing efficient swirl-enhanced heat exchangers. This section synthesises foundation and modern correlations, emphasising their assumption, limitations and applicability to annular flows. The foundational correlations include:

- Baker [51] proposed an empirical correlation for swirl decay in long pipes. This was limited to specific experimental conditions. This correlation was used in various applications including heat exchanger, combustion chambers, and chemical reactors.
- Senoo and Negata [52] refined and expanded upon the Baker correlation, incorporating additional parameters and considering different swirl generator designs.
- Kreith and Sonju [53] have theoretically derived a correlation for tape-induced turbulent swirl:

  $$X_n(x) = A_n e^{-\frac{\lambda_n^2(1+\epsilon)}{N_R}x} \qquad (2.1)$$

  $X_n(x)$ is the function of swirl number of x which is the axial location in the pipe. λ_n is the decay rate. ϵ is the eddy diffusivity. N_R is the Reynolds number. This was significant as it linked swirl decay to turbulence parameters.

- Scott [54] published an analytical solution showing that the decay rate was found to present a consistent multiple of 5.23λ.
- Kitoh [55] proposed an exponential correlation to provide a more accurate representation of turbulent annular swirl decay:

  $$\Omega \;=\; \Omega_r e^{2a_1\frac{x-x_r}{d}} \qquad (2.2)$$

  Ω is the local swirl intensity at axial location, x. x is the axial position. Ω_r is the swirl intensity at the selected reference point. x_r is the axial position of the selected reference point. a_1 is the first coefficient of the power series evaluating the wall shear stress. d is the hydraulic diameter of the annulus. This version was considered to be a cornerstone in understanding annular swirl decay for the following benefits:

- **Exponential Decay:** It establishes the exponential nature of swirl decay, indicating a rapid initial decrease in swirl intensity followed by a more gradual decline.
- **Decay Constant:** This parameter quantifies the rate of swirl decay and is influenced by various factors, such as Reynolds number, swirl generator geometry, and annulus dimensions.
- **Predictive Capability:** The correlation provides a simple yet effective means of predicting the swirl intensity at any axial location, facilitating the design and optimization of swirl flow devices.

Some of the limitations that restricted the use of this correlation include:

- Specific swirl generator configuration (tangential inlet).
- Fully developed turbulent flow regime.
- Validation was conducted for low swirl number (<0.04).

For higher swirl numbers of results led to an approximately linear relationship of constant rate of decay (at 6).

Modern advances were built on the Kitoh correlation following the exponential form of the equation and expanding the range of applications it could be applied in. These are included in Table 2.1.

Table 2.1: List of recent developments in the evaluation of swirl decay and decay rate.

Author	***Contribution***	***Equation No.***	***Limitations***
Reader-Harris [56]	$w \propto e^{-\frac{\beta x}{D}}$ $\beta = 1.07\lambda$	(2.3) (2.4)	Pipe
Steenbergen et al. [57]	$S = \alpha e^{-\frac{\beta x}{D}}$ $\beta = (1.49 \pm 0.07)\lambda$	(2.5) (2.6)	$0 \leq S \leq 0.18$
Sheen et al. [58]	$S = C_1(Re)\sigma(\phi)$	(2.7)	Air Radial-type swirl generators Annulus $300 \leq Re \leq 6{,}000$
Najafi et al. [59]	$\beta = 0.0401$	(2.8)	Pipe $0.144 \leq S \leq 0.594$ $15{,}000 \leq Re \leq 60{,}000$
Cavazzuti et al. [60]	$\beta = 0.14 f^{0.49}$	(2.9)	Air and Water Annulus $3{,}000 \leq Re \leq 1{,}000{,}000$
Yan et al. [61]	$\beta = (1.73 \pm 0.03)f$	(2.10)	Pipe Water $50{,}000 \leq Re \leq 125{,}000$

w represents the tangential component of velocity. S is the swirl number. Re represents the Reynolds number. β is the rate of decay. λ is the friction coefficient. f is the friction factor. $C_1(Re)$ and $\sigma(\phi)$ are the Reynolds number and geometrical functions, respectively [58].

From the aforementioned table, it was found that there were several trends followed in the correlations developed. These included the decay rate being consistently linked to the friction factor/coefficient, and the geometry of the swirler dominates decay dynamics more than the fluid properties.

Recent analyses, notably by Seibold et al. [62], emphasize that the swirl decay parameter, β, remains valid only for low swirl intensities ($S \leq 0.04$), where tangential wall shear stress exhibits a linear relationship with S. For higher S, β inherently varies with local swirl intensity, rendering constant-β models theoretically inconsistent. Despite this, β persists as a practical metric in studies of high-S flows ($S > 0.04$ to $S = 18.9$ [63], [64], [65]), as secondary factors (e.g., fluid properties, geometric nuances) are often negligible within experimental uncertainty. This compromise stems from β's empirical correlation with friction factor, which scales predictably with Reynolds number across regimes ($S \leq 0.18$ [57], $S \leq 0.8$ [66]) due to diminishing viscous effects at high Reynolds number [67]. However, the reliance on β as a universal decay metric underscores a critical gap:

- High swirl number applications (e.g., compact heat exchangers).
- Variable flow regimes (laminar to turbulent transitions).
- Geometric adaptability (e.g., adjustable vane angles).

These limitations motivate the exploration of discontinuous swirler configurations, where decay is dynamically controlled through modular geometry and strategic placement, addressing both theoretical inconsistencies and practical scalability.

2.4 Discontinuous Swirler Arrangement

Discontinuous swirlers, strategically spaced devices inducing intermittent swirl, offer a promising solution to balance heat transfer enhancement and pressure drop penalties. Unlike continuous designs, they localise rotational motion, reducing flow obstruction while amplifying turbulence through repeated boundary layer disruption.

Saha et al. [68] investigated regularly spaced twisted tapes in a tube under constant wall heat flux. The studies found that spaced tapes reduced friction by 40% against full-length tapes, with slight heat transfer loss. Force-fit installations outperformed rod-connected designs. Phase angle variations showed negligible impact and besides adding manufacturing complexity.

Rahman [69] designed conical deflector baffles with variable inclination angles in shell-side flow. The maximum overall performance achieved was 1.96 times that of a smooth plain shell at highest inclination angle and lowest height ratio. However, there was no analysis of swirl decay dynamics between baffles.

Esmaeili et al. [70] proposed vanes extruded on inner and outer surfaces of double pipe heat exchanger concentric tubes. Nusselt number and pressure drop increased at minimal spacer distances up to 73% and 87%, respectively. Maximum overall performance was evaluated 1.41.

Sheikholeslami et al. [8], [9] developed and compared the performance between perforated rings and helical turbulators shown in Figure 2.5. Results showed that perforated rings achieved higher overall performance due to the greater reduction in pressure drop in comparison to loss in Nusselt number. However, higher Nusselt number enhancement was achieved by helical turbulators but with a lower overall performance with increasing holes and pitch. The trade-off found in this research was the hole configuration critically balances the Nusselt number and pressure drop.

Figure 2.5: Discontinuous perforated rings and helical turbulators proposed by Sheikholeslami et al. [8], [9]

Kumar et al. [71] designed hemispherical turbulators inducing recirculation zones, boosting local turbulence achieving increases in Nusselt number of 44% and pressure drop of 96%. Optimal pitch ratio minimised flow resistance while maximising mixing of the flow.

Yadav et al. [72] investigated the effects of helical surface disks. These achieved a maximum overall performance 1.5 times at high helix angles and low diameter ratios. Smaller pitch ratios increased Nusselt number by 201% and pressure drop by 196% via intensified recirculation. Complex manufacturing offsets performance gains.

In light of innovative approaches, Figure 2.6 presents the freely rotating swirlers [73], [74]. Flow-driven rotation cut pressure drop penalties by 60% in comparison to fixed designs. This self-adaptive feature to flow conditions was found to stand out for transient operations. Another approach was the mesh inserts [75]. These disrupted the flow with minimal blockage showing a small increase in pressure drop of about 25%-40% improving the overall performance of the heat exchanger by 1.3-1.8 times than the smooth plain heat exchanger. This method holds a potential of being scalable for low-cost retrofitting in existing systems.

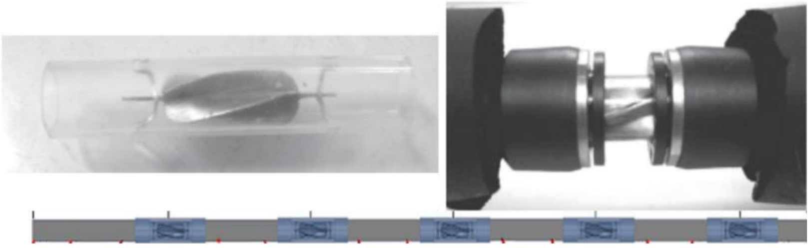

Figure 2.6: Freely rotating turbine type swirl generators by Duangthongsuk et al. [74]

With regards to the critical synthesis of this section, key advantages can be listed as the following:

- Reduced Pressure Drop: Spacing lowers flow obstructions in comparison to continuous designs.
- Enhanced Mixing: Periodic swirl regeneration disrupts thermal boundary layers.
- Design Flexibility: Modular placement adapts to thermal load variations.

On the other hand, some limitations associated with this technique includes:

- Swirl Decay Neglect: Most studies ignore decay between devices, overestimating gains.
- Geometric Fragmentation: Reduces the thermal gain in the heat exchanger.

The gaps that can be extracted from this section are:

- Untapped Potential: No studies combine discontinuous placement with variable swirl intensity.
- Decay Management: Absence of predictive models for localised decay between swirlers.
- Optimisation Framework: Limited tools for spacing and geometry trade-off analysis.

This thesis bridges these gaps by introducing:

- Decay Percentage: Quantifying allowable swirl loss between devices.
- Full Swirling Configuration: Discontinuous arrays with angle optimised vanes.

While discontinuous swirlers improve design flexibility, their static geometries cannot adapt to dynamic flow conditions. The following section explores variable-swirl-intensity generators to address this limitation.

2.5 Variable Swirl Intensity Swirl Generators

Variable swirl intensity generators dynamically modulate rotational momentum along the flow path by altering vane angles or twist ratios. Unlike fixed designs, they optimise heat transfer by adapting to local flow conditions, enhancing upstream mixing while mitigating downstream pressure penalties.

Saha et al. [76] used segmented twisted tapes with gradually decreasing pitch (four equal segments). This reduced Nusselt number along with the pressure drop by 15% when compared to the tape with uniform pitch. Also, overall performance decreased as a consequence of inconsistent swirl generation.

Sivashanmugam et al. [77] proposed a full-length helical screw with increasing and decreasing twist ratios. Two examples are shown in Figure 2.7. Results showed that lower twist ratios increased swirl intensity, increasing Nusselt number and pressure drop regardless it was increasing or decreasing twist ratios. No performance difference was found between either configuration.

Figure 2.7: Helical screw inserts of increasing twist ratio and decreasing twist ratio. [77]

On the other hand, Yang et al. [78] utilised twist tapes with increasing and decreasing twist ratios in thermoelectric generators. Significant observations included that increasing twist ratios increased the output power by 25% via flow instabilities and reduced upstream pressure drop.

This outperformed constant ratio tapes by 5.9% in efficiency. However, observation of similar results in other applications have not been found in the literature.

This section presented the advantages of using variable swirl intensity swirl generators which include:

- Adaptive Optimisation: Higher swirl upstream (where thermal gradients are steepest) improves temperature uniformity.
- Pressure Management: Increasing ratios reduced pressure drop penalties.

Through the literature, the gaps that were bridged by this thesis are listed as:

- Discontinuous Variable Intensity Arrays: Modular swirlers with location specific angles (30-60) to sustain optimal swirl.
- Decay Percentage Optimisation: Quantifying allowable intensity drop between modules.

While variable intensity generators improve spatial adaptability, their inability to manage transient swirl decay necessitates advanced turbulence modelling. The following section evaluates predictive tools for swirl flow dynamics.

2.6 Review of Turbulence Models and Prediction Capabilities in Swirl Flow

Turbulence models provide computationally efficient alternatives to physical experiments, enabling detailed insights into complex swirl flow behaviour. While laminar flows are governed by standard Navier-Stokes equations (provided in the upcoming chapter 4: Methodology), turbulent flows require additional transport equations to model turbulent kinetic energy and dissipation rate. Important approaches include:

- Direct Numerical Simulation (DNS) [79]:
  - Solves all turbulent scales without modelling.
  - Strength: Achieves highest accuracy for fundamental flow physics.
  - Limitation: Is a less favoured approach due to the high computational costs (weeks or months for industrial cases).
- Large Eddy Simulations (LES) [80]:
  - Resolves large eddies directly; models subgrid scales.
  - Strength: Captures transient structures in high-swirl flows.
  - Limitation:
    - Mesh-sensitive demanding high mesh density.
    - Moderate computational cost but remains to be considerably high (days or weeks per simulation).
- Reynolds-Averaged Navier Stokes (RANS) Models: Balance accuracy and efficiency via turbulence averaging:
  - Reynolds Stress Model (RSM) [81]: Solves transport equations for all stresses.
    - Pro: Accurate for strong swirl anisotropy.
    - Con: High cost (10 times slower than other models [82])
  - Standard $K - \epsilon$ Model [83]:
    - Pro: Robust for simple shear flows; low computational cost.
    - Con: Overpredicts swirl decay rate in rotating or curved streams.

- Re-Normalisation Group (RNG) $K - \epsilon$ Model [84]: Modifies the turbulence equations for rotational flows.
    - Pro: Robust for moderate swirl.
    - Con: Underpredicts near-wall effects.
- Realizable $K - \epsilon$ Model [85]:
    - Pro: Improved vortex stability which is suitable for moderate swirl.
    - Con: Underpredicts separation in high-swirl annular flows.
- Shear Stress Transport (SST) $K - \omega$ Model [86]: Blends $K - \epsilon$ (free stream) and $K - \omega$ (near-wall).
    - Pro: Excels in boundary layer separation and swirl decay prediction.
    - Con: Sensitive to initial boundary conditions and more computationally expensive.

The following table, Table 2.2, evaluates these models against experimental data, quantifying their accuracy for key swirl flow parameters.

Table 2.2 A review of different models and the outcomes achieved in recent annular investigations.

Author	Model	Governing Parameters	Research Outcomes
Jawarneh et al. [87]	RNG	• $5000 \leq Re \leq 10000$ • Swirl Number= $0-3$ • $r^* = 0.8$	• Predictions calculated by the model showed excellent agreement with experimental data. • Increasing swirl number: ○ Improved Nu at the inner wall of the annulus. ○ Increased the axial velocity profile near-wall and reduced it at the core of the annulus resulting in higher heat transfer rates.
Rahman et al. [88]	SST	• $17500 \leq Re \leq 68500$ • $r^* = 0.4$	• Axial fully developed flow were simulated accurately using SST. • The simulations predicted the velocity and near wall velocity profiles accurately. • Accurately capturing the near wall vorticity and K provides evidence for an enhanced turbulent activity in the near wall viscous sub-layer and log-law regions.
Parra et al. [89]	RNG	Mixing of Two Confined Coaxial Jets: • $\theta_{sw} = 22^\circ, 54^\circ$ and 64° • $SN = 0.14, 0.74$ and 0.95 • $r^* = 0.43$	• Pressure distribution in high and intermediate swirling cases result in the formation of a vortex bulb around the central axis of the chamber. • Utilising a swirler in the burning chamber allows lean burning of mixtures near the exit of the swirler due to the deflection of the shear and increased gradients caused by the inner recirculation zone.
Xiong et al. [90]	SST	• $8900 \leq Re \leq 38700$ • $r^* = 0.4, 0.5$	• Annular fully turbulent axial velocity profile showed an asymmetry deviating towards the inner wall which along with position of maximum axial velocity, Reynolds shear stress and average vorticity were accurately captured by the SST model. • Variation in Re and r^* affected the velocity profile. • Increasing Re resulted in the change near-wall velocity profile indicating the decay of the viscous sublayer. • Due to the larger surface area provided, Reynolds stress was approximated to be higher at the outer wall supporting higher turbulent energy.

			• Increase in Re caused higher shear production but the peak location was independent of both variables. • Compared to DNS, SST failed to capture the inverse cascade of K in the buffer layer causing a deviation in the results of the viscous dissipation terms.
Xu et al. [91]	RNG	• Swirling Impinging Jet and Multi-Channel Impinging Jet. • $4000 \leq Re \leq 12000$ • $r^* = 0.56$, 0.67 and 0.83. • $\theta_{sw} = 0° - 75°$ • Jet spacing = 1, 2, 3, 4, 6 and 8	• The model showed excellent agreement with the experimental data. • For all $\theta_{sw} > 0°$, the radial Nu was higher than that in $\theta_{sw} = 0°$. • When Re increased, the swirling impinging jet improved the radial uniformity of heat transfer enhancing U. • The effect of the swirl was mostly limited to the stagnation region. • As θ_{sw} increased the swirl intensity increased resulting in the enhancement of the radial Nu. • Good radial uniformity of Nu was achieved by $\theta_{sw} = 60°$ in the turbulent regime with jet spacing = 3. • Jet spacing proved to be the most influential factor on the radial uniformity of Nu.
Baiman et al. [46]	• Laminar • Standard $K - \epsilon$	• $\theta_v = 60°$, 45° and 30° • $1215 \leq Re \leq 3472$ • $r^* = 0.65$	• Increasing Re increased Nu, but was limited by the local swirl number. • A function of Nu was proposed. • In steady state: ○ Nu increases for all angles in comparison to axial flow. ○ In case of the 30°, Nu increased near the exit of the swirler before decaying. • In transient: ○ Cooling of the solid rod varied linearly when $Re < 500$. ○ Increasing Re caused the temperature of the solid to vary non-linearly. ○ Cooling time was shown to be inversely proportional to Re. ○ As θ_v increases, local SN decreases resulting in decreasing heat transfer rate.

Luo et al. [92]	Laminar	• Twist Pipe Ratio: $1-2$ • $r^* = 0.5, 0.57, 0.67, 0.8, 0.89$ and 1 • $1215 \leq Re \leq 3472$	• Different twist pipe ratio between the annulus and the tube can generate strong annular pipe allowing better heat transfer. • Nu and f increased significantly with unequal twist pitches. • Optimum twist pipe ratio was found to 1.5 obtaining the highest PEC. • Correlations were developed for Nu, f and PEC.
Hangi et al. [93]	Laminar	Annular Helical Strip with Tubular Helical Screw-Type Insert: • $Re \approx 750$ • Number of Helical Periods • Number of Helical Fins • $r^* = 0.65$	• Increasing number of periods and fins increased U. • Increasing the nanoparticles concentration increased U. • The most intense mixing was found with 4 periods and fins resulting in the highest exergy efficiency generating the most uniform temperature distribution.
Shakeel et al. [82]	RNG	• $4000 \leq Re \leq 16000$ • Straight, diverging and converging annular cross sections. • r^* = 8/16, 8/20 and 8/26. • θ_{sw} = 30°, 45°, 60° and 70°	• SN increase to a peak after exiting the swirler. • Increasing Re increased the SN except in the converging annulus. • Decreasing r^* increased SN. • Increasing θ_v increased the SN.
El Maakoul et al. [94]	Realizable	• Helical and Longitudinal Fins • Helical Fin Spacing = $0.05-0.2m$ • $12700 \leq Re \leq 17700$ • $r^* = 0.5$	• Helical fins provide higher heat transfer area, rate and PEC than longitudinal fins. • Spacing $0.1m$ produced the highest PEC, while 0.05m produced the highest rate of heat transfer.
Liu et al. [95]	RNG	• Double-stage counter-rotating swirler • θ_{sw} = 45° for both stages • $5425 \leq Re \leq 54{,}245$	• RNG demonstrated a superior performance in predicting recirculation zone length, transverse velocity and vorticity. • SN presented a fluctuating behaviour with increasing Re downstream from the swirler. The fluid impact on the wall was significant increasing turbulent kinetic energy at the wall. • The fiction coefficient presented fluctuations near the swirler exit. • Vorticity distributions were shown to follow an alternating pattern of positive and negative values in the shear layer of the confining the zone.

2.7 Summary

This review synthesises critical advancements and unresolved challenges in swirl flow applications for double-pipe heat exchangers. Key findings reveal that swirl generators, including twisted tapes, helical inserts, and inlet vanes, significantly enhance heat transfer by disrupting thermal boundary layers, with Nusselt number improvements depending on geometry and flow conditions. However, these gains are invariably accompanied by pressure drop penalties, creating fundamental trade-off between thermal performance and pumping power. Passive techniques like discontinuous swirlers mitigate this by localising swirl induction, reducing pressure drop while maintaining heat transfer enhancement. Nevertheless, critical knowledge gaps persist.

First, annular swirl decay dynamics remain inadequately quantified. While exponential decay models (e.g., Kitoh's correlation) predict behaviour for low swirl numbers ($S \leq 0.18$) in turbulent flows, they fail in transitional regimes ($1500 < Re < 3000$) and high swirl scenarios ($S > 1.0$), where viscous interactions and geometric effects decay rates. Second, existing discontinuous swirler studies neglect axial decay between devices, overestimating performance in long heat exchangers. Third, variable-intensity designs (e.g., decreasing-pitch tapes) show promise for spatial adaptation but lack integration with modular placement strategies. Finally, turbulence models like RNG $K - \epsilon$ and SST $K - \omega$ offer reasonable predictive accuracy for moderate swirl.

This research addresses these gaps through the following innovations:

- ❖ Decay Percentage Parameter: A novel metric defining allowable swirl loss between discontinuous swirl generators to optimise thermal-fluidic balance.
- ❖ Full Swirling Configuration: Discontinuous arrays with location-specific vane angles (30°➔60°) sustaining swirl intensity along the exchanger length.

Building on these foundations, Chapter 3 establishes standardised performance evaluation parameters, including Nusselt number, friction factor, and the Performance Evaluation Criterion, to quantitatively assess the thermal-hydraulic trade-offs in double-pipe heat exchangers. These metrics provide the analytical framework for evaluating the novel strategies proposed in this thesis.

Chapter 3: Performance Evaluation Parameters

3.1 Introduction

In this chapter, the correlations acquired from the literature are used to evaluate target parameters and validate against the numerical simulations. As water is used as the working fluid in both the hot and cold domains of the $DPHE$, the acquirement of the physical properties required for calculations will be described. The analysis of a heat exchanger starts with finding the film temperature (T_m) of the working fluid. This is the average temperature of the working fluid between the inlet and the outlet of the test section. At this temperature physical properties of the working fluid can be extracted from the steam tables provided by Roger and Mayhew in [96]. In this investigation cold water will flow through the annulus while hot water will flow in the tube in a counter flow configuration. The film temperature will be evaluated as:

$$T_m = \frac{T_{h,in} + T_{c,in}}{2} \tag{3.1}$$

Where the subscripts h, c and in represent hot, cold and inlet of the test section, respectively. Based on Newton's law of cooling [97], the rate of convective heat transfer is the rate of heat transfer supplied by the hot water and absorbed by the cold water. The rate of convective heat transfer ($\dot{Q}$) for the hot and cold fluids can be expressed as:

$$\dot{Q}_h = \dot{m}_h c_{p,m}(T_{h,in} - T_{h,out}) \tag{3.2}$$

$$\dot{Q}_c = \dot{m}_c c_{p,m}(T_{c,out} - T_{c,in}) \tag{3.3}$$

Where $\dot{m}$ represents the mass flow rate at which the fluid enters the test section. This is evaluated using the cross-section area (A_{cs}) of the duct as:

$$\dot{m} = \rho_m A_{cs} u_{avg} \tag{3.4}$$

3.2 Nusselt Number

Nusselt number (Nu) is another important output acquired by researchers to represent a dimensionless form of the heat transfer coefficient (h) of the system. It is evaluated using:

$$Nu = \frac{h \cdot D_{hd}}{k_m} \tag{3.5}$$

where the hydraulic diameter (D_{hd}) and the thermal conductivity at film temperature (k_m) are constants. A legion of correlations has been developed over the years for various configurations of heat exchangers. However, some are distinguished from others where some are specific for laminar regimes which can be derived theoretically [98], and some are specific for turbulent regimes which can only be correlated empirically [99]. Most of these correlations have been gathered and listed in great textbooks such as [100], [101] and published work such as [99], [102] . However, since the focus of this investigation is on the annular side in both laminar and turbulent flows, evaluating Nu was found to be more complex in comparison to the correlations found in the tube due to the different effects, namely shear stresses, present at the inner and the outer walls have on the velocity profile of annular flow.

In laminar flow, a recent publication made by Hirbodi et al. [103] where they propose an accurate way to evaluate local and average Nusselt numbers for a hydrodynamically developed flow while thermally developing (Nu_D) and a fully developed flow (Nu_{FD}). There are four kinds of boundary conditions under which these correlations apply:

1. The **temperature** of either the inner or outer walls is **equal to** that of the **incoming fluid** while the **other wall** is at a **different** temperature.
2. There is a **constant heat flux** on either wall while the other is **insulated**.
3. There is **constant temperature** on one wall **different from** that of the **incoming fluid** while the other wall is **insulated**.
4. There is **constant heat flux** on one wall while the other is at a **temperature equal to** that of the **incoming fluid**.

Some parameters that need to be defined are Graetz Number (Gz) from [100] (which is redefined in this paper as the dimensionless axial distance ($\bar{x}$)), a dimensionless radial distance ($\bar{r}$) and radius ratio (r^*).

$$Gz^{-1} = \bar{x} = \frac{z}{D_{hd}(Re)Pr} \tag{3.6}$$

$$\bar{r} = \frac{r}{r_0} \tag{3.7}$$

$$r^* = \frac{r_i}{r_0} \tag{3.8}$$

The current investigation involves a $DPHE$ in counter flow arrangement in which heat transfer occurs along the wall of the inner tube. Among the previous four conditions, the best condition to assume with regards to a $DPHE$ in counter flow arrangement is the constant heat flux at the tube wall while the outer wall of the annulus is insulated. This led to a general form of local Nusselt number, when the flow is fully developed in the laminar regime, to be expressed as:

$$Nu_{FD}{}_{i,i}^{2} = 1.27r^{*-0.781} + 0.035r^{*-1.091} + 4.133 \tag{3.9}$$

The superscript 2 indicates that the second condition is applied, and the subscripts indicate that the inner wall of the annulus is the target wall of this calculation, and the inner wall is also the nonzero boundary condition. This correlation is applicable in the range of $0 \leq r^* \leq 1$. The coefficients and exponents of r^* are constants collected from Table 2 in [103]. Furthermore, in case of the thermally developing flow, the general correlation can be expressed in terms of Nu_{FD} and is broken down to several equations:

$$Nu_{D}{}_{i,i}^{2} = Nu_{FD}{}_{i,i}^{2} + H_{i,i}^{2} \tag{3.10}$$

$$H_{i,i}^{2} = B_{i,i}^{2}\bar{x}^{(C_{i,i}^{2})}e^{(D_{i,i}^{2}\bar{x})} \tag{3.11}$$

$$B_{i,i}^{2} = 0.038r^{*-0.868} + 0.552 \tag{3.12}$$

$$C_{i,i}^{2} = 0.007r^{*-0.452} - 0.426 \tag{3.13}$$

$$D_{i,i}^{2} = -124.8r^{*0.023} + 62.41 \tag{3.14}$$

The constants in Eqs.(3.12)-(3.14) are collected from Table 3 in [103]. It is important to note that Eqs.(3.10)-(3.14) are applicable in the ranges of $0.02 \leq r^* \leq 1$ and $\bar{x} \geq 0.0001$. Similarly, when it came to calculating the average Nusselt number of a thermally developing flow ($\overline{Nu}$), the general form can be expressed as:

$$\overline{Nu}_{i,i}^2 = {Nu_{FD}}_{i,i}^2 + \bar{B}_{i,i}^2 \bar{x}^{(\bar{C}_{i,i}^2)} e^{(\bar{D}_{i,i}^2 \bar{x})} \tag{3.15}$$

$$\bar{B}_{i,i}^2 = 0.085 {r^*}^{-0.778} + 0.78 \tag{3.16}$$

$$\bar{C}_{i,i}^2 = 0.005 {r^*}^{-0.578} - 0.411 \tag{3.17}$$

$$\bar{D}_{i,i}^2 = 10.03 {r^*}^{-0.054} - 30.04 \tag{3.18}$$

The constants in Eqs.(3.16)-(3.18) are collected from Table 4 in [103]. Along with Eq.(3.15), these equations are applicable in the ranges of $1/50 \leq r^* \leq 10/11$ and $\bar{x} \geq 0.0001$. Eqs.(3.6)-(3.18) will be used in the validation of the numerical methodology described in section 4.3.5. With regards to turbulent flow, validation will be done against the annular correlations found in the literature listed in Table 3.1

The author would like to extend their appreciation to Dirker and Meyer's work in helping to assemble most of this table in their thesis in [102]. This table is reordered in a chronological order and three more correlations have been developed since and added to this table. It should be noted that all thermophysical properties and hydraulic diameter considered in this table are the ones corresponding to those evaluated at film temperature and annulus, respectively.

It is noteworthy to mention that the correlation in Eq. (3.19) commonly referred to as the Dittus Boelter equations, but in their technical note Winterton [104] clarified that McAdams [105] modified the Dittus Boelter's correlation. However, further reading of the note [104] is recommended for a full understanding of the "Origin of $Nu = 0.023Re^{0.8}Pr^{0.4}$".

Table 3.1 Nusselt number correlations from the literature for smooth concentric annulus.

Year	Author (s)	Correlation	Operation Range	Re	Medium	Equation
1930	Dittus-Boelter [106]	$\mathrm{Nu}_{DB} = 0.023\mathrm{Re}^{0.8}\mathrm{Pr}^{n}$ $n = 0.4$ for heating $n = 0.3$ for cooling	Not specified	Not specified	Not specified	(3.19)
1940	Foust and Christian [107]	$\mathrm{Nu}_{\mathrm{FC}} = \frac{0.04a}{(a+1)^{0.2}}\mathrm{Re}^{0.8}\mathrm{Pr}^{0.4}$	$1.2 \leq a \leq 1.84$	$3000 - 60000$	Water	(3.20)
1942	Monrad and Pelton [108]	$\mathrm{Nu}_{\mathrm{MP}} = 0.023\left[\frac{2\ln(a) - a^2 + 1}{a - 1/a - 2a\ln(a)}\right]\mathrm{Re}^{0.8}\mathrm{Pr}^{n}$	$1.65, 2.45, 17$	12000 $- 220000$	Water and air	(3.21)
1943	Davis [109]	$\mathrm{Nu}_{DA} = 0.038a^{0.15}(a-1)^{0.2}\mathrm{Re}^{0.8}\mathrm{Pr}^{1/3}\left(\frac{\mu}{\mu_w}\right)^{0.14}$	$1.18 \leq a \leq 6800$	Not specified	All mediums	(3.22)
1945	Wiegand et al. [110]	$\mathrm{Nu}_{WG} = 0.023a^{0.45}\mathrm{Re}^{0.8}\mathrm{Pr}^{n}\left(\frac{\mu}{\mu_w}\right)^{0.14}$	$1 \leq a \leq 10$	> 10000	Fluids of $\mu_{material} \leq 2\mu_{water}$	(3.23)
1954	McAdams [105]	$\mathrm{Nu}_{MA1} = 0.03105a^{0.15}(a-1)^{0.2}\mathrm{Re}^{0.8}\mathrm{Pr}^{1/3}\left(\frac{\mu}{\mu_w}\right)^{0.14}$	$1.18 \leq a \leq 6800$	Not specified	All mediums	(3.24)
1954	McAdams [105]	$\mathrm{Nu}_{MA2} = 0.023\mathrm{Re}^{0.8}\mathrm{Pr}^{1/3}\left(\frac{\mu}{\mu_w}\right)^{0.14}$	Not specified	Not specified	Not specified	(3.25)
1958	Stein and Begell [111]	$\mathrm{Nu}_{SB} = 0.0200a^{0.5}\mathrm{Re}^{0.8}Pr^{1/3}$	a $= 1.232, 1.463, 1.694$	30000 $- 390000$	Water	(3.26)
1963	Kays and Leung [112]	Results are listed different tables depending on operating conditions.	$1 \leq a \leq \infty$	10000 $- 1000000$	Not specified	(3.27)

1964	Petukhov and Roizen [113]	$\mathrm{Nu}_{PR} = \frac{0.06759a^{0.16}}{(a+1)^{0.2}} f\,\mathrm{Re}^{0.8}$ $\mathrm{f} = 1 + 7.5\left[\frac{a-5}{(a+1)Re}\right]^{0.6}$ for $a \geq 5$ $\mathrm{f} = 1$ for $a \leq 5$	$1 \leq a \leq 14.3$	10000 − 300000	Air	(3.28)
1968	Crookston et. al. [114]	$\mathrm{Nu}_{CS} = 0.023a^{1/4}\mathrm{Re}^{3/4}\mathrm{Pr}^{1/3}$	$a = 10,16,31$	17000 − 100000	Air	(3.29)
1990	H. Martin [115]	$Nu_{HM} = (Nu_1^3 + Nu_2^3)^{1/3}$ $Nu_1 = 3.66 + 1.2r^{*-0.8}$ $Nu_2 = f_{g,i}\sqrt[3]{Re \cdot Pr \cdot D/L}$ $f_{g,i} = 1.615\left[1 + 0.14r^{*-1/2}\right]$		≤ 2300	Air	(3.30)
1995	Gnielinski [116]	$Nu_{avg} = (1-\gamma)Nu_{lam,2300} + \gamma Nu_{turb,10^4}$ $\gamma = \frac{Re - 2300}{10^4 - 2300}$ $Nu_{lam,2300} = \left(Nu_{1,i}^3 + Nu_{2,2300,i}^3 + Nu_{3,2300}^3\right)^{1/3}$ $Nu_{1,i} = 3.66 + 1.2r^{*-0.8}$ $Nu_{2,2300,i} = f_{g,i}(2300Pr \cdot D/L)^{\frac{1}{3}}$ $Nu_{3,2300,i} = \left\{\frac{2}{1+22Pr}\right\}^{\frac{1}{6}}(2300Pr \cdot D/L)^{1/2}$ $Nu_{turb,10^4,i} = \frac{\frac{f_a}{8}(Re - 1000)Pr}{k_1^* + 12.7\sqrt{\frac{f_a}{8}}\left(Pr^{\frac{2}{3}} - 1\right)}\left[1 + \left(\frac{D}{L}\right)^{\frac{2}{3}}\right]F_a$	$0 \leq \gamma \leq 1$	2300 − 10000	Not specified	(3.31)

		$f_{g,i} = 1.615[1+0.14r^{*-1/2}]$ $f_a = (1.8\log(Re^*) - 1.5)^{-2}$ $Re^* = Re\frac{[1+r^{*2}]\ln(r^*)+[1-r^{*2}]}{[1-r^{*2}]\ln(r^*)}$ $k_1^* = 1.07+\frac{900}{2300}-\frac{0.63}{(1+10Pr)}$ $F_a = 0.75r^{*-0.17}$				
2004	Dirker et al. [117]	$\mathrm{Nu}_{DM} = \mathrm{C}_0\mathrm{Re}^P Pr^{1/3}\left(\frac{\mu}{\mu_\mathrm{w}}\right)^{0.14}$ $P = 1.013e^{-0.067a}$ $C_0 = \frac{0.003a^{1.86}}{0.063a^3-0.674a^2+2.225a-1.157}$	$1.7-3.2$	$4000-30000$	Water	(3.32)
2007	Gnielinski [118] (Modified from Petukhov and Kirillov [119])	$Nu_{GN} = \frac{\frac{f_a}{8}(Re-1000)Pr}{k_1+12.7\sqrt{\frac{f_a}{8}}\left(Pr^{\frac{2}{3}}-1\right)}\left[1+\left(\frac{D}{L}\right)^{\frac{2}{3}}\right]\left(\frac{Pr}{Pr_w}\right)F_a$ $k_1 = 1.07+\frac{900}{Re}-\frac{0.63}{(1+10Pr)}$ $f_a = (1.8\log(Re^*) - 1.5)^{-2}$ $Re^* = Re\frac{[1+r^{*2}]\ln(r^*)+[1-r^{*2}]}{[1-r^{*2}]\ln(r^*)}$ $F_a = 0.75r^{*-0.17}$	$0.6 \le Pr \le 1000$ $0 \le D/L \le 1$	$10000-1000000$	Water and Air	(3.33)
2009	Bernardi et. al. [120]	$\mathrm{Nu}_{BR} = 2.38\delta^{1/3}\mathrm{Gz}^{0.33}(\mathrm{r}^*)^{0.33}\left(\frac{\mathrm{K}}{\mathrm{K}_w}\right)^{0.14}$	$0.188 \le r^* \le 0.5$ $130.6 \le Gz \le 34000$	$42.8 \le Re_{mr} \le 2263.4$	Liquid egg yolk	(3.34)

		$\delta = \frac{3n+1}{4n}$ $K = 8.182 \times 10^{-9} e^{\frac{44195}{R \cdot T}}$ $R = 8.31451\, J \cdot mol^{-1} \cdot {}^\circ\mathrm{C}^{-1}$ $Re_{mr} = \left(\frac{\rho u_{avg} D^n}{8^{n-1} K}\right)\left(\frac{1}{\delta}\right)^n$ $n = 0.855 \pm 0.006$	$20.3 \leq L/D_h \leq 87.6$ $0.1 \leq K \leq 2.3$			
2021	Abou- Ziyan [121]	$\mathrm{Nu}_{AZ} = 0.0244\mathrm{Re}^{0.834}\mathrm{Pr}^{0.4} r^{*-0.15}$	$0.2 \leq r^* \leq 0.8$ $3.71 \leq Pr \leq 6.94$	$2000 - 123{,}618$	Water	(3.35)

3.3 Friction Factor

Friction factor correlations evolved through foundational work by Darcy-Weisbach [122] and Moody who put together the Moody chart [19] in Figure 3.1. The Darcy-Weisbach friction factor equation is applied in this study to evaluate hydraulic losses across duct geometries. The equation is defined as:

$$f = \frac{\Delta P}{\frac{L}{D_{hd}} \frac{\rho u_{avg}{}^{2}}{2}} \tag{3.36}$$

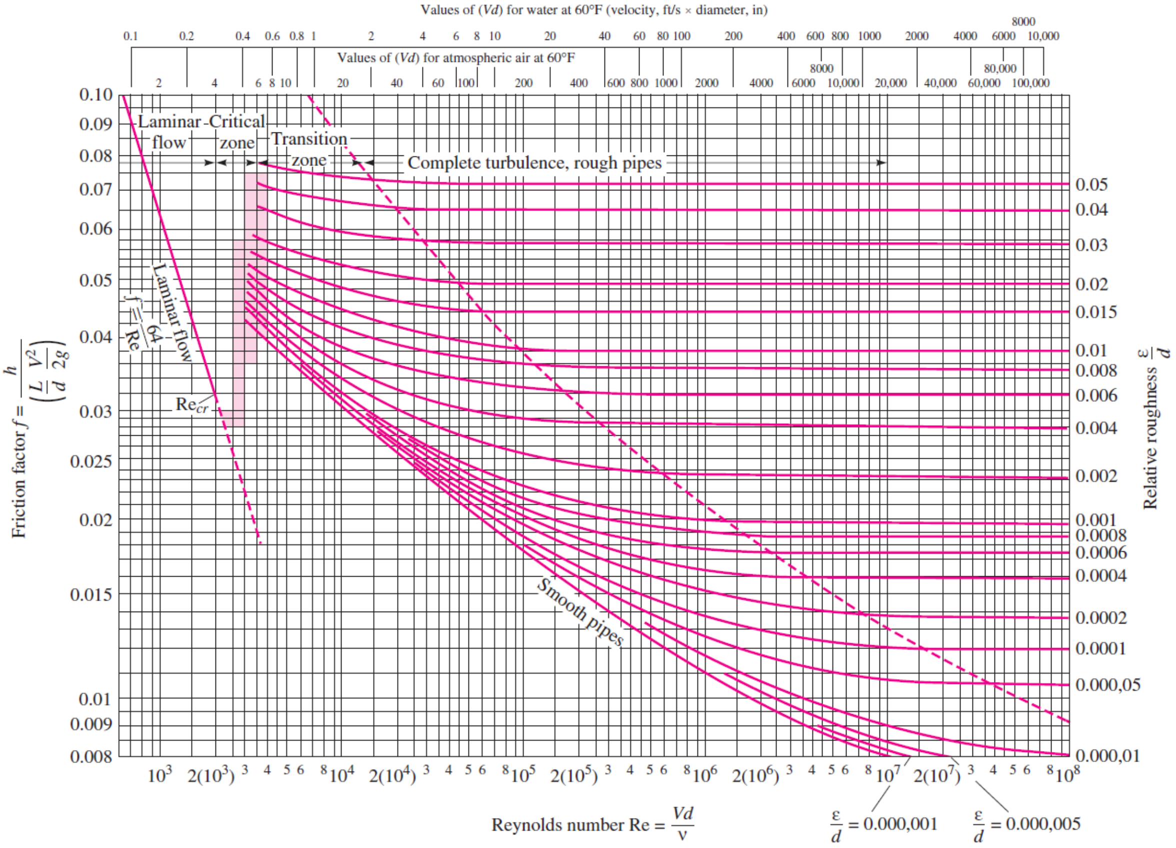

Figure 3.1: Friction coefficient chart evaluated at different Reynolds numbers and surface roughness developed by Moody [19].

According to the chart, when the flow is laminar ($Re \leq 2000$) friction factor in a pipe can be equated as:

$$f = \frac{64}{Re} \tag{3.37}$$

However, inside an annulus the equation is modified to account for the different shear stresses present at the walls where the stress at the inner wall is greater than the one at the outer wall. In turn, the hydraulic diameter of the annulus is used in evaluating Re (from Eq. (4.1)) and a dimensionless correction factor (ζ) is introduced in Eq. (3.37) in the form of:

$$f_a = \frac{64\zeta}{Re} \tag{3.38}$$

Where ζ is evaluated as:

$$\zeta = \frac{(r_o - r_i)^2({r_o}^2 - {r_i}^2)}{{r_o}^4 - {r_i}^4 - ({r_o}^2 - {r_i}^2)^2/\ln{(r_o/r_i)}} \tag{3.39}$$

When the flow is turbulent, Jones and Leung [123] concluded that the annular friction factor can be obtained with great accuracy by replacing the diameter used in Figure 3.1 by the effective diameter ($D_{eff} = 2(r_o - r_i)/\zeta$).

3.4 Performance Enhancement Criterion

A key metric for evaluating heat exchanger augmentation methods is the Performance Enhancement Criterion (PEC), introduced by Webb and Eckert [124]. The PEC compares the thermal performance gain and pressure drop penalty of an augmented double-pipe heat exchanger to that of a plain tube under constant pumping power.

The PEC is derived by equating the pumping power of the plain and augmented tubes, leading to the relationship:

$$(f.Re^3)_0 = (f.Re^3)_{aug} \tag{3.40}$$

This simplifies to:

$$\frac{Re_0}{Re_{aug}} = \left(\frac{{f_{aug}}^{\frac{1}{3}}}{f_0^{\frac{1}{3}}}\right) \tag{3.41}$$

Considering that the Nusselt number scales with Re^m, the thermal enhancement factor (η) at constant pumping power is:

$$\eta = \frac{Nu_{aug}/Nu_0}{(f_{aug}/f_0)^{1/3}} \tag{3.42}$$

The final form balances heat transfer improvement against the friction penalty providing a practical criterion for assessing augmentation techniques. For full mathematical derivation, see Appendix A. Furthermore, different functions of PEC have been used by different researchers in the literature. Karwa et. al. [125] have compared several different variations of Eq. (3.42) and gave a clearer explanation of the operating conditions that need to be satisfied to apply PEC correctly.

Chapter 4: Methodology

4.1 Introduction

This chapter presents the systematic methodology employed to achieve the research objectives:

- Characterising annular swirling flow topology and vortex dynamics
- Analysing heat transfer induced fluid behaviour changes
- Developing new method to improve overall thermal performance of the heat exchanger.

The approach integrates theoretical, numerical and analytical stages to investigate swirl intensity effects on double-pipe heat exchanger performance, focusing on two configurations: Single Swirling Configuration (SSC) and Full Swirling Configuration (FSC).

The methodology is structured in two sections. Governing parameters defines key variables (e.g., swirl angle, Reynolds number) and their ranges, justified through literature and preliminary simulations. Development of numerical model outlines the computational workflow, including:

- CAD Modelling: Replication of experimental geometries (e.g., swirlers at angles $30^{\circ}, 45^{\circ}, 60^{\circ}$) for cost-effective parametric testing.
- Mesh Optimisation: Grid independence tests to balance accuracy and computational efficiency.
- CFD Protocols: Implementation of RNG $\mathrm{K}-\epsilon$ turbulence model and boundary conditions.

This computational strategy enables precise visualisation of swirl decay and thermal performance trends, circumventing the logistical constraints of physical experiments. By coupling theoretical validation (Chapter 3 correlations) with numerical rigor, the methodology ensures reproducible insights into DPHE enhancement mechanisms.

4.2 Governing Parameters

In this research the governing parameters will include the inlet Reynolds Number (Re) which is dependent on the physical properties of the working fluid at the selected operating temperatures. Also, the swirl angle (θ_{sw}), swirl number (SN), decay percentage (DP) and axial location ($\tilde{Z}$) of the swirlers bring about a significant interest in investigating the effect of variation of these parameters on the thermal performance of the heat exchanger.

4.2.1 Reynolds Number

Reynolds number was introduced by Osborne Reynolds in 1883 [126] and is defined as the ratio of inertial forces to the viscous forces of the fluid. When Re is large enough, the inertial forces are dominating, therefore particles start moving against the viscous forces holding them which will eventually results in separation of the particles and random movement in all directions (i.e., *Turbulent* flow). When the opposite occurs and the viscous forces are dominating, the flow is maintained in a smooth form (i.e., *Laminar* flow) [127]. At a certain average velocity (u_{avg}) of a fluid with density (ρ_m) and dynamic viscosity (μ_m) obtained at film temperature (T_m) flowing in a duct of hydraulic diameter (D_{hd}), Re can be evaluated as:

$$Re = \frac{\rho_m u_{avg} D_{hd}}{\mu_m} \tag{4.1}$$

Where D_{hd} is evaluated as:

$$Hydraulic\ Diameter = \frac{4 \times Area}{Perimeter} \tag{4.2}$$

The geometries used in this investigation are a circular tube of $D_{hd,t}$,

$$D_{hd,t} = \frac{4\pi\left(\frac{1}{4}\right)D^2}{\pi D} = D \tag{4.3}$$

And a concentric annulus of $D_{hd,a}$:

$$D_{hd,a} = \frac{4\pi\left(\frac{1}{4}\right)(D_o - D_i)^2}{\pi(D_o - D_i)} = D_o - D_i \tag{4.4}$$

where the subscripts t and a denote the locations tubular and annular, while o and i represent the location of the annular outer and inner walls, respectively.

4.2.2 Swirl Angle

This parameter defines the angle at which the fluid exits the swirling device with respect to the radial axis ($r - axis$) of the global coordinate system. This parameter is defined by the geometrical design of the helical pitch of the swirler vanes. This research is undertaken at three swirling angles: 60°, 45° and 30°. Their popularity among the literature such as Chen et al. [46] and Ahmadvand et al. [128] provides an opportunity to compare between different methods generating similar swirl intensities. The choice of these angles provides a range of different behaviours to be investigated, high (30°), intermediate (45°) and low (60°) swirl intensities.

4.2.3 Swirl Number

A parameter that was initially introduced in 1964 by Chigier and Beer [129] was the swirl number. It was defined as the ratio the axial flux of the tangential momentum (G_θ) to the axial flux of the axial momentum (G_z):

$$Swirl\ Number = \frac{Axial\ flux\ of\ the\ Tangential\ Momentum}{Axial\ flux\ of\ the\ axial\ momentum} \tag{4.5}$$

$$SN = \frac{G_\theta}{rG_z} = \frac{2\pi\rho \int_0^r u_z u_\theta r^2 dr}{2\pi\rho r \int_0^r {u_z}^2 r dr + 2\pi \int_0^r P r dr} \tag{4.6}$$

Where u_z and u_θ were taken as the axial and tangential velocity components of the cross-section at various axial locations, respectively. r and P represent the radius and pressure, respectively. This was then modified by Kerr and Fraser [130] where the pressure term was regarded negligible, and the modified swirl number was evaluated as:

$$SN = \frac{2\pi\rho \int_0^r u_z u_\theta r^2 dr}{2\pi\rho r \int_0^r {u_z}^2 r dr} = \frac{2u_\theta}{3u_z} \tag{4.7}$$

Various versions of SN have been found in the literature used in different applications some of which were summarised and compared by Vaziri et. al. [131]. It was concluded that the form displayed in Eq. (4.7) showed excellent presentation of swirling flow. This was further supported by relevant applications such as [132], [133], [134], [135], [136], [137].

4.2.4 Dimensionless Locations and Temperature

Dimensionless locations, shown in Figure 4.1, allowed the normalisation of the results. In the annulus two main locations were described: axial and radial locations both of which are expressed in terms of percentage of the total span in the respective direction. The dimensionless axial location along the heat exchanger is denoted as $\tilde{Z}$ and is expressed as a ratio of the axial coordinate from the exit of the swirler to the remaining length of the annulus:

$$\tilde{Z} = \frac{z}{L} \times 100 \tag{4.8}$$

The radial location is described as the ratio of the difference between the active and inner radii to the hydraulic radius, from Eq.(4.4), and is denoted as $\tilde{r}$:

$$\tilde{r} = \frac{(r - r_i)}{r_{hd}} \times 100 \tag{4.9}$$

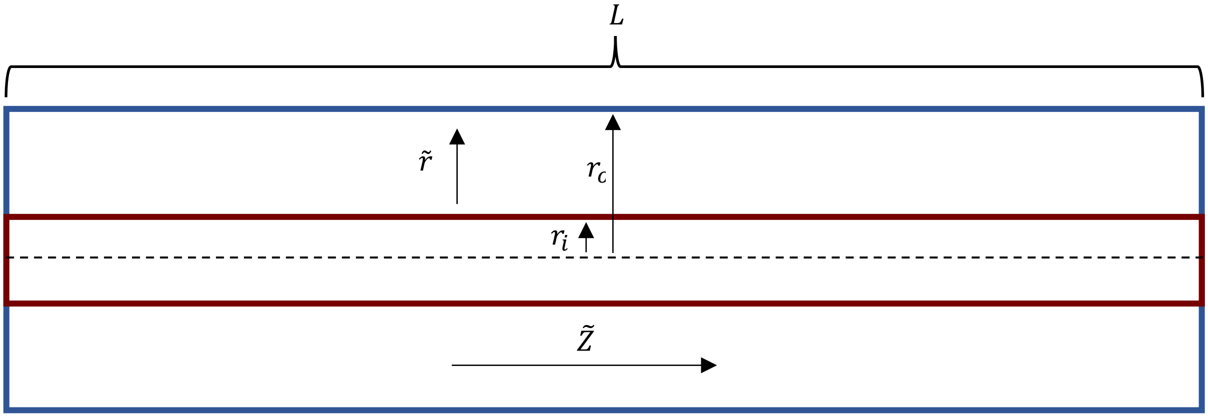

Figure 4.1: Graphical orientation of the dimensionless locations.

4.2.5 Decay Percentage

Decay Percentage (DP) is a novel parameter that is introduced for the first time as a designing parameter replacing the spacing parameter which was viewed as an arbitrarily selected parameter when designing discontinuous enhancement methods either in the annular or tubular zones. A reasonable deduction behind this decision was that the swirl generating devices downstream were of equivalent swirl angle. However, this research aims to introduce a new technique and research area of investigating the enhancements when the swirling devices are of different angles placed at one instant in the heat exchanger. The significance of this parameter is to maintain the swirl intensity of the flow at a specific range before a complete decay of the swirling flow allowing the targeted amount of heat transfer to be achieved at a shorter length of the heat exchanger. To obtain this parameter:

1) A test is first required to be run on each swirl angle under investigation by placing the swirler at the inlet of the test section in a single swirling configuration (SSC).
2) Monitor the swirl number and evaluate the distance at which it achieves a complete decay.
3) Determine the maximum swirl number achieved by the swirler (expectedly at the exit of the swirler).
4) Decide on the percentage of interest, evaluate it from the maximum swirl number achieved and take the corresponding axial length at which this percentage was evaluated.
5) This is the axial location at which the following swirler will be placed in the full swirling configuration (FSC).
6) Repeat this procedure for every swirler placed and every Reynolds number required for the investigation.

This procedure will be presented later in Section 5.4.

4.3 Development of Numerical Model

4.3.1 Geometrical Modelling of Swirlers

The current case being studied is a double pipe heat exchanger (DPHE) in counterflow arrangement. The general model consists of an outer concentric annulus and an inner tube in which cold water and hot water flow, respectively. Several designs have developed for the investigations: Single Swirling Configuration (SSC) and Full Swirling Configuration (FSC). For comparison purposes, a two-dimensional model was designed for the plain DPHE. Before diving into the simulations, the CAD was first developed using SOLIDWORKS software. Three swirlers of angles: 30°, 45° and 60° were designed and used for the investigations are shown in Figure 4.2. The justifications behind the selection of these swirlers can be presented in two points:

1. **Swirler Shape:** The shape of the swirlers was selected due to its popularity among inlet swirl generating devices observed in the literature and simplicity in its manufacturing which further adds to the relevance of this research to industrial applications.
2. **Swirl Angles:** These angles cover the average range of angles mentioned in the literature which enables relevance of the results extracted in the literature to be provided. At intervals of 15°: 30°, 45° and 60°; provide intense, intermediate and weak swirling conditions, respectively.

The detailed drawings of the swirlers are shown in Appendix B. The CAD of each case investigated are presented at the beginning of the discussion. The height of the vanes of the swirlers cover the difference between the central hub and the outer wall of the annulus. This allows the tube matching the inner diameter of the central hub to be held in a concentric position inside the heat exchanger.

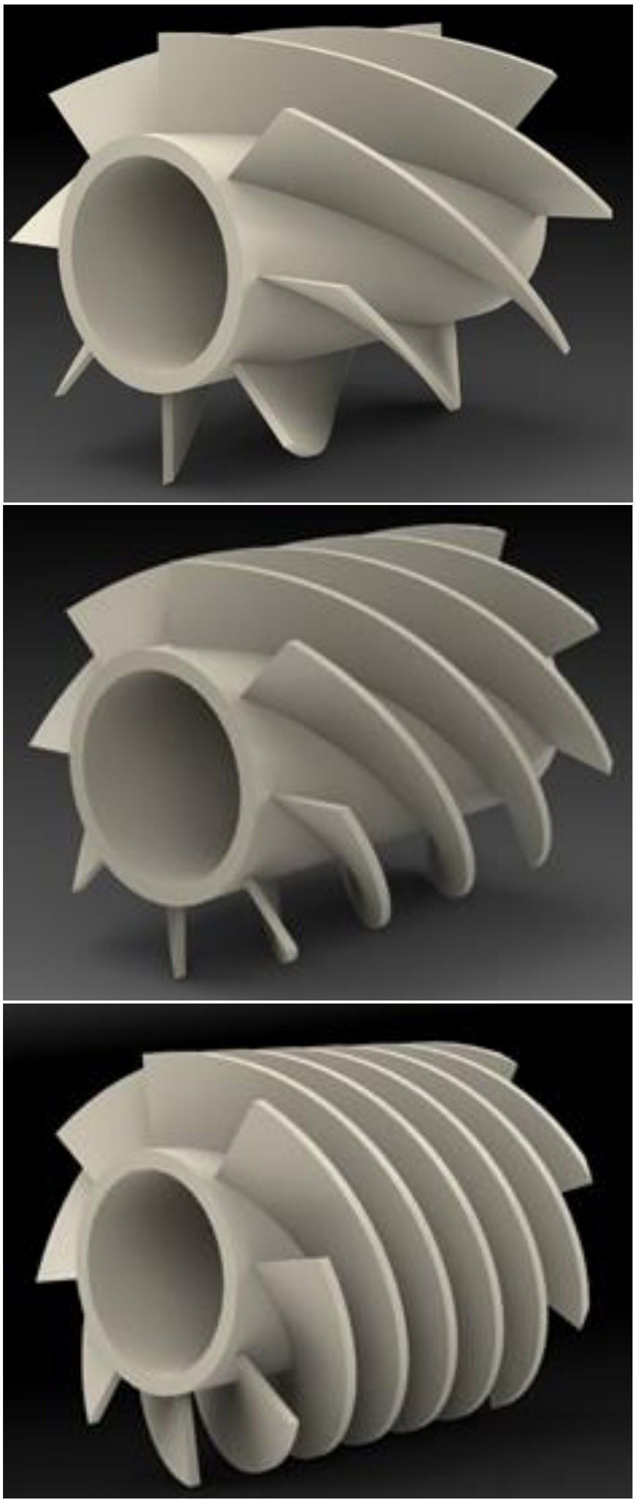

Figure 4.2: Computer aided designs of the three swirlers: 60°, 45° and 30° (from top to bottom).

4.3.2 Governing Equations and Material Properties

By applying the user-defined boundary conditions and assigning materials to both the solid and fluid domains, the simulations solved the governing equations to predict the behaviour of the fluid in both axial and tangential directions in the plain DPHE and the tube and swirl decaying flow when swirlers are introduced into the annulus using the finite volume method. The numerical platform used the computational fluid dynamics (CFD) codes provided by ANSYS. In these investigations, steady state simulations will be utilised to present results focused on the hydrodynamic and thermal behaviour of the fluid flow in each case. These will include and not limited to the velocity components, shear stress, helicity, pressure and temperature distributions along the flow.

Generally, CFD is governed by the Navier Stokes equations: *continuity*, *momentum* and *energy* which are provided by the ANSYS guide [138] and the full derivation in cylindrical coordinates can be found in [139]. These equations are solved in both laminar and turbulent regimes, so a selection of turbulence model is presented. It should be noted that the thermal resistance at the tube wall is considered negligible since the thickness is relatively very small. The equations expressed in steady state cylindrical coordinates are:

Continuity:

$$\frac{\partial(\mathrm{u}_z)}{\partial \mathrm{z}}+\frac{\partial(\mathrm{u}_r)}{\partial \mathrm{r}}+\frac{1}{\mathrm{r}}\frac{\partial(\mathrm{u}_\theta)}{\partial \theta}=0 \tag{4.10}$$

Momentum:

$$r: \quad \begin{aligned} &\mathrm{u}_r\frac{\partial \mathrm{u}_r}{\partial \mathrm{r}}+\frac{\mathrm{u}_\theta}{\mathrm{r}}\frac{\partial \mathrm{u}_r}{\partial \theta}+\mathrm{u}_z\frac{\partial \mathrm{u}_r}{\partial \mathrm{z}}-\frac{{\mathrm{u}_\theta}^2}{\mathrm{r}} \\ &=-\frac{1}{\rho}\frac{\partial \mathrm{P}}{\partial \mathrm{r}}+\nu\left[\frac{1}{\mathrm{r}}\frac{\partial}{\partial \mathrm{r}}\left(\mathrm{r}\frac{\partial \mathrm{u}_r}{\partial \mathrm{r}}\right)+\frac{1}{\mathrm{r}^2}\frac{\partial^2 \mathrm{u}_r}{\partial \theta^2}+\frac{\partial^2 \mathrm{u}_r}{\partial \mathrm{z}^2}-\frac{\mathrm{u}_r}{\mathrm{r}^2}-\frac{2}{\mathrm{r}^2}\frac{\partial \mathrm{u}_\theta}{\partial \theta}\right]+g_r \end{aligned} \tag{4.11}$$

$$\theta: \quad \begin{aligned} & u_r\frac{\partial u_\theta}{\partial r}+\frac{u_\theta}{r}\frac{\partial u_\theta}{\partial \theta}+u_z\frac{\partial u_\theta}{\partial z}+\frac{u_r u_\theta}{r} \\ & =-\frac{1}{\rho r}\frac{\partial P}{\partial \theta}+\nu\left[\frac{1}{r}\frac{\partial}{\partial r}\left(r\frac{\partial u_\theta}{\partial r}\right)+\frac{1}{r^2}\frac{\partial^2 u_\theta}{\partial \theta^2}+\frac{\partial^2 u_\theta}{\partial z^2}+\frac{2}{r^2}\frac{\partial u_r}{\partial \theta}-\frac{u_\theta}{r^2}\right]+g_\theta \end{aligned} \tag{4.12}$$

$$z: \quad u_r\frac{\partial u_z}{\partial r}+\frac{u_\theta}{r}\frac{\partial u_z}{\partial \theta}+u_z\frac{\partial u_z}{\partial z}=-\frac{1}{\rho}\frac{\partial P}{\partial z}+\nu\left[\frac{1}{r}\frac{\partial}{\partial r}\left(r\frac{\partial u_z}{\partial r}\right)+\frac{1}{r^2}\frac{\partial^2 u_z}{\partial \theta^2}+\frac{\partial^2 u_z}{\partial z^2}\right]+g_\theta \tag{4.13}$$

Energy:

$$\rho c_p\left(u_z\frac{\partial T}{\partial z}+u_r\frac{\partial T}{\partial r}+\frac{u_\theta}{r}\frac{\partial T}{\partial \theta}\right)=k\left(\frac{\partial^2 T}{\partial z^2}+\frac{1}{r}\frac{\partial}{\partial r}\left(r\frac{\partial T}{\partial r}\right)+\frac{1}{r^2}\frac{\partial^2 T}{\partial \theta^2}\right)+Sc \tag{4.14}$$

Where g_r, g_θ and g_z are the gravitational acceleration components in the radial, circumferential and axial directions. Sc is the source term representing an external source applied on the system. Since this is primarily a convective heat transfer investigation with no external heat flux applied, the source term has been neglected from Eq. (4.14). Moreover, the flow is assumed to be incompressible, and the flow is in a horizontal orientation nullifying the gravitational effects simplifying Eqs. (4.11)-(4.14) into:

Momentum:

$$r: \quad \begin{aligned} & u_r\frac{\partial u_r}{\partial r}+\frac{u_\theta}{r}\frac{\partial u_r}{\partial \theta}+u_z\frac{\partial u_r}{\partial z}-\frac{{u_\theta}^2}{r} \\ & =-\frac{1}{\rho}\frac{\partial P}{\partial r}+\nu\left[\frac{1}{r}\frac{\partial}{\partial r}\left(r\frac{\partial u_r}{\partial r}\right)+\frac{1}{r^2}\frac{\partial^2 u_r}{\partial \theta^2}+\frac{\partial^2 u_r}{\partial z^2}-\frac{u_r}{r^2}-\frac{2}{r^2}\frac{\partial u_\theta}{\partial \theta}\right] \end{aligned} \tag{4.15}$$

$$\theta: \quad \begin{aligned} & u_r\frac{\partial u_\theta}{\partial r}+\frac{u_\theta}{r}\frac{\partial u_\theta}{\partial \theta}+u_z\frac{\partial u_\theta}{\partial z}+\frac{u_r u_\theta}{r} \\ & =-\frac{1}{\rho r}\frac{\partial P}{\partial \theta}+\nu\left[\frac{1}{r}\frac{\partial}{\partial r}\left(r\frac{\partial u_\theta}{\partial r}\right)+\frac{1}{r^2}\frac{\partial^2 u_\theta}{\partial \theta^2}+\frac{\partial^2 u_\theta}{\partial z^2}+\frac{2}{r^2}\frac{\partial u_r}{\partial \theta}-\frac{u_\theta}{r^2}\right] \end{aligned} \tag{4.16}$$

$$z: \quad u_r\frac{\partial u_z}{\partial r}+\frac{u_\theta}{r}\frac{\partial u_z}{\partial \theta}+u_z\frac{\partial u_z}{\partial z}=-\frac{1}{\rho}\frac{\partial P}{\partial z}+\nu\left[\frac{1}{r}\frac{\partial}{\partial r}\left(r\frac{\partial u_z}{\partial r}\right)+\frac{1}{r^2}\frac{\partial^2 u_z}{\partial \theta^2}+\frac{\partial^2 u_z}{\partial z^2}\right] \tag{4.17}$$

Energy:

$$\rho c_p\left(u_z\frac{\partial T}{\partial z}+u_r\frac{\partial T}{\partial r}+\frac{u_\theta}{r}\frac{\partial T}{\partial \theta}\right)=k\left(\frac{\partial^2 T}{\partial z^2}+\frac{1}{r}\frac{\partial}{\partial r}\left(r\frac{\partial T}{\partial r}\right)+\frac{1}{r^2}\frac{\partial^2 T}{\partial \theta^2}\right) \tag{4.18}$$

In laminar flow regimes inside a circular pipe, these equations simplify to describe the Hagen-Poiseuille flow characteristics. In the case of turbulent flow, additional transport equations need to be considered to evaluate the turbulent kinetic energy (K) and rate of turbulent dissipation (ϵ). In the literature, it was found that there are several turbulence models were found relevant to the current field of investigation. These were discussed in section 2.6 above.

A detailed procedure of the selection and the validation of the turbulence model will be carried out in sub-section 4.3.4. The thermo-physical properties of the solid copper and liquid water at film temperature are summarised in Table 4.1. All properties are assumed to be constant except for the dynamic viscosity of water which is taken as a *piecewise-linear* function plotted by ANSYS in Figure 4.3.

Table 4.1 The thermo-physical properties of water (at $T = 39$ ℃) extracted from the steam tables [96] *and copper from Ansys.*

Quantity	Value	Units
Water		
Density (ρ)	992.5	$\mathrm{kg \cdot m^{-3}}$
Specific Heat Capacity at Constant Pressure (c_p)	4178.8	$\mathrm{J \cdot kg^{-1} \cdot K^{-1}}$
Thermal Conductivity (k)	0.631	$\mathrm{W \cdot m^{-1} \cdot K^{-1}}$
Dynamic Viscosity (μ)	0.000664	$\mathrm{kg \cdot m^{-1} \cdot s^{-1}}$
Prandtl Number (Pr)	4.4	–
Copper		
Density (ρ_s)	8978	$\mathrm{kg \cdot m^{-3}}$
Specific Heat Capacity at Constant Pressure $(c_{p,s})$	381	$\mathrm{J \cdot kg^{-1} \cdot K^{-1}}$
Thermal Conductivity (k_s)	387.6	$\mathrm{W \cdot m^{-1} \cdot K^{-1}}$

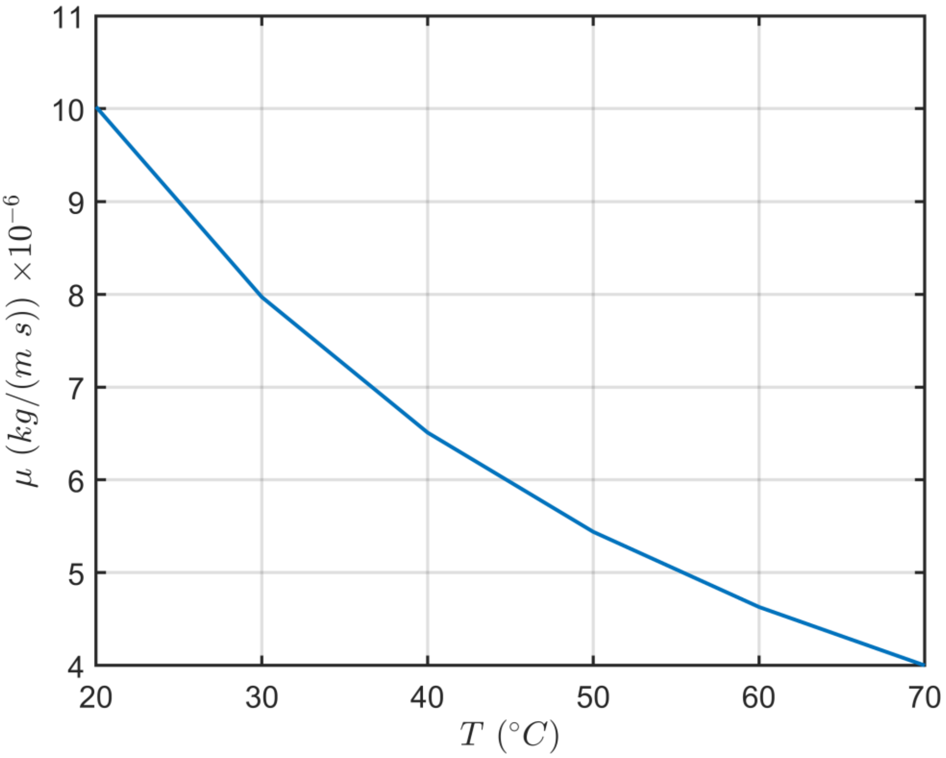

Figure 4.3 Piecewise-linear plot generated for the dynamic viscosity of water. Data was collected from the steam tables [96].

4.3.3 Model Selection and Boundary Condition

The boundary conditions applied in the system include no slip boundary condition at all walls in the heat exchanger, thermal conductivity through the wall of the tube is negligible, and the working fluid is considered Newtonian and incompressible. Currently, the inlet temperature of the annulus is set at 28 °C and the tube at 50 °C, therefore the film temperature is evaluated at 39 °C. The outer wall of the annulus and the walls of the swirlers' vanes are assumed to be adiabatic (i.e. wall heat flux = 0). Both laminar and turbulent flows are considered in these investigations where $Re = 300 - 4000$ at the inlet of both the annulus and the tube. Both Reynolds numbers matched at each design point. With reference to Table 4.2, the flow is assumed to be laminar in plain DPHE when $Re \leq 2000$. The velocities considered for the upcoming investigations are presented in Table 4.2. At the velocity inlets, the turbulence specification method was chosen to be turbulent intensity which remained at its default value (5%) and hydraulic diameters of $24\,mm$ and $20\,mm$ of the annulus and the tube, respectfully. Gauge pressure was set to zero at each of the pressure-outlets. It is important to note that in the case of heat transfer, the surface area is an important parameter to modify based on the geometry studied to accurately evaluate the heat transfer coefficients using Fluent. The Semi-Implicit Method for Pressure Linked Equations (SIMPLE) algorithm was chosen as the pressure-velocity coupling scheme. In addition, the spatial discretisation was performed using least squares cell based gradient method. PREssure STaggering Option (PRESTO!) and QUICK schemes were defined for pressure and momentum solutions, respectively. Finally, the swirl velocity, turbulent kinetic energy and dissipation rate were solved using the second order upwind scheme.

Table 4.2 Inlet velocities of cold and hot fluids to achieve the required inlet Reynolds number.

Re	Velocity (m/s)	
	Cold	Hot
300	0.008367	0.010041
500	0.013946	0.016735
800	0.022313	0.026776
1200	0.027891	0.03347
1800	0.03347	0.040164
2000	0.050205	0.060246
3000	0.055783	0.06694
4000	0.083674	0.100409

4.3.4 Validation of 3D Numerical Model

4.3.4.1 Experimental Setup

The numerical model was validated against experimental data obtained from the apparatus shown in Figure 4.4 (components detailed in Table 4.3). The close-loop system used the same working fluid and boundary conditions as the simulations. A 1800 W boiler maintained hot water at 50 ± 0.1 °C for the tube side, while 0.1 m^3 constant-head tank stabilised annular flow by preventing air bubble formation through elevated outlet pressure. The 2 m test section consisted of an acrylic annulus (46 mm hydraulic diameter) and concentric copper tube (20 mm diameter), with alignment maintained by swirler vanes.

Flow rates were precisely controlled, annular flow (up to 500 l/hr) via tap water supply and tubular flow (up to 5 l/min) through a boiler, connected pump with cross-diversion cooling. Low flow measurements used a measuring cylinder ($\pm$1 ml) and stopwatch ($\pm$0.005 s). Temperature monitoring employed Type K thermocouples ($\pm$0.6 °C) at five strategic locations, logged via PicoLog ($\pm$0.05 °C) at 1-minute intervals under PID control. Three 45° swirlers were spaced 500 mm apart in the annulus, with testing conducted at $Re = 300 - 4000$. Each flow condition underwent three measurement cycles after a 5-minute stabilisation period to ensure repeatability and account for human error.

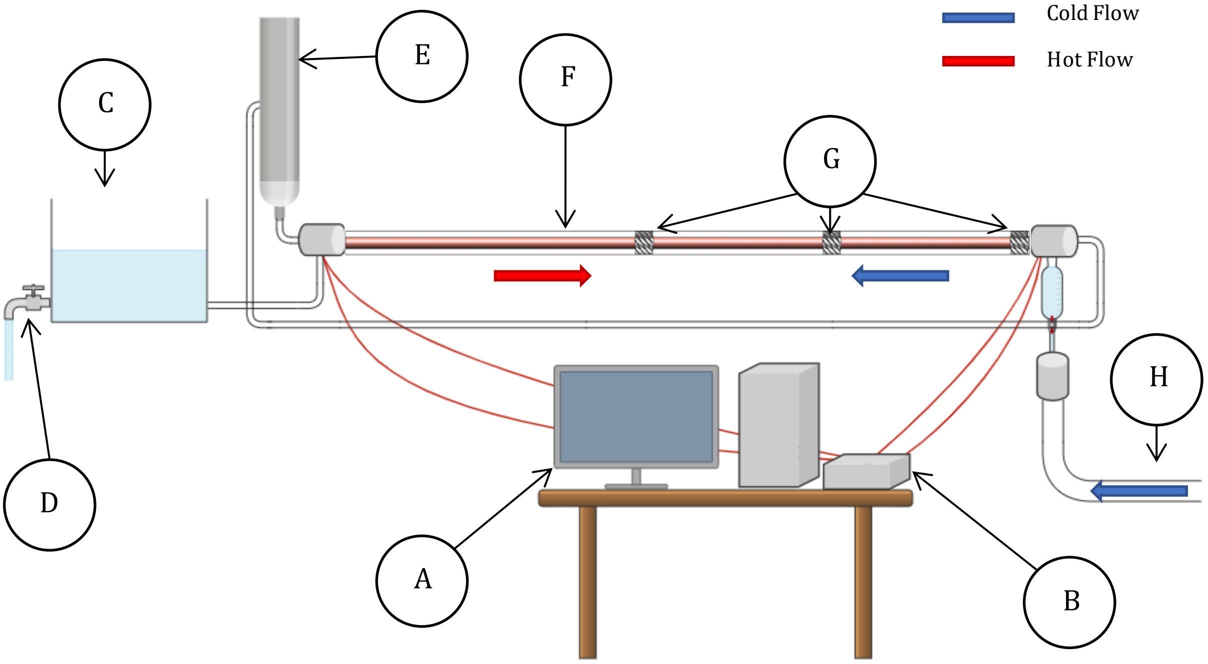

Figure 4.4: A graphical presentation of the experimental setup. (Image was generated using https://chemix.org)

Table 4.3: Components of the experimental setup.

Component	**Label**
Workstation	A
PicoLog	B
Constant Head Tank	C
Discharge Tap	D
Boiler + Microprocessor	E
Test Section	F
Swirlers	G
Direct Line	H

4.3.4.2 Model Discretisation

Model Discretisation is an essential part of any numerical investigation on which the calculations of the governing equations in terms of accuracy and computation time and resources required depend. A three-dimensional presentation of the experimental test section that was used for validation is shown in Figure 4.5. In this figure, an example of what an FSC would look like when three 45° swirlers are used at the same instant in the annulus. The geometry was divided into different bodies to account for the partitioning of the FLUENT software assigning each zone to a physical processor of the workstation when the simulation is set to run in parallel. Structured mesh was developed as shown in Figure 4.6. The relatively most complex part of the mesh was the curved structure of the flow along the vanes of the swirlers. However, the swirlers have been subtracted from the annular domain while preserving the wall effects in the form of cavities leaving behind the curved path of the flow. This is done to reduce the computational resources of unnecessary addition of elements. An axial section view of the mesh can be observed in Figure 4.7 where the variation in element size is shown at certain regions throughout the annulus. Elements were designed to be more populated inside the swirlers and downstream from $\tilde{Z} = 0$, 11 and 22 at the exit of the swirlers to $\tilde{Z} = 0.4, 11.4$ and 22.4. This was done to capture any significant axial fluctuations in the flow at the peak of the swirling intensity where impingement zones were expected to exist. In addition, inflation layers were added to the flow domains to capture the boundary layers near the walls. This is better presented at the outlet of the of annulus in Figure 4.8. Velocity inlet was assigned to the inlets of both fluid domains while pressure outlet at zero-gauge pressure was assigned for each of the outlets. Bonded mesh interfaces were assigned at the contact regions between the tube inner and outer walls and the hot and cold domains, respectively.

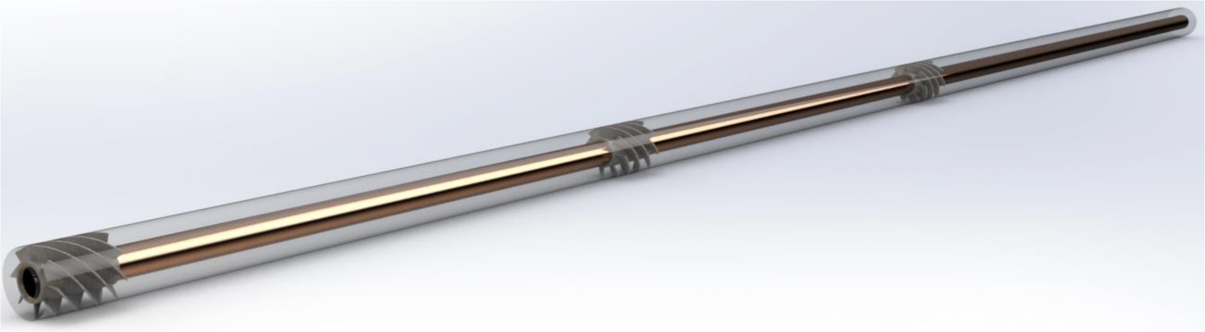

Figure 4.5 Computer aided design of the full swirling configuration when three 45° swirlers were used.

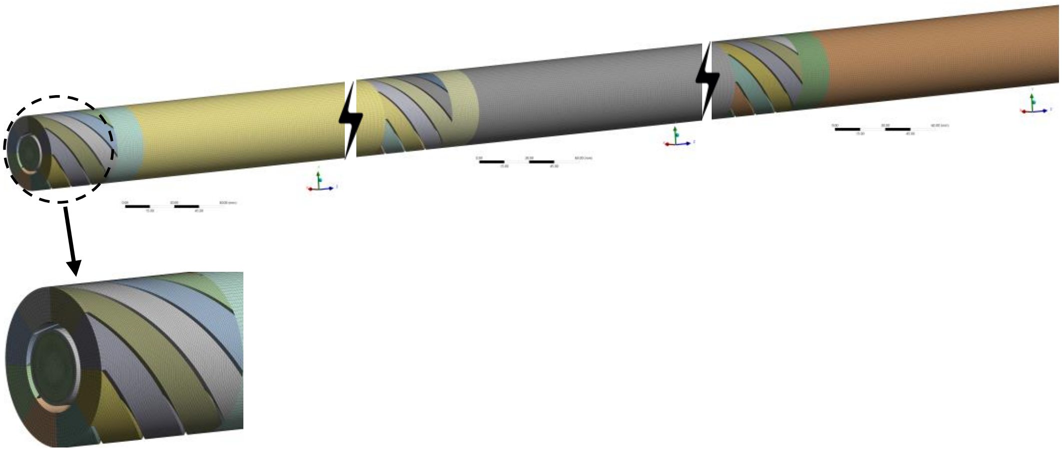

Figure 4.6 Demonstration of the mesh applied on the 3-D replication of the experimental setup.

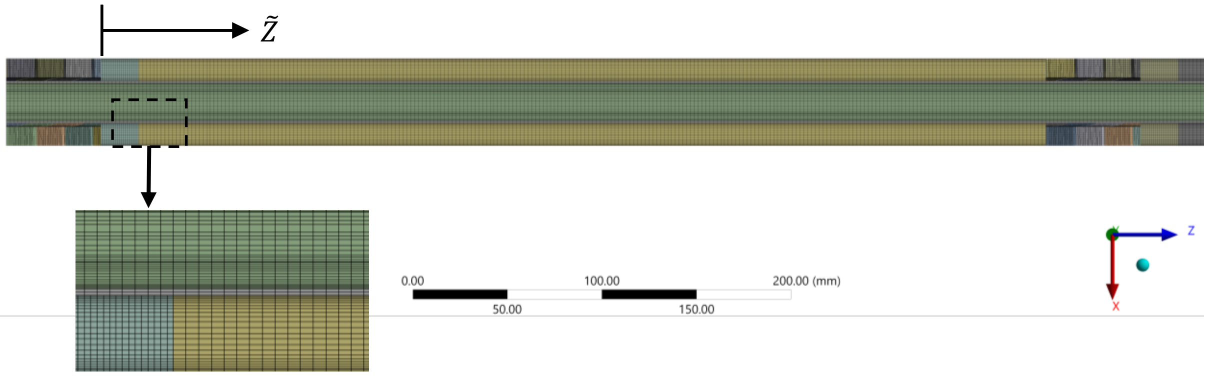

Figure 4.7 Axial section of the mesh showing the element distribution in all the domains.

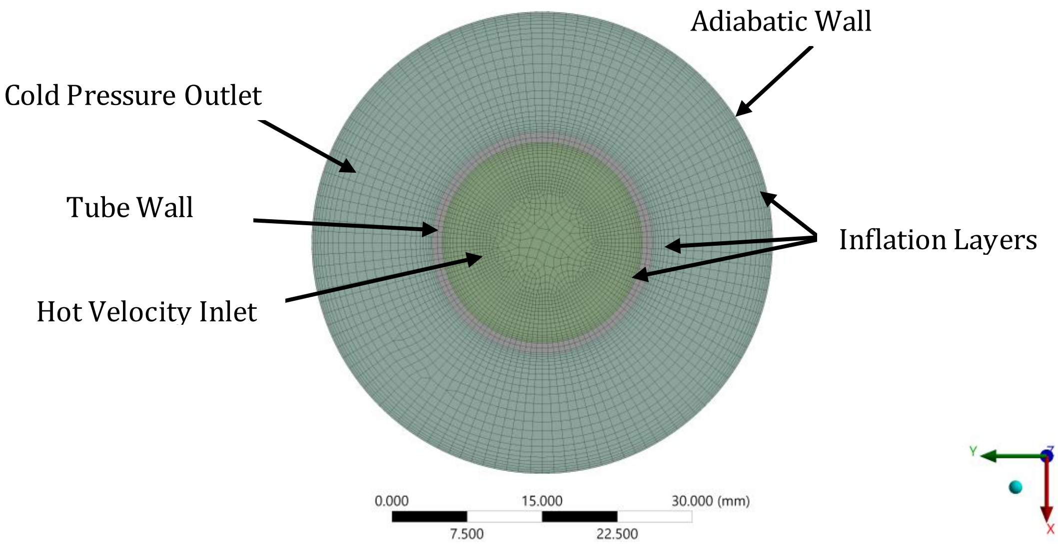

Figure 4.8 Radial cross section of the mesh with the types of the boundary conditions.

A mesh independence test is the next step after generating a presumably satisfactory mesh. A numerical solution should not depend on the mesh to be reliable. The outputs from a finer mesh are not the same as a coarser mesh. However, an accepted tolerance should be realised by varying the mesh. This is called the mesh (otherwise known as "grid") independence test. Four types of mesh were developed and compared, Grid 1 (~3,200,000 elements), Grid 2 (~3,700,000 elements), Grid 3 (~4,000,000 elements) and Grid 4 (~5,400,000 elements). These were compared to a very fine mesh defined as the reference grid (~10,200,000 elements). The output parameters selected to judge the accuracy of the mesh were the facet-area average heat transfer coefficients (h_a and h_t), the mass-weighted average pressure drop (ΔP_a and ΔP_t) and tangential velocities at ($u_{\theta 1}, u_{\theta 2}$ and $u_{\theta 3}$) at $Z^* = Z^* = 0.4, 11.4$ and 22.4. From Figure 4.9, Grid 4 showed a percentage difference of $0 - 1.6\%$ in terms of all output parameters making it the most effective grid, therefore this grid was chosen to run the validation test. The quality of the mesh can be seen in Table 4.4. Important qualities that would have a direct impact on the accuracy of the simulations include skewness, orthogonal quality, and aspect ratio. A reference was provided by ANSYS in [140] to aid the user in judging the quality of the mesh developed. From the table, the mesh quality was found to be satisfactory to proceed with the simulations.

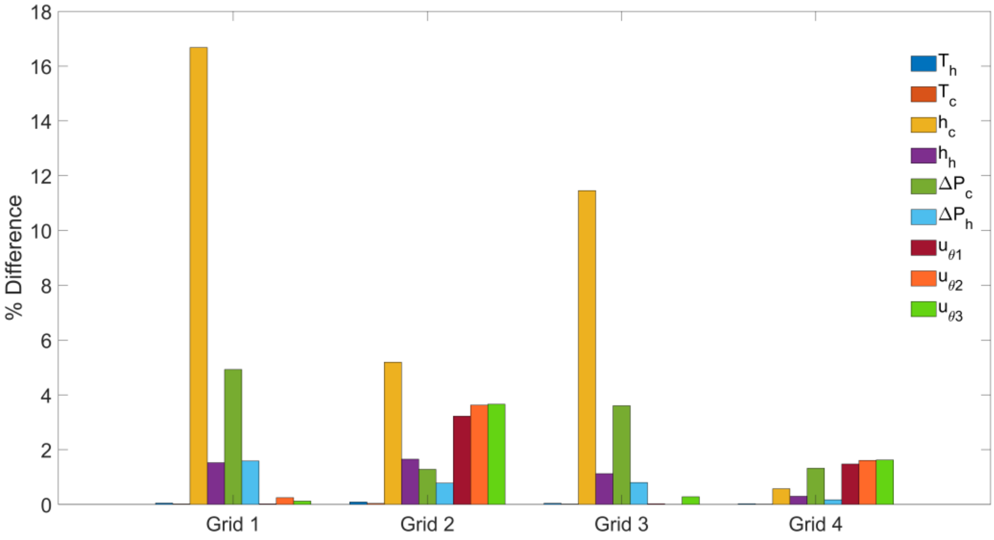

Figure 4.9 Results of the mesh independent test of the numerical model with respect to the reference grid.

Table 4.4 Mesh quality with reference to the guide provided by ANSYS.

Mesh Metric	**Benchmark**	**Grid 4**	
		Maximum	**Average**
Skewness	0	0.64	0.063
Orthogonal Quality	1	1.00	0.98
Aspect Ratio	1 – 5	21.31	5.77

In terms of validation, several numerical models have been considered in the validation procedure in comparison to the experimental results. As mentioned in the in experimental set up, at the time, only the temperature data were available from the experiment. Therefore, the mass-weighted average temperatures at the outlets of the annular and tubular domains were recorded and compared in Figure 4.10. The experimental results had some discrepancies hence, lines of best fit were generated to average these results and get a more accurate variation with Reynolds numbers where each was equated as function of Reynolds number in a power form as:

$$\mathrm{T_{0,c}} = 38.59\mathrm{Re}^{-0.029} \tag{4.19}$$

$$\mathrm{T_{0,h}} = 12.53\mathrm{Re}^{0.14} \tag{4.20}$$

At Re = 2000, 3000 and 4000 the deviations in SST model were 1.9, 1.2 and 0.7%, and 12.6, 7.5 and 3.9%, in the realizable model were 1.2, 0.5 and 2.0%, and 10.6, 5.5 and 1.7%, and in the RNG model were 0.2, 0.6 and 1.3% from the cold and hot temperature results, respectively. The rest of the deviations are presented in Table 4.5. Significant deviations were observed between $300 \leq \mathrm{Re} \leq 2000$ where all the turbulence models had underpredicted and overpredicted the results with respect to the cold and the hot experimental best fit lines, respectively. Possible justifications for these deviations are:

1. The thermocouples used to measure the temperatures of the experiment were measuring a single point at the outlets. Meanwhile, the simulation results recorded were mass-weighted averages of the entire outlet surface.
2. The thermocouples might have not been immersed fully in the core of the flow, especially the one placed inside the tube, where significant deviations were observed.
3. At low Reynolds numbers, the swirling intensity in the annulus was weaker, also the tubular flow was laminar which resulted in less mixing of the fluid, hence thermal energy was not distributed uniformly.
4. The outer wall of the annulus was not insulated. Therefore, the heat loss or gain caused by the difference in annular and ambient temperatures (depending on the time of day) had an impact on the experimental results.
5. The swirlers are manufactured with a 3D printer using Polylactic Acid (PLA) as the filament material which has a certain degree of roughness on the surface which was not accounted for in the simulations.

In conclusion, based on the average deviations of each of the models, $\mathrm{K}-\epsilon$ RNG was found to be the most accurate. Moreover, the computational time consumed by each turbulence model was recorded where SST took about 43.5 hours and realizable took about 39.5 hours. Meanwhile, RNG took about 32 hours to complete the simulations for all the Reynolds numbers investigated. Given the accuracy and efficiency, the swirl modified $K-\epsilon$ RNG model was adopted for all three-dimensional simulations.

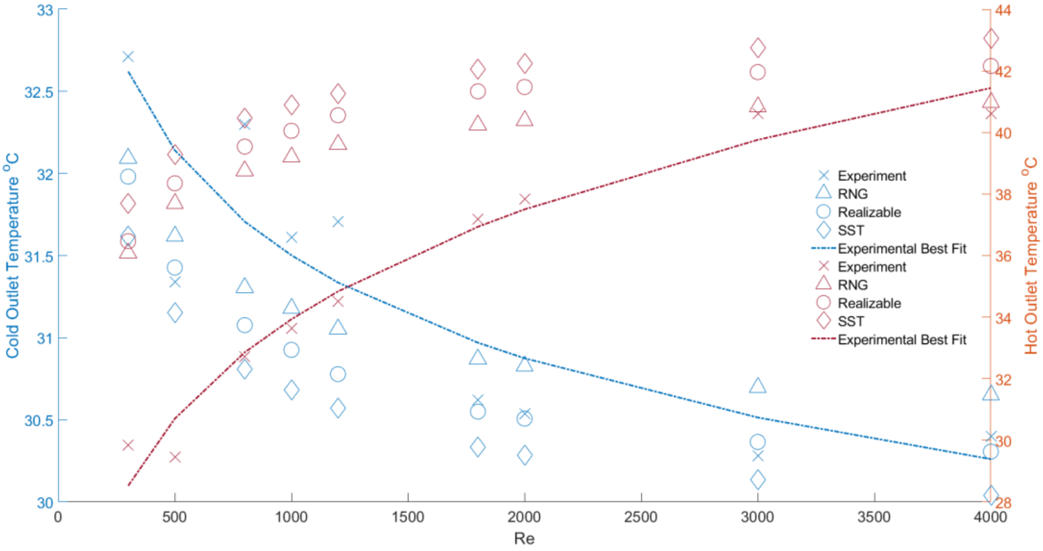

Figure 4.10 Temperature plot of the numerical against the experimental results for validation.

Table 4.5 Percentage deviations of the turbulence model used in the validation against the experimental temperature results for all Reynolds numbers studied.

Re	Deviation (%)					
	SST		Realizable		RNG	
	Cold	Hot	Cold	Hot	Cold	Hot
300	3.1	32.2	2.0	27.8	1.6	26.5
500	3.1	27.9	2.2	24.9	1.6	22.8
800	2.8	23.1	2.0	20.3	1.3	18.0
1000	2.6	20.5	1.8	18.0	1.0	15.5
1200	2.4	18.4	1.8	16.4	0.9	13.7
1800	2.0	13.9	1.4	11.9	0.3	8.9
2000	1.9	12.6	1.2	10.6	0.2	7.7
3000	1.2	7.5	0.5	5.5	0.6	2.7
4000	0.7	3.9	0.2	1.7	1.3	1.1
Average	2.2	17.8	1.4	15.3	1.0	13.0

In the swirl modified RNG $\mathrm{K}-\epsilon$ model formulation, the modified turbulent viscosity function directly influences the effect viscosity, which is a key component in the transport equations. First, the effective viscosity (μ_{eff}) is defined as the sum of the laminar viscosity (μ_{l}) and the turbulent viscosity (μ_{t}):

$$\mu_{\mathrm{eff}} = \mu_{\mathrm{l}} + \mu_{\mathrm{t}} \tag{4.21}$$

This is used to define the effect thermal conductivity ($\mathrm{k}_{\mathrm{eff}}$):

$$\mathrm{k}_{\mathrm{eff}} = \alpha \mathrm{c}_{\mathrm{p}} \mu_{\mathrm{eff}} \tag{4.22}$$

Then, this will be used in the modified energy conservation equation in Eq. (4.18) to be expressed as:

$$\begin{aligned}(\rho \mathrm{E} + \mathrm{p})\left(\frac{\partial}{\partial \mathrm{r}}\mathrm{u}_{\mathrm{r}} + \frac{\partial}{\partial \theta}\frac{\mathrm{u}_{\theta}}{\mathrm{r}} + \frac{\partial}{\partial \mathrm{z}}\mathrm{u}_{\mathrm{z}}\right) \\ = \frac{\partial}{\partial \mathrm{r}}\left(\mathrm{k}_{\mathrm{eff}}\frac{\partial \mathrm{T}}{\partial \mathrm{r}}\right) + \frac{1}{\mathrm{r}^2}\frac{\partial}{\partial \theta}\left(\mathrm{k}_{\mathrm{eff}}\frac{\partial \mathrm{T}}{\partial \theta}\right) + \frac{\partial}{\partial \mathrm{z}}\left(\mathrm{k}_{\mathrm{eff}}\frac{\partial \mathrm{T}}{\partial \mathrm{z}}\right)\end{aligned} \tag{4.23}$$

The turbulent viscosity in the in the standard $\mathrm{K}-\epsilon$ RNG is initially calculated based on the turbulent kinetic energy and its dissipation rate as:

$$\mu_{\mathrm{t}} = \rho \mathrm{C}_{\mu}\frac{\mathrm{K}^2}{\epsilon} \tag{4.24}$$

where C_{μ} is a constant evaluated at 0.0845. The turbulent viscosity is a critical component in the generation of turbulence kinetic energy (G_{K}), which is expressed as:

$$\mathrm{G}_{\mathrm{K}} = \mu_{\mathrm{t}}\mathrm{S}^2 \tag{4.25}$$

$$\mathrm{S} = \sqrt{2\mathrm{S}_{\mathrm{ij}}\mathrm{S}_{\mathrm{ij}}} \tag{4.26}$$

where S is the modulus of the mean rate-of-strain tensor. For swirling flows, the RNG model introduces a swirl modification that alters the turbulent viscosity. The modified turbulent viscosity (μ_{t}') is given by the function:

$$\mu_t' = \mu_t f\left(\alpha_s, \Omega, \frac{K}{\epsilon}\right) \tag{4.27}$$

Here, μ_t represents the turbulent viscosity calculated without the swirl modification, α_s is the swirl constant (by default is set to 0.07) dependent on the swirling flow's intensity, and Ω is the characteristic swirl number calculated by the software. Crucially, μ_t' is then used as the turbulent viscosity component when calculating μ_{eff}. μ_{eff} is then directly utilised in the transport equations which can be expressed as:

$$\begin{aligned}\frac{\partial}{\partial r}(\rho K u_r) + \frac{1}{r}\frac{\partial}{\partial \theta}(\rho K u_\theta) + \frac{\partial}{\partial z}(\rho K u_z) \\ = \frac{\partial}{\partial r}\left[(\alpha_K \mu_{eff})\frac{\partial K}{\partial r}\right] + \frac{1}{r^2}\frac{\partial}{\partial \theta}\left[(\alpha_K \mu_{eff})\frac{\partial K}{\partial \theta}\right] + \frac{\partial}{\partial z}\left[(\alpha_K \mu_{eff})\frac{\partial K}{\partial z}\right] + G_K \\ - \rho\epsilon\end{aligned} \tag{4.28}$$

$$\begin{aligned}\frac{\partial}{\partial r}(\rho \epsilon u_r) + \frac{1}{r}\frac{\partial}{\partial \theta}(\rho \epsilon u_\theta) + \frac{\partial}{\partial z}(\rho \epsilon u_z) \\ = \frac{\partial}{\partial r}\left[(\alpha_\epsilon \mu_{eff})\frac{\partial \epsilon}{\partial r}\right] + \frac{1}{r^2}\frac{\partial}{\partial \theta}\left[(\alpha_\epsilon \mu_{eff})\frac{\partial \epsilon}{\partial \theta}\right] + \frac{\partial}{\partial z}\left[(\alpha_\epsilon \mu_{eff})\frac{\partial \epsilon}{\partial z}\right] + C_{1\epsilon} G_K \frac{\epsilon}{K} \\ - C_{2\epsilon}^* \rho \frac{\epsilon^2}{K}\end{aligned} \tag{4.29}$$

where α_K and α_ϵ are the inverse effective Prandtl numbers. These are derived using the RNG theory [141] as:

$$\left|\frac{\alpha - 1.3929}{\alpha_0 - 1.3929}\right|^{0.6321} \left|\frac{\alpha + 2.3929}{\alpha_0 + 2.3929}\right|^{0.3679} = \frac{\mu_l}{\mu_{eff}} \tag{4.30}$$

α_0 is evaluated at 1.0. In the free stream flow, where $\frac{\mu_l}{\mu_{eff}} \ll 1$, $\alpha_K = \alpha_\epsilon \approx 1.393$.

The term $C_{2\epsilon}^*$ is a primary distinction of the RNG model, making it more sensitive to effects of rapid strain and streamline curvature. It is expressed as:

$$C_{2\epsilon}^* = C_{2\epsilon} + \frac{C_\mu \rho \eta^3 (1 - \eta/\eta_0)}{1 + \beta\eta^3} \tag{4.31}$$

Here, $C_{1\epsilon}$ and $C_{2\epsilon}$ are constants evaluated at 1.42 and 1.68, respectively. Additionally, $\eta = SK/\epsilon$, $\eta_0 = 4.38$ and $\beta = 0.012$. The variation of turbulent transport with effective Reynolds number $(\mathrm{Re}_{\mathrm{eff}})$ is described by the integral:

$$d\left(\frac{\rho^2 K}{\sqrt{\epsilon\mu}}\right) = \left(1.72\frac{\hat{v}}{\sqrt{\hat{v}^3 - 1 + C_v}}\right)d\hat{v} \tag{4.32}$$

$$\hat{v} = \mu_{\mathrm{eff}}/\mu \tag{4.33}$$

and C_v is a constant evaluated at approximately 100. This provides enhanced resolution for near-wall flows. Thus, the swirl-modified turbulent viscosity directly impacts the effective viscosity, which in turn influences the diffusion terms in the transport equations, thereby accounting for the effects of swirl in the flow simulation.

4.3.5 Validation of 2D Numerical Model

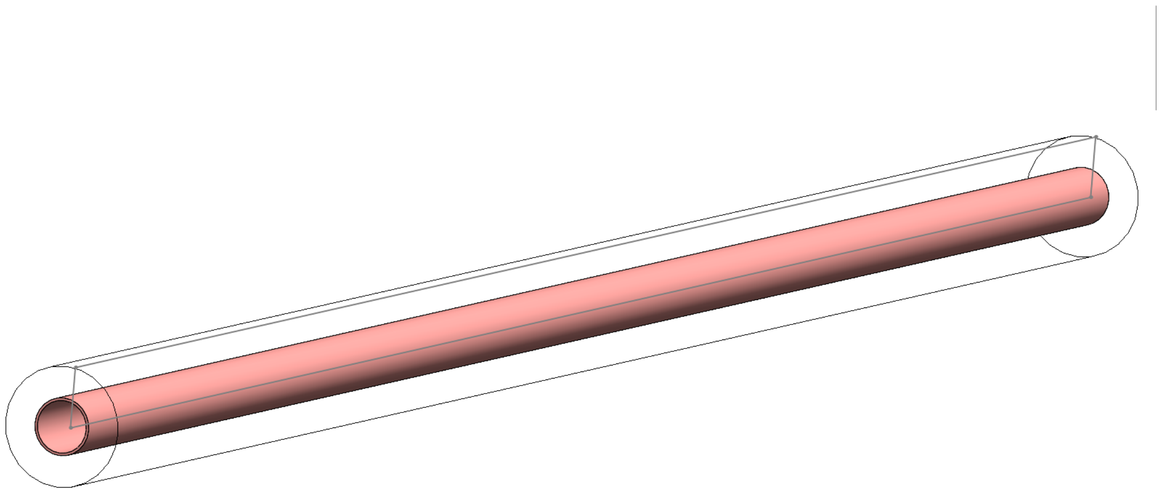

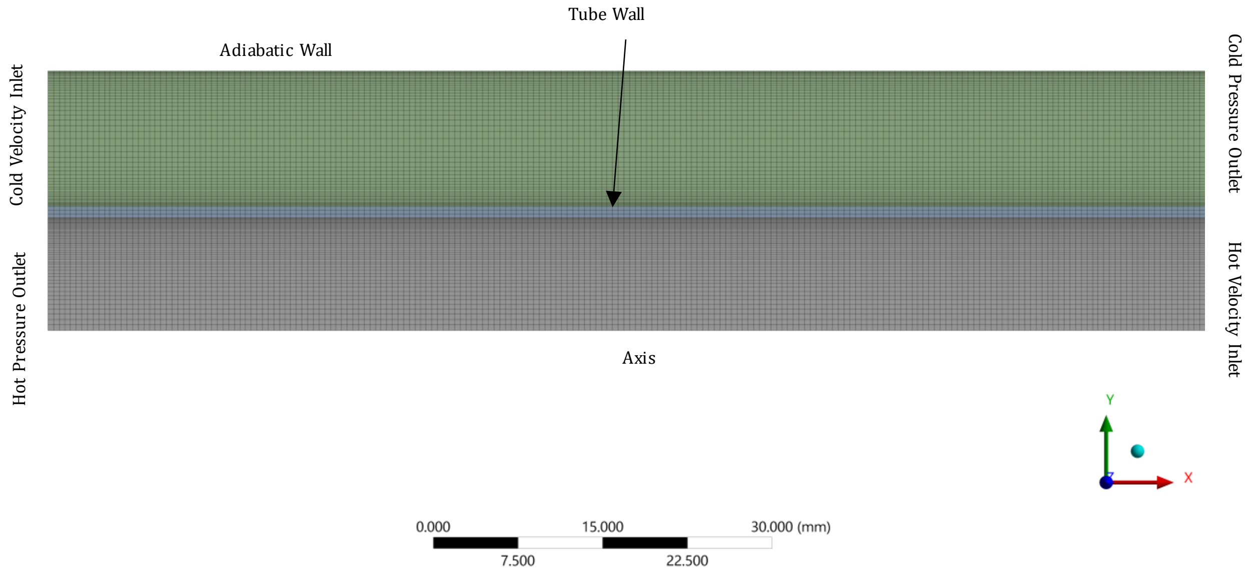

Figure 4.11 A two-dimensional axial section of plain DPHE.

A two-dimensional axisymmetric solver will be used to replicate the plain $DPHE$. In doing this, there will be more room for higher mesh to be developed and a higher resolution for low Re regions. Figure 4.11 presents the fine mesh on a two-dimensional axisymmetric section of the three-dimensional setup. The mesh is radially divided into 50 elements in the radial direction of each fluid domain. Elements are biased towards the walls with a bias factor of 10 while providing inflation layers enough to capture the low-Re regions near the walls. Velocity-inlet is assigned to the edge at $x = 0$ and cold-water flow in the positive x –direction while hot water flows in the opposite direction as pressure-outlet at zero gauge pressure is assigned at the same location. The bottom edge of the hot domain is defined as a central axis to allow for 2-D axisymmetric solver to be utilised. With the axial element being $0.5mm$ in size a total of 206,000 elements were obtained.

Validation is obtained by running the models against the correlations mentioned in sections 3.2 and 3.3. It is worth recalling that these correlations were made for a hydrodynamically developed flow, therefore a hydrodynamically developed profile should be defined at the inlets. The expressions used to define these profiles are defined in Table 4.6. With regards to laminar annular profile, the gravitational term is neglected, and the remaining pressure term can be replaced with Eq. (3.38). These were validated against the profiles extracted from the simulations in Figure 4.12. The laminar profiles were in excellent agreement with the correlations obtained from the literature. However, with regards to the turbulent profile, numerical profiles were extracted from a $3m$ tube (>hydrodynamic length required) using the transition $k - kl - \omega$ and RNG models were compared to the turbulent tubular correlation with constant m and two values for $n = 3$ and 7. While the transition $k - kl - \omega$ model produced a nearly laminar profile after extracting the annular profile from the outlet, as shown in Figure 4.12, a significant deviation of averaged at 36% and 60% across the radius was observed in the tubular domain due to limitations by the correlation for $n = 3$ and 7 respectively, suggested by Salama A. [142]. The model does not perfectly capture the transition zone between laminar and turbulent flow regimes. The application of the model relies on optimising the exponents m and n to fit experimental data. The article concluded that further refinements and empirical correlations are needed to improve the model's predictive ability during turbulent annular flow conditions. Therefore, like the annular domain, the tubular inlet in the test section was extracted from the outlet of the long developing section for $Re = 3000$ and 4000.

With regards to the friction factor, validation of several potential models were performed against the theoritical calculations. These models were laminar for the laminar regime only, transition $k-kl-\omega$, transition SST for both laminar and turbulent regimes, gamma-algebraic transition model dervied from $K-\omega\ SST$ and $K-\epsilon\ RNG$ for the turbulent regime only. Friction factor was evaluated by evaluating the mass-weighted average downstream pressure gradient ($\Delta P = P_{inlet} - P_{outlet}$). When the flow was laminar, friction factor was calculated using Eq. (3.38) while turbulent flow was calculated using Eq. (3.36) but with the adjustment of replacing the D_{eff} with D_{hd}. Figure 4.13 presents the result of the comparison between the simulations and the theoretical calculations with increasing Re. In the laminar regime, the laminar and the transition $k-kl-\omega$ models showed excellent agreement with less than 0.2% accuracy in comparison to $0.25\% - 11.48\%$ and $0.11\% - 40\%$ achieved by the transition SST and the gamma-algebraic transition models, respectively. In the turbulent regime, the simulation evaluated the most accurate results using gamma-algebraic transition and RNG with an accuracy of $0.42\% - 4.93\%$ and $5.33\% - 11.30\%$, respectively in comparison to $34\% - 42\%$ and $42\% - 53\%$ achieved by transition SST and transition $k-kl-\omega$, respectively.

Table 4.6 Velocity profile expressions in laminar and turbulent flows inside the annulus and the tube.

	Annulus [127]	Tube [142]
Laminar	$\frac{1}{4\mu}\left[-\frac{d}{dz}(p+\rho gz)\right]\left[{r_o}^2 - r^2 + \frac{{r_o}^2 - {r_i}^2}{\ln\left({r_i}/{r_o}\right)}\ln\left(\frac{r_o}{r}\right)\right]$	$u = u_{max}\left(1-\left(\frac{r}{R}\right)^m\right)^{1/n}$
		$m = 2, n = 1$
Turbulent	Profile extracted from a long annulus.	$m = 2, n = 3,7$

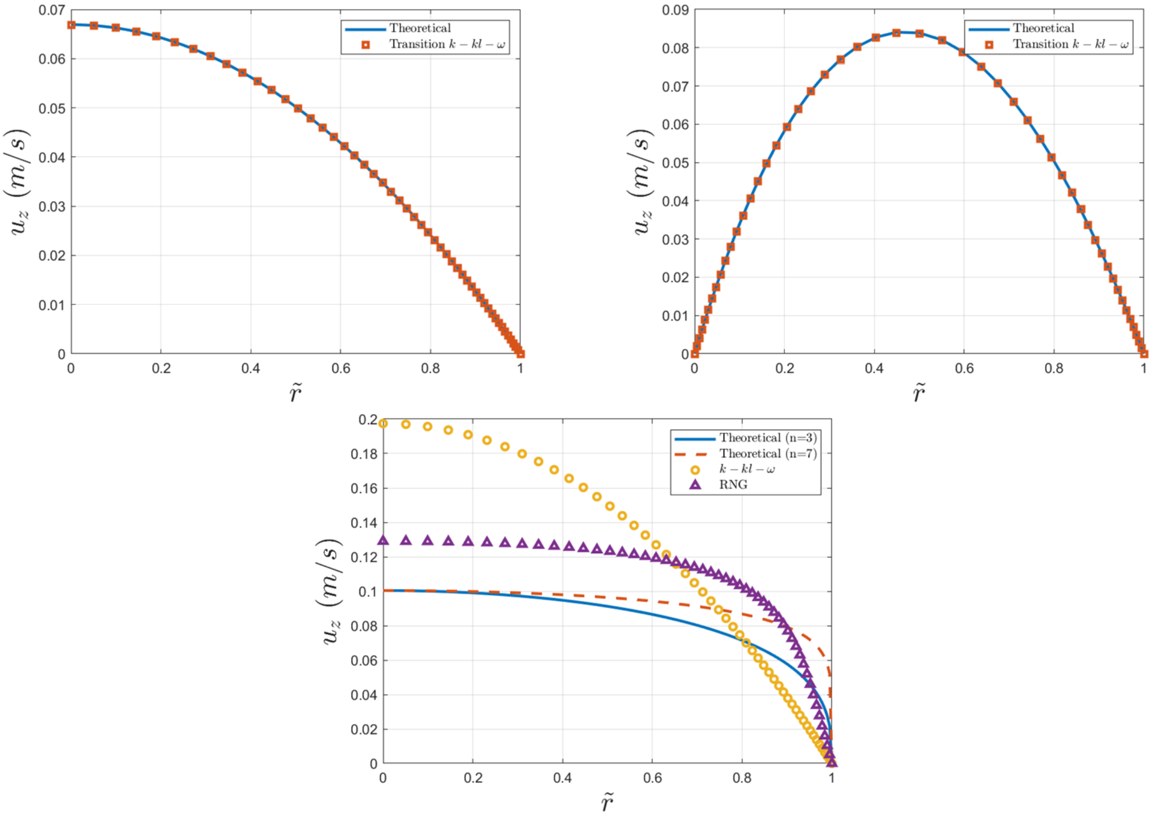

Figure 4.12: Axial velocity profiles plotted against the dimensionless radial location comparing the theoretical results to the results obtained by the Transition $k-kl-\omega$ model of both the tubular (top-left) and annular (top-right) fluids at Re=2000. Axial velocity profiles plotted against the dimensionless radial location comparing the theoretical results at n=3 and n=7 to the results obtained by the Transition $k-kl-\omega$ and RNG models of tubular (bottom) fluid at Re=3000 in the unheated double pipe heat exchanger.

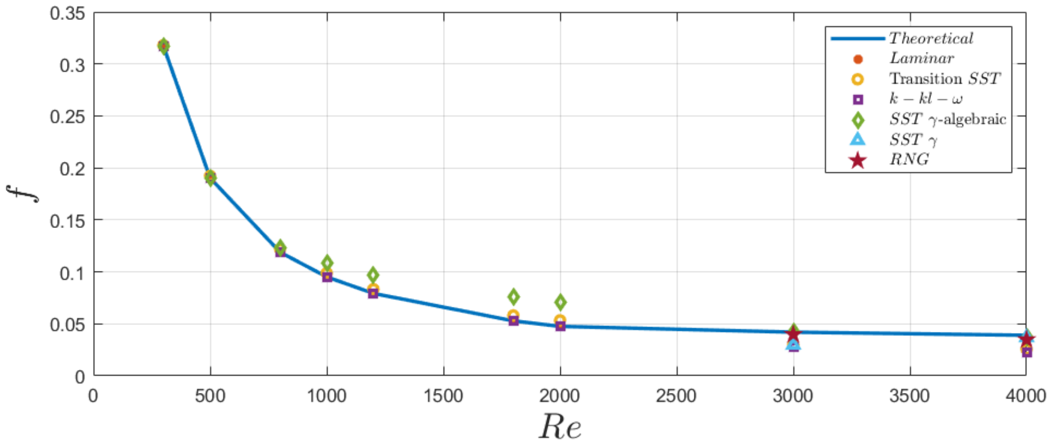

Figure 4.13: Validation of the laminar, Transition SST, Transition $k-kl-\omega$, Transition SST gamma and gamma-algebraic, and RNG models to predict the friction factor evaluated by the correlations by Moody [19] and Jones and Leung [123] against Reynolds number.

In terms of Nusselt number, the correlations summarised in Table 3.1 are compared with simulation results. Figure 4.14 presents the results from annular Nu calculated by the laminar model when compared to the correlation expressed in Eq. (3.10). The model is observed to be in great agreement with the correlation with an accuracy ranging between 2% and 12%. However, the 38% in deviation at the outlet of the annulus is due to the lack of detection of counter flow effect where the highest temperature of the hot domain is also located at the annular outlet giving a rise in the local numerical Nusselt number (Nu_0).

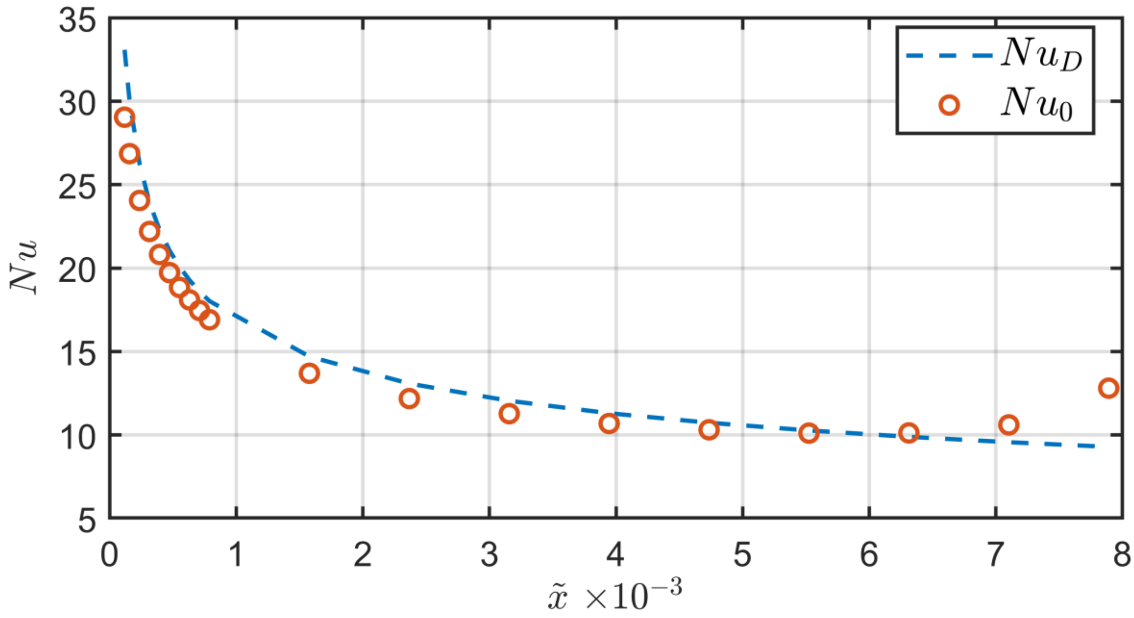

Figure 4.14 Validation against local Nusselt number using the laminar model at $Re = 1200$.

In terms of average Nusselt number, when $Re \leq 2000$ the laminar model was adopted and compared to Eq. (3.15). When $Re \geq 2000$ several correlations were used to compare the turbulent Nusselt number to the results obtained by $K - \epsilon\, RNG$. From Figure 4.15, it can be observed that the laminar model shows complete agreement with the correlation ranging between 0% and 10% accuracy. In terms of $K - \epsilon\ RNG$ it was found that the simulations were mostly accurate when compared to the correlations developed by Monrad and Pelton [108], Wiegand [110], McAdams [105] and Petukhov and Roizen [113] ranging from $< 1\% - 12\%$. The more recent correlations by Dirker [102] and Abou-Ziyan [121] were deviated by a 41% and 45% and 15% and 18% at $Re = 3000$ and 4000, respectively.

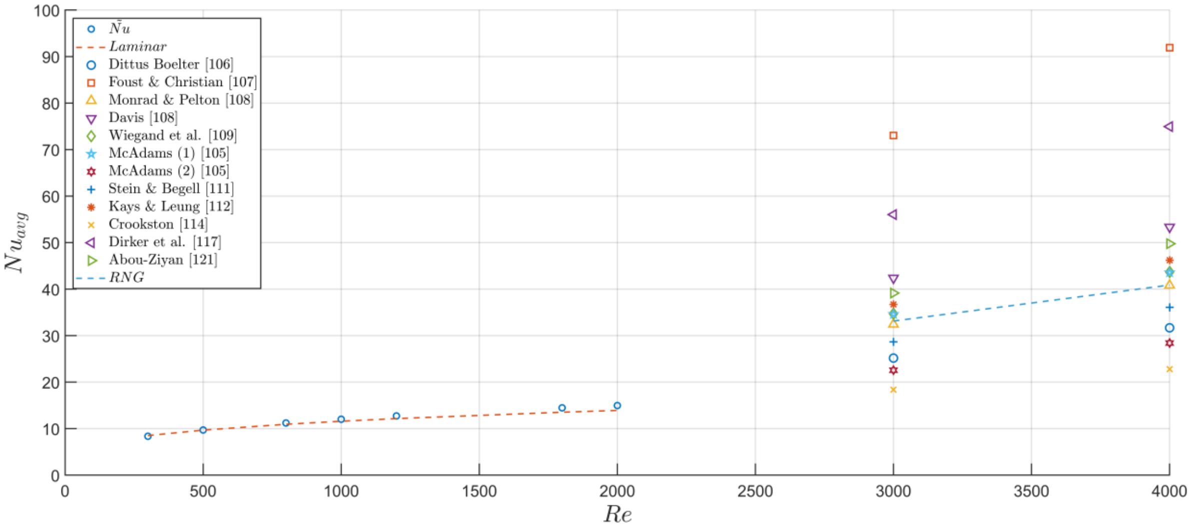

Figure 4.15 Validation of both laminar and $K - \epsilon$ RNG models against average Nusselt number calculated by the empirical correlations from the literature.

Chapter 5: Single and Full Swirling Configurations

5.1 Introduction

This chapter presents CFD analyses of Single Swirling Configurations (SSC) and Full Swirling Configuration (FSC) to address the research objective 1 (velocity and temperature profiles), 2 (decay model development) and 3 (thermal performance evaluation). Simulations examine $\theta_{sw} = 30°, 45°\ and\ 60°$ under heated and unheated conditions to quantify:

- Swirl decay dynamics
- Recirculation zone behaviour
- Thermal boundary layer evolution

Findings inform industrial double pipe heat exchanger design by balancing thermal gain and pressure drop through novel Decay Percentage (DP) parameter introduced in section 5.4. In the upcoming investigations, steady-state simulations were conducted. The SSCs were investigated under unheated and heated conditions. The reference to the configurations is in the form $SSC\boldsymbol{\theta_{sw}}\_\boldsymbol{Re}$, where the swirl angle and Reynolds number are added accordingly.

5.2 Swirling Flow Structure Breakdown

5.2.1 Unheated Case

5.2.1.1 Axial Velocity

Axial velocity profiles quantify initial swirl decay progression, directly informing Research Objectives 1 (velocity profiles) and 2 (decay model development). The axial velocity profiles are presented in Figure 5.2 - Figure 5.6, were extracted from the axial plane located at $\theta = 0°$. The annulus was cut into three zones axially, as shown in Figure 5.1, at which the velocity profiles were extracted. The first zone (upstream) was defined at $0.1\% \leq \tilde{Z} \leq 1.1\%$, the second (intermediate) was at $2\% \leq \tilde{Z} \leq 10.5\%$, and the third (downstream) was at $21\% \leq \tilde{Z} \leq 95\%$. The radial coordinate of the free stream velocity (u_{99}) of the hydrodynamically fully developed flow in the annulus can be calculated using:

$$r_m = \left[\frac{r_o^2 - r_i^2}{2\ln{(r_o/r_i)}}\right]^{1/2} \tag{5.1}$$

yielding a peak velocity located at $r = 16.63$ mm at $\tilde{r} = 47\%$.

Figure 5.2 reveals strong outer-wall bias at swirler exit ($\tilde{Z} = 0.8\%$, $\tilde{r} = 88\%$). This bias persists until $\tilde{Z} < 21\%$, where decay initiates. Velocity peak recentres at $\tilde{r} = 50\%$ as the flow developed downstream. This demonstrates the delay in the hydrodynamic development caused by swirling flow.

Increasing Re (in Figure 5.3 and Figure 5.4) reduces peak velocities and flattens profiles. $SSC30\_2000$ achieved an inner-wall bias of $\tilde{r} = 40\%$ at $\tilde{Z} < 0.3\%$ while stronger bias was achieved by $SSC30\_4000$ of $\tilde{r} = 30\%$ at $\tilde{Z} < 2\%$.

Figure 5.4 - Figure 5.6 show the different profiles produced by different swirl angles at a constant $Re = 4000$. The results showed that outward bias increased with increasing θ_{sw}; weaker swirl leads to stronger axial momentum. Peak velocity was highest in SSC45 followed by SSC30 then SSC60 in the upstream zone. In addition, SSC30 dominates bias magnitude in the intermediate zone. This angle-dependent bias aligns with García-Villalba et al. [143]. PIV data for swirling jets. With regards to design implication, high θ_{sw} (60°) minimises oscillations in the decay zone, favouring stable industrial operation.

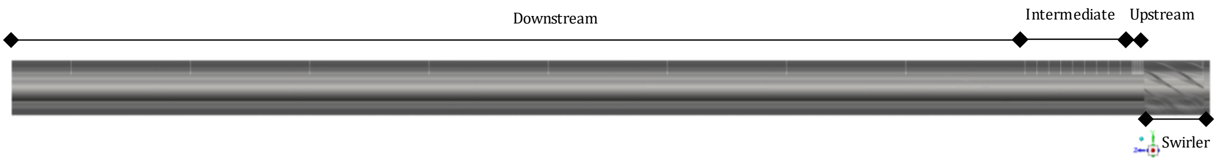

Figure 5.1: Demonstration of the axial zones at which the velocity profiles were extracted.

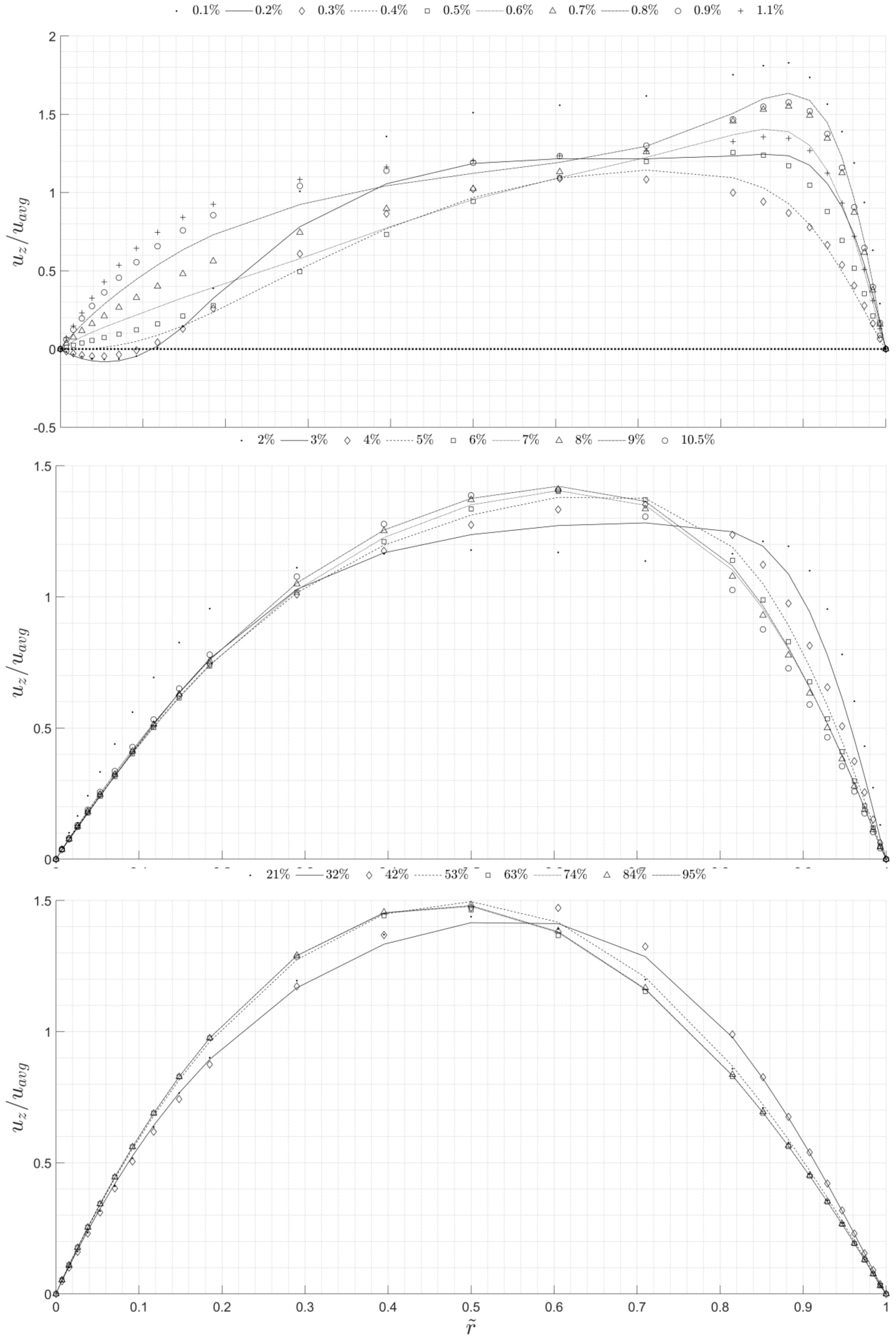

Figure 5.2: Normalised unheated axial velocity profile at various locations for SSC30_300.

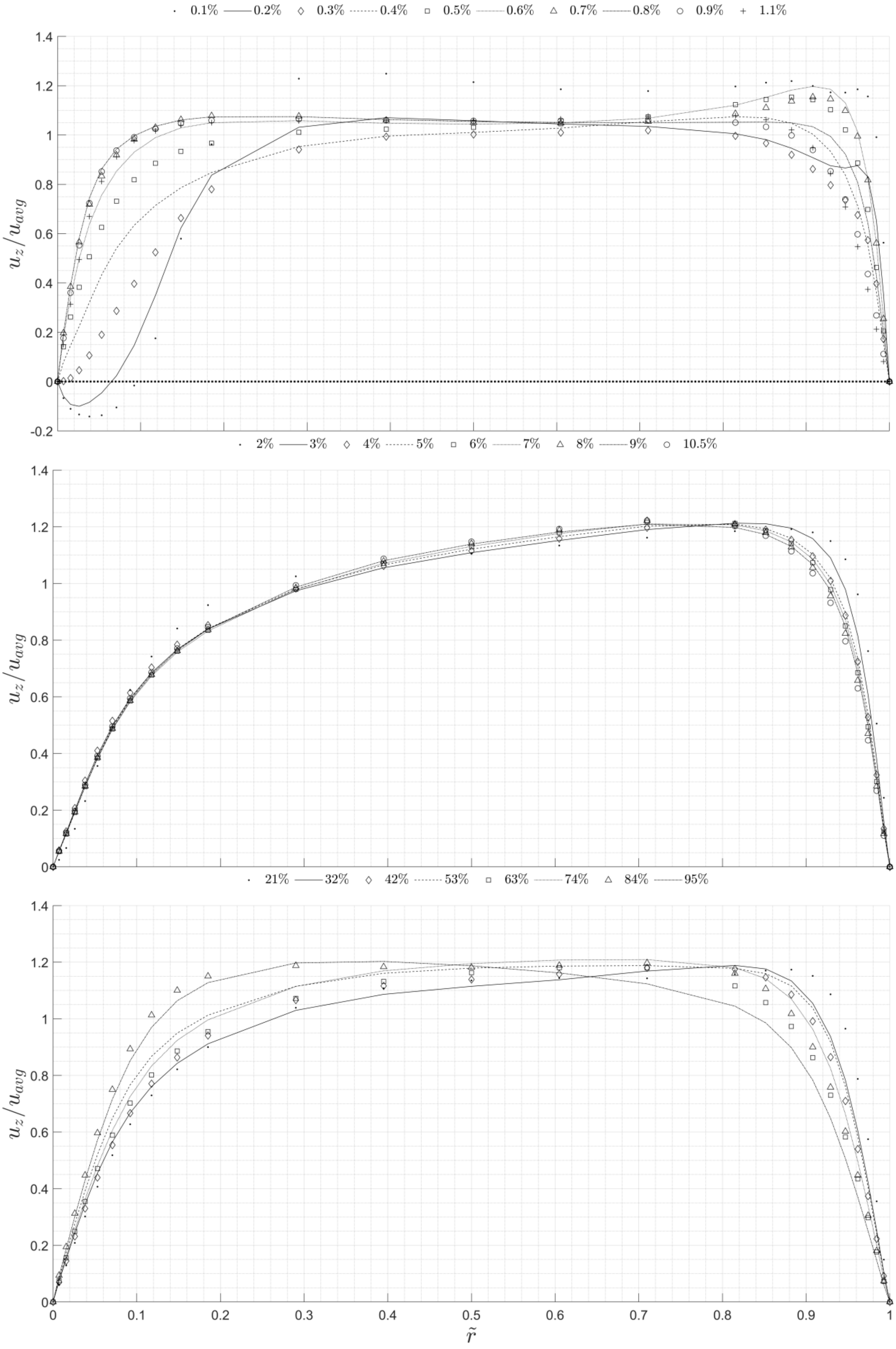

Figure 5.3: Normalised unheated axial velocity profile at various locations for SSC30_2000

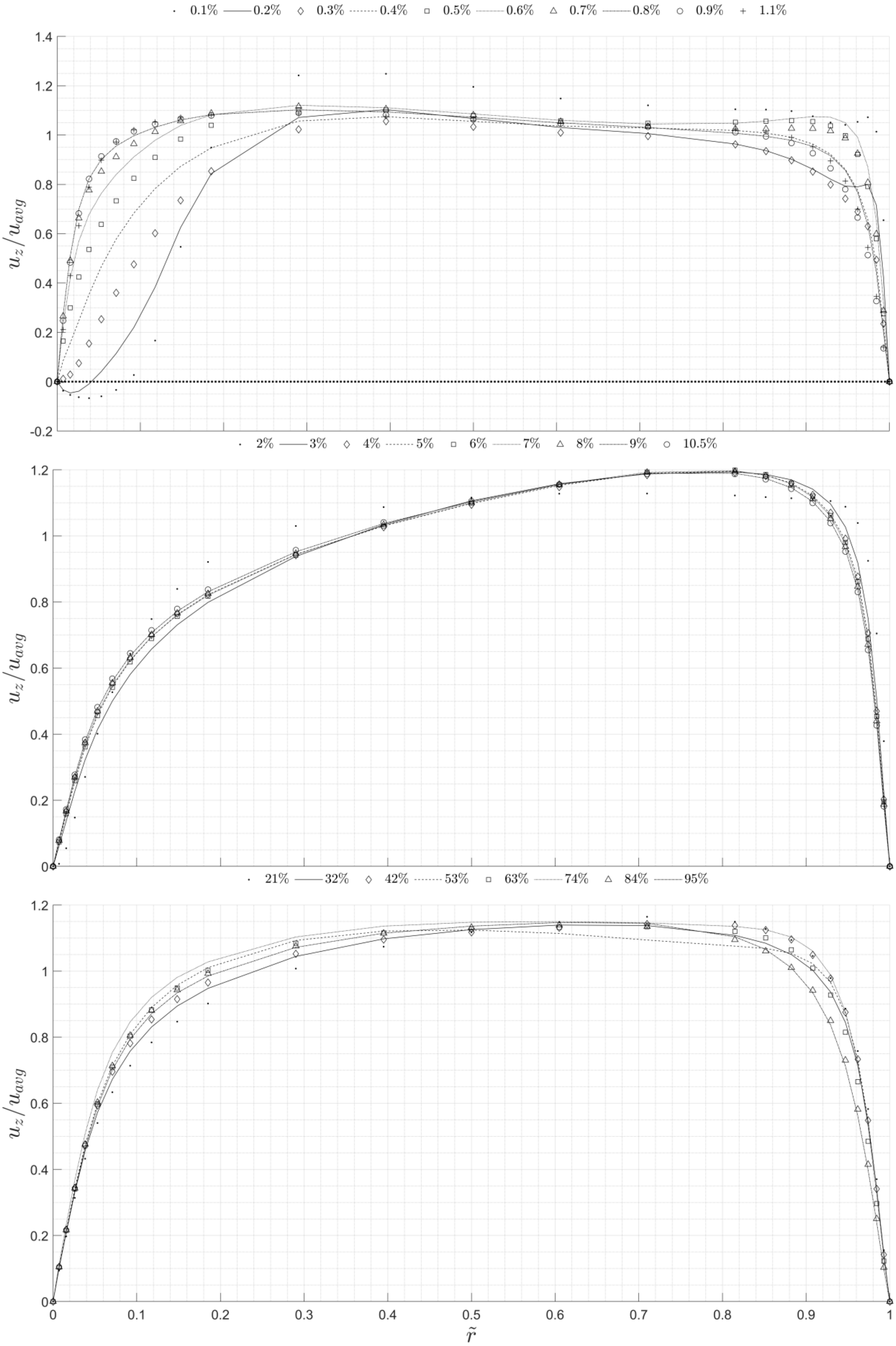

Figure 5.4: Normalised unheated axial velocity profile at various locations for SSC30_4000

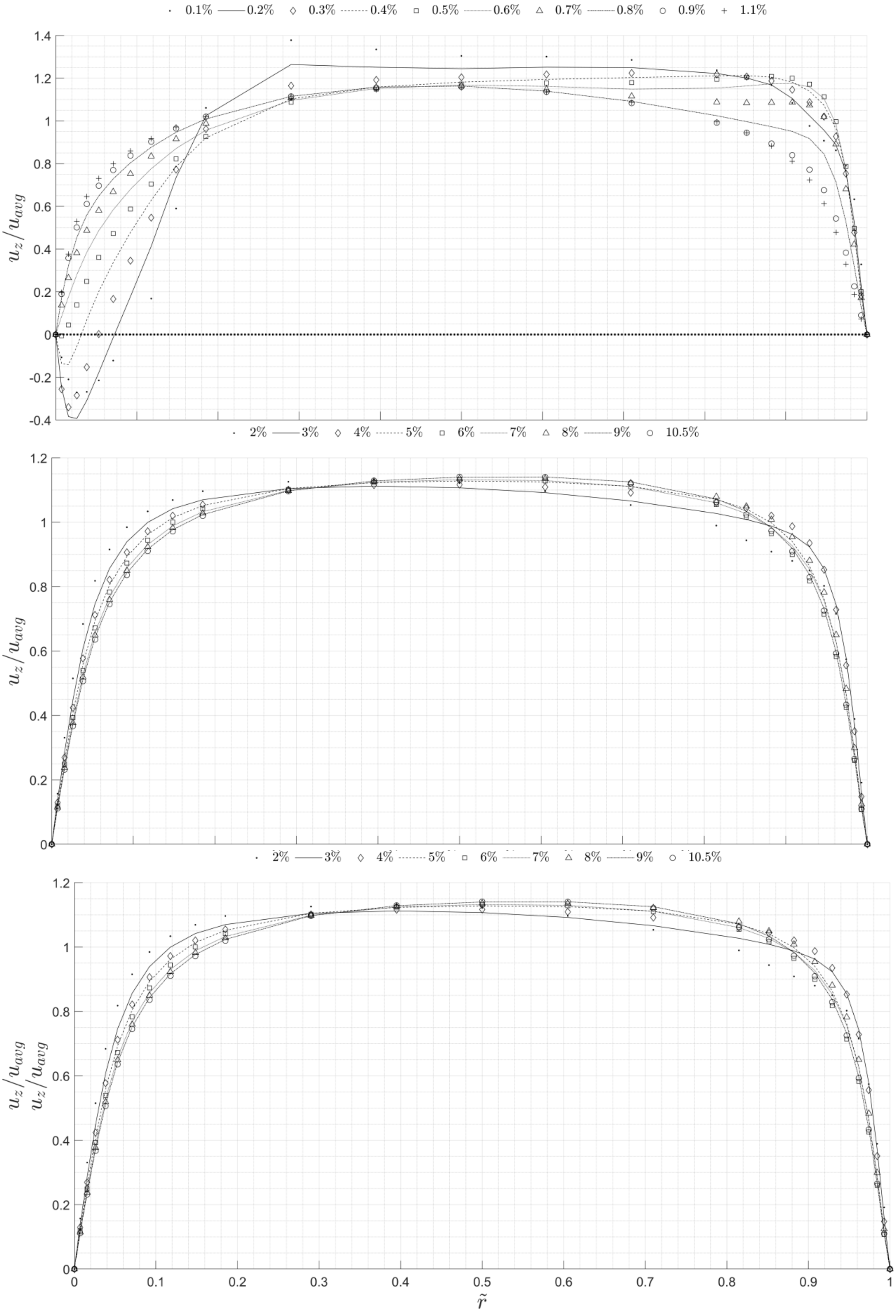

Figure 5.5: Normalised unheated axial velocity profile at various locations for SSC45_4000

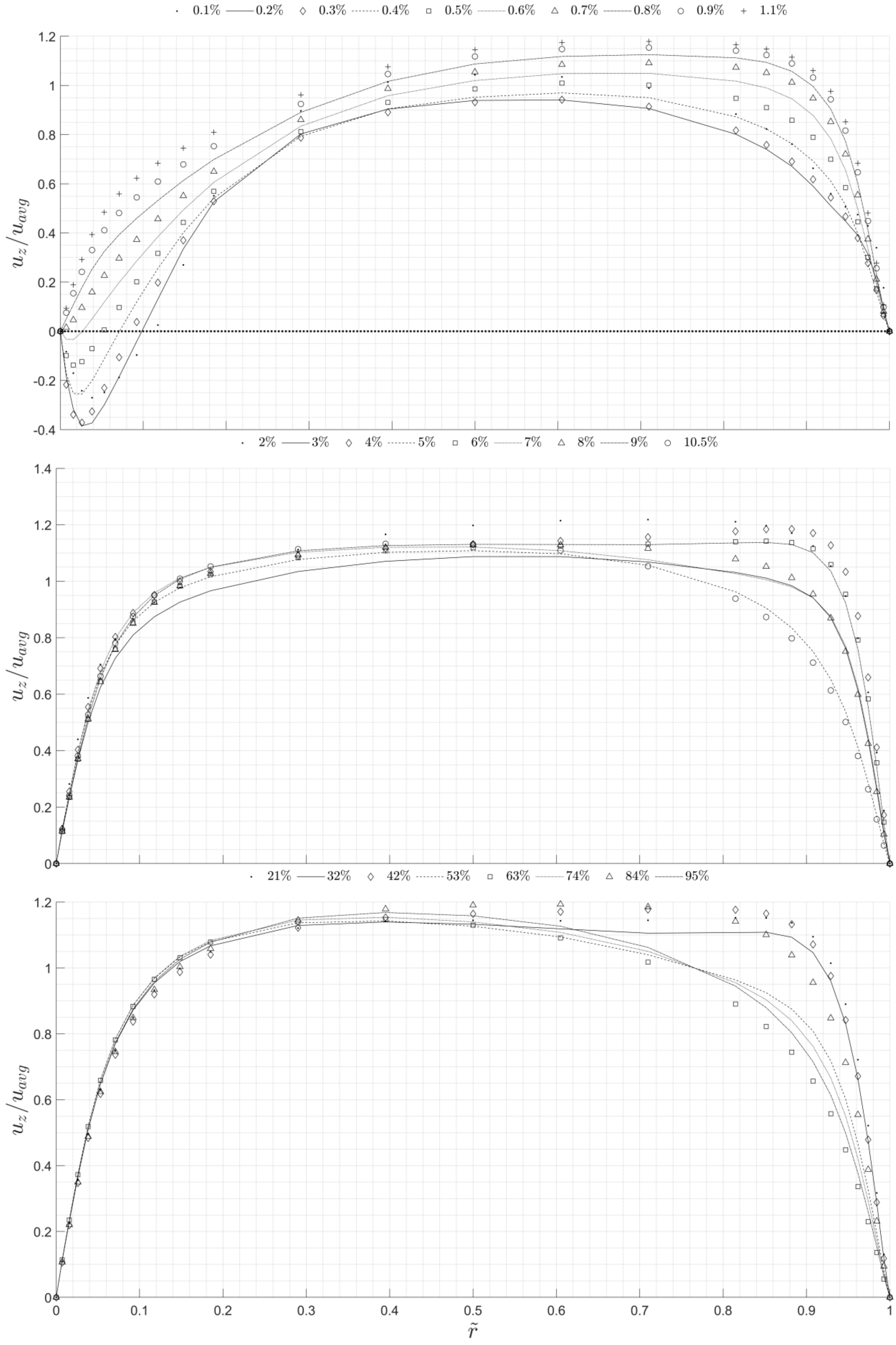

Figure 5.6: Normalised unheated axial velocity profile at various locations for SSC60_4000

5.2.1.2 Recirculation Zone

Analysis of recirculation zones reveals critical mechanisms governing upstream swirl decay flow. Negative axial velocities in Figure 5.2 - Figure 5.6 identify recirculation zones, with two dominant trends: 1) Reynolds number dependence where the length of the zone decreases with increasing Re. Namely, 40% reduction from Re=300 to 4000 for SSC60. Due to thinner boundary layers, separation susceptibility was reduced. 2) Swirl angle dependence where the zone length increases with θ_{sw}. The zone was observed to be 250% longer than SSC30 at Re=1000 due to the stronger rotational momentum.

Figure 5.7 presents details of the zone morphology with the aid of iso-surfaces evaluated at $\mathrm{u_z} = 0\ \mathrm{m/s}$. SSC60 zones develop along inner wall with helical edges during dissipation, indicating tangential convection. SSC45 shows secondary zones at vane walls ($Re \leq 1000$) that vanish at $Re \geq 3000$. SSC30 exhibits unique inlet zones at convex and concave vane walls, with convex regions dominating at $Re \leq 1000$ and concave at $Re \geq 1800$. The observed variation of the zone matches the LES simulations of annular swirl decay by Schlatter et al. [144].

Figure 5.8 and Figure 5.9 quantify central zone dimensions. In terms of the axial reach, SSC60 peaks at $\mathrm{Re} = 1000$ (250% increase from Re=300), then decreases 61% by Re=4000. With regards to radial height, SSC30 shows exponential decrease (50% reduction at Re=4000) vs. linear decrease for SSC45 and SSC60. Maximum radial occupation at Re=800 of 15% and 20% for SSC60 and SSC30, respectively, suggests optimal thermal performance in mid-Re range for industrial DPHEs.

These recirculation patterns demonstrate how zone location and reach govern swirl decay behaviour (in objective 1) while providing the physical basis for friction correlations in objective 2. The angle-dependent zone development directly informs swirler selection for thermal performance optimisation in objective 3.

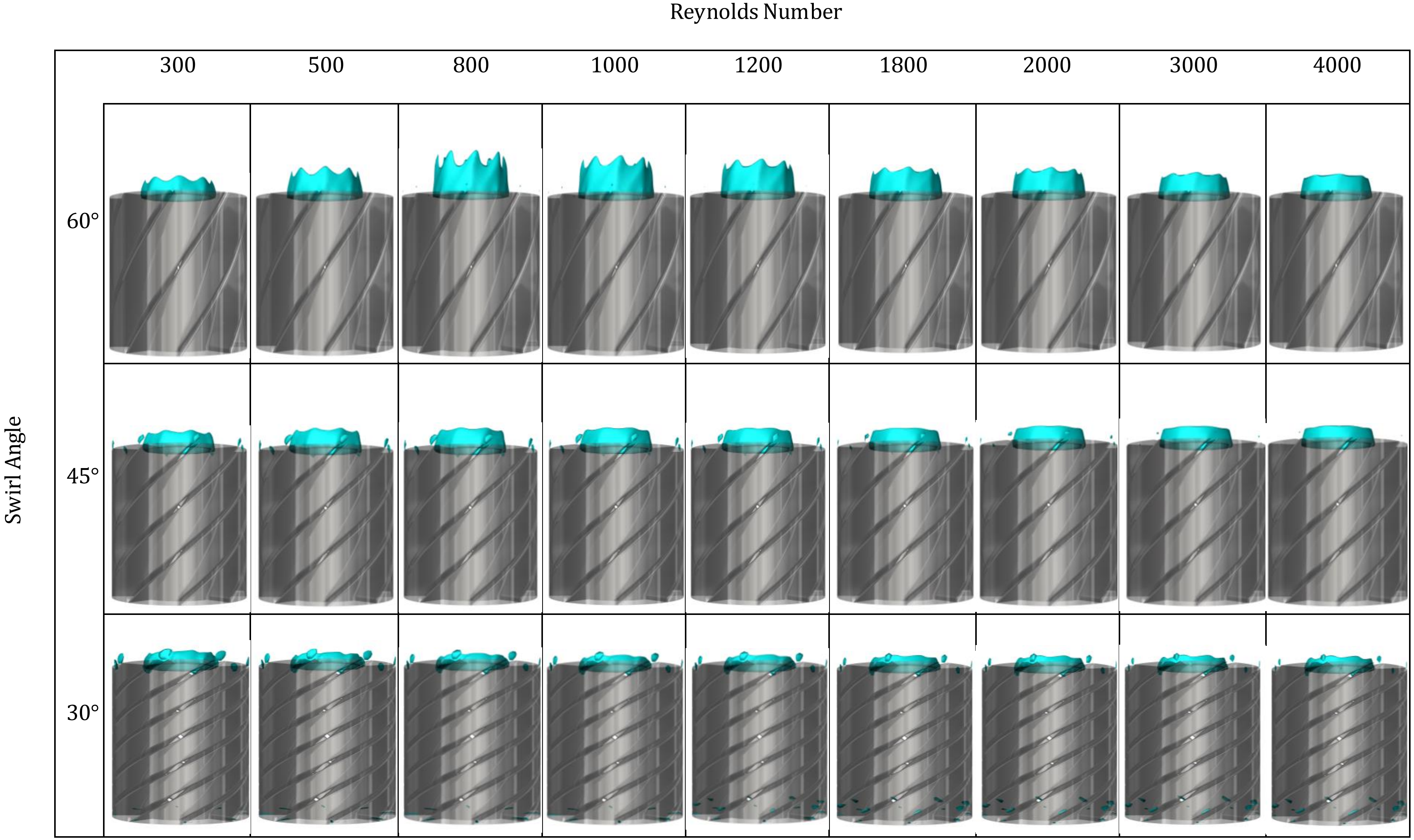

Figure 5.7: Axial velocity iso-surfaces evaluated at $u_z = 0$ representing the dividing surface of the unheated recirculation zones at varying θ_{sw} and Re.

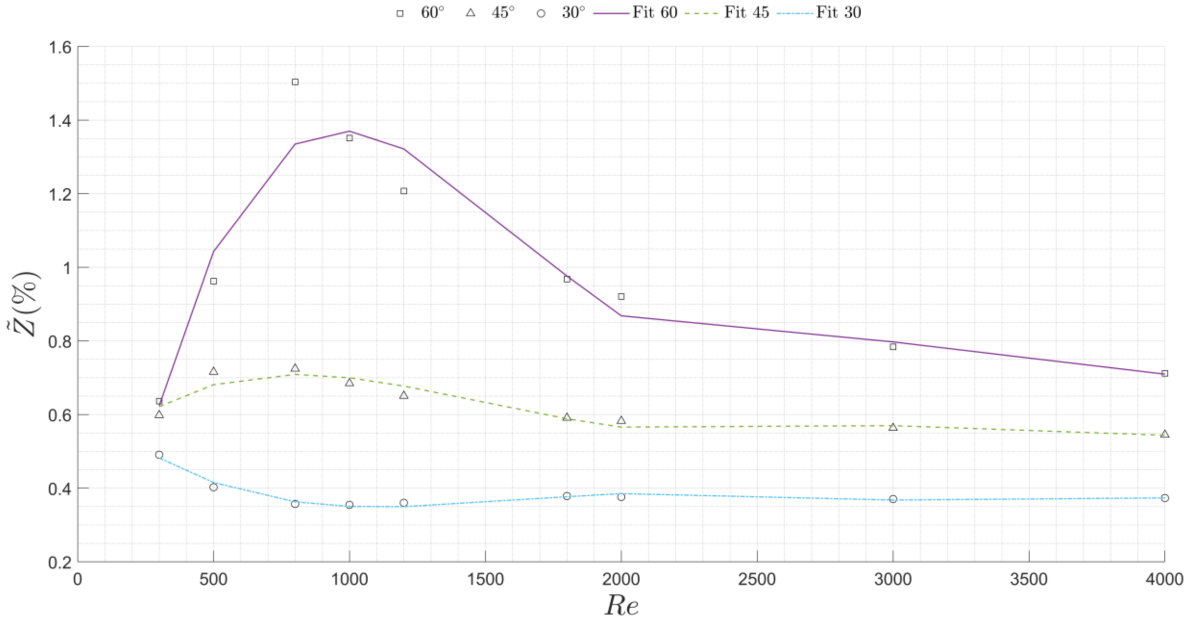

Figure 5.8: Axial variation of the maximum reach of unheated recirculation zone at the central region.

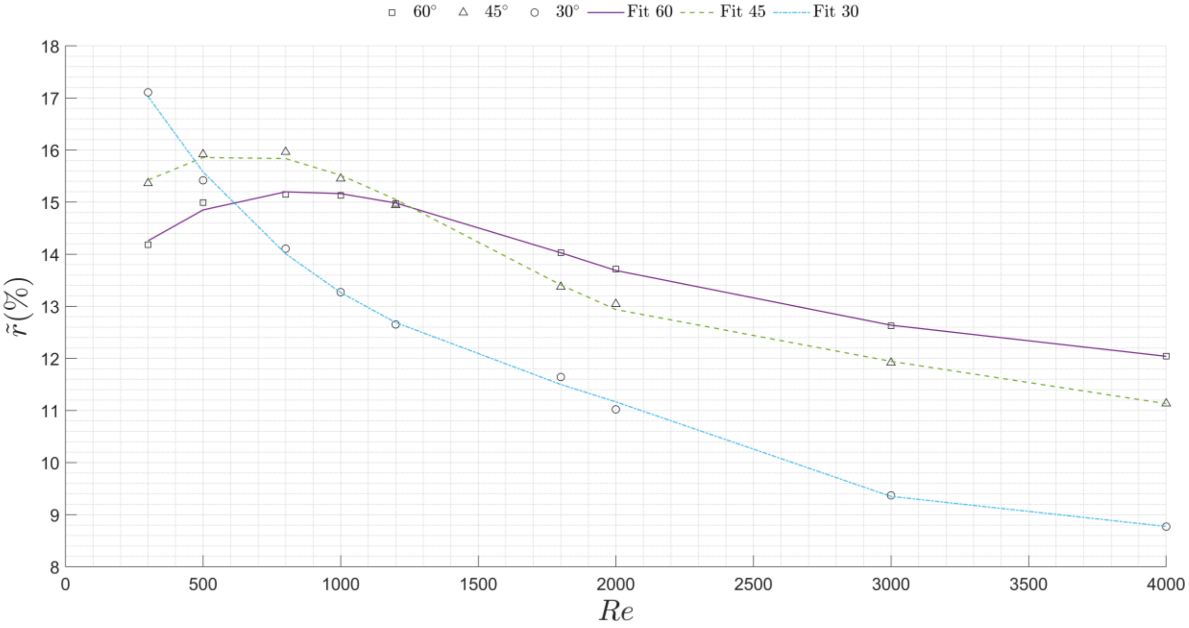

Figure 5.9: Radial variation of the maximum height of unheated recirculation zone at the central region.

5.2.1.3 Tangential Velocity

Figure 5.10 reveals consistent outer-wall bias peaking at $\tilde{r} = 85\%$ and $\tilde{Z} = 0.6\%$, decaying downstream due to viscous dissipation. Higher Re $(2000 - 4000)$ flattens profiles but maintains peak locations $(\tilde{r} = 88\%)$ with decay initiation consistently at $0.5 < \tilde{Z} < 0.6\%$..

Decreasing θ_{sw} to 45° and 30° (Figure 5.10 to Figure 5.14) reduces peak velocities, in the range 50%-102% when compared to SSC30_4000 but preserves maximum radial deviations ($\tilde{r} = 88\% - 90\%$), confirming angle-independent radial bias. Profile extraction along straight planes introduces minor deviations as flow follows helical paths. Observed tangential decay rates align with Kim and Boysan's LDV measurements in swirling pipes [145], supporting RANS model accuracy. Potential tangential component over-prediction necessitates the 10% velocity ratio threshold for decay completion.

The observed flattening of tangential velocity profiles at higher Reynolds number $(Re \geq 2000)$ suggests diminished mixing efficiency due to weakened swirl intensity. For industrial applications operating at lower Reynolds numbers $(Re < 1000)$, selecting swirl angles $\theta_{sw} < 45°$ is recommended to enhance turbulence generation and maintain effective heat transfer performance.

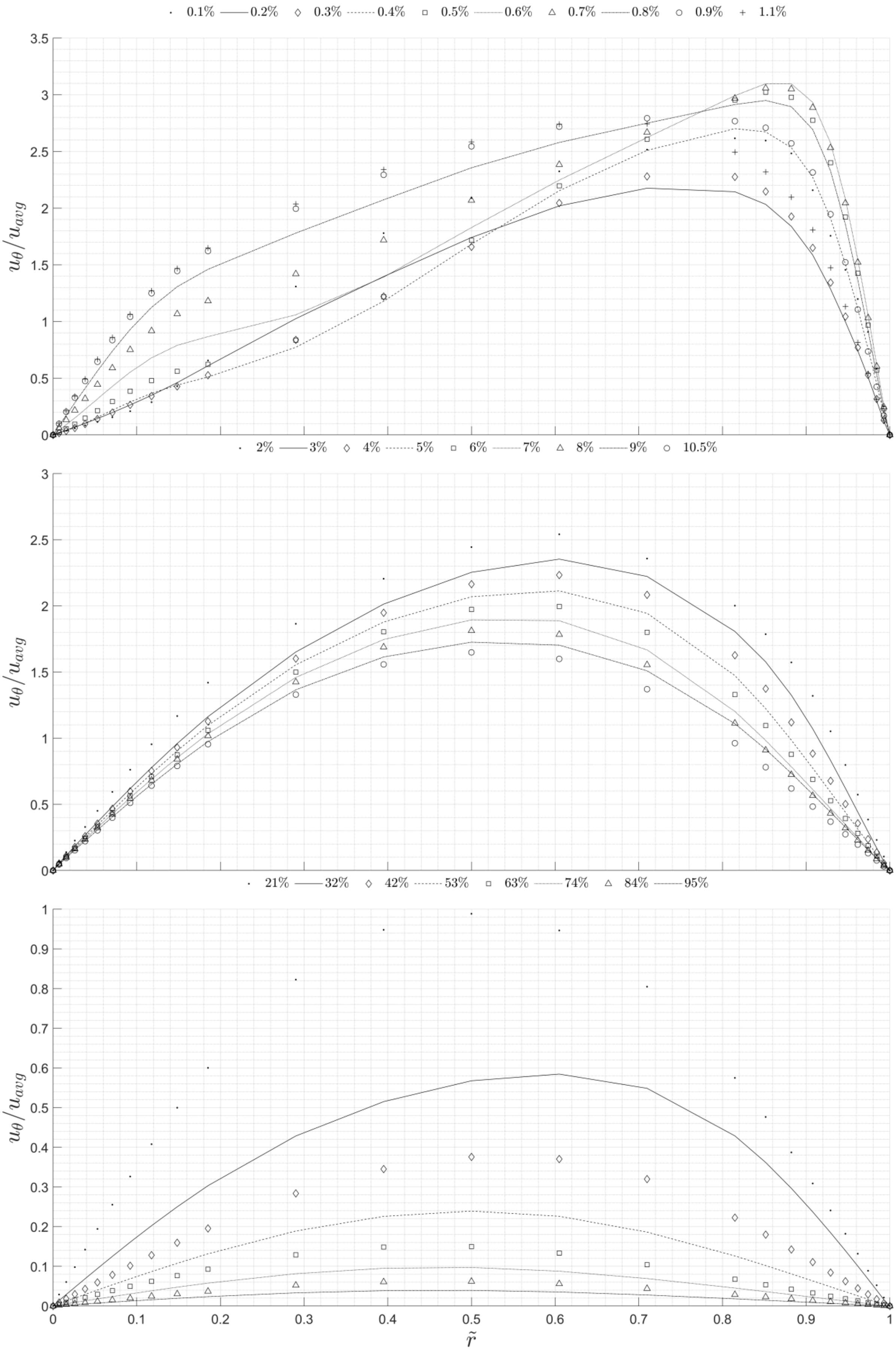

Figure 5.10: Normalised unheated tangential velocity profile at various locations for SSC30_300.

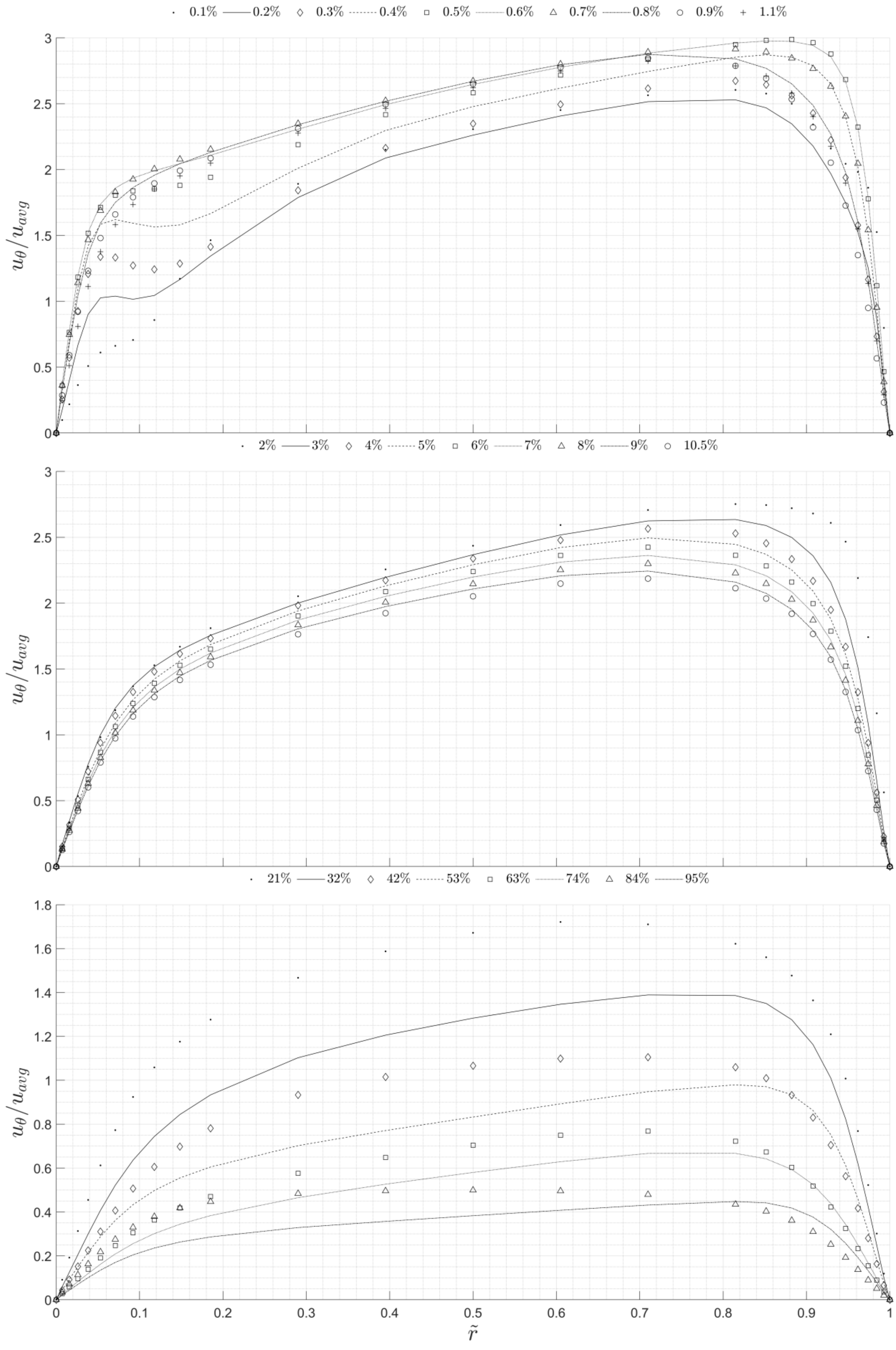

Figure 5.11: Normalised unheated tangential velocity profile at various locations for SSC30_2000.

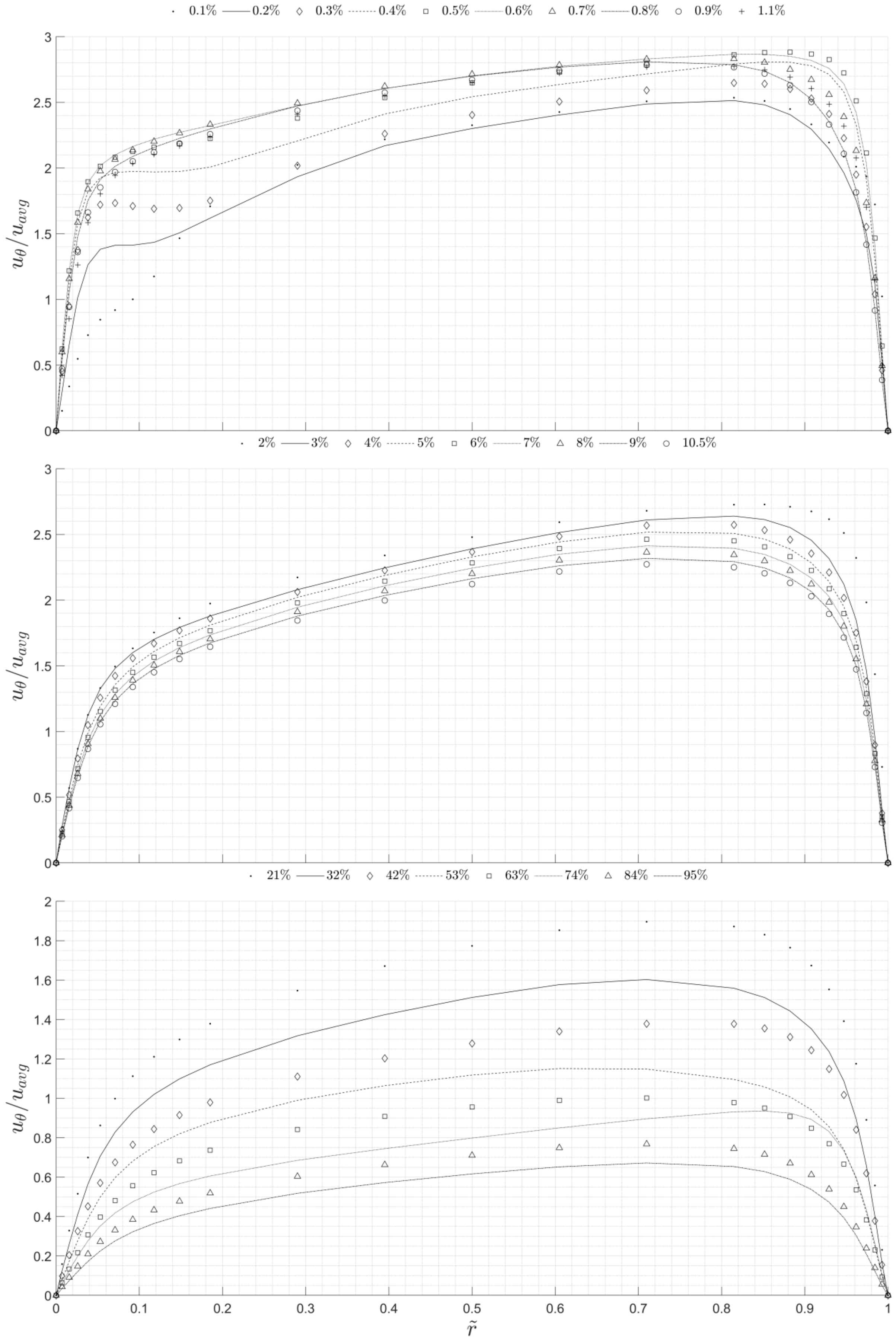

Figure 5.12: Normalised unheated tangential velocity profile at various locations for SSC30_4000.

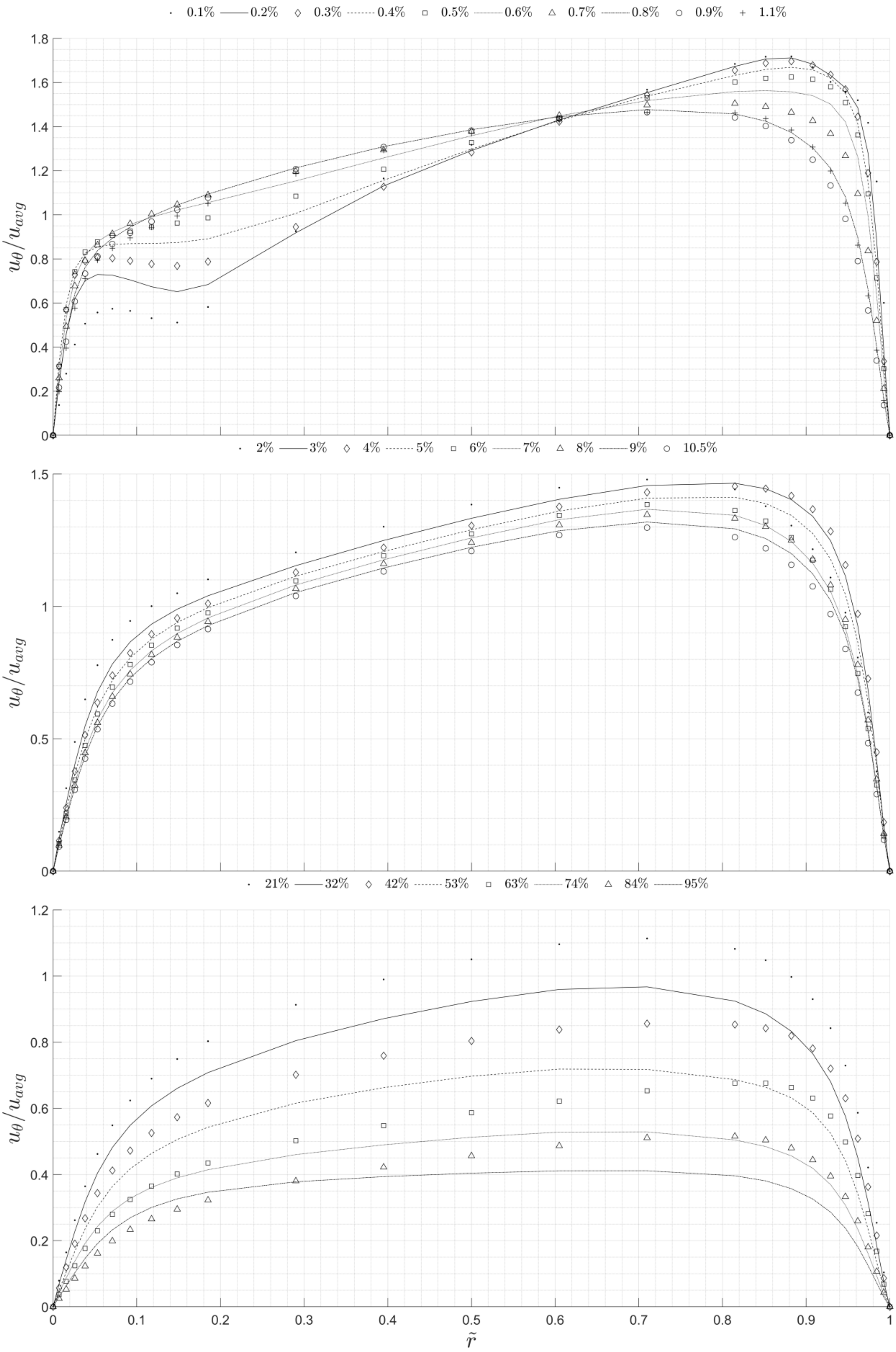

Figure 5.13: Normalised unheated tangential velocity profile at various locations for SSC45_4000

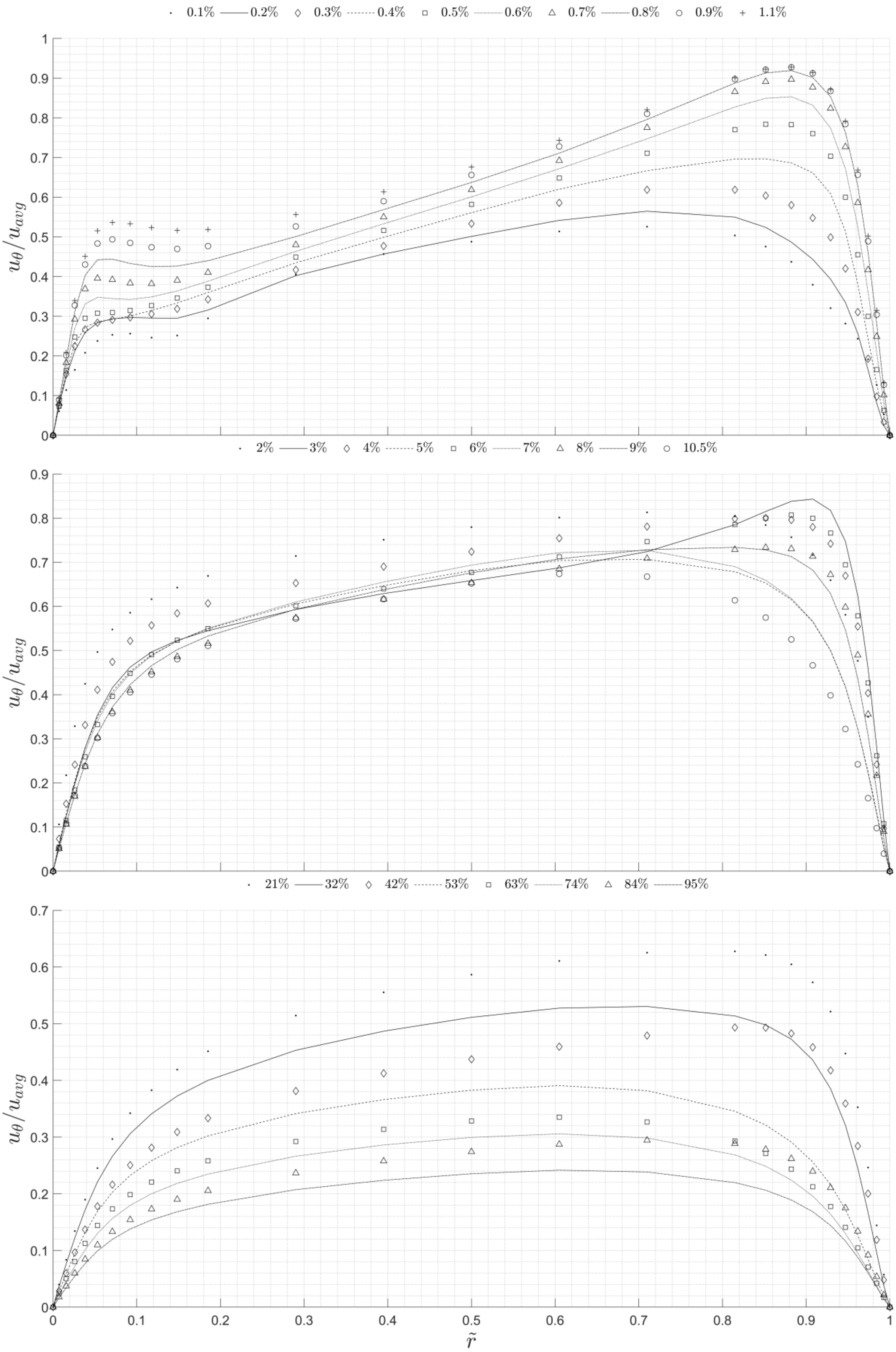

Figure 5.14: Normalised unheated tangential velocity profile at various locations for SSC60_4000.

5.2.2 Heated Case with Equivalent Reynolds Numbers

This section delves into the hydrodynamic behaviour of the swirling flow under heated conditions, specifically analysing the axial velocity profiles with Reynolds numbers equal for the annular and the tubular sides. Understanding these profiles is crucial for assessing thermal effects on flow dynamics and ultimately on heat exchanger performance.

5.2.2.1 Axial Velocity

Heated axial velocity profiles reveal thermal effects on swirl decay. Figure 5.15 and Figure 5.16 shows intensified outer-wall bias, with velocity oscillations (e.g., 192% to 109% to 170% at $\tilde{Z} = 0.3\% - 0.9\%$) indicating thermal disruption. Higher Re $(2000 - 4000)$ reduces bias magnitude but amplifies oscillatory decay, evidenced by false parabolic profiles at $\tilde{Z} = 42\%$ $(\text{Re} = 4000)$. Thermal acceleration near inner wall counters centrifugal forces, shortening decay zones by $20\% - 25\%$.

Increasing θ_{sw} to 45°, as shown in Figure 5.18, strengthens initial outer bias (radial deviation: 29% to 91% at $\tilde{Z} = 0.1\% - 0.7\%$) but shortens decay duration vs. θ_{sw} to 30°. Weakest swirl ($\theta_{sw} = 60°$) exhibits minimal radial bias ($\leq 52\%$) and rapid stabilisation, confirming that higher angles (lower intensity) reduce flow disruption during heating.

Observed thermal bias reduction at $\theta_{sw} = 60°$ aligns with heat transfer studies by Song et al. [146]. Low-intensity swirl ($\theta_{sw} \geq 45°$) minimizes thermal oscillations, favouring high-ΔT industrial applications.

Thermal effects amplify velocity oscillations during decay, weaken radial bias with increasing θ_{sw}, and accelerate hydrodynamic development – collectively informing heated swirl decay models and heat exchanger design.

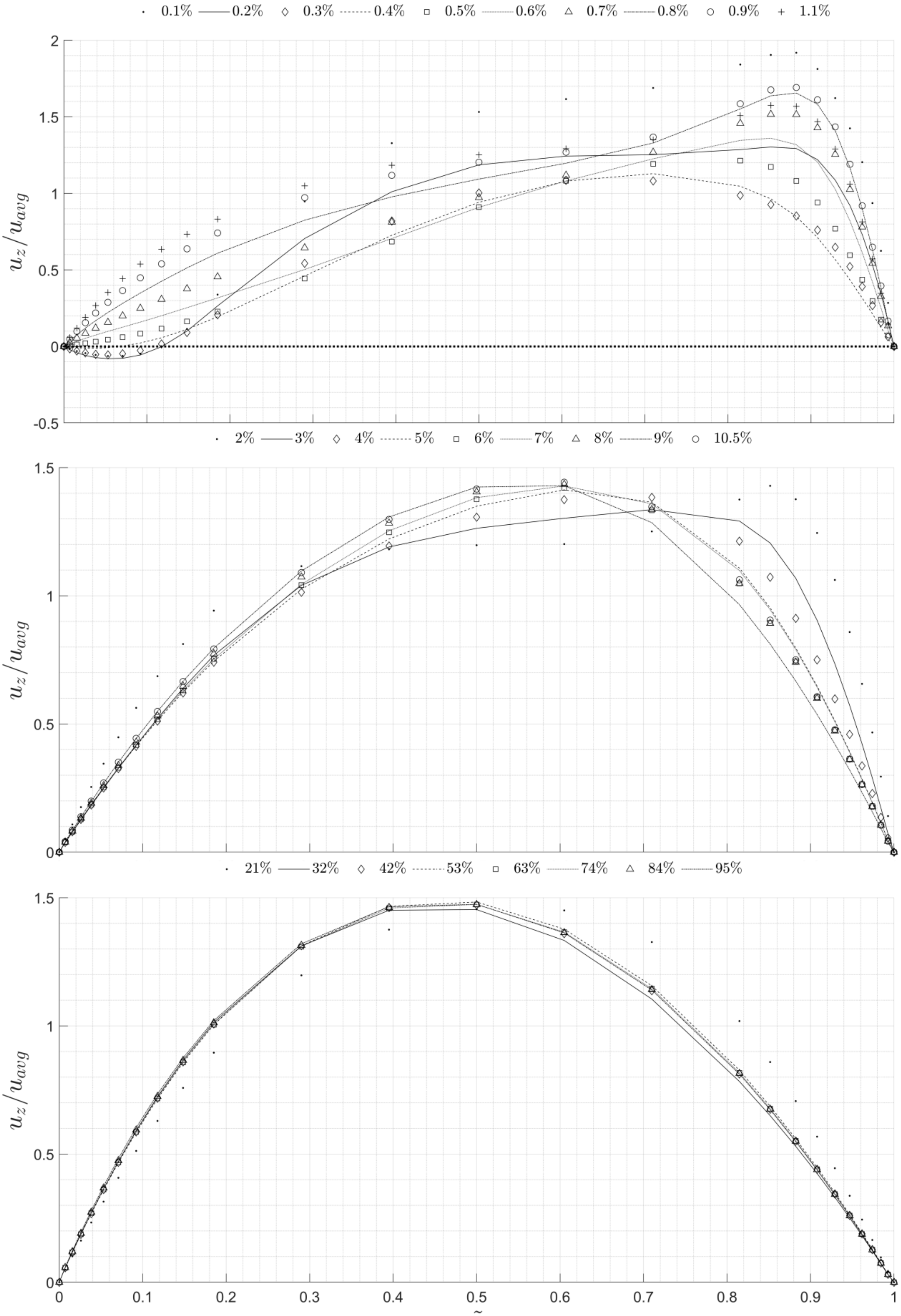

Figure 5.15: Normalised axial velocity profile of the equivalent case downstream variation with the presence of heat transfer SSC30_300.

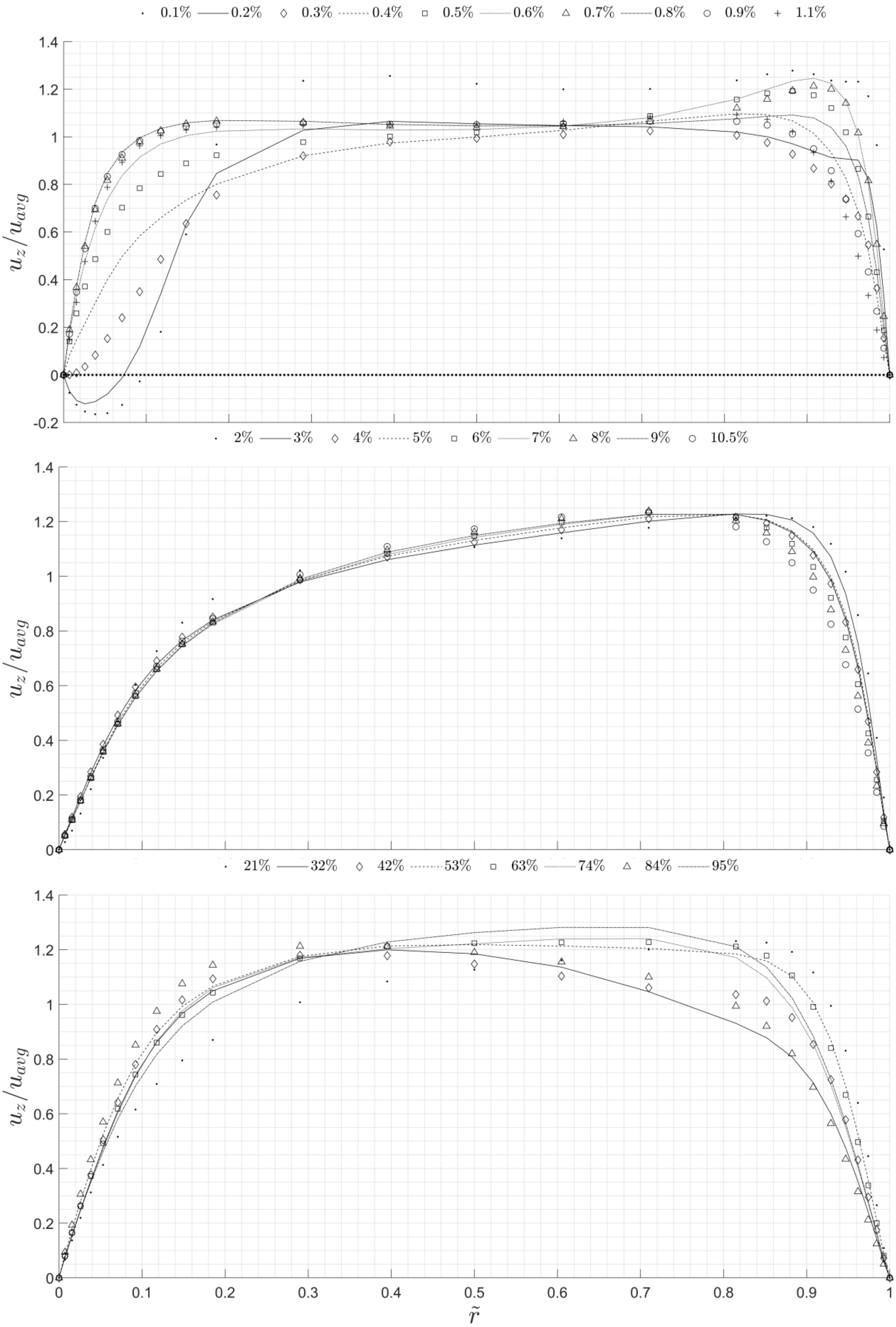

Figure 5.16: Normalised axal velocity profile of the equivalent case downstream variation with the presence of heat transfer SSC30_2000.

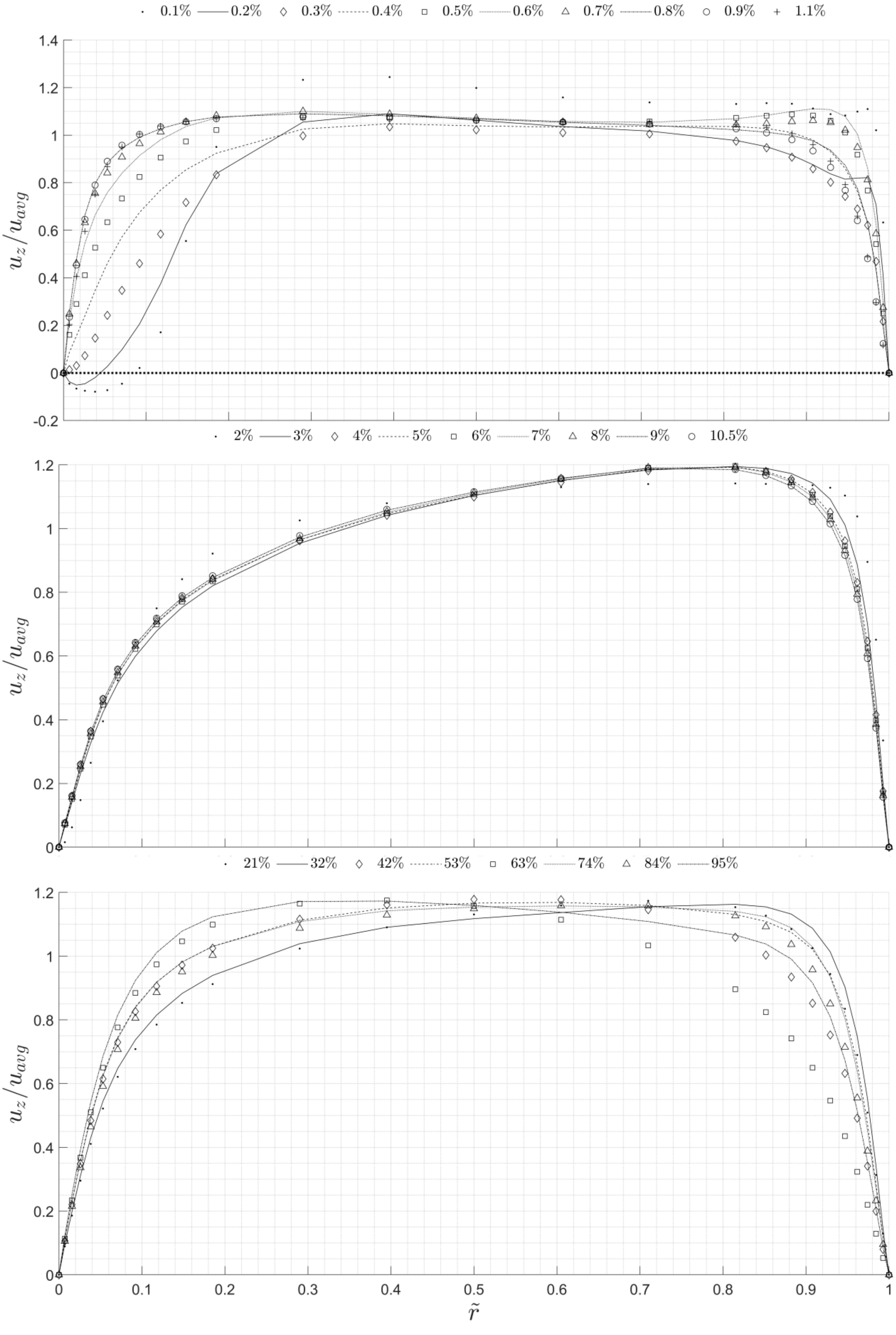

Figure 5.17: Normalised axial velocity profile of the equivalent case downstream variation with the presence of heat transfer SSC30_4000.

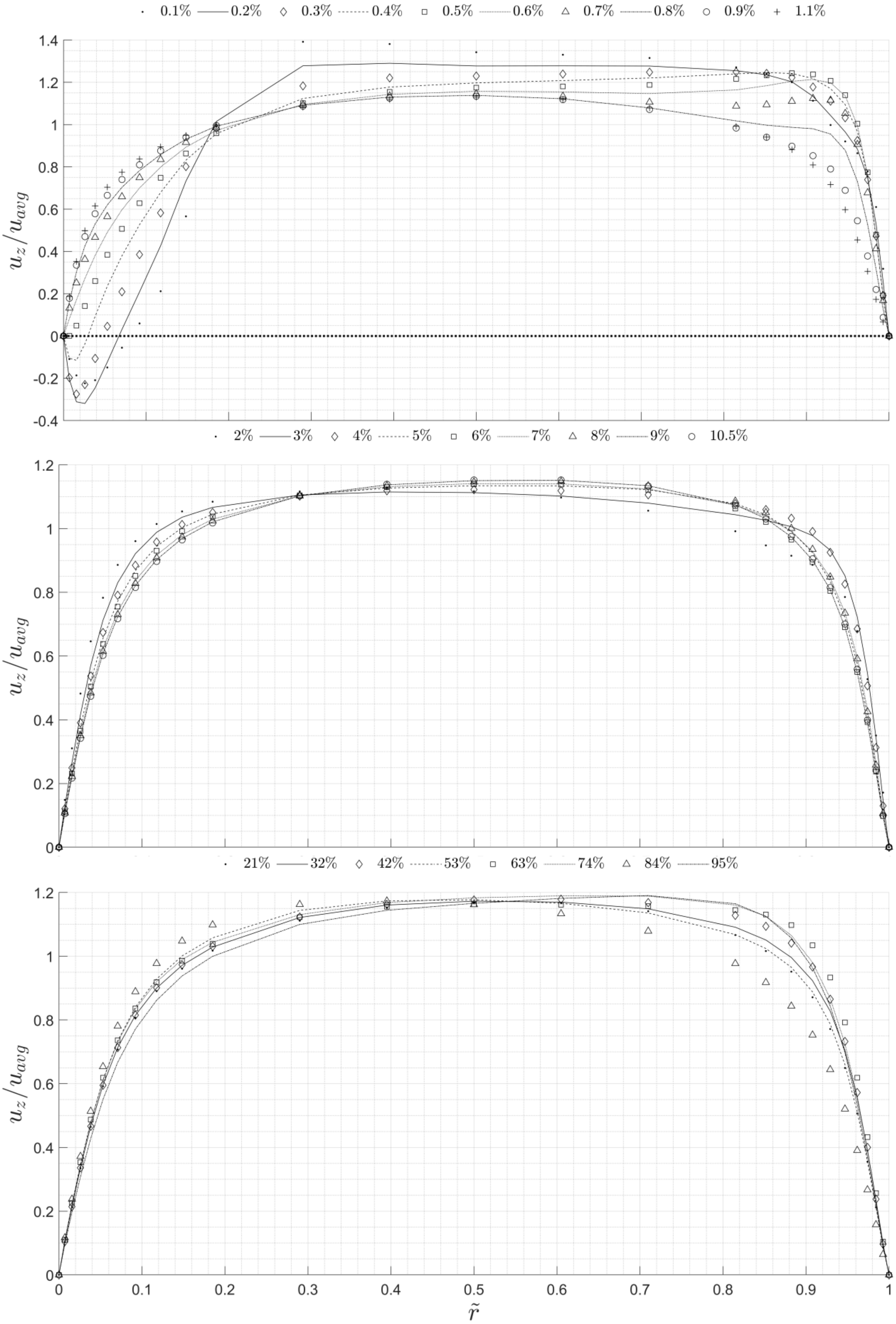

Figure 5.18: Normalised axial velocity profile of the equivalent case downstream variation with the presence of heat transfer SSC45_4000.

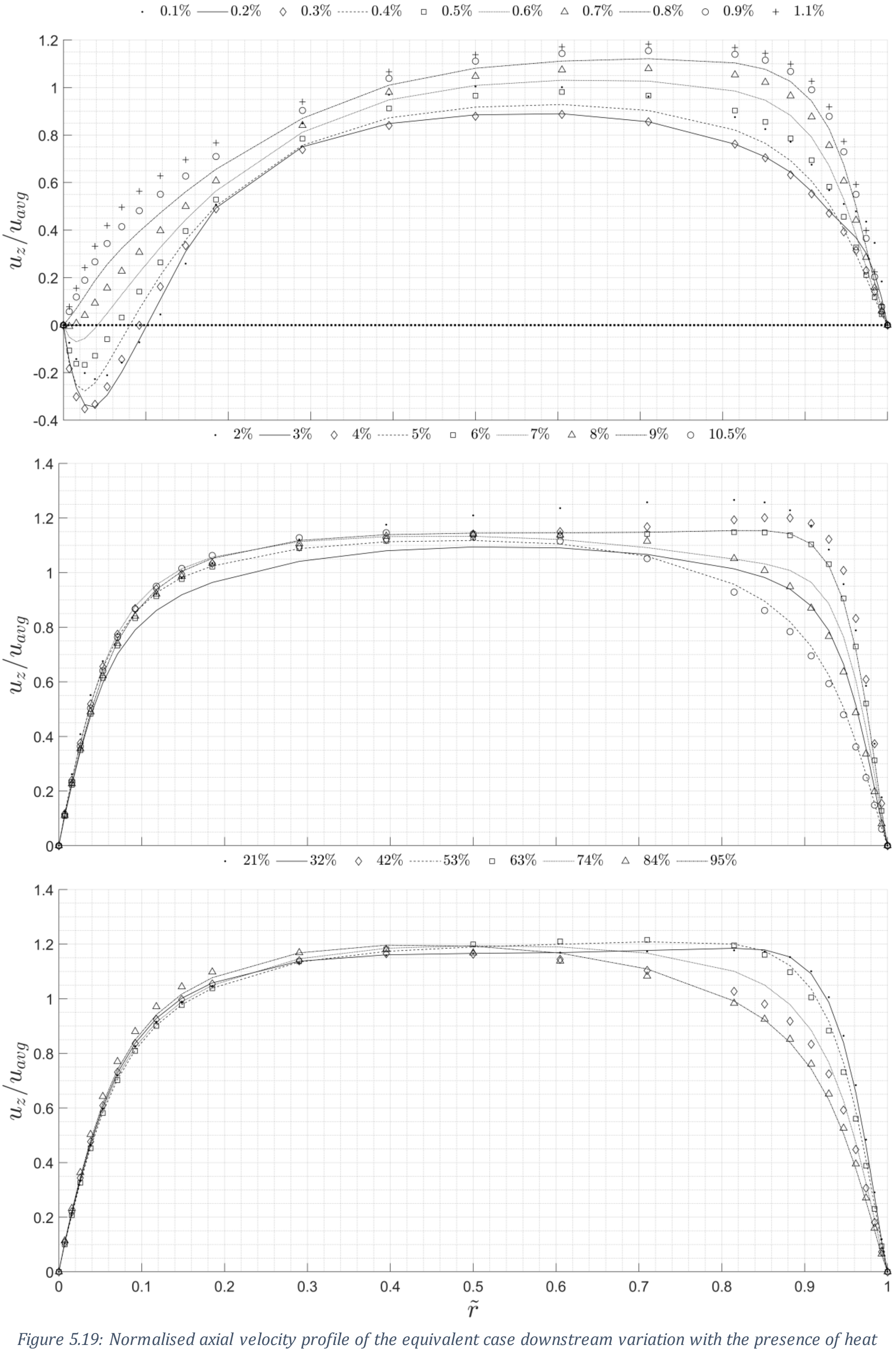

Figure 5.19: Normalised axial velocity profile of the equivalent case downstream variation with the presence of heat transfer SSC60_4000.

5.2.2.2 Recirculation Zone

Heated conditions significantly alter recirculation dynamics versus unheated cases in section 5.2.1.2. At higher Re, thinner boundary layers resist separation, but thermal gradients disrupt this trend: SSC60 zones expand axially ($300 \leq Re \leq 1000$) then contract sharply (61% at $Re = 4000$), while SSC45 develops dual zones (central hub and vane walls) that dissipate by $Re \geq 3000$. Thermal acceleration near walls destabilizes zones, particularly at high swirl intensities ($\theta_{sw} = 30°$).

Swirl intensity has shown a significant impact on the zone morphology:

- SSC30: Inlet zones form at convex and concave vane walls, with convex regions domination $Re \leq 1000$ before concave zone emerge ($Re \geq 1800$).
- SSC45: Vane-wall zones decay continuously without full dissipation.
- SSC60: Central hub zones dominate with minimal thermal disruption.

Figure 5.21 and Figure 5.22 quantify the thermal effects. Axial reach shows θ_{sw} dependence. SSC60 showed a 250% increase in comparison to SSC30, but Re independence. Radial height decreases exponentially with Re for SSC30 in comparison to linear variation of SSC45 and SSC60. High intensity swirl maintains zone persistence under heating, extending thermal enhancement zones by $15\% - 20\%$ in heat exchangers but requires managing accelerated dissipation at $Re > 2000$.

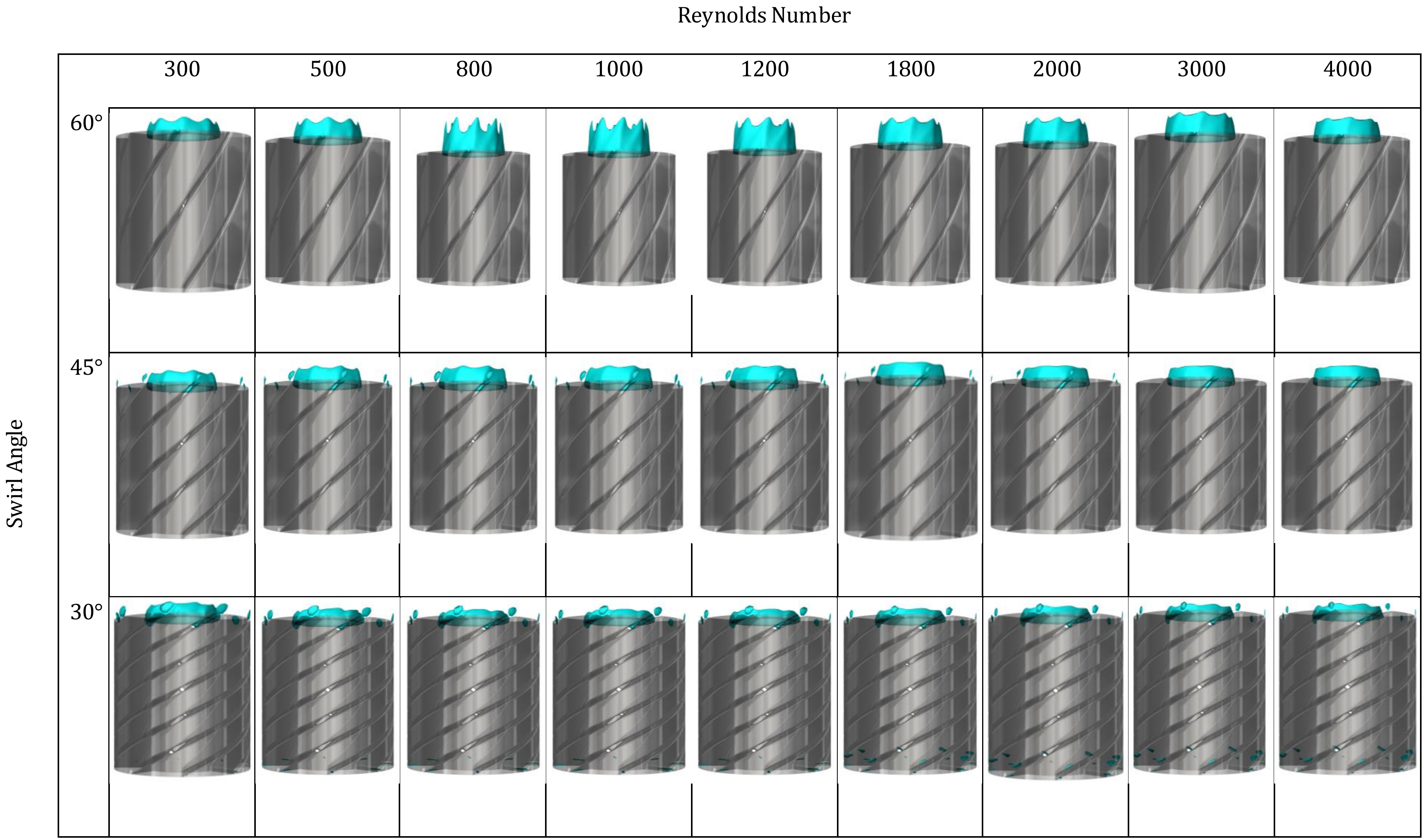

Figure 5.20: Heated axial velocity iso-surfaces evaluated at $u_z = 0$ *representing the dividing surface of the recirculation zones at varying* θ_{sw} *and equivalent* Re*.*

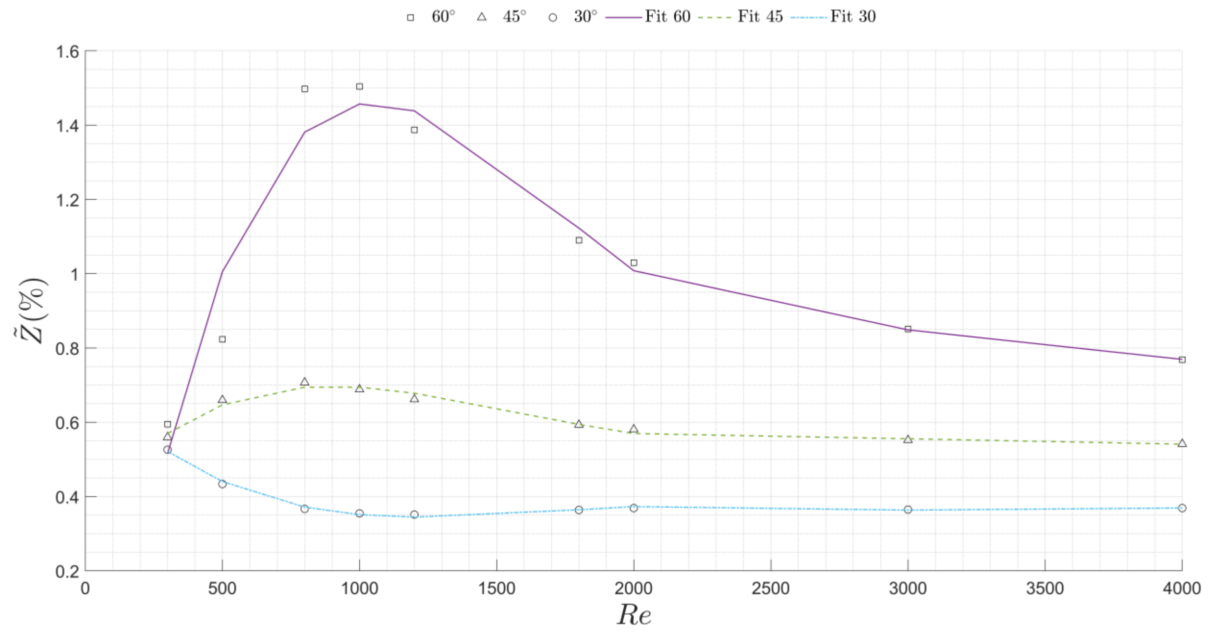

Figure 5.21: Variation of the maximum reach of the heated central region recirculation zone in the axial direction.

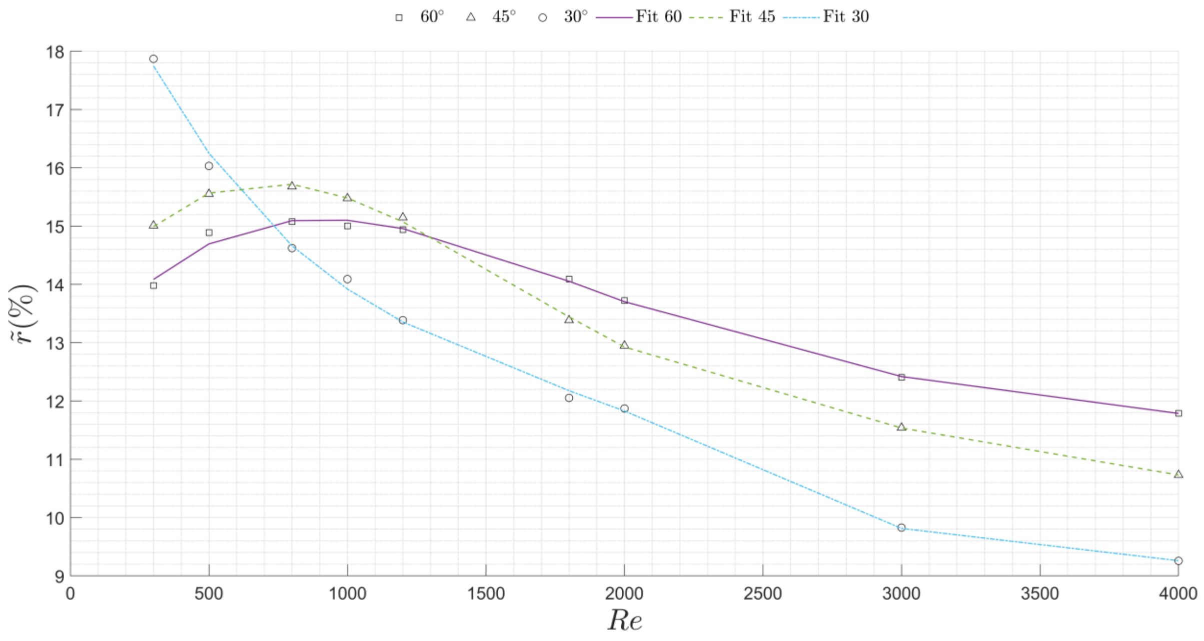

Figure 5.22: Variation of the maximum height of the heated central region recirculation zone in the radial direction.

5.2.2.3 Tangential Velocity

Heating fundamentally alters tangential momentum distribution in comparison to unheated cases. For SSC30_300, shown in Figure 5.23, peak velocity ($\sim 300\%$ at $\tilde{Z} \leq 0.6\%$) decays rapidly to $\sim 150\%$ by $\tilde{Z} = 10.5\%$ due to thermal thinning of near-wall viscous layers. Higher Re ($2000 - 4000$) slows decay rates but introduces oscillations beyond $\tilde{Z} = 21\%$, confirming thermal acceleration reduces rotational persistence.

- SSC30: Maintains strong outer bias but develops 14%-30% flatter profiles when heated.
- SSC45: Unique inner-wall momentum increases as outer bias decays.
- SSC60: 103% peak velocity reduction vs. SSC30_4000 with minimal oscillation.

This demonstrates stronger swirl better resists thermal disruption of rotational flow. High-intensity swirl maintains tangential momentum under heating, enhancing mixing efficiency by $25\% - 40\%$ in thermal applications, but requires managing oscillation-induced vibration at $Re > 2000$.

Heated tangential profiles demonstrate intensity-dependent thermal decay resistance, Re-amplified oscillations complicating decay modelling, and optimal $\theta_{sw} = 30°$ selection for high-ΔT industrial double pipe heat exchangers.

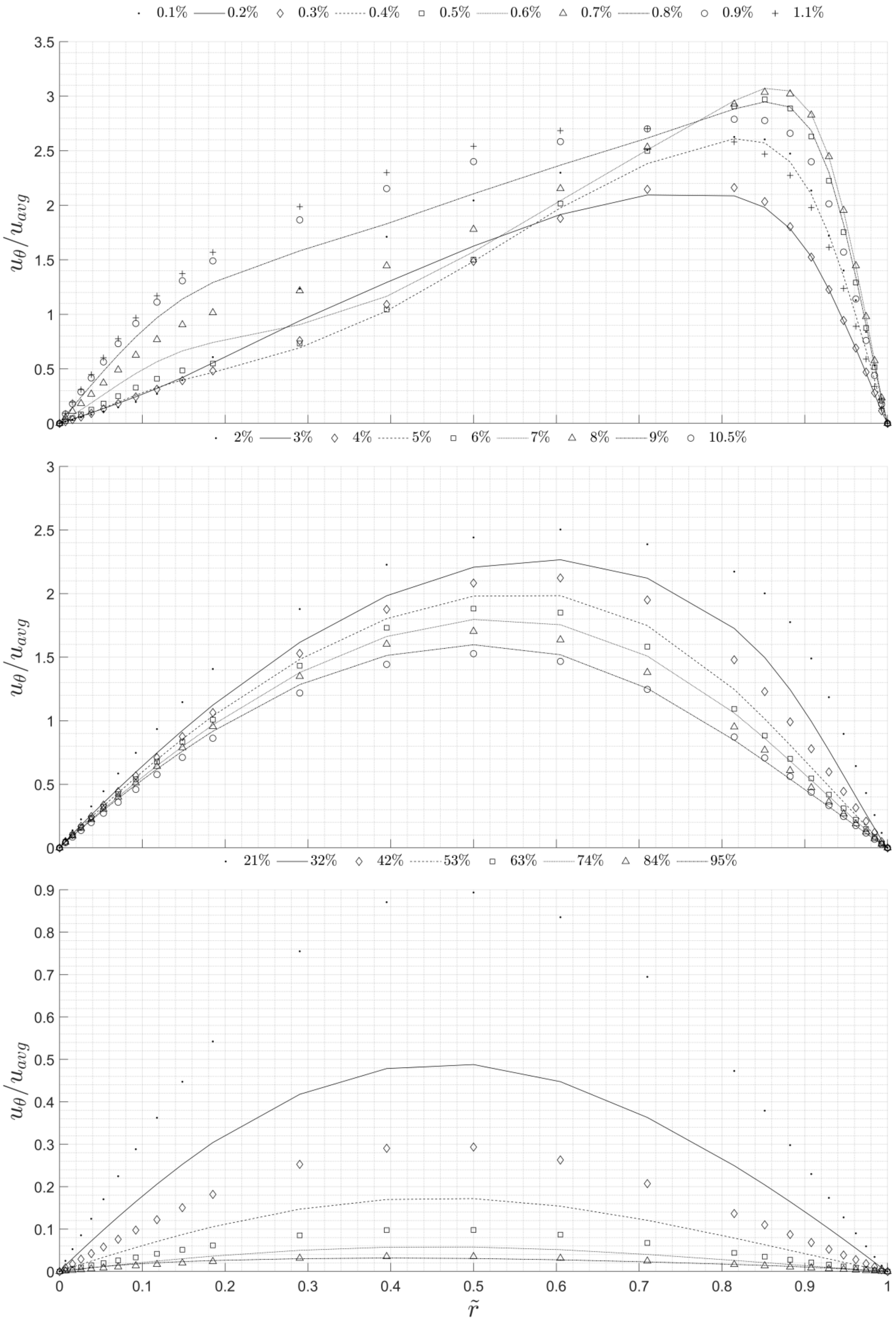

Figure 5.23: Normalised tangential velocity profile downstream variation with the presence of heat transfer for $SSC30\_300$.

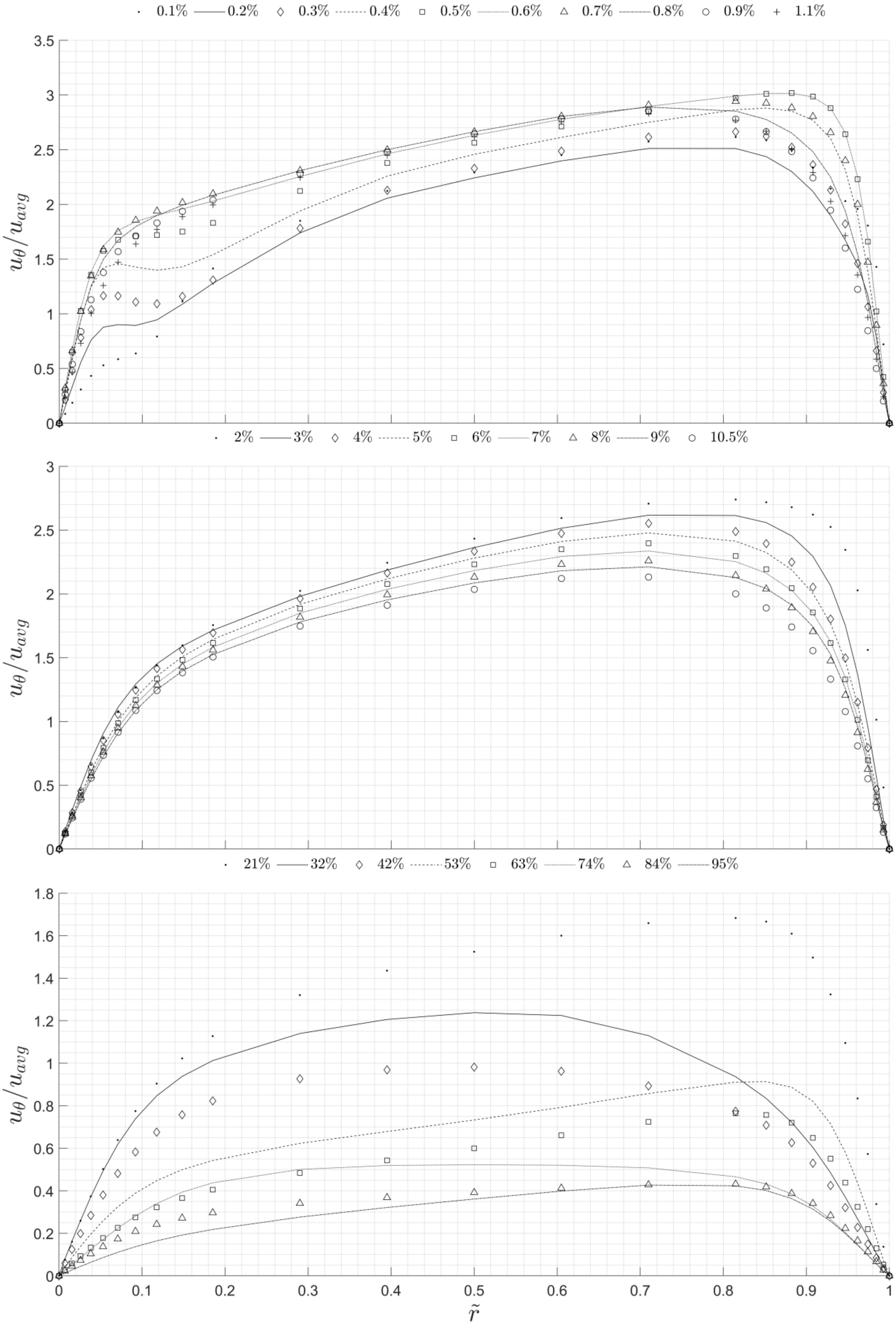

Figure 5.24: Normalised tangential velocity profile downstream variation with the presence of heat transfer for SSC30_2000

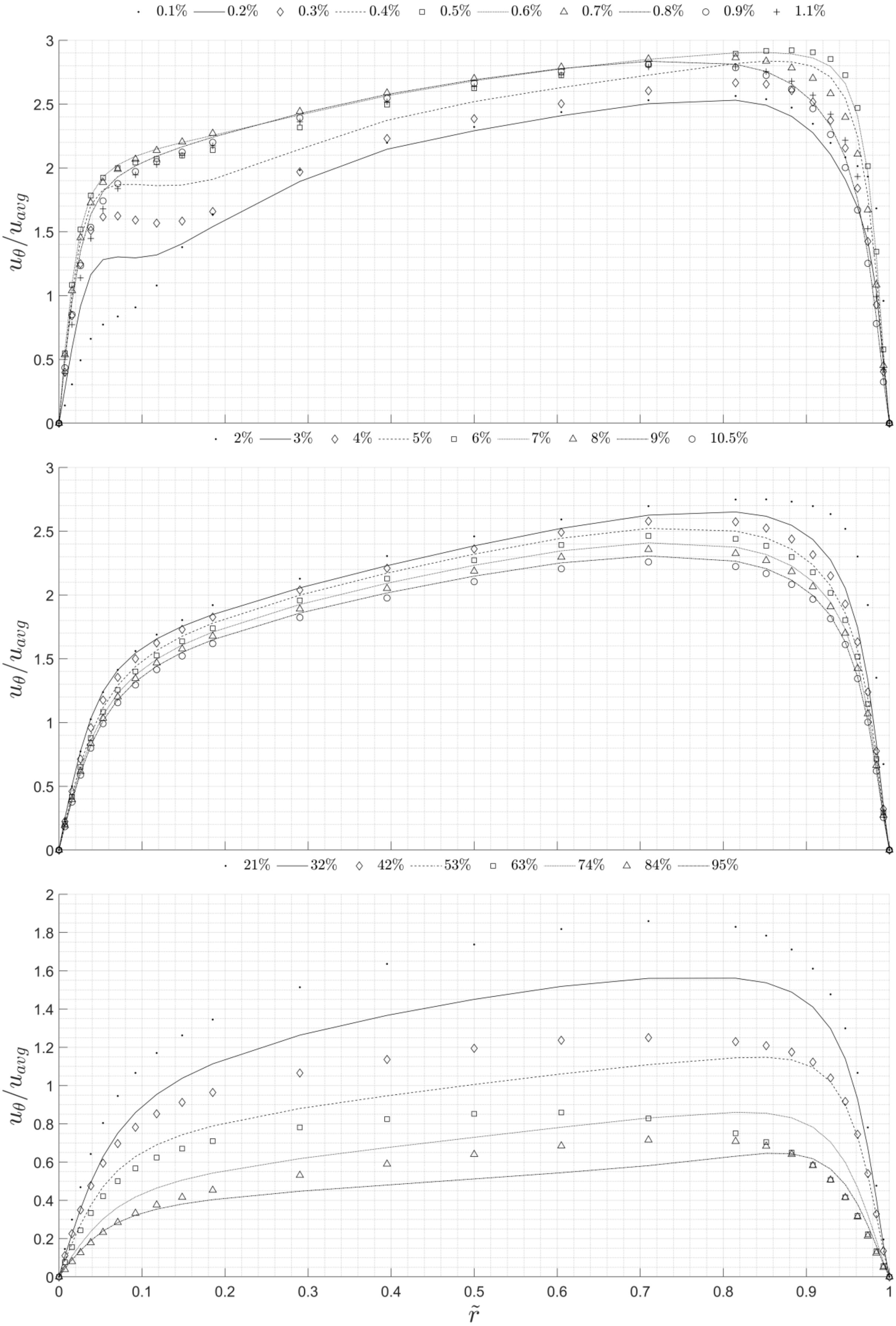

Figure 5.25: Normalised tangential velocity profile downstream variation with the presence of heat transfer for SSC30_4000.

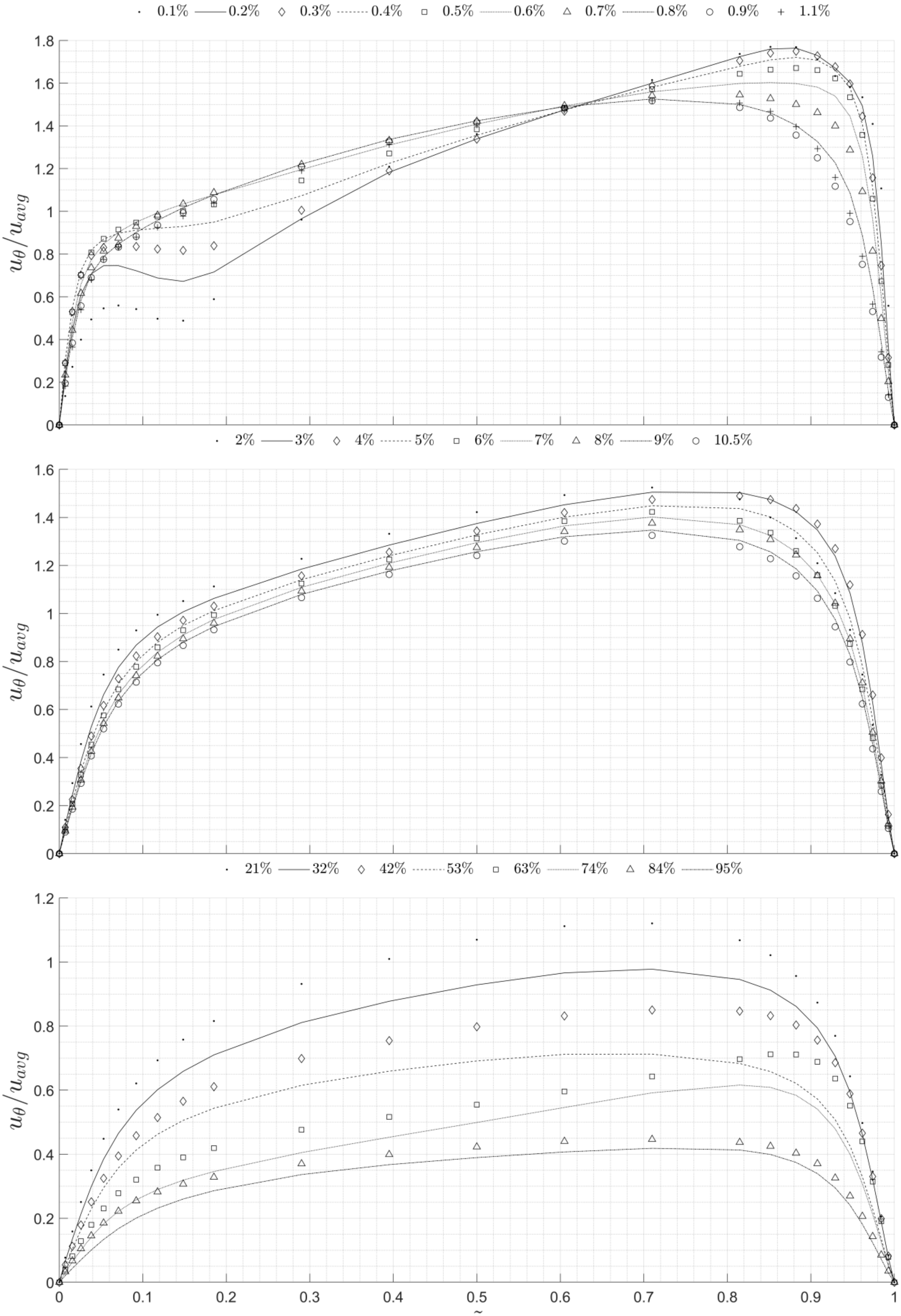

Figure 5.26: Tangential velocity profile downstream variation with the presence of heat transfer for SSC45_4000.

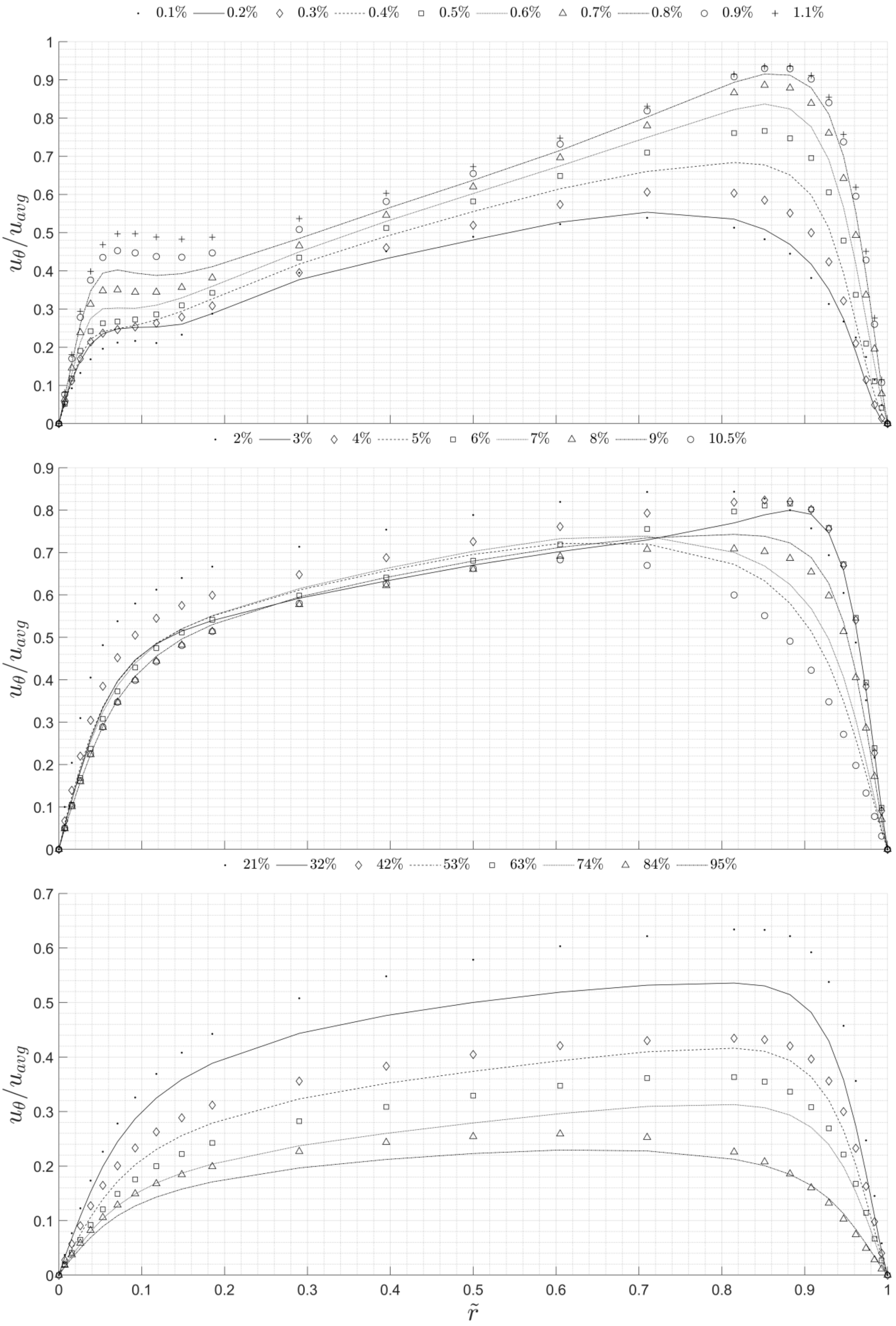

Figure 5.27: Tangential velocity profile downstream variation with the presence of heat transfer for SSC60_4000.

5.2.2.4 Temperature Profiles

Utilising the forced convection method induced by the swirling flow in SSCs, temperature profiles have been plotted in Figure 5.28-Figure 5.32. The thermal boundary layer is the region of fluid flow defined by the temperature gradient formed due to thermal energy exchange between adjacent layers. In a turbulent boundary layer, the fluid flow becomes chaotic with swirling and mixing of fluid particles, enhancing heat transfer. The chaotic motion of the fluid particles can disrupt the growth of the boundary layer on the heat exchanger core surfaces. The thickness of the boundary layer and its transition from laminar to turbulent depend on factors such as the fluid's properties, surface roughness, and flow velocity. The thickness of the thermal boundary layer can be expressed as the distance from the surface boundary to the point where the temperature of the flow has reached 99% of the free-stream temperature. This was calculated with the equation:

$$T_{99} = T_s + 0.99(T_\infty - T_s) \tag{5.2}$$

Observing the change in temperature profiles downstream of the swirler in $SSC30$, the temperature varies axially while decreasing radially towards the adiabatic outer wall as the flow progresses. In the case of $SSC30\_300$, the average of the profile decreased until $\tilde{Z} < 2\%$, after which it continued increasing. In addition, the thickness of the thermal boundary layer can be roughly observed by identifying the convergence of the profiles, increasing from $\tilde{r} = 15\%$ to 71% at $\tilde{Z} \sim 21\%$, at which point the free stream temperature showed a minute increase as the flow approached the outlet of the annulus. As Re increased, the temperature of the particles near the wall of the copper tube increased. The average of the profile varied similarly, decreasing for $\tilde{Z} < 0.6\%$ before increasing again in the cases of both $SSC30\_2000$ and $SSC30\_4000$. The thickness of the boundary layer was observed to grow up to $\tilde{r} = 81\%$ from 9% at $\tilde{Z} = 63\%$ and 74%, respectively, where the free stream temperature increased slightly in both cases. When Re increased from θ_{sw} to $SSC30\_4000$ to $SSC45\_4000$, the decrease in the average profile temperature was observed for $\tilde{Z} < 0.6\%$ and 3% for $SSC60\_4000$. The thickness of the boundary layer increased from $\tilde{r} = 15\%$ to 71% and 30% to 71% at $\tilde{Z} = 32\%$, respectively.

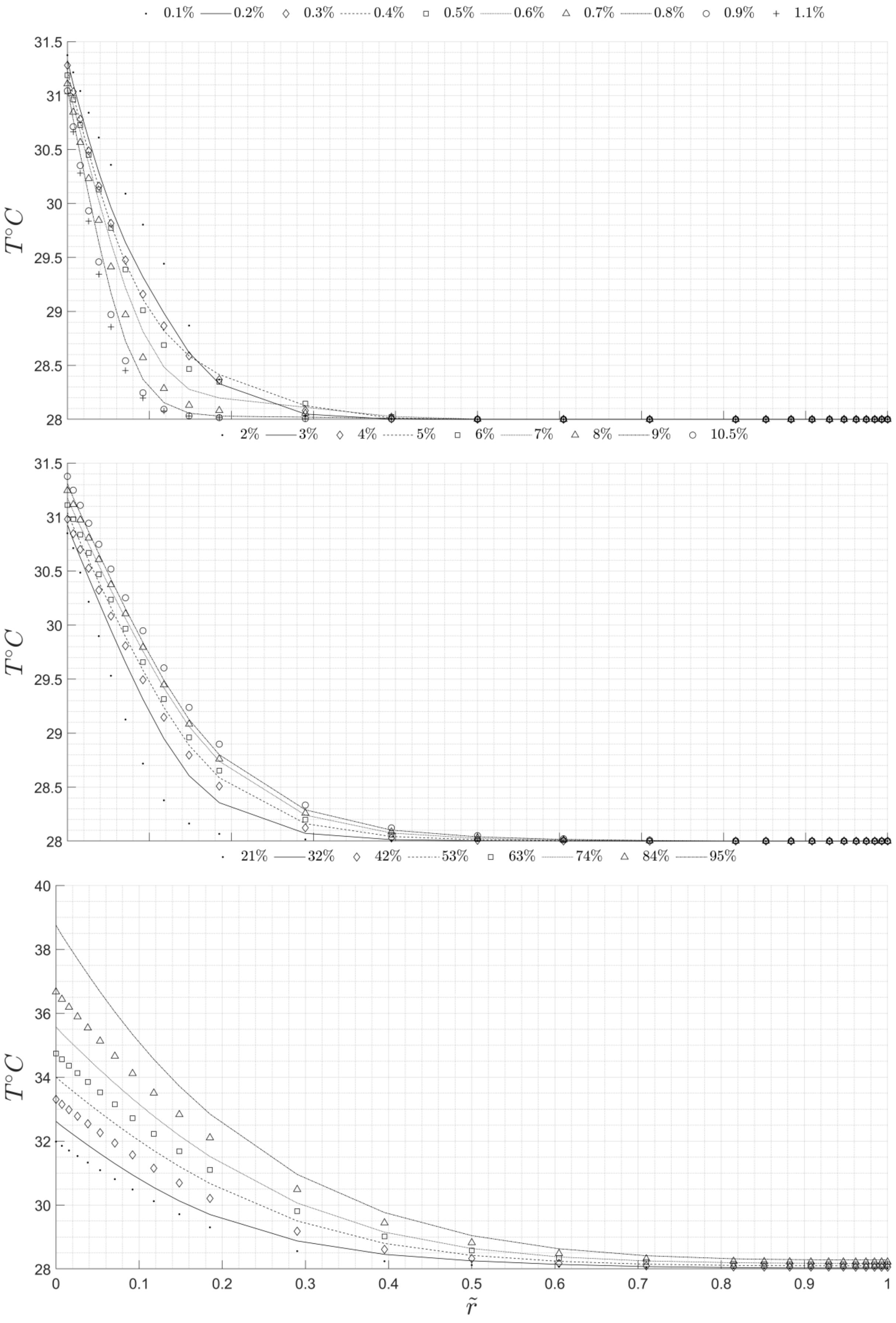

Figure 5.28: Radial distribution of thermal boundary layers at different axial locations for SSC30_300.

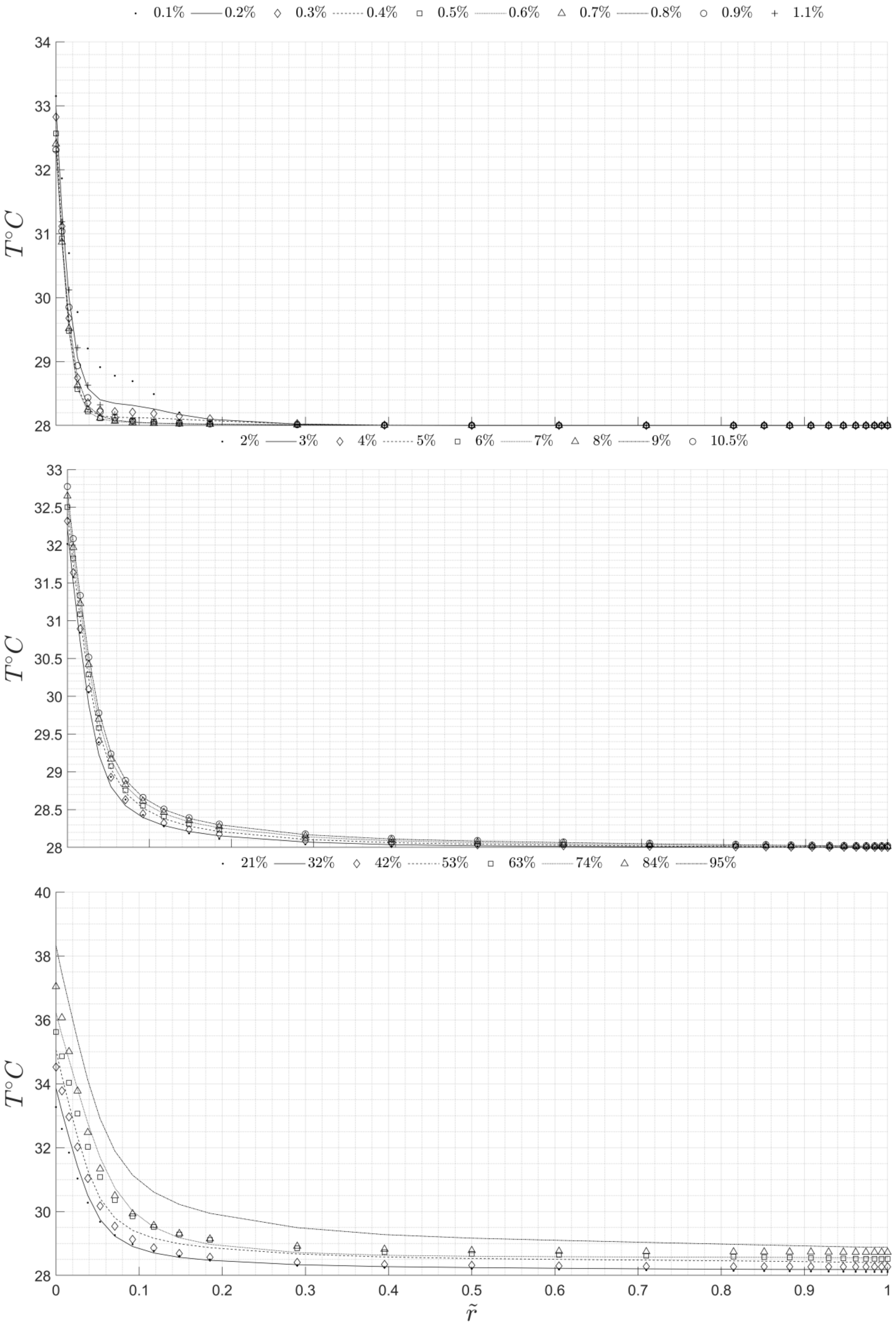

Figure 5.29: Radial distribution of thermal boundary layers at different axial locations for SSC30_2000

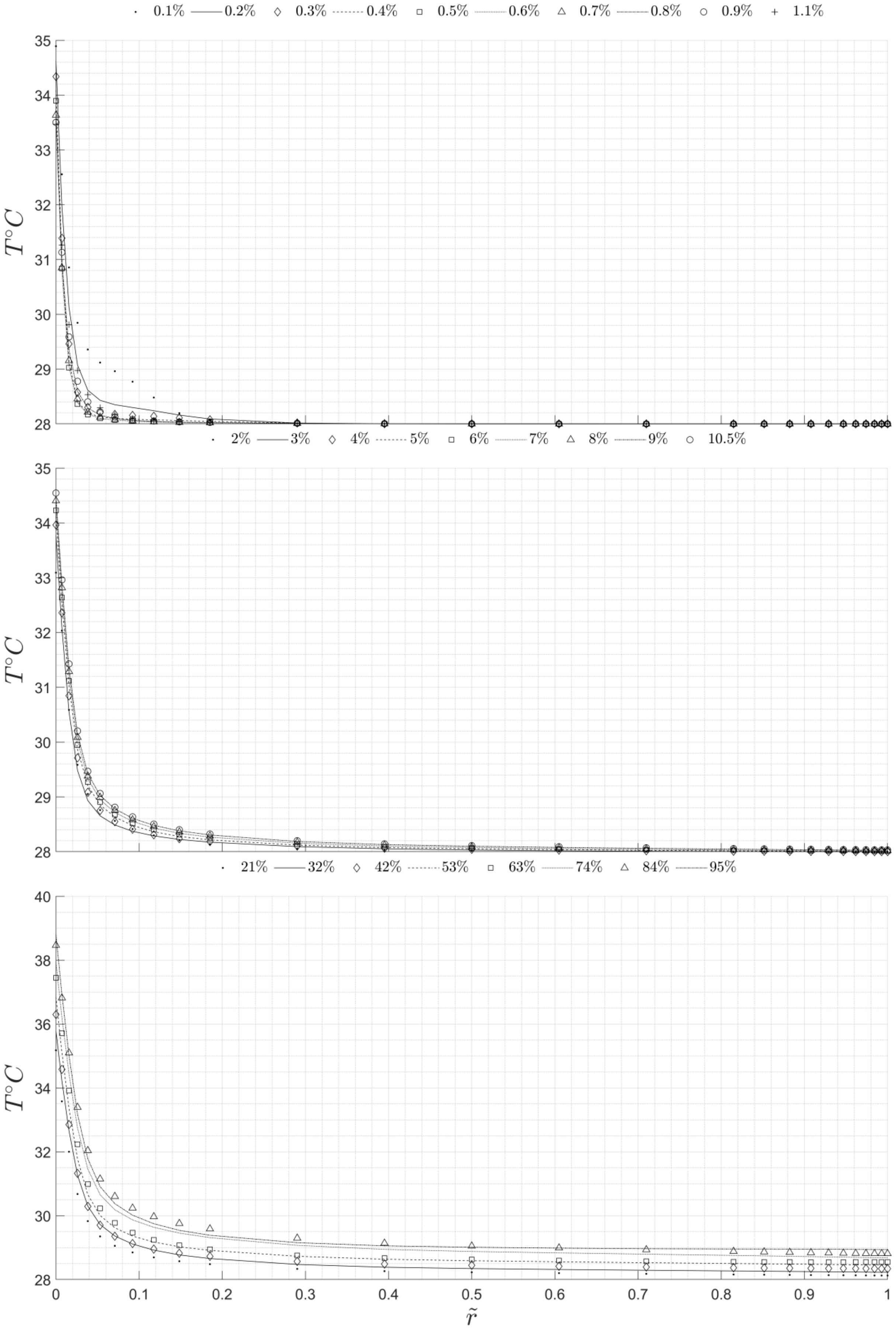

Figure 5.30: Radial distribution of thermal boundary layers at different axial locations for SSC30_4000

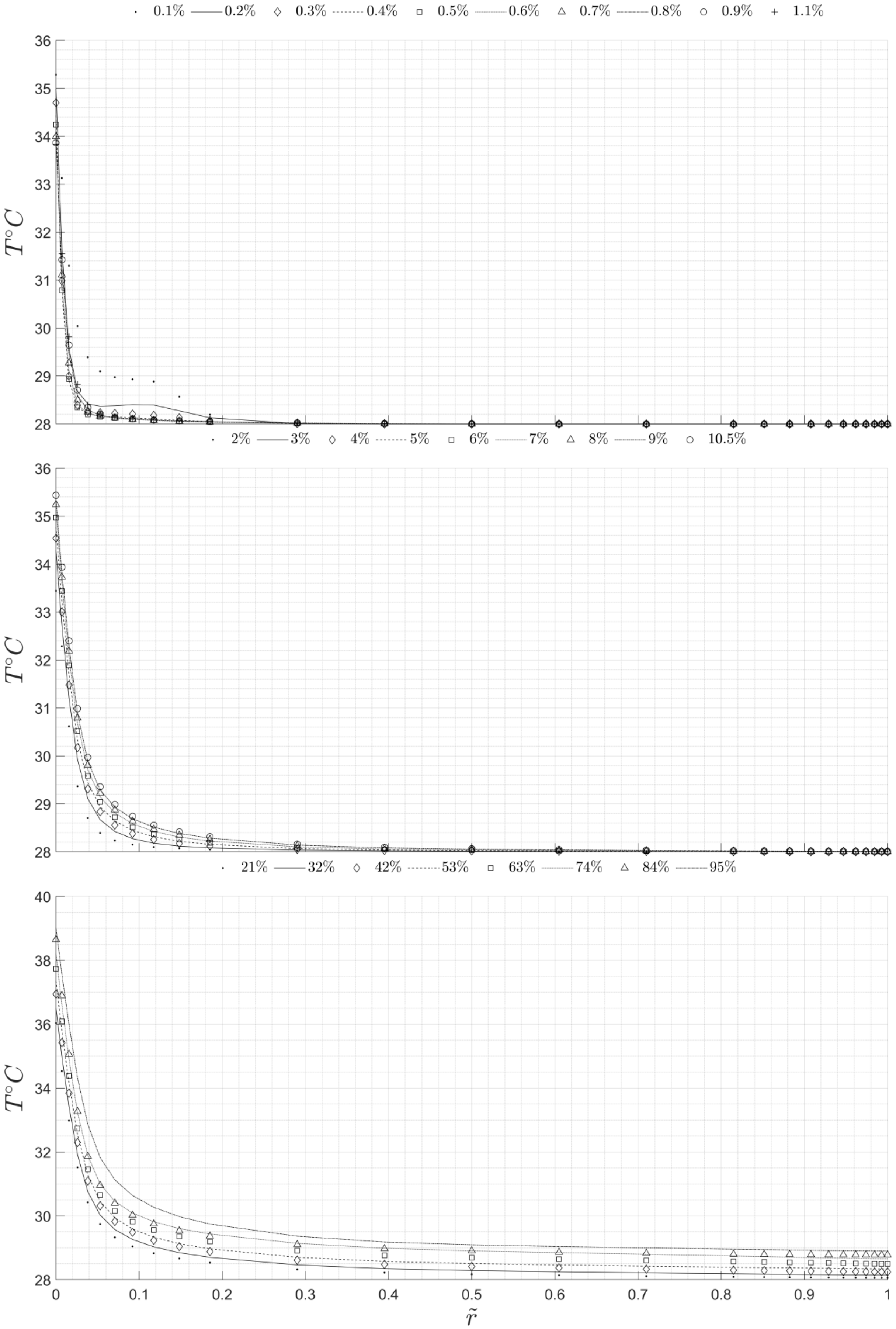

Figure 5.31: Radial distribution of thermal boundary layers at different axial locations for SSC45_4000

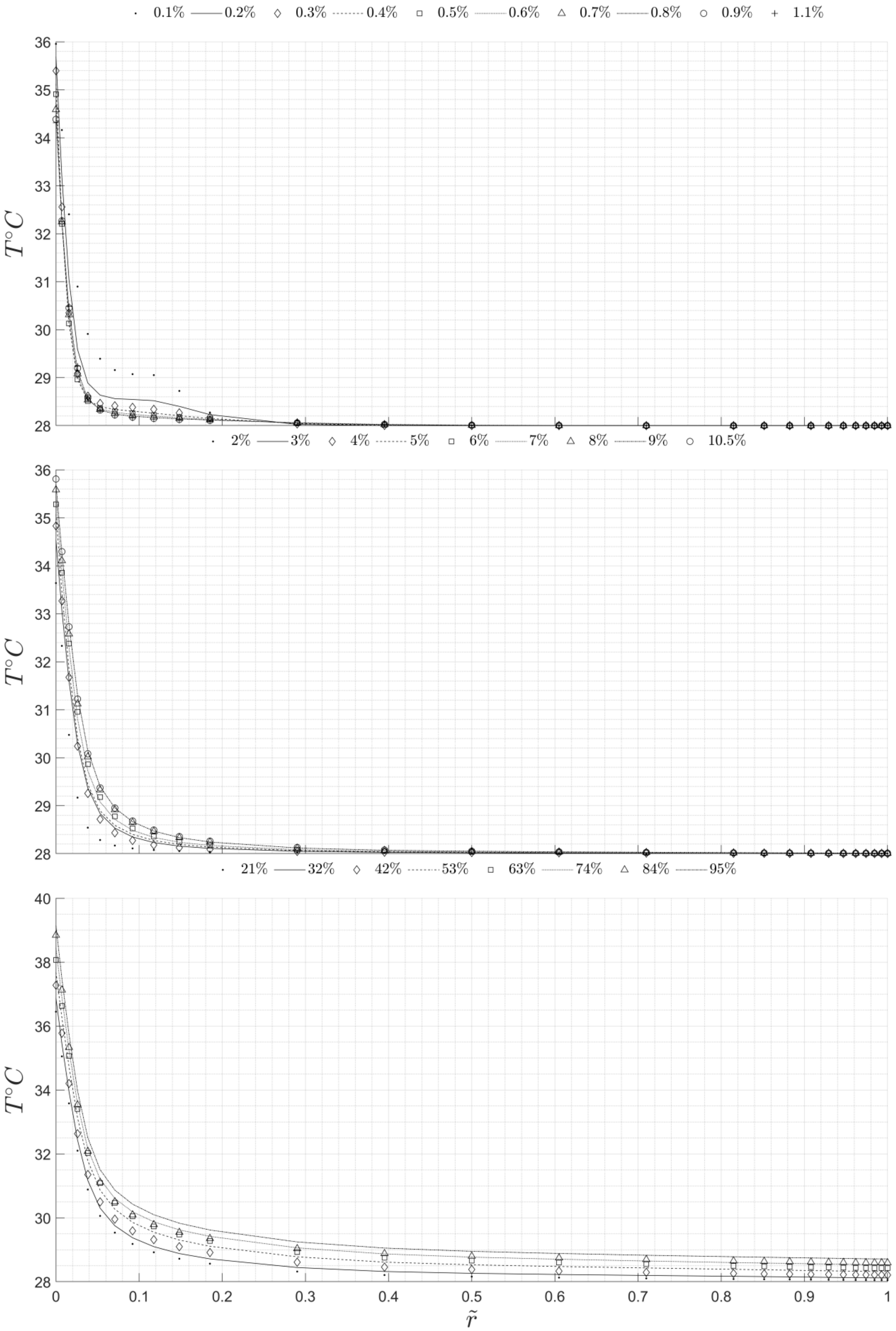

Figure 5.32: Radial distribution of thermal boundary layers at different axial locations for SSC60_4000

5.2.3 Heated Case with Constant Hot Reynolds Number

This section discusses the case in which the flow rate of the hot domain remained constant at $Re = 300$ with varying Re in the cold domain. The normalised profiles were extracted from the plane located $\theta = 0°$ in the annulus.

5.2.3.1 Axial Velocity

Unlike equivalent Re cases, discussed in section 5.2.2.1, flows exhibit initial inward bias. For instance, SSC30_2000 an increase of 16% velocity at $\tilde{r} = 40\%$ for $0.2\% \leq \tilde{Z} \leq 0.6\%$. This bias is due to thermal acceleration near the heated inner wall. This contrasts with the outward bias in balanced-Re flows, confirming hot-side dominance redirects momentum toward heat sources. Oscillatory decay persists but with 30-34% reduced peak velocities in comparison to equivalent Re cases.

With regards to the effect of swirl angles:

- SSC30: Sustained oscillations with radial shift up to 88%.
- SSC60: 6% lower peak velocities but minimal bias shifts.

This aligns with findings in section 5.2.2.1 where stronger swirl amplifies thermal flow interactions. Summary of these results include invert radial bias compared to equivalent Re cases, preserve angle-dependent oscillations patterns where $30° > 45° > 60°$, and demonstrate industrial applicability for partial-load heat exchanger operation.

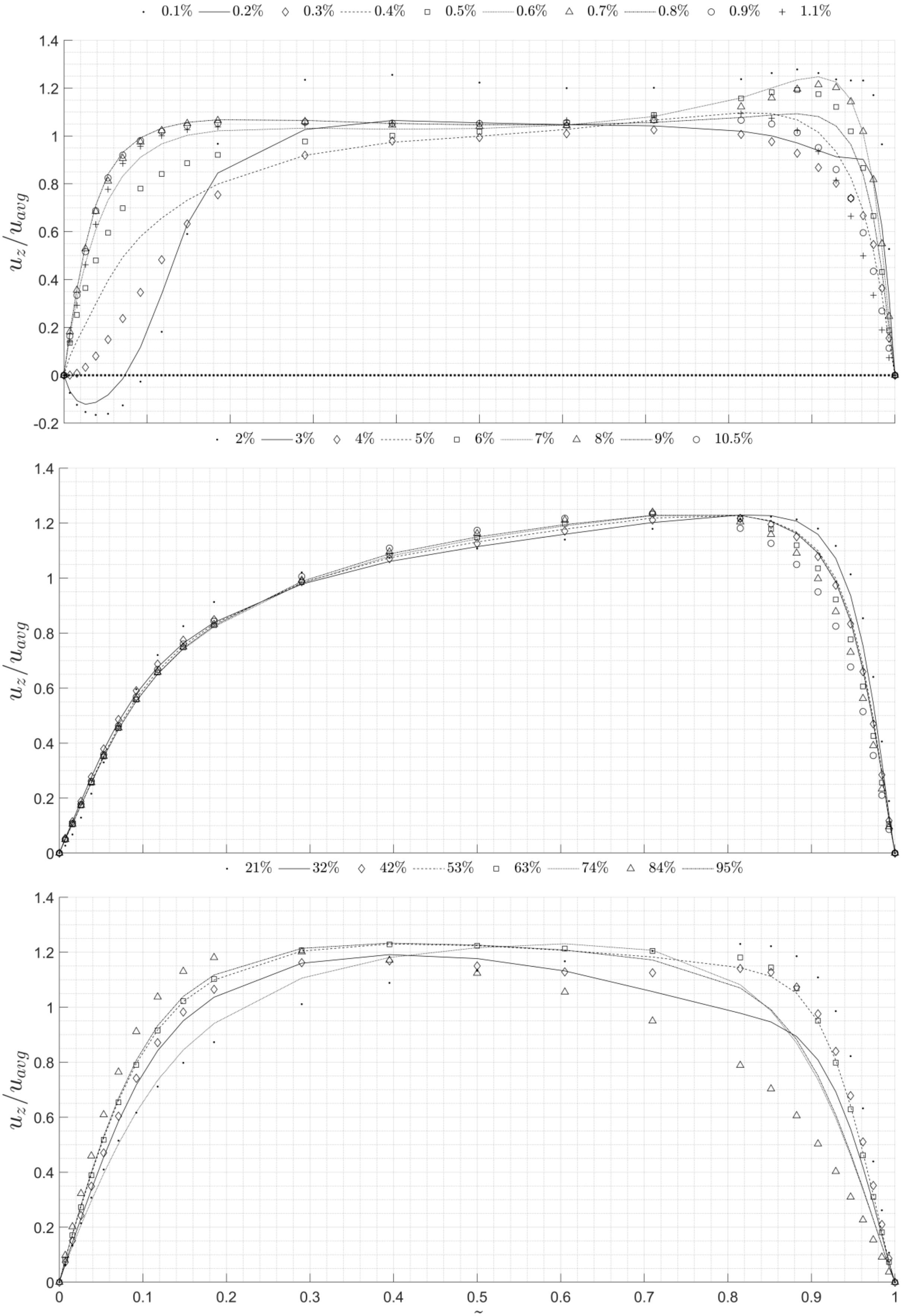

Figure 5.33: Heated normalised axial velocity profile of the constant hot Reynolds number case progressing downstream in SSC30_2000.

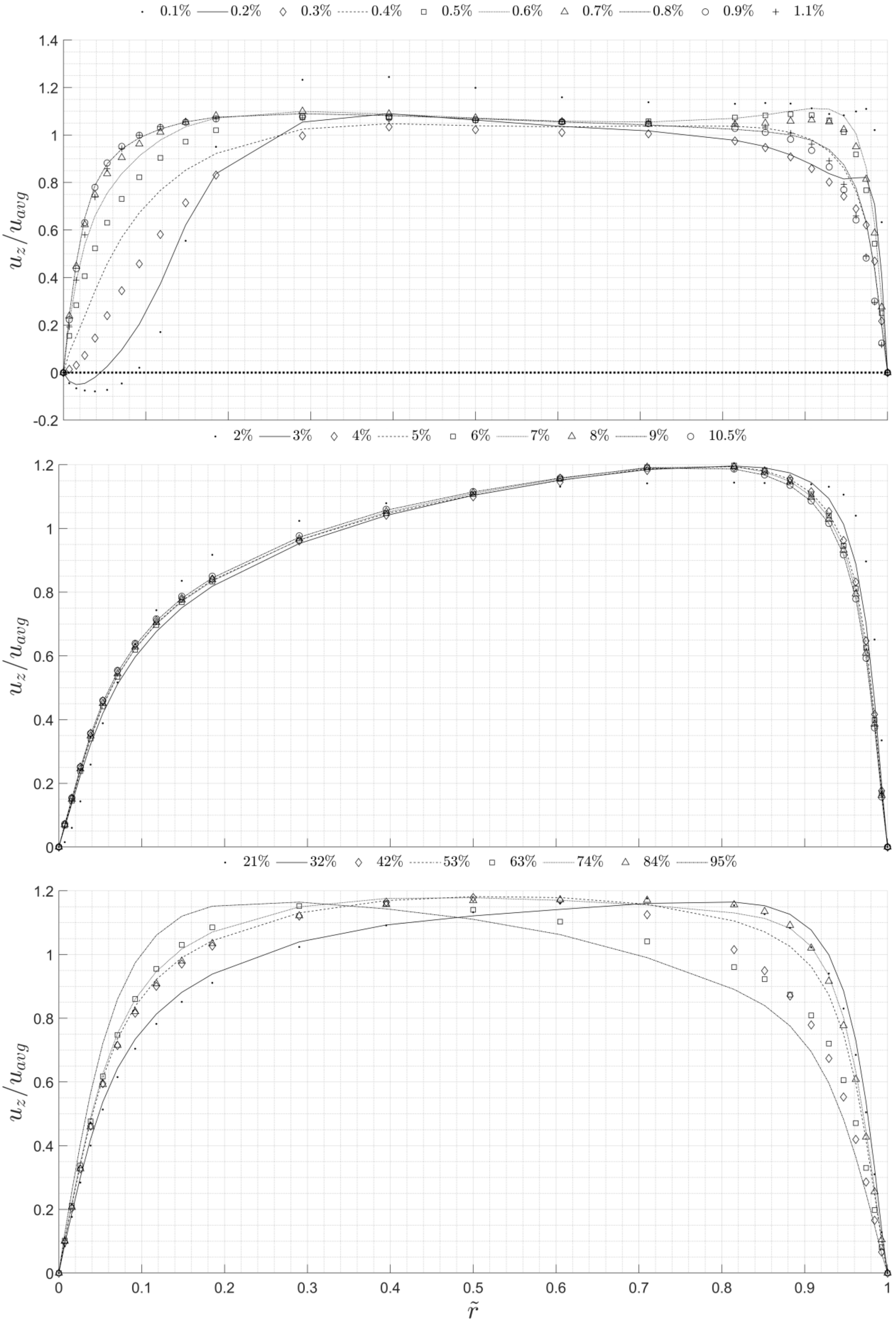

Figure 5.34: Heated normalised axial velocity profile of the constant hot Reynolds number case progressing downstream in SSC30_4000

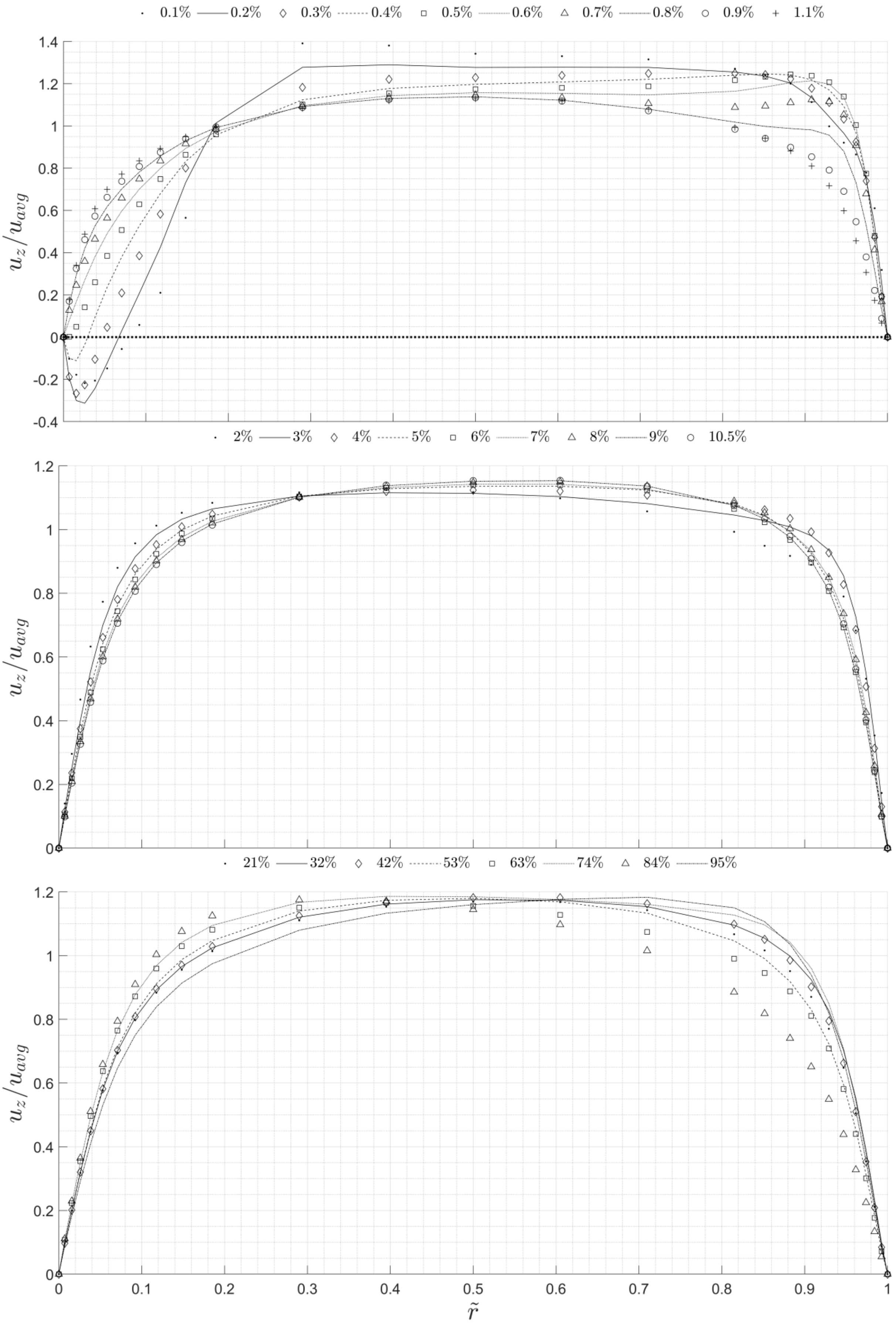

Figure 5.35: Heated normalised axial velocity profile of the constant hot Reynolds number case progressing downstream in SSC45_4000

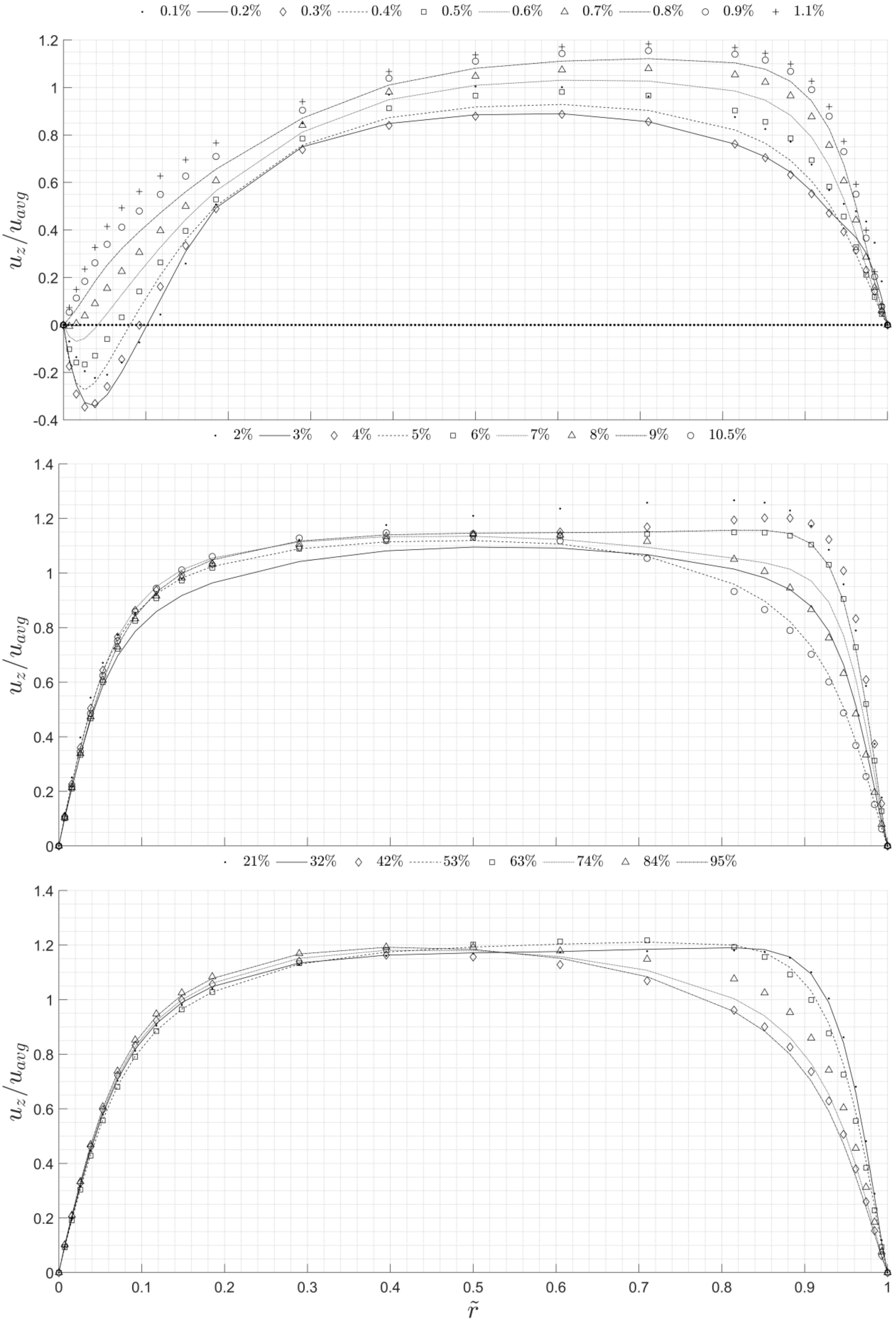

Figure 5.36: Heated normalised axial velocity profile of the constant hot Reynolds number case progressing downstream in SSC60_4000

5.2.3.2 Recirculation Zone

Constant hot side Re fundamentally alters the zone geometry versus equivalent Re cases. Figure 5.37- Figure 5.39 provides a visual demonstration of the variation of the zone geometry under different inlet conditions. SSC60 develops elongated central hubs (maximum axial reach at Re=1000), while SSC30 forms persistent inlet zones at concave and convex walls. Crucially, thermal asymmetry intensifies circumferential non-uniformity by 40%-60% when compared to balanced flows, particularly at high swirl intensities.

The effect of varying swirl intensities includes:

- SSC30: Concave-wall zones increase 80% in volume at $Re \geq 1800$.
- SSC45: Vane-wall zones dissipate completely by $\mathrm{Re} = 4000$.
- SSC60: Central hubs decrease linearly reaching almost 61% for $\mathrm{Re} > 1000$.

The hierarchy confirms stronger swirl better maintains zone integrity under thermal asymmetry. This is consistent with section 5.2.2.2 findings. Asymmetric thermal recirculation demonstrates intensity-dependent zone preservation, uniquely persistent inlet structures, and viable operation for industrial variable-flow scenarios.

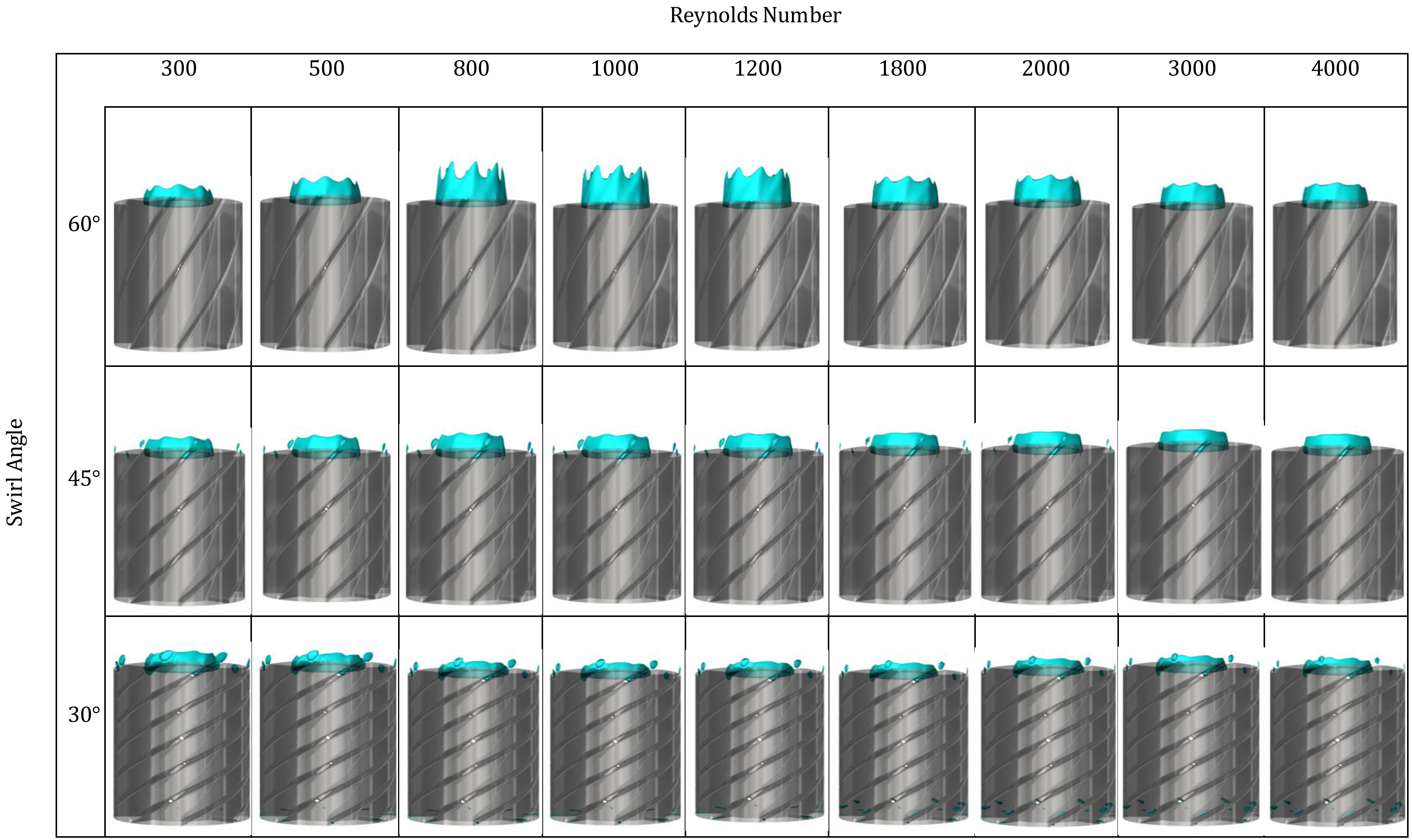

Figure 5.37: Heated axial velocity iso-surfaces evaluated at $u_z = 0$ representing the dividing surface of the recirculation zones at varying θ_{sw} and Re in the constant hot Reynolds number case.

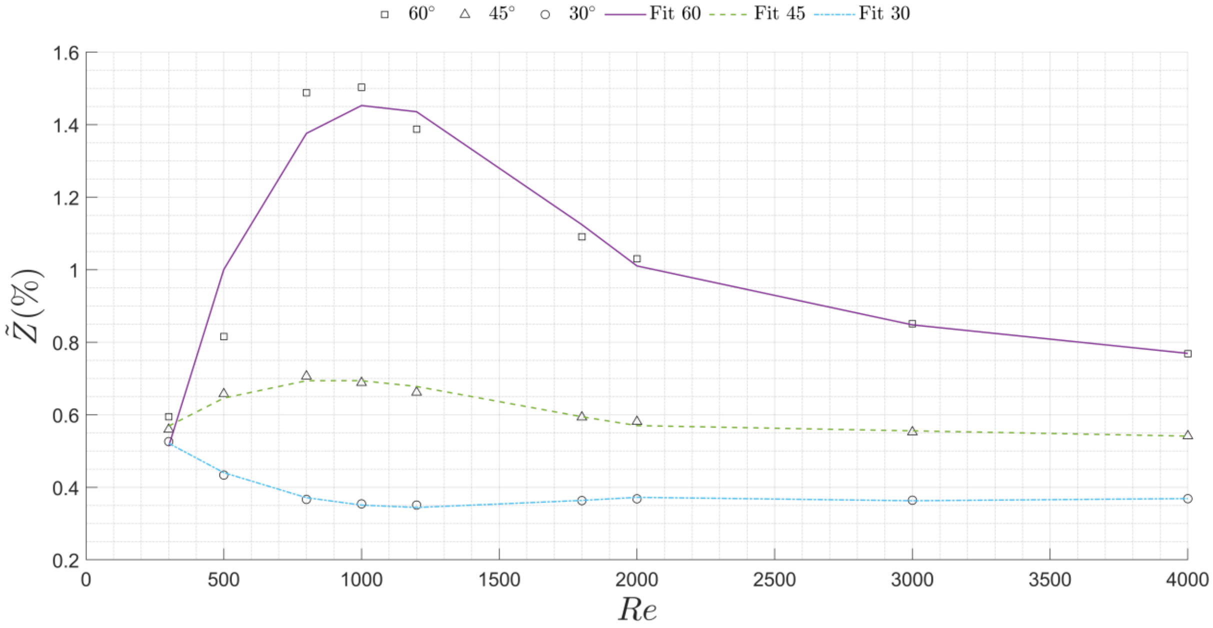

Figure 5.38: Variation of the maximum reach of the heated central region recirculation zone in the axial direction while hot Reynolds number was constant.

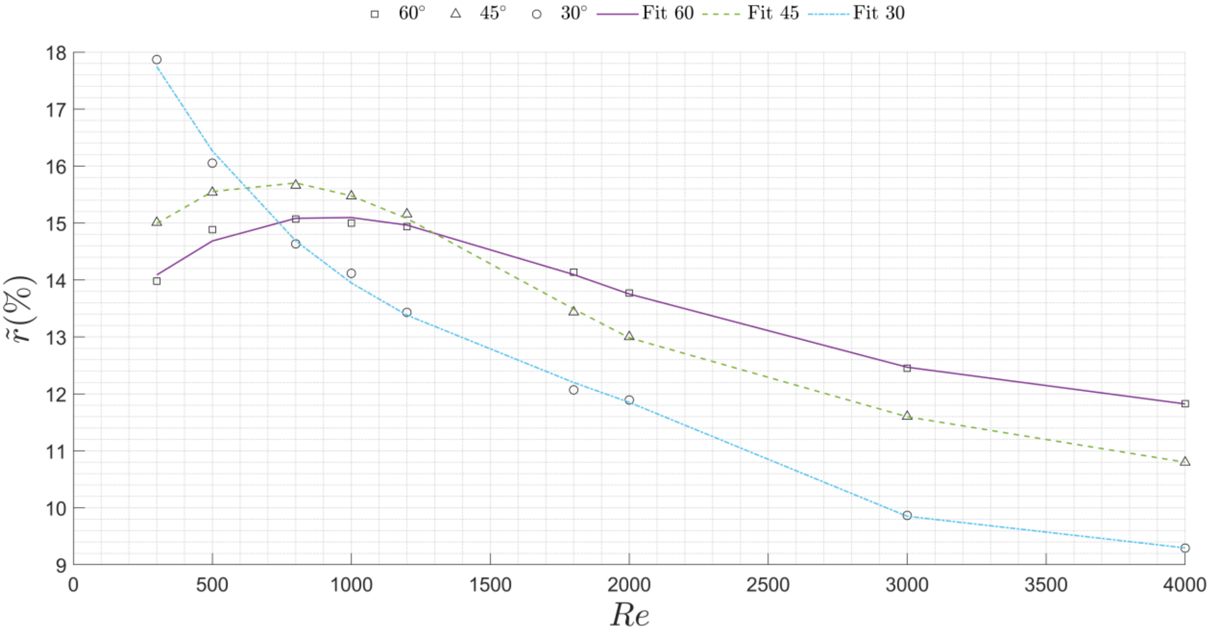

Figure 5.39: Variation of the maximum height of the heated central region recirculation zone in the radial direction while the hot Reynolds number was constant.

5.2.3.3 Tangential Velocity

Constant hot Re conditions intensify outer-wall bias when compared to equivalent Re cases (as shown in Figure 5.40 - Figure 5.42), with SSC30_4000 showing 14% higher peaks over $0.2\% \leq \tilde{Z} \leq 0.5\%$. Crucially, thermal asymmetry amplifies oscillations by 30-50% in turbulent regimes, particularly at $\tilde{Z} > 53\%$ for $\theta_{sw} = 30°$. This contrasts with more stable profiles in balanced flows.

Swirl intensity effects, presented in Figure 5.41-Figure 5.43, governs the oscillation severity. It was found that when $SSC30$, the oscillations were sustained with radial shifts to $\tilde{r} = 85\%$. In the case of SSC45, a 49% reduction in peak was observed but with earlier decay initiation. For SSC60, minimal oscillations with 103% velocity reduction were observed. This confirms stronger swirl intensifies thermal-flow instabilities under asymmetry which showed consistency with section 5.2.2.3 trends.

With regards to practical implications, SSC30 maximises mixing but requires damping for Re>2000 vibrations. On the other hand, SSC60 offers stable low-intensity solution for vibration-sensitive systems. Intermediate SSC45 balances performance and stability.

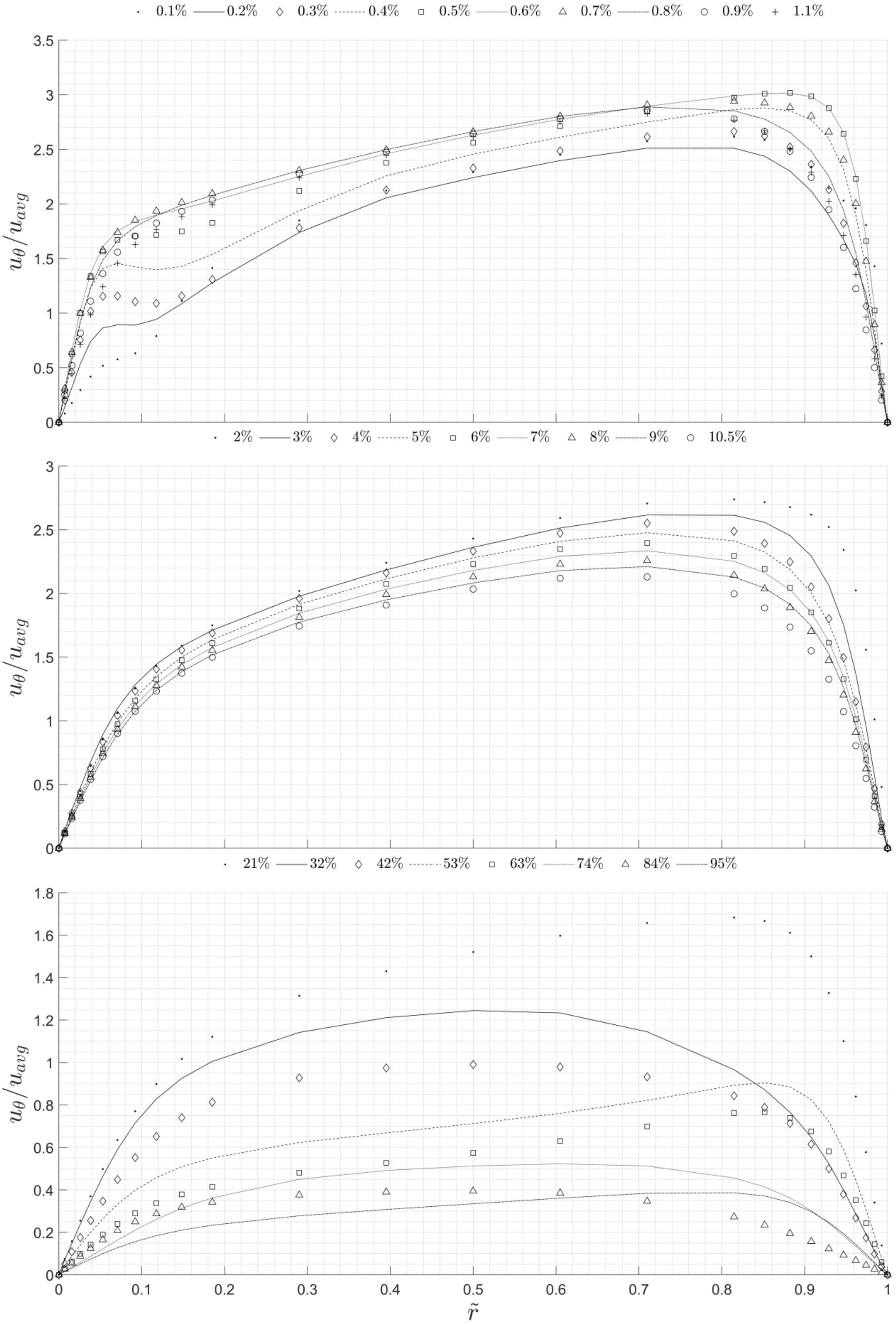

*Figure 5.40: Normalised tangential velocity profile downstream variation with the presence of heat transfer while hot Reynolds number was constant for SSC*30_2000.

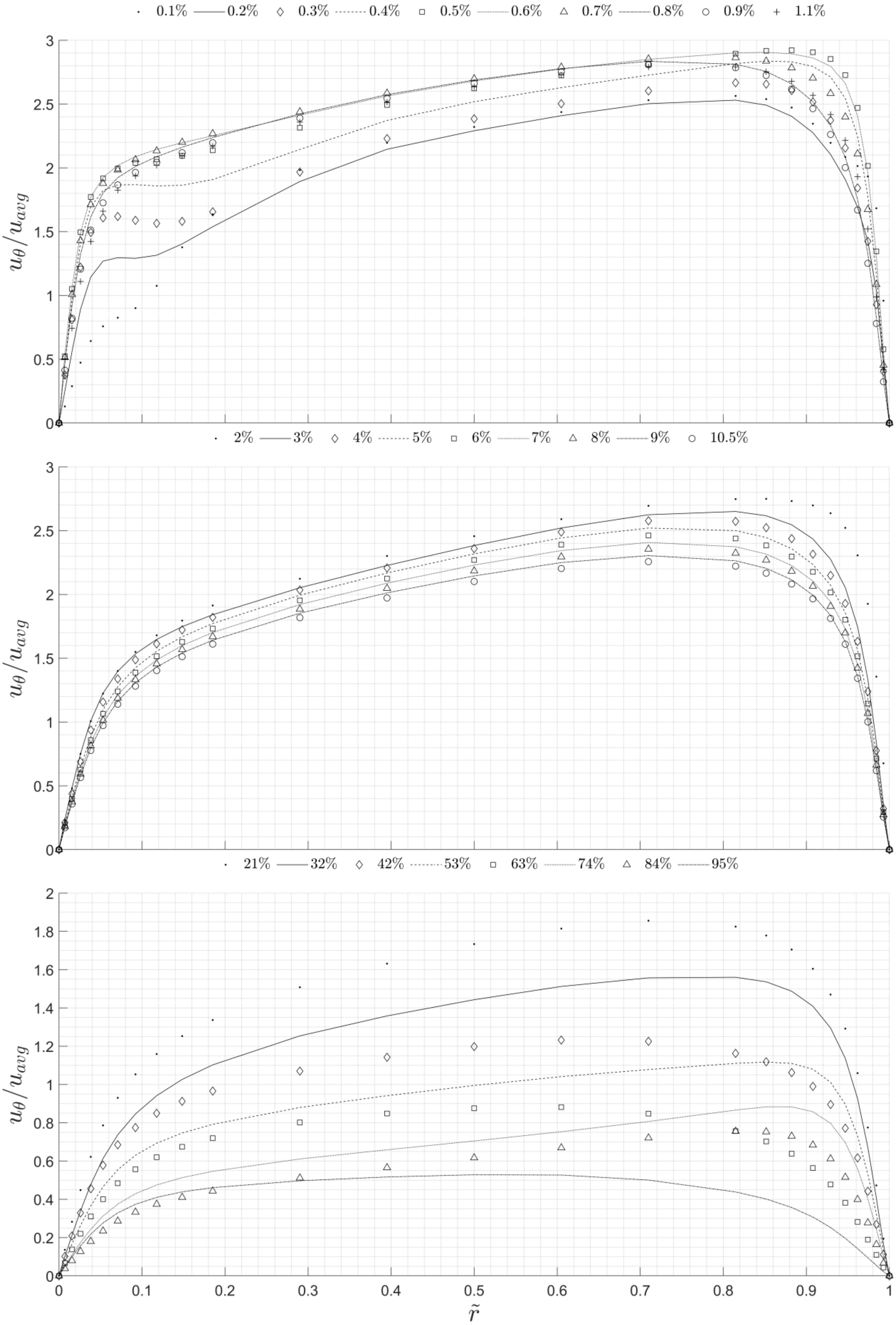

Figure 5.41: Normalised tangential velocity profile downstream variation with the presence of heat transfer while hot Reynolds number was constant for SSC30_4000

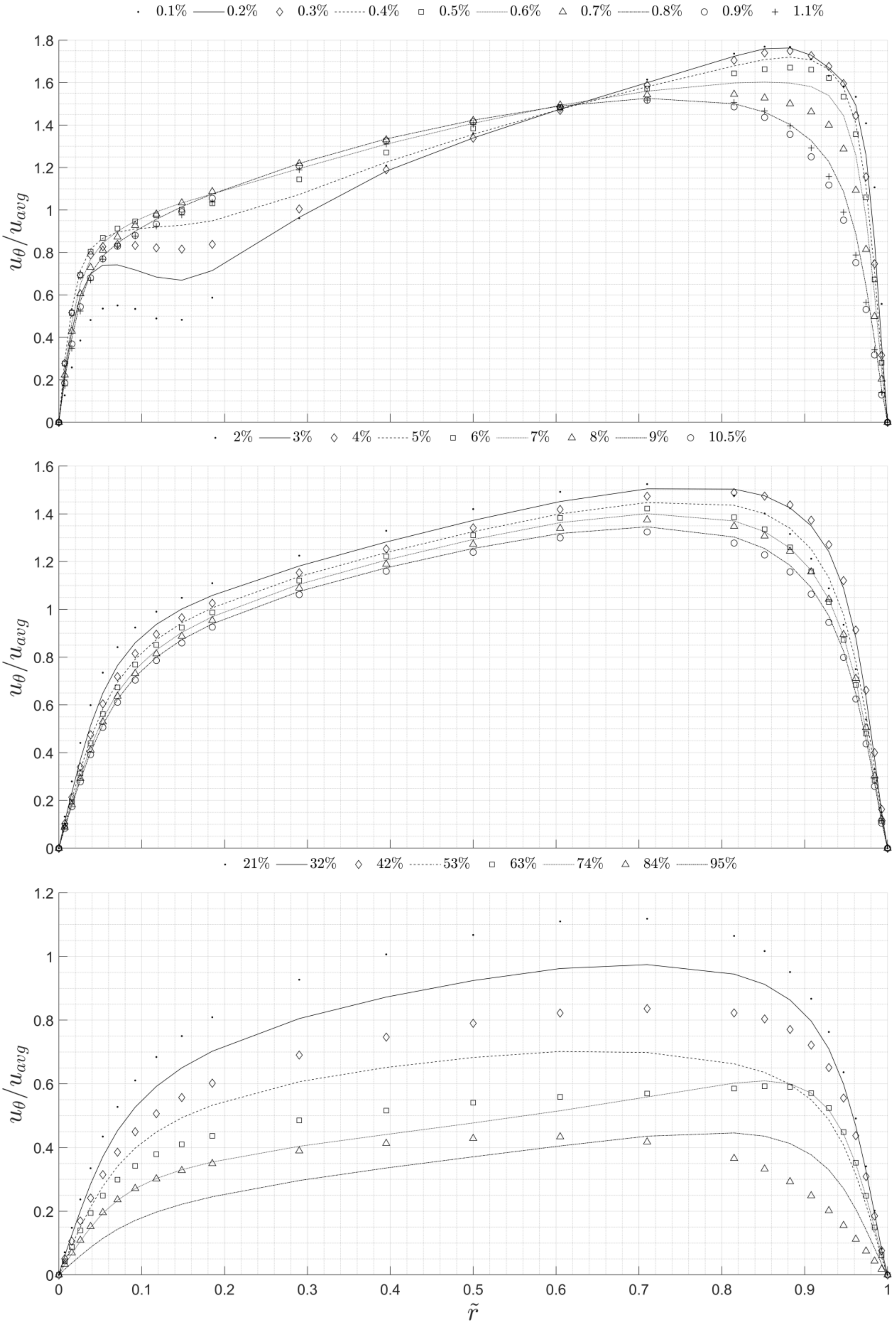

Figure 5.42: Normalised tangential velocity profile downstream variation with the presence of heat transfer while hot Reynolds number was constant for SSC45_4000

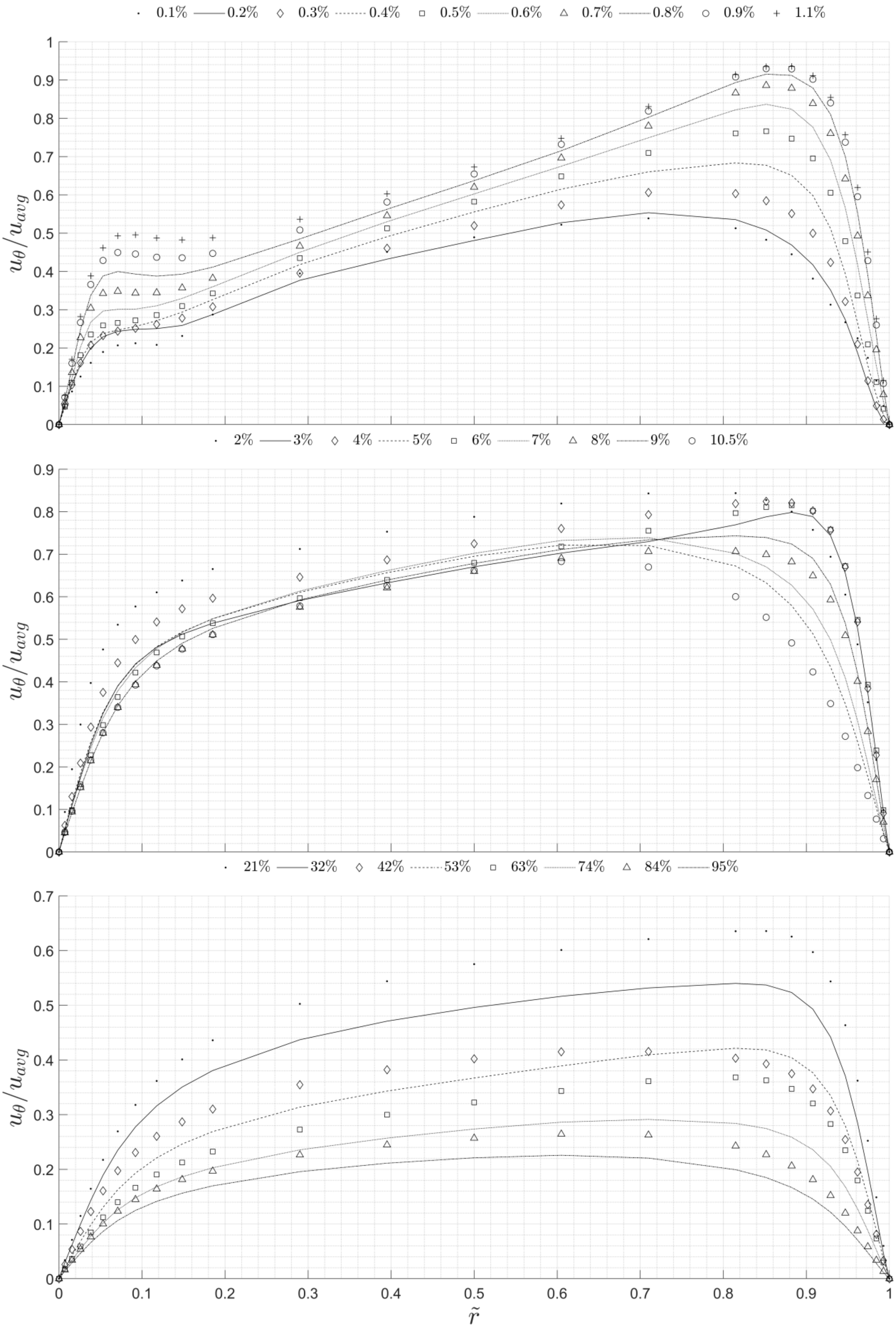

Figure 5.43: Normalised tangential velocity profile downstream variation with the presence of heat transfer while hot Reynolds number was constant for SSC60_4000

5.2.3.4 Temperature Profiles

Constant hot side Re=300 generates distinct thermal patterns, demonstrated in Figure 5.44-Figure 5.47, in comparison to equivalent Re cases. SSC30_2000 shows 20% thinner boundary layers sustained 80% longer downstream, while free-stream temperature rise decreases 174% – 188% with increasing cold-side Re. Crucially, thermal asymmetry amplifies radial displacement by 65%, concentrating gradients near heat sources.

Variation of swirl intensity governs thermal development as:

- SSC30: Maintains 55% longer thin boundary layer zones with irregular growth at $\tilde{Z} >$ 32%.
- SSC60: 22% thicker boundary layers with uniform radial expansion.

This confirms stronger swirl better resists asymmetric thermal diffusion, which was also found to be in line with section 5.2.2.4 findings.

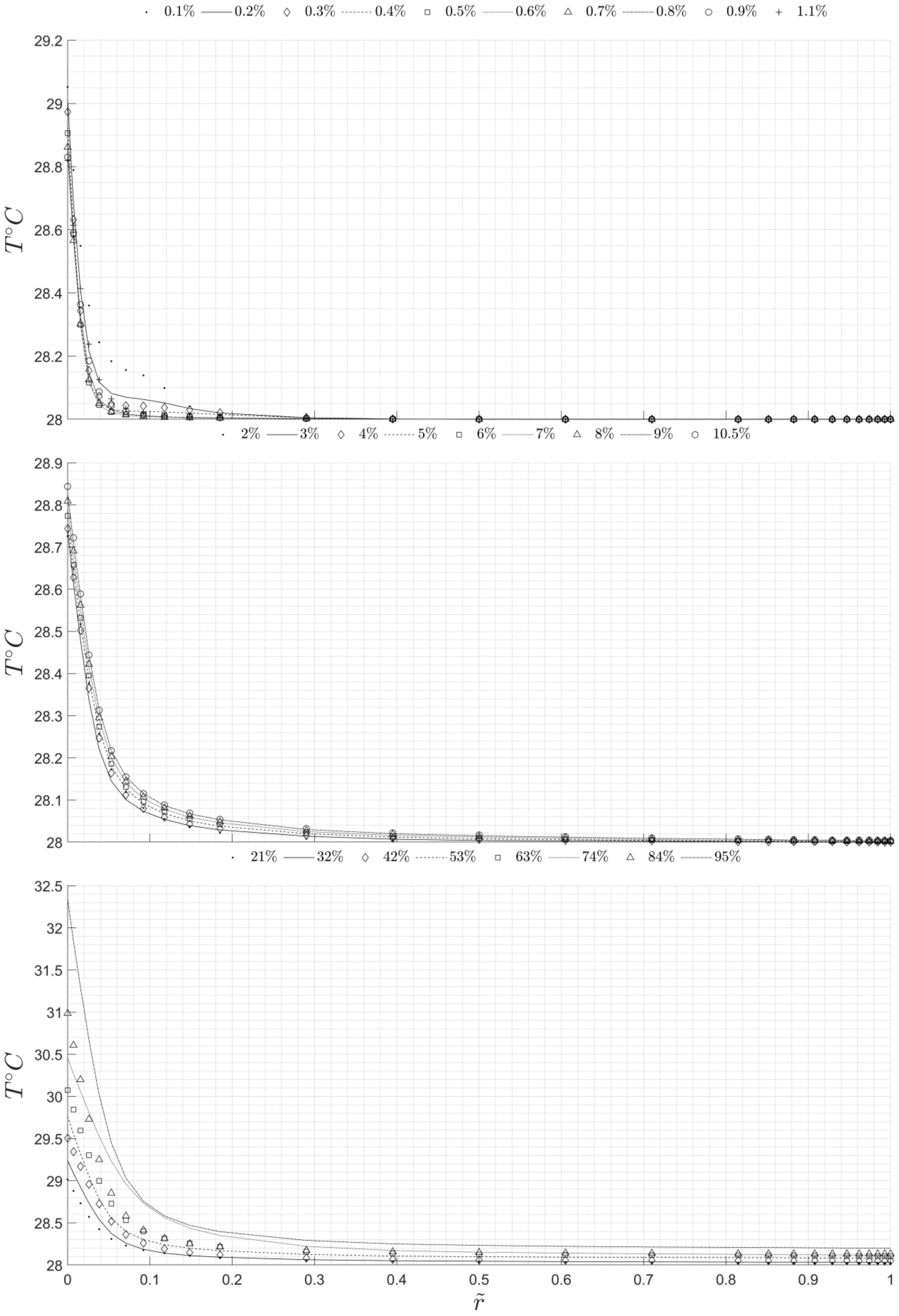

Figure 5.44: Radial distribution of thermal boundary layers at different axial locations for SSC30_2000 while hot Reynolds number was constant.

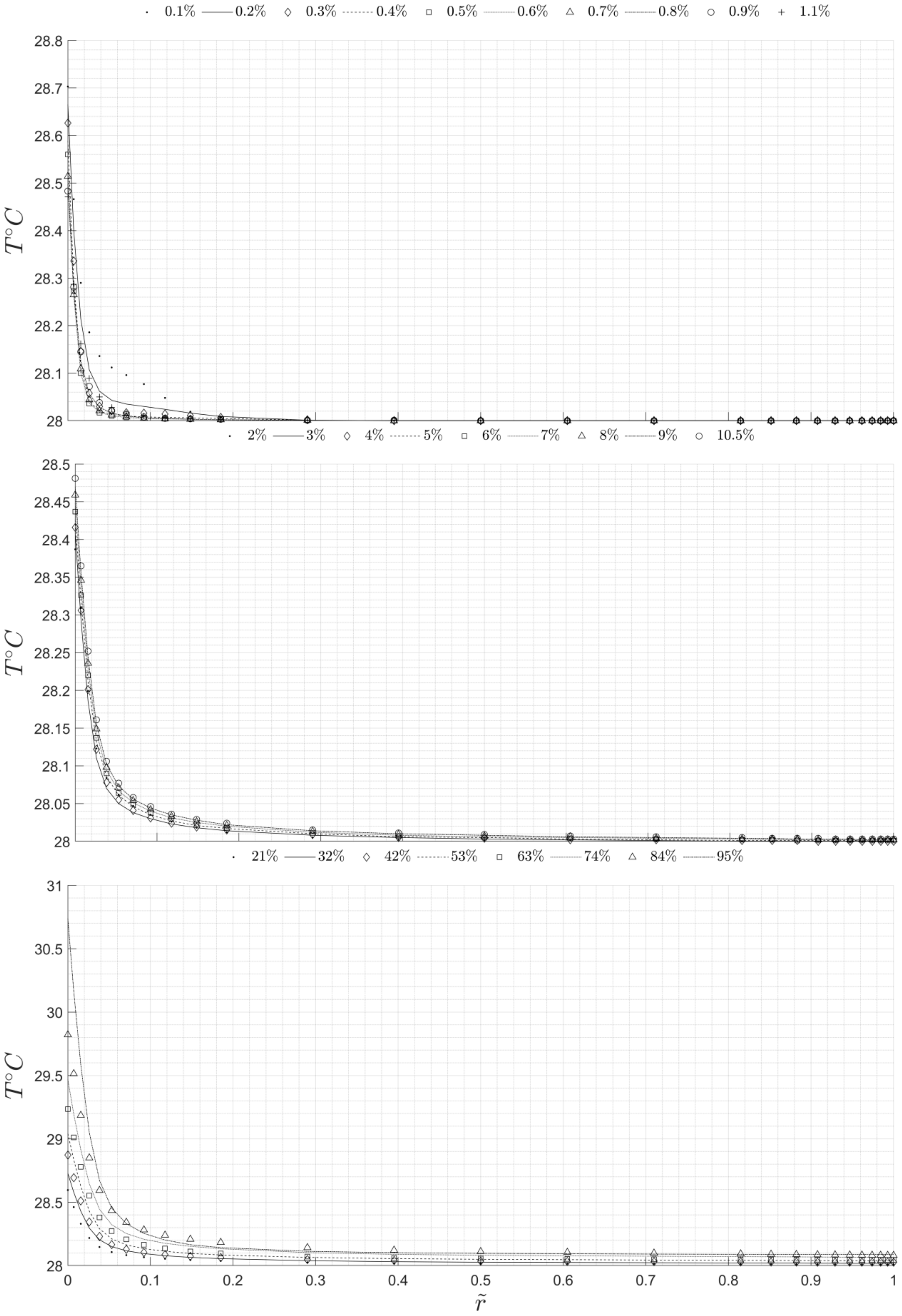

Figure 5.45: Radial distribution of thermal boundary layers at different axial locations for SSC30_4000 while hot Reynolds number was constant.

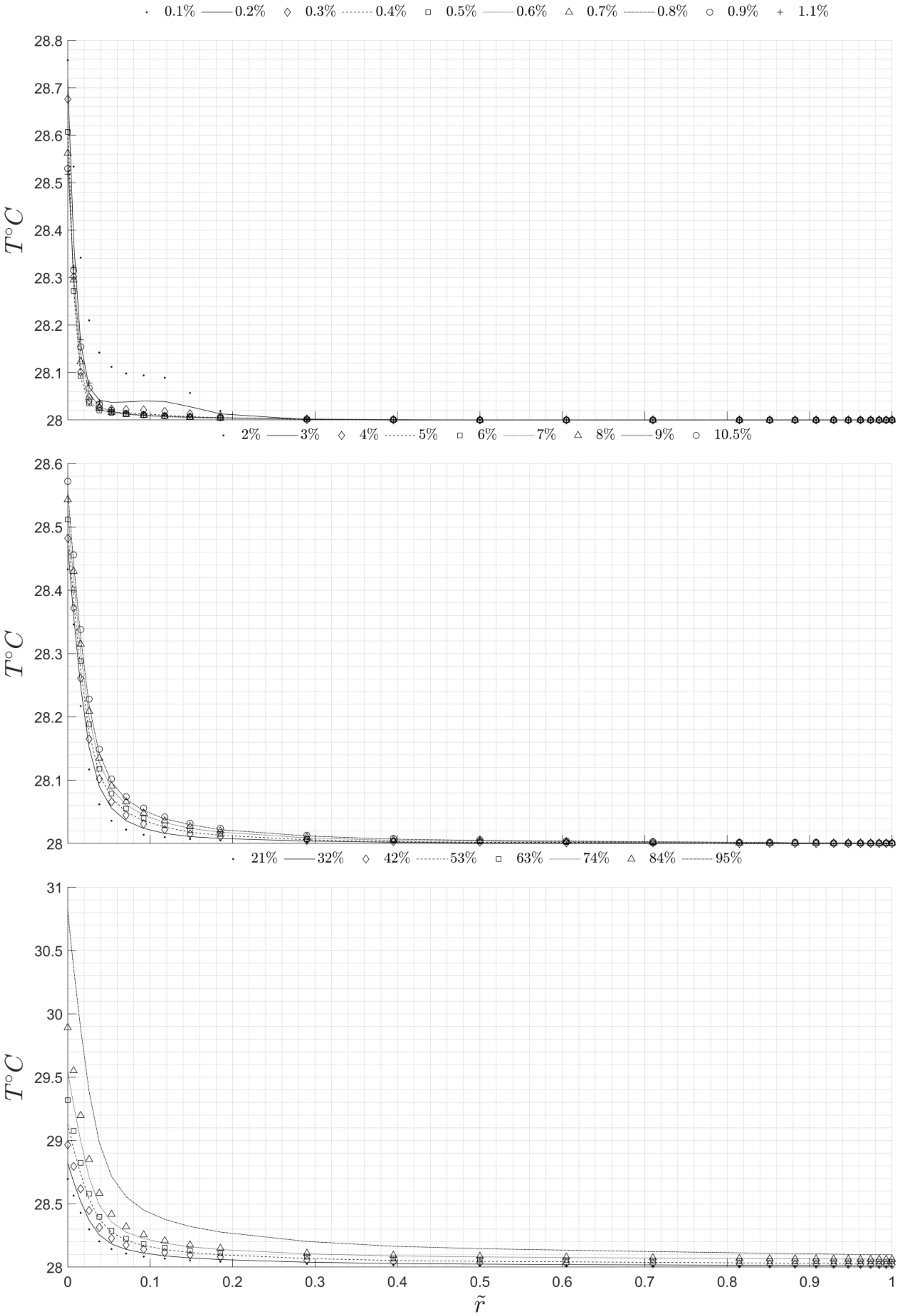

Figure 5.46: Radial distribution of thermal boundary layers at different axial locations for SSC45_4000 while hot Reynolds number was constant.

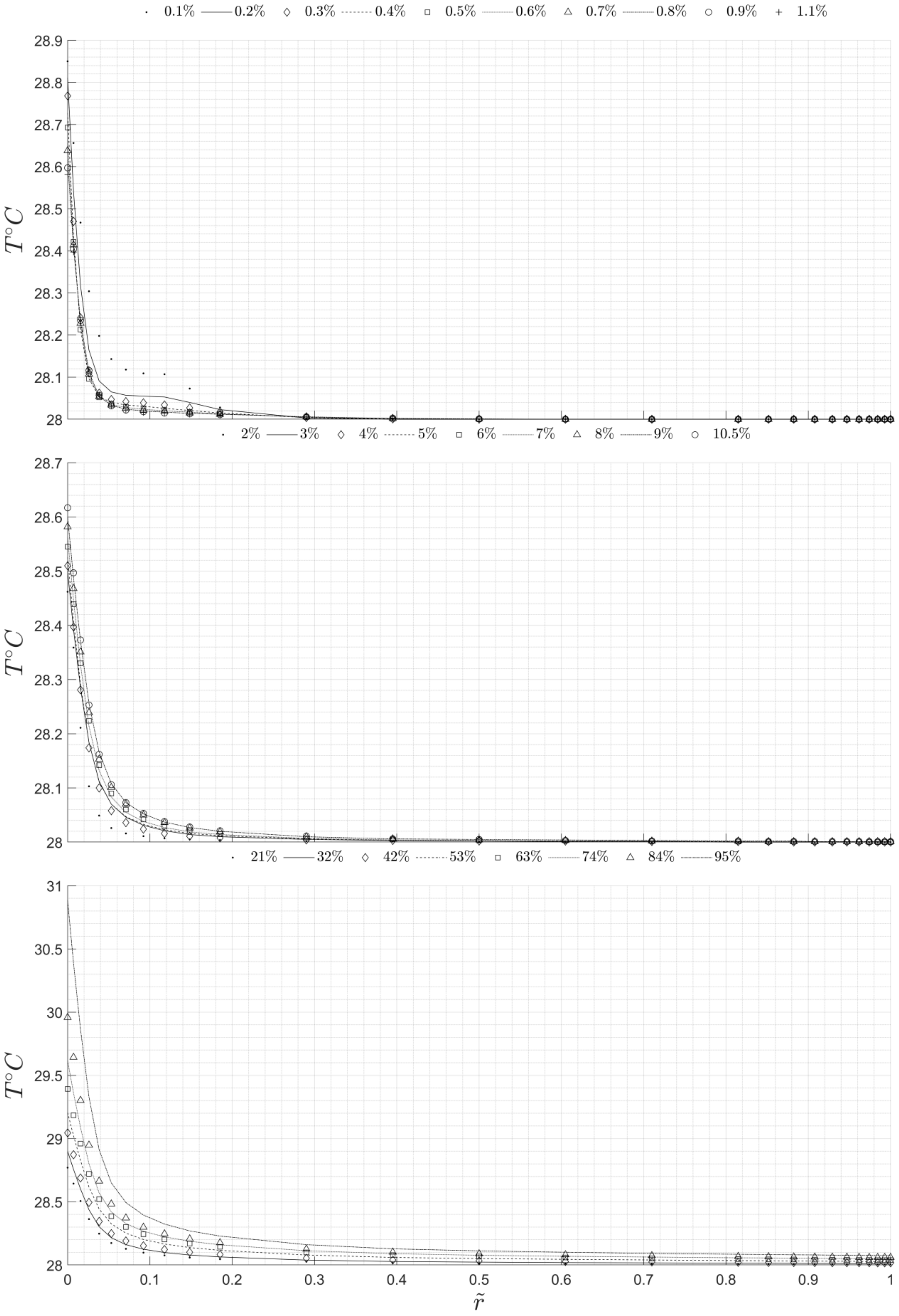

Figure 5.47: Radial distribution of thermal boundary layers at different axial locations for SSC60_4000 while hot Reynolds number was constant.

5.2.4 Unheated vs. Heated Profiles

The velocity components in a plain annulus were plotted and compared to visualise the different behaviours caused by heat transfer. Figure 5.48 presents the hydrodynamically developed axial profiles in the thermal entry region at the annular inlet and outlet at $Re = 300$, 2000 and 4000. A slight deviation was observed in the normalised axial velocity profile of the flow inside the annulus as the fluid was heated. This agrees with results provided by McAdams [105].

The heated flow shows inner bias towards the inner wall of the annulus (i.e., the heat source). This is due to the rise in temperature of the particles near the inner wall, which led to a reduction in dynamic viscosity compared to the lower temperature found at the centre axis of the annulus. As the mass flow rate remained constant, some of the liquid from the centre flowed near the wall to maintain continuity.

Reasons for these effects not being significant enough include the annular ratio, where the hydraulic diameter was not large enough to produce a significant difference [121], and the heat transfer rate not being high enough to provide a notable difference. While there are numerous articles discussing the effects of various annular passage ratios and eccentricity, as provided by [121], it is not among the objectives of this research. However, variation of the maximum heat transfer rate can be devised by changing ΔT (from Eq. (3.2)) at the inlets. In addition to the current $\Delta T = 22°C$, simulations with 42°C and 62°C were completed to compare the new heated profiles to the unheated in Figure 5.49. These were done on the turbulent profile at $Re = 4000$.

The full velocity distribution supported the claim of increasing inward deviation with an increasing rate of heat transfer, due to reduced resistance to the flow at the wall. A more detailed view of the profiles was shown, where the radial range was bounded by the inner wall and the radial location of the unheated (u_{99}). The profile at $\Delta T = 22°C$ still showed some layers to be slower than the unheated near the wall for the range ($2 \leq \tilde{r} \leq 12.5\%$); however, this was another consequence of the stretching of the profile, resulting in a typical overall inward deviation.

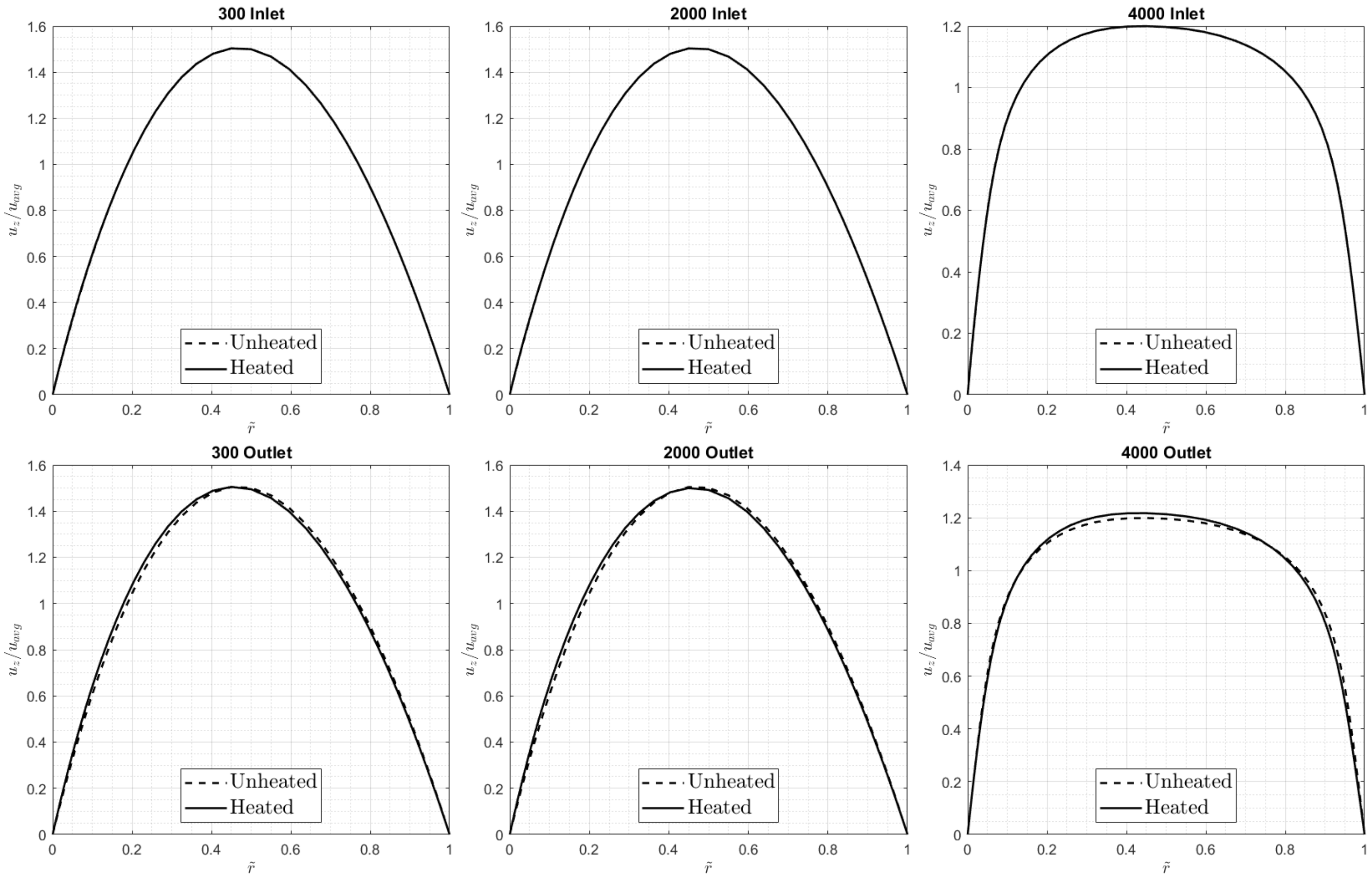

Figure 5.48: Velocity profiles before and after thermally developing in laminar and turbulent flows when delta T=22°C.

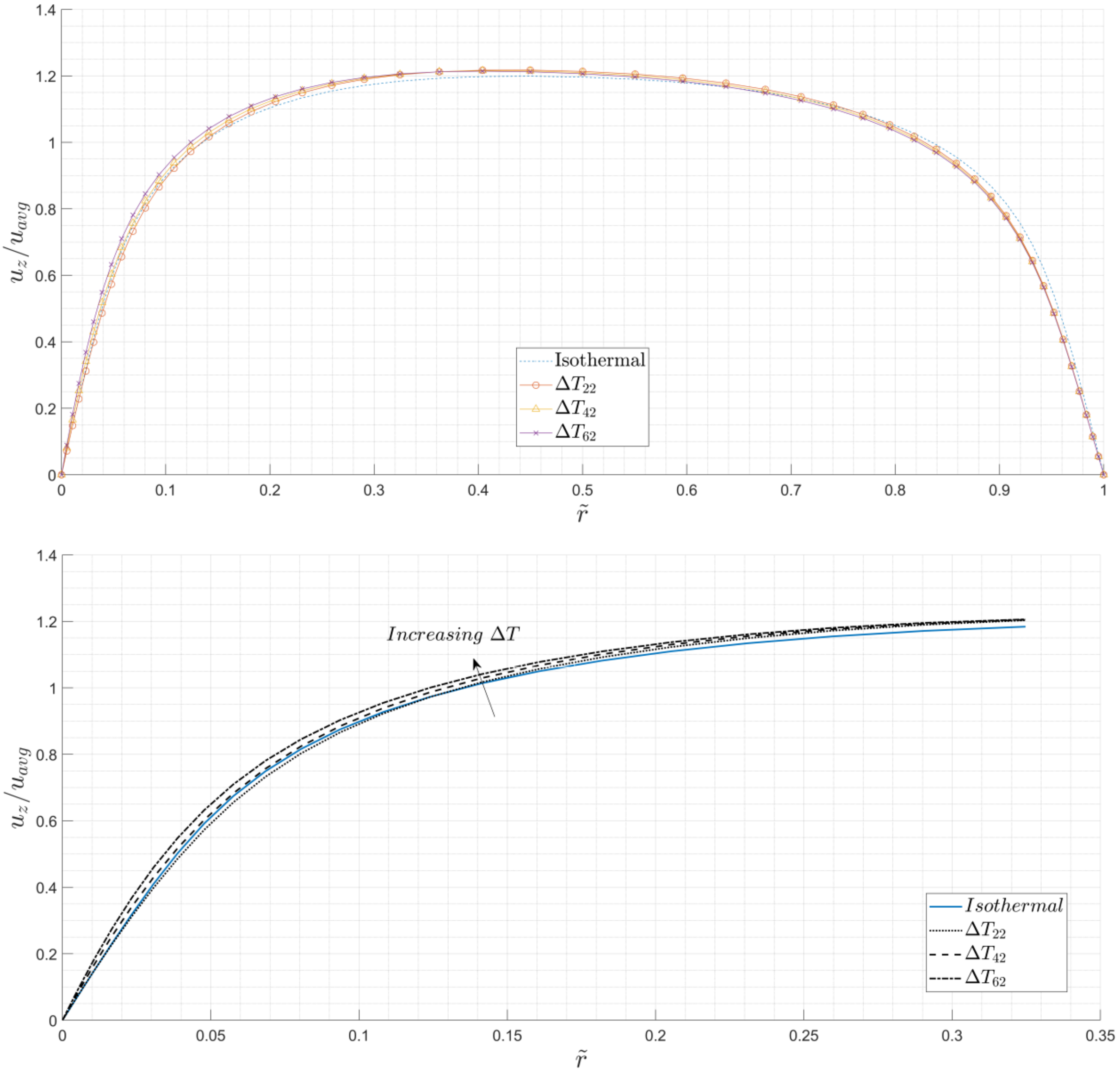

Figure 5.49: Turbulent velocity profiles inside a plain annulus at $Re = 4000$ with increasing rate of heat transfer. Top: Full velocity distribution. Bottom: Radial range from inner wall to the unheated u_{99}.

Similarly, this behaviour was observed in the case of swirling flow. Figure 5.50 presents the normalised axial and tangential velocity components of $SSC30\_300$. Near the exit of the swirler, the heated axial component showed slower particles near the walls compared to the unheated case. This was primarily attributed to the higher dynamic viscosity of the fluid during heat transfer. With reference to Figure 4.6, the piecewise linear function was applied when calculating the energy equation, Eq.(4.18), allowing improved capture of thermal effects on the fluid.

In this simulation, the viscosity corresponding to the cold inlet temperature of the annular fluid was significantly higher than the constant viscosity assumed in the unheated case, which was evaluated at the film temperature. Consequently, these elevated viscous forces acted like brakes on the tangential component, making it slower than its unheated counterpart. Nevertheless, within the first 10% of the annulus, thermal effects influenced both velocity components. Particles near the inner wall experienced an increase in temperature, lowering their viscosity and, in turn, accelerating their speed. Such deviations were consistently observed across various locations.

Similar behaviour was noted when Re was increased to 2000, although thermal effects were most pronounced at $\tilde{Z} = 32\%$, where both profiles appeared to be approximately opposites. With increasing Re, the axial component continued to show noticeable deviations downstream, while the tangential component consistently exhibited a slower profile than the unheated. This resulted from particles initially concentrated outward as they exited the swirler. In the heated case, however, a resistance formed near the inner wall, pulling the flow inwards and decreasing the outward momentum. This shift redirected focus to the initially slow-moving particles near the inner wall.

Increasing the angle of the swirlers, as shown in Figure 5.53 and Figure 5.54, produced similar patterns with less pronounced differences between the unheated and heat profiles.

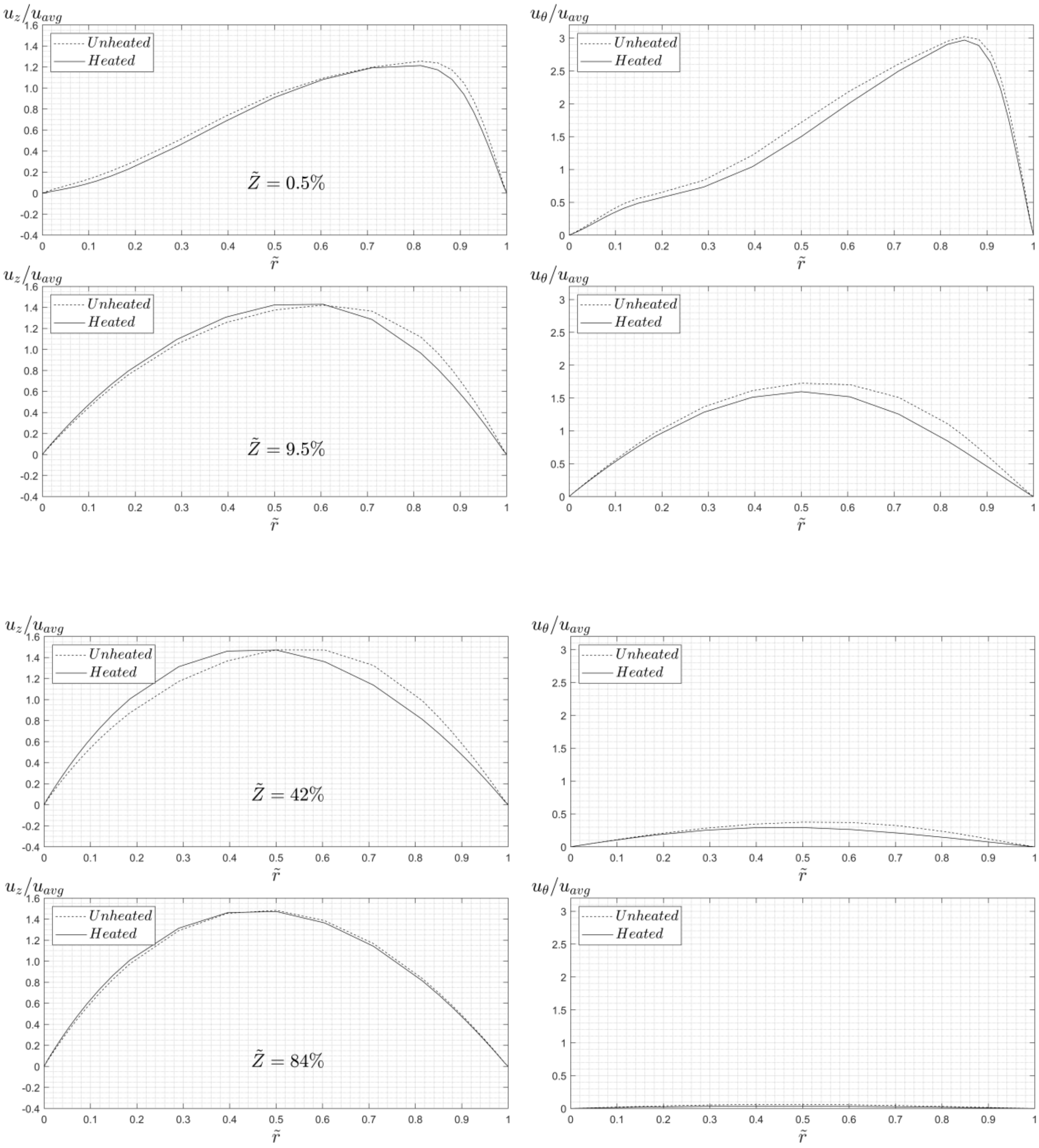

*Figure 5.50: Unheated and heated normalised velocity profiles at SSC*30_300*.*

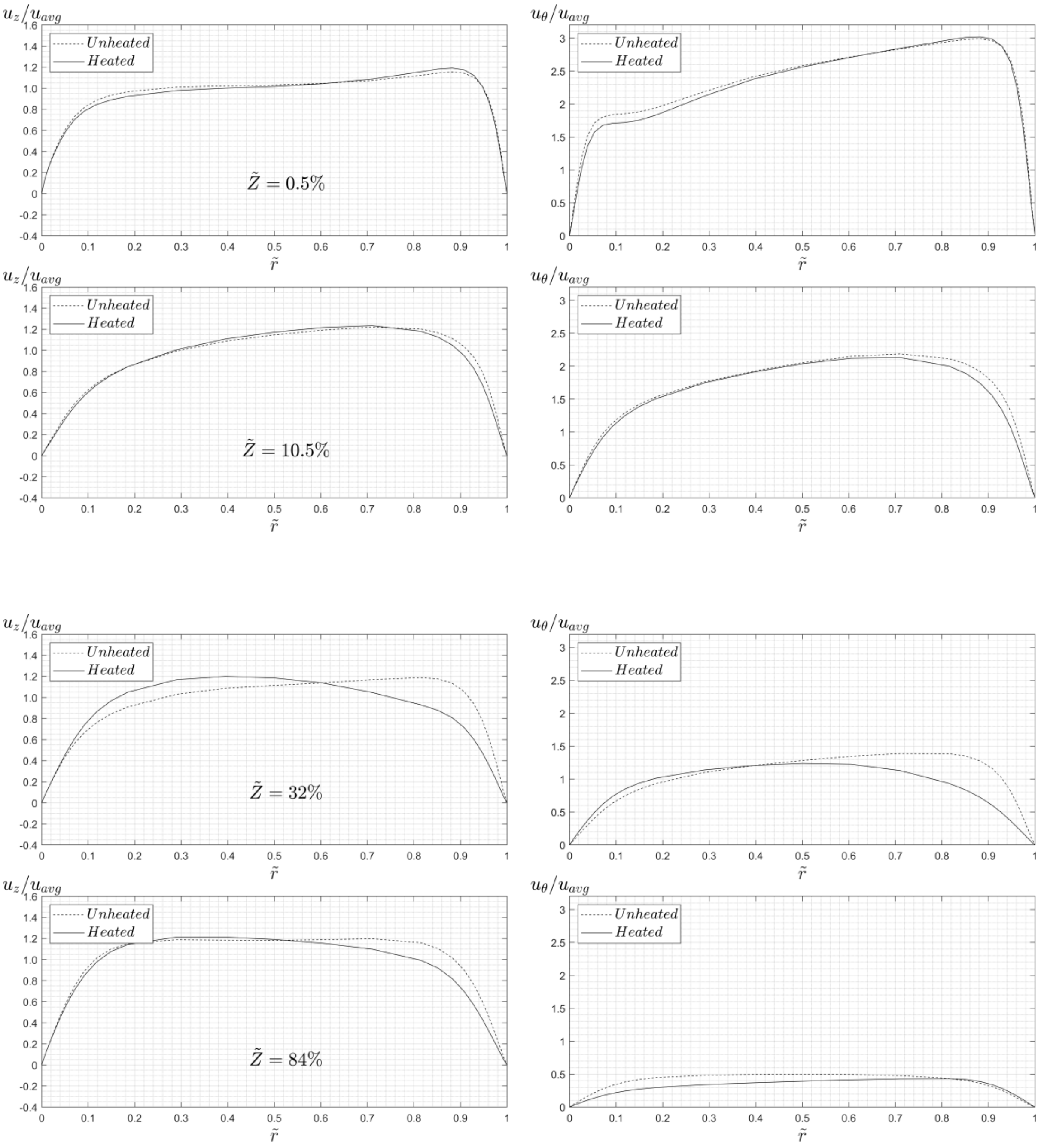

*Figure 5.51: Unheated and heated normalised velocity profiles at SSC*30_2000

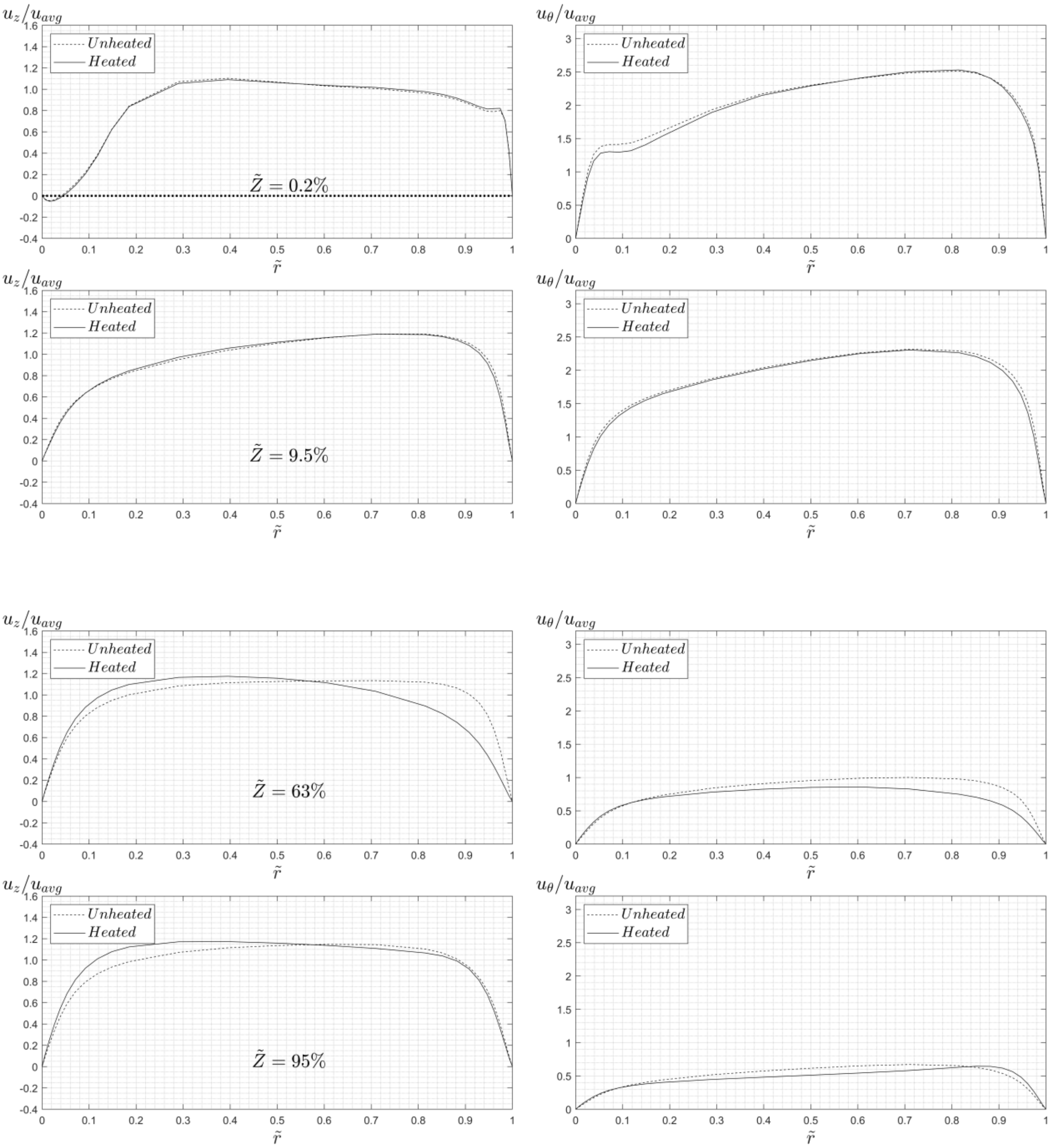

Figure 5.52: Unheated and heated normalised velocity profiles for SSC30_4000.

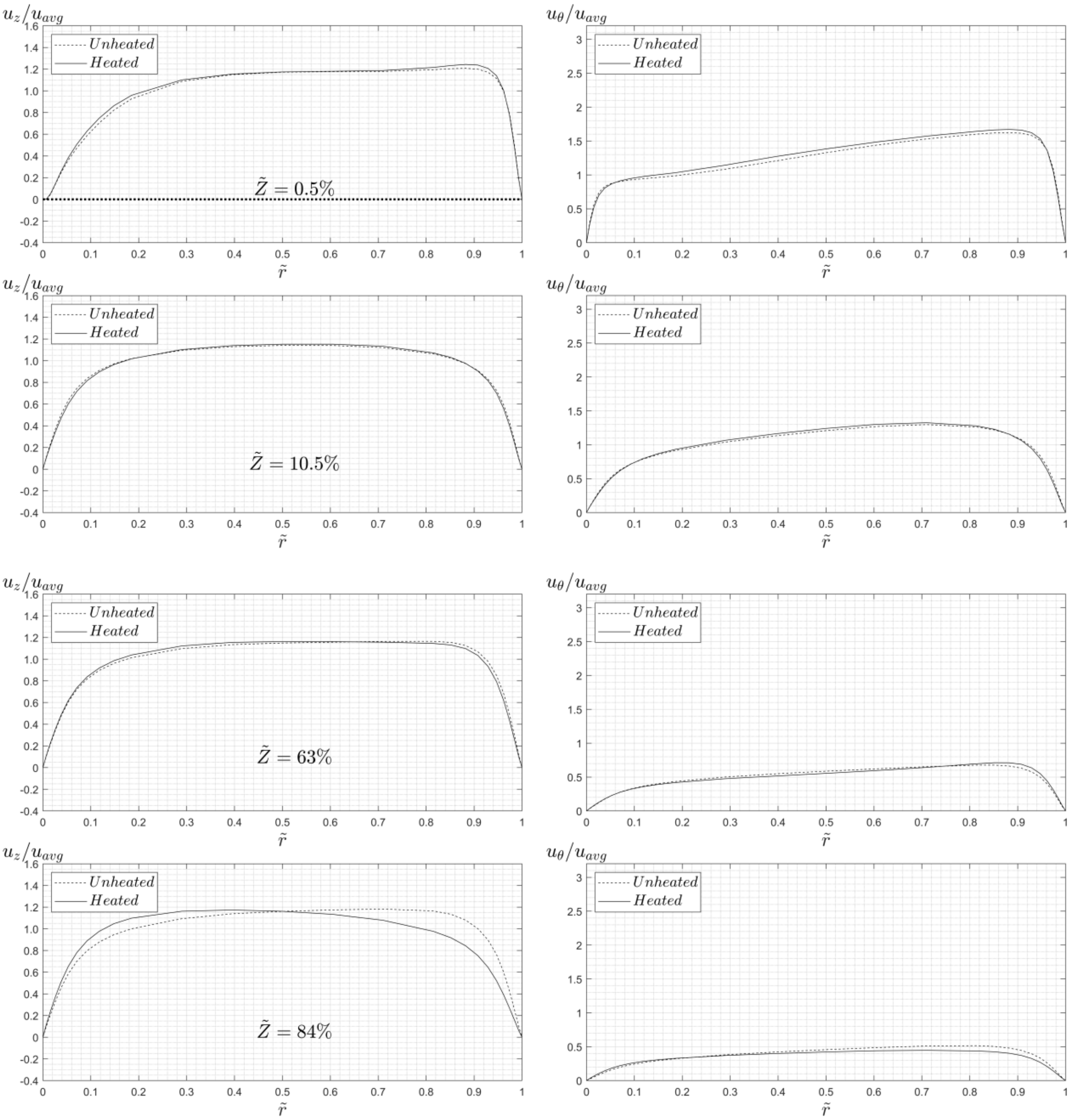

Figure 5.53: Unheated and heated normalised velocity profiles for $SSC45\_4000$

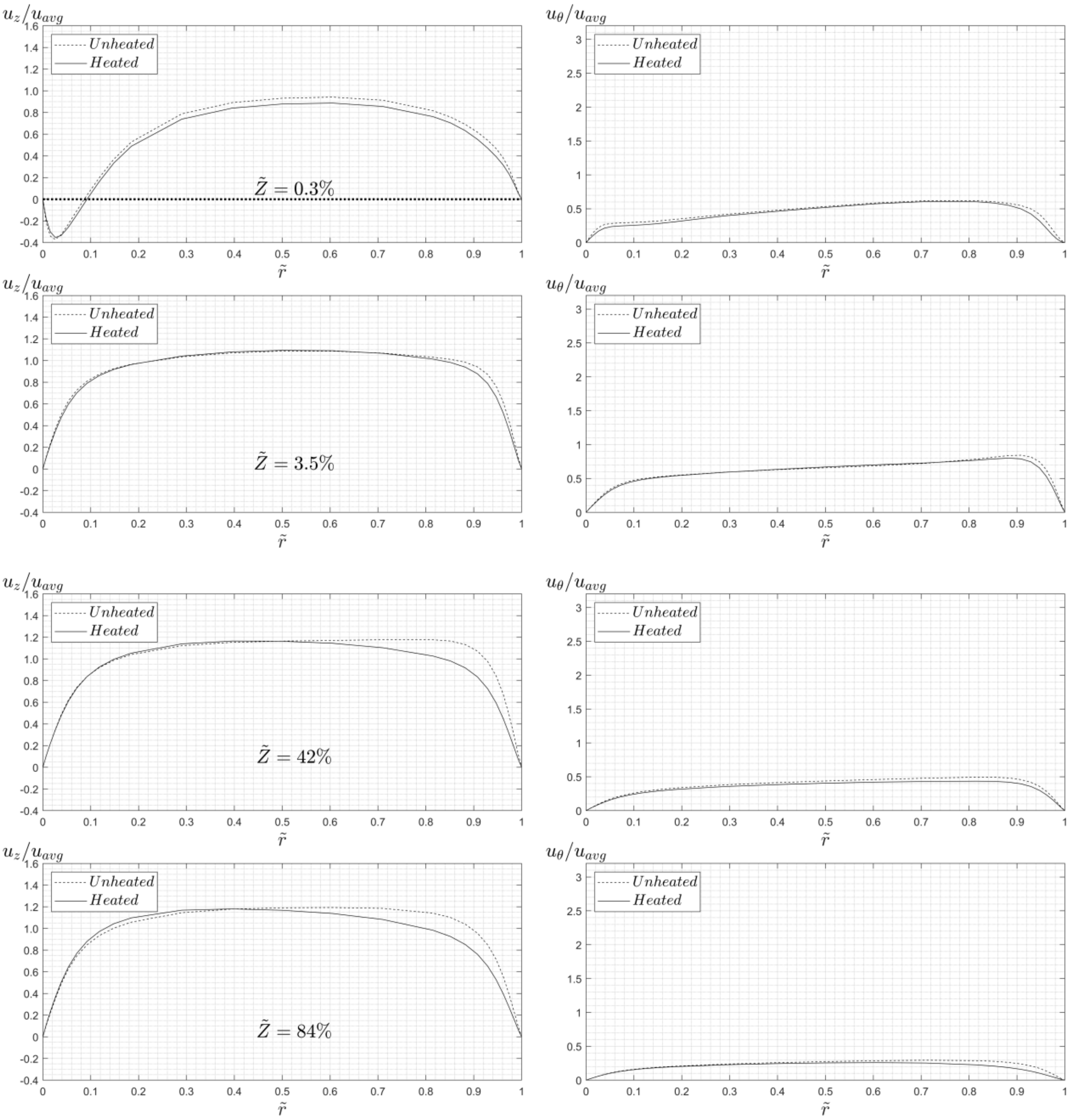

Figure 5.54: Unheated and heated normalised velocity profiles for SSC60_4000.

5.2.5 Flow Contours

5.2.5.1 Axial Contours

Contours of the normalised axial velocity in the unheated case of $SSC30$ at $Re = 4000$ can be seen in Figure 5.55. At the exit of the swirler, eight confinements occupied by the fluid are observed. As previewed by the velocity profiles and recirculation zone iso-surfaces, negative axial velocities were observed in areas adjacent to the vane walls and the central hub of the swirlers. Between these walls, a high-velocity region was detected. Isolating a single fluid confinement, a local maximum was detected near the inner wall, adjacent to the convex side of the vane wall (i.e., the leading side of the confinement). This observation was found to be axisymmetric among all eight confinements.

These contours provide an opportunity to validate the surfaces initially defined, located on a plane at an angular location of $\theta = 0°$. This could be observed as a non-optimal location to best capture the axial velocity profile behaviour in the high-speed region at the exit of the swirler within the same confinement. However, rotating the line by 20° confirms that the profiles agree, independent of the angular position, as long as the line is positioned downstream of the fluid flow and not at the solid walls of the vanes. This agreement was presented in Figure 5.57. Additionally, the maximum region was found to be at constant intervals of approximately 45°, anticlockwise, starting from the first local maximum located at 20°.

Proceeding $1mm$ downstream, the region defined as the recirculation zone between the confinements was observed to have almost completely dissipated downstream from the top edge of the vanes and the central hub, which can be distinguished as the borders of the confinements entraining from the exit of the swirler. This dissipation is caused by fluid diffusion from regions of higher pressure to lower ones to stabilise the flow. Furthermore, as the swirling motion is presented anticlockwise (as per the view of the figure), the trailing high-pressure region flows towards and fills the leading low-pressure region, commencing its angular occupation, which was observed as an axisymmetric recurrence.

On the next plane, the fluid has nearly occupied the annular region, with vane wall entrainment fully dissipated. However, the entrainment caused by the central hub remains. The confinements remain visible, but the high-velocity region shifts towards the centre, stretching radially outward with constant magnitude and forming local maximum columns. This radial distribution reduces the magnitude of the local maxima compared to earlier planes.

At 3 mm, the higher-pressure region expands into the central recirculation zone. The local maximum columns weaken as the region splits into two smaller zones near the inner and outer annulus walls. The maximum near the inner wall occupies a larger area and is displaced forward due to lower shear forces, resulting in a trailing arc shape. In contrast, the outer wall maximum is smaller and dissipates by 4 mm as shear forces intensify with swirling flow.

At 5 mm, the maximum columns have vanished, and the confinements merged into a shuriken-like shape. This merging begins near the inner wall and progresses outward. Although central hub entrainment dominates, faster fluid particles initiate the merge from above the recirculation zone's radial thickness. Between 5 $mm - 7$ mm, the shuriken edges become blunter as outer wall decelerate and the inner wall maximum shrinks.

At 9 mm, the edges dissipate, and a uniform axial velocity fills the upper half of the annulus. The shuriken transitions into a clover shape with eight rounded peaks, marking the remnants of the confinements. As the flow continues downstream, the clover expands outward, and the maximum region disintegrated by 15 mm. A new maximum forms near the annulus centre, growing between 16 $mm - 20$ mm into a uniformly distributed axial velocity, concluding axial component's development within the jet impingement (i.e., the vena contracta) zone.

Beyond this point, the fluid swirls freely. From 345 mm onwards, an instability resembling a cyclic quadrilateral appears, with four nearly axisymmetric peaks. These peaks rotate with the swirling flow, causing oscillations observed in the velocity profiles. This instability is best interpreted through the tangential component results.

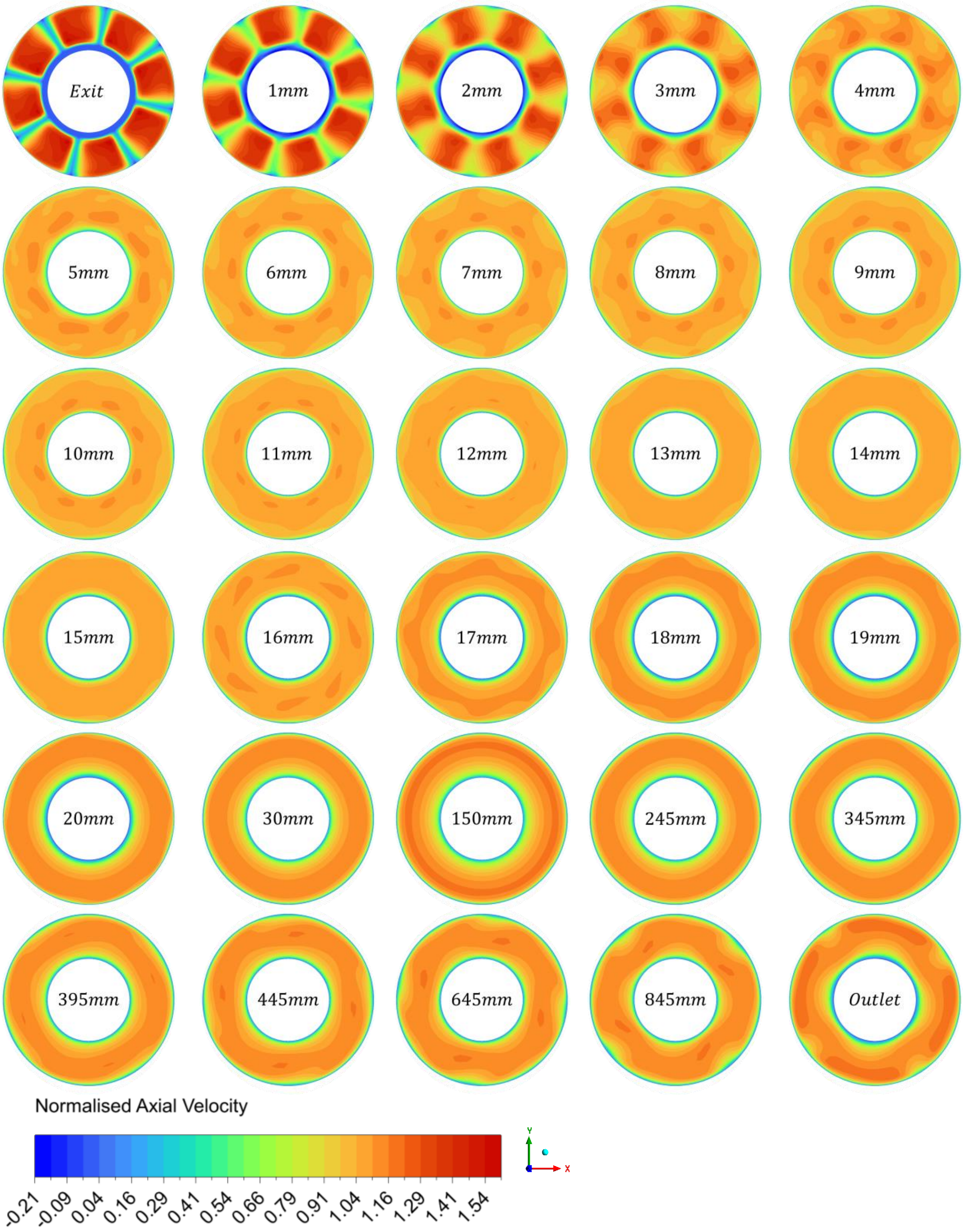

Figure 5.55: Cross-sectional normalised axial contours of unheated SSC30_4000 at different axial locations.

5.2.5.2 Tangential Contours

Figure 5.56 presents the cross-sectional contours of the normalised tangential component. Similar to the axial contours, eight confinements were observed downstream from the swirler, with the exit fluid presenting the local maximum located at the leading side of the confinement. In contrast to the axial contour at the exit, the local maximum was located near the outer wall of the annulus. The recirculation zones adjacent to the swirler's solid walls border these confinements. The tangential component was not present in these regions. Figure 5.57 shows a confirmed agreement of the outward deviation of the tangential velocity profile with the previously defined surfaces (at $\theta = 0°$) and the region where the local maximum was located (at $\theta = 25°$) within the same confinement. The local maximums were found to be located at approximately 45° angular spacings about the axis of the annulus.

As the flow progressed for 1 mm, the entrainment of the wall effects was shown as lower-speed regions bordering the confinements. In comparison to the axial component, the tangential component pierced through the recirculation zone much more quickly due to its significant magnitude. At 2 mm, the recirculation zone had completely dissipated, and the majority of the annular domain was dominated by the tangential component, with a magnitude of about three times that of the inlet velocity. Additionally, the confinements had already begun to merge, which was seen twice as early as in the results of the axial component.

Also, it should be noted that the merge between the confinements began from the outer wall region, diffusing inwards, which is the opposite of the direction observed in the axial results. These conventions are primarily dependent on the initial location of the local maximum when the flow exits the swirler, diffusing from a high-flow region to a lower one with respect to the component of interest.

Moreover, from 2 mm to 6 mm, the slower region expanded radially outward as the high-speed particles near the outer wall decelerate due to the large wall shear stress exerted by the outer wall on the adjacent particles at 7 mm. This behaviour continues with the deceleration of the tangential component, as the lower-speed region leads the higher-speed region to stabilise, transitioning into a circular shape as the flow exits the jet impingement zone at 20 mm. From this point onwards, the flow was once again swirling freely, with the entire annular domain swirling uniformly. This was observed to begin at the end of the jet impingement zone and before the results showed an instability. The uniformity remained, but the decay of the tangential component was observed from 150 mm onwards. As the normalised tangential magnitude reaches unity at 345 mm, an instability (non-uniform boundary layers) driven by the tangential component, forming four local maximum regions, is observed as the flow approaches the outlet. This instability resonated with the axial results and is what caused the oscillations of the velocity profile plotted earlier, as the local maxima rotate about the annular axis. It is believed that this is the final stage of the swirling flow before the axial flow begins to develop hydrodynamically, where the viscous forces dominate, applying "virtual brakes" in the tangential direction, streamlining the swirling flow into an axial one.

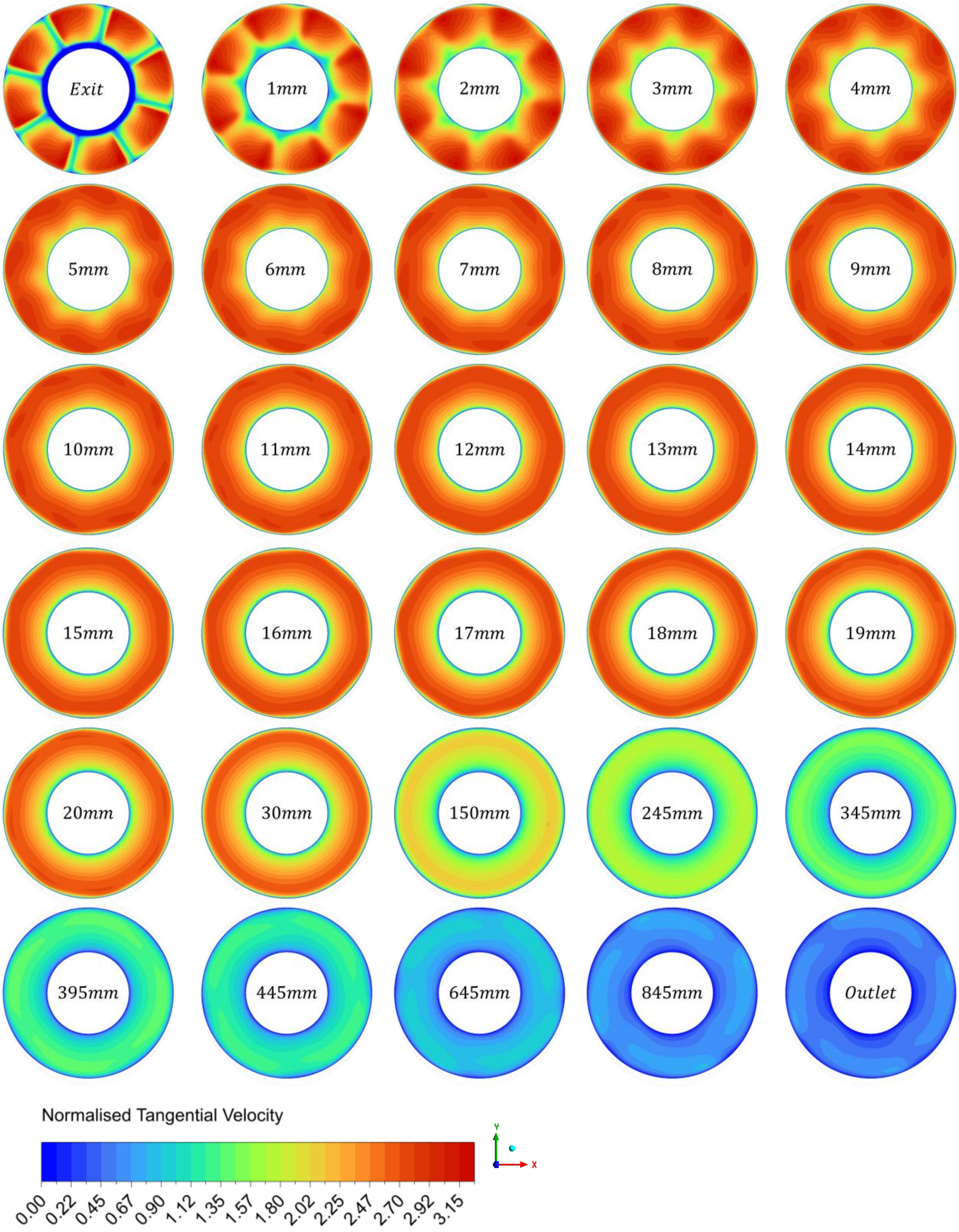

Figure 5.56: Cross-sectional normalised tangential contours of unheated SSC30_4000.

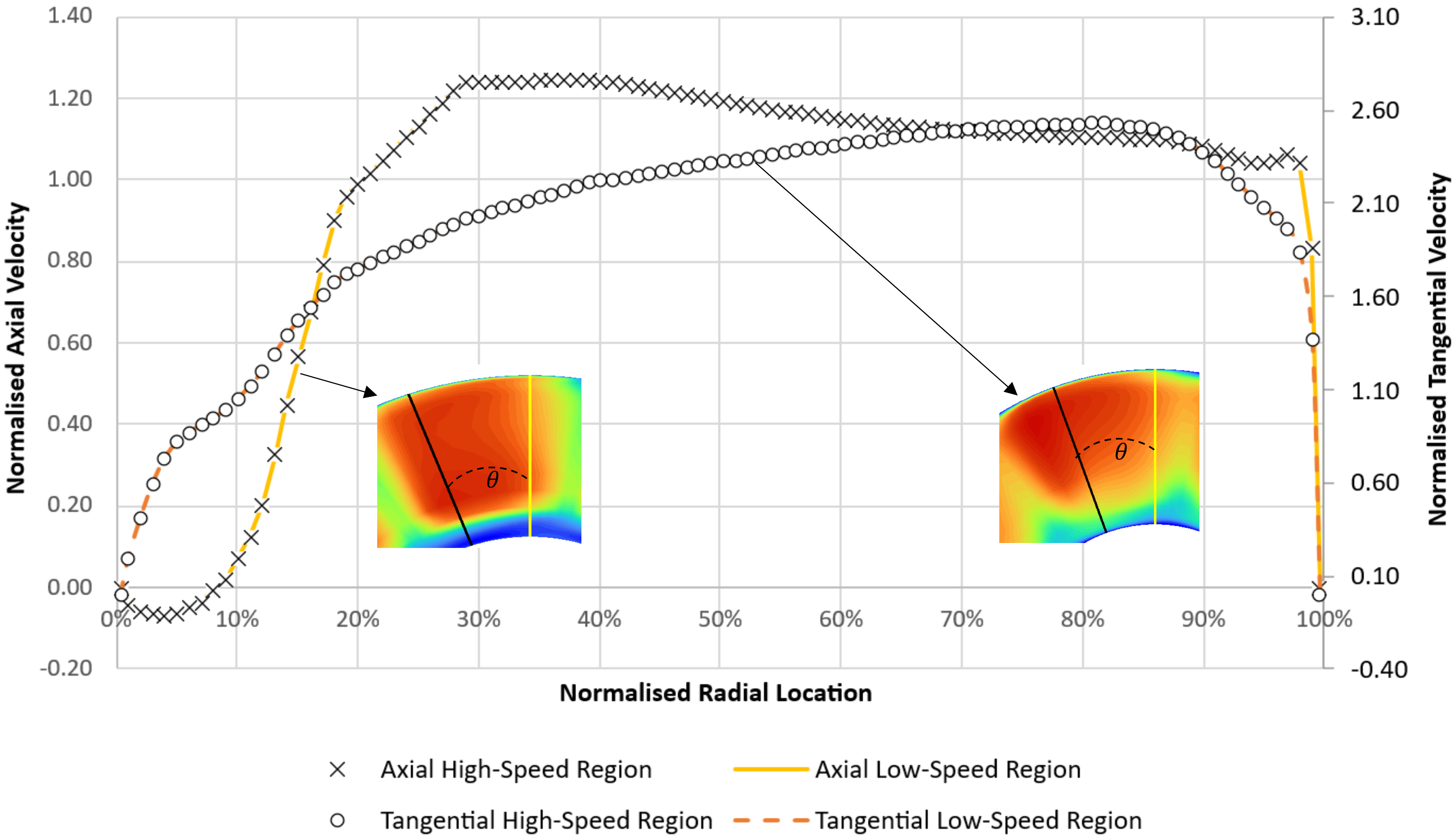

Figure 5.57: Validation of the surface angular location defined to plot the velocity profiles.

5.2.5.3 Reynolds Number Effect

Figure 5.58 presents the different stages observed throughout the swirl decay cycle, showing the differences in attributes and axial locations caused by the variation of the Reynolds number. The normalised axial velocity exhibited distinct characteristics across different Re values. At the swirler exit, in the case of $Re = 1000$, local maxima were observed near the outer wall, on the concave side of the vanes. Interestingly, these regions gradually shifted from the inner wall at the convex side of the vane when $Re = 4000$ towards the outer wall, then became almost entirely distributed within the fluid confinement as Re decreased to 2000. This suggests a potential interaction between the decreasing Re and the centrifugal forces generated by the swirler, influencing the axial flow distribution within the annulus.

Furthermore, the presence of the swirler's jet effect persisted within the annulus at all Re values, evident from the observable local maximum regions in the impingement zone. This effect intensified with decreasing Re, as indicated by the increasing length of the zone downstream by 34% at $Re = 2000$ and 74% at $Re = 1000$, in comparison to $Re = 4000$. This observation suggests that when Re decreased (i.e., swirling intensity decreased), the axial momentum of the fluid's resistance to the jet impingement zone also decreased. As Re increases, the diffusion of the fluid among the confinements increases, resulting in significant dissipation of the impingement effect. This agrees with the results obtained by Xu Y. et. al. [147] in an experimental investigation focused on the influence of Re on impinging synthetic jet vortices. It was also shown that increasing Re resulted in increased viscous dissipation within the vortex rings, which contributes to the loss of their coherent structure over time.

Travelling $3mm$ downstream, the local maximum regions exhibited a fascinating trend. Their magnitude increased with decreasing Re, and the regions within the fluid confinements began to merge, overcoming the entrainment effect of the swirler's solid walls. Additionally, the low-speed entrainment due to the central hub grew thicker. However, the merging process displayed an intriguing contrast. For both $Re = 1000$ and 2000, the merging initiated from the outer wall inwards, while the opposite was observed at $Re = 4000$, where merging began from the inner wall outwards. At higher Re, the increased inertial forces lead to stronger swirling motion. As the wall shear stress of the inner wall is smaller than that of the outer wall, the local maximum develops at the inner wall and then expands outwards. However, in the case of lower Re, viscous forces become more dominant, which weakens the swirl intensity. In this case, the smaller inertial forces result in the difference between the wall shear forces not significantly affecting the flow, allowing the local maximum to be driven by the tangential component. The fluid exhibited free swirling flow before the occurrence of circumferentially convective instability in the normalised axial component downstream. This was observed to be proportional to increasing Re between $50 - 55mm$, $35 - 98mm$, and $20 - 245mm$ when $Re = 1000$, 2000 and 4000, respectively. First, the boundary layers near the inner wall thicken then similarly the boundary layer at the outer wall thickens further downstream at 60, 106 and $345mm$, respectively. The instability persisted while gradually rotating about the axial axis downstream, with regions of thick and thin boundary layers defining four distinct zones as the tangential component approached unity. Four local maxima were observed as the flow approached the outlet of the annulus, with higher normalised axial velocity associated with decreasing Re.

The normalised tangential velocity is displayed in Figure 5.59, consistent behaviour across all Re values. As the flow exited the swirler until $7mm$, it exhibited instability in the form of eight peaks. These peaks indicated thicker boundary layers near the inner wall, likely due to entrainment from the solid walls of the swirler. Additionally, local maximum regions were observed in the entrainment of fluid confinements. For Re = 1000, this behaviour continued further downstream until $35mm$, while for $Re = 2000$ and 4000, it ended at $24mm$, where the component was uniformly distributed circumferentially. This variation in the persistence of the instability confirms the influence of Re on the development and decay of the tangential flow downstream.

Zones	4000	2000	1000
Start of Jet Effect	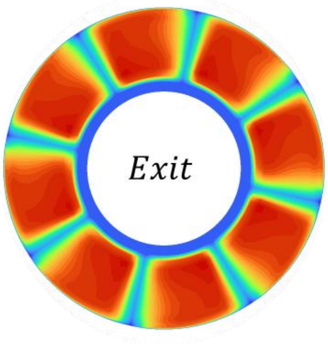	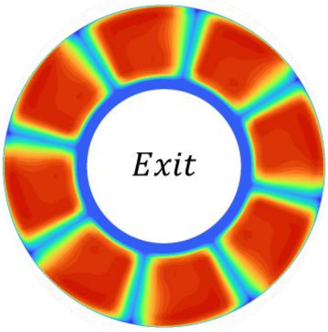	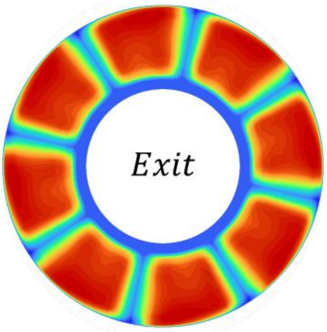
Local Maxima Columns	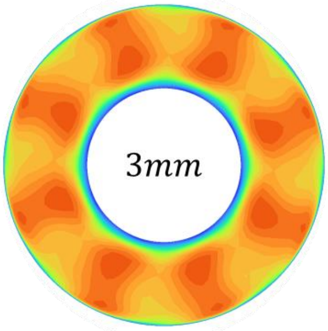	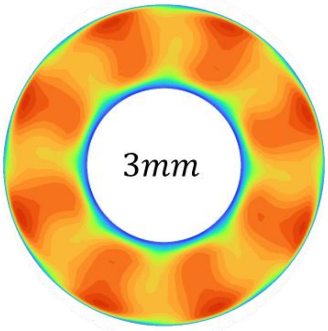	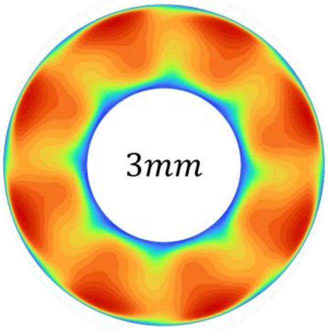
End of Jet Effect	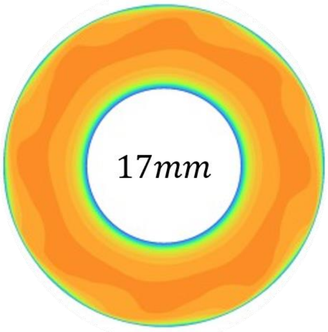	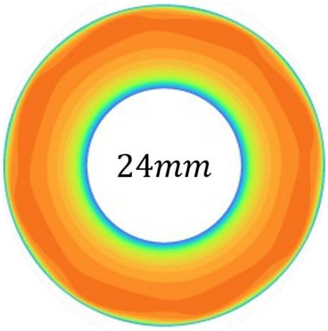	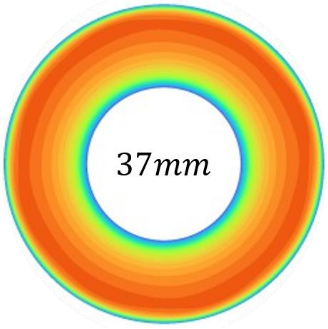
Free Swirling Zone	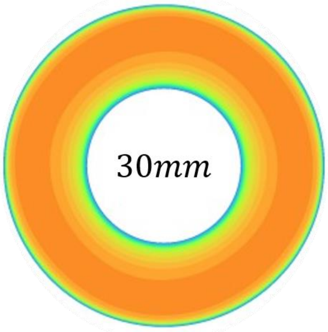	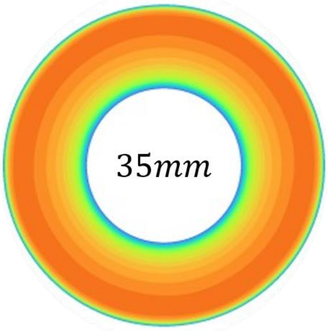	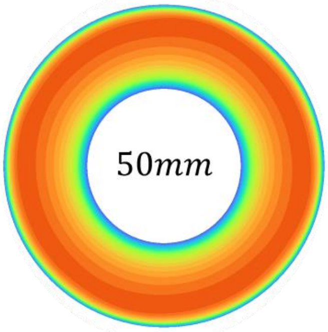

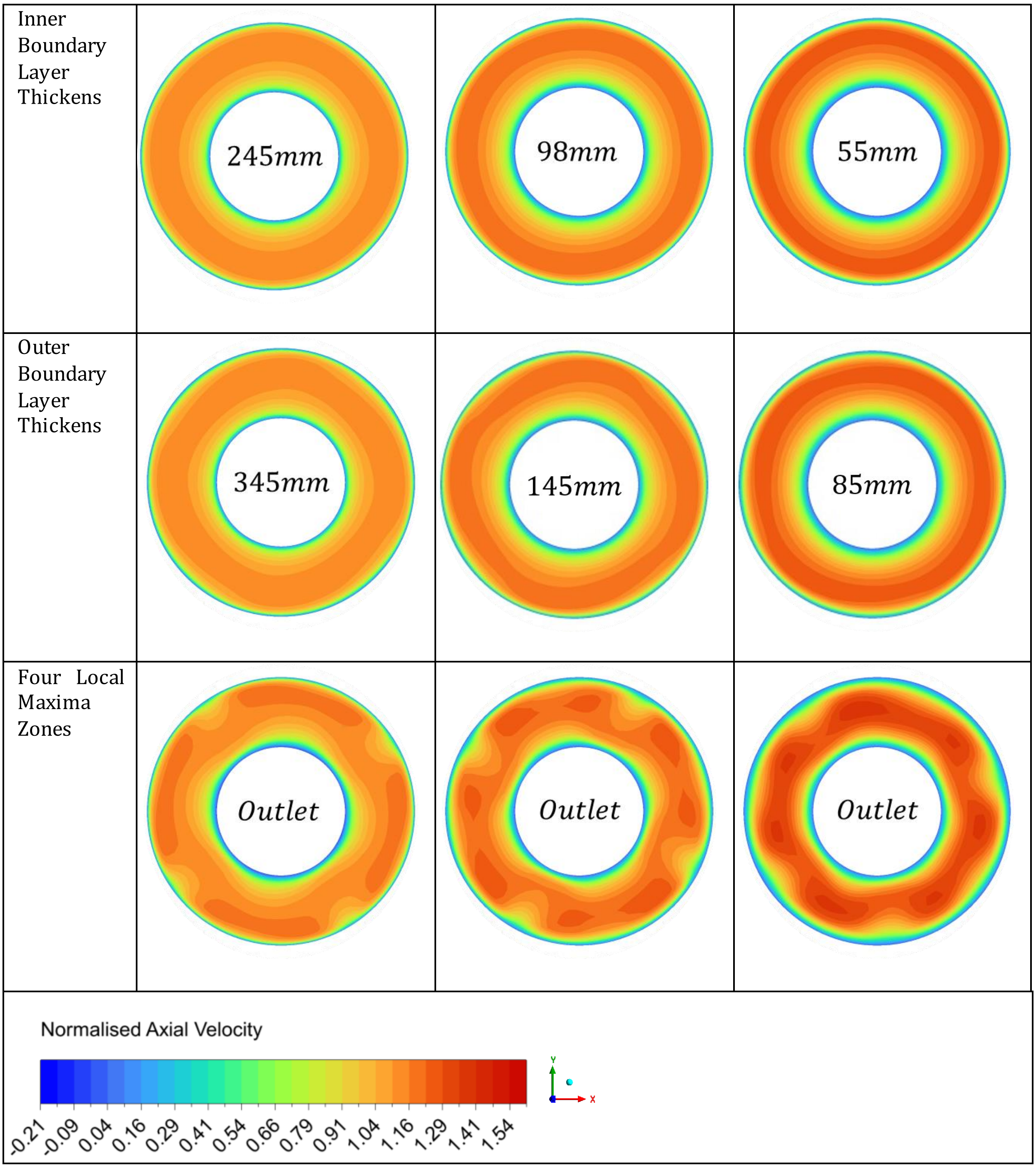

Figure 5.58: Unheated cross-sectional contours of the normalised axial velocity in the case of SSC30 at different inlet Reynolds numbers.

Zones	4000	2000	1000
Start of Jet Effect	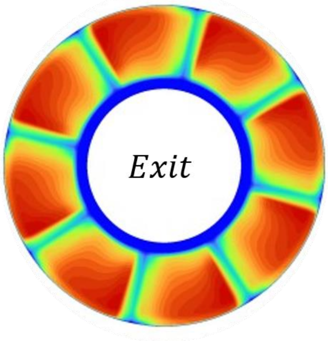	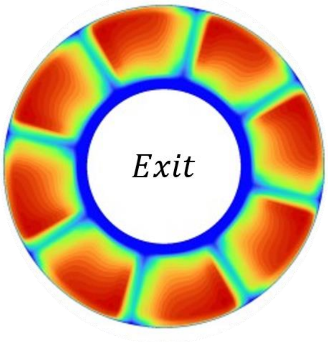	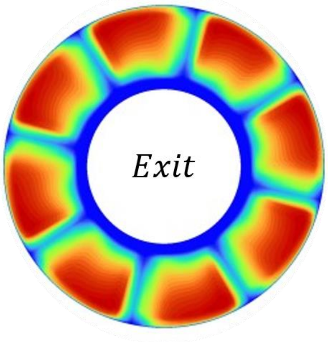
Inner Boundary Layer Thickens	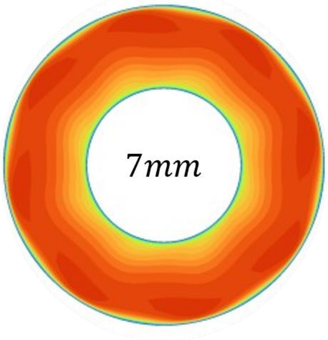	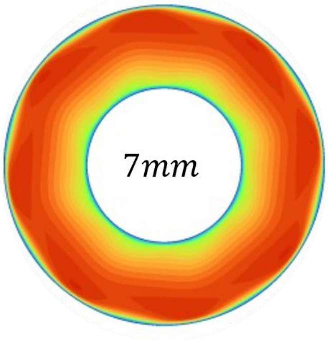	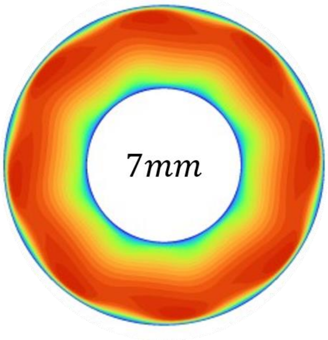
End of Jet Effect	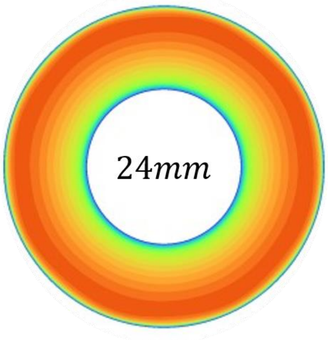	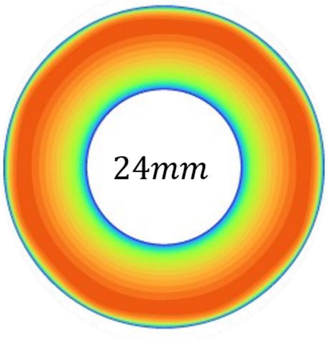	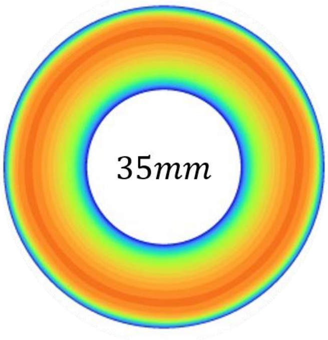
Swirl Free Flow	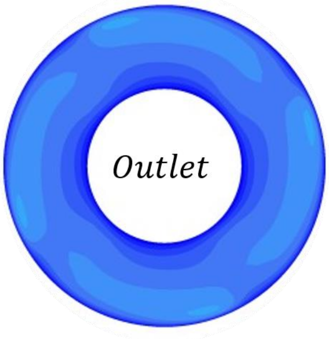	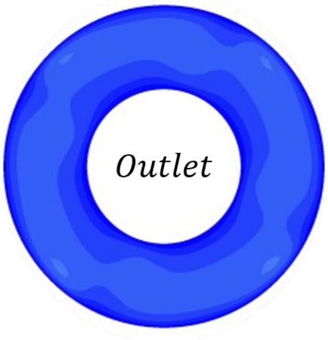	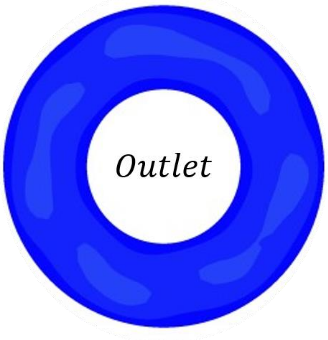

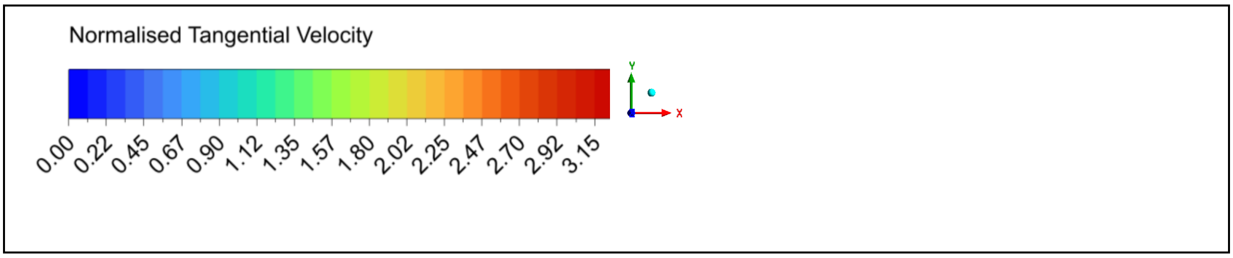

Figure 5.59: Unheated cross-sectional contours of the normalised tangential velocity in the case of SSC30 at different inlet Reynolds numbers.

To compare the effect of changing Re between heated and unheated stages, the results of the heated annulus are shown in Figure 5.60 and Figure 5.61 for both normalised axial and tangential velocities, respectively. At $Re = 4000$, the added heat increased the jet impingement zone length by approximately 34%. The inner and outer boundary layers occurred 57% and 76% sooner, respectively.

For lower Re, the zone remained constant at $Re = 2000$ but expanded by nearly 30%. The inner wall boundary layer developed earlier at $Re = 2000$ but delayed at $Re = 1000$, while outer wall thickening consistently occurred sooner with decreasing Re.

The extended jet impingement zone resulted from multiple factors. First, thermal boundary layer growth created low-velocity velocity regions near the walls due to viscous drag. Downstream. Swirling flow resisted outer wall boundary layer growth, while inner wall thickening disrupted main flow momentum, further elongating the impingement zone [148].

Swirling flow also enhanced circumferential uniformity of axial velocity, mitigating thermal boundary layer effects on the inner wall. This reduced axial velocity decay, sustaining the impingement zone [149]. Although inner wall boundary layers showed no clear heating trend, outer wall thickening accelerated at lower Re, indicating earlier flow development. Outer velocity contours confirmed this, showing axial velocity increases of 0.3%, 4%, and 2.2% with decreasing Re.

Finally, temperature gradients induced *thermal expansion forces*, a buoyancy-like mechanism where non-uniform thermal energy distribution created pressure gradients opposing swirl flow downstream. This contributed significantly to jet impingement zone extension, independent of incompressibility effects.

Zones	4000	2000	1000
Beginning of Jet Impingement Effect	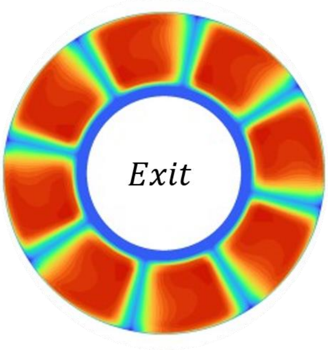	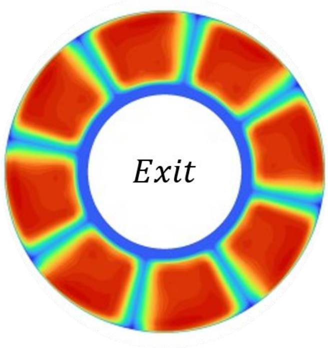	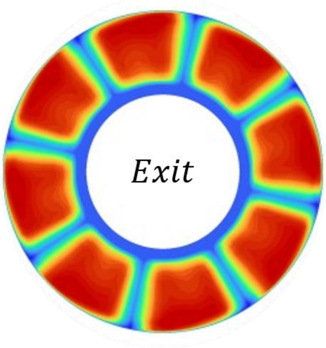
Local Maxima Columns	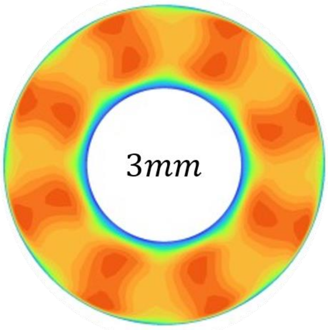	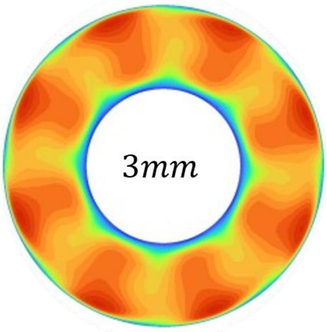	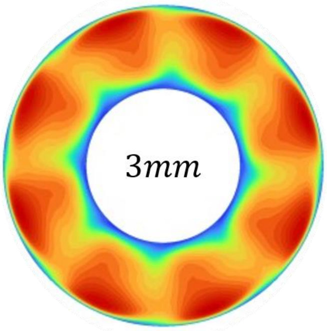
End of Jet Impingement Zone	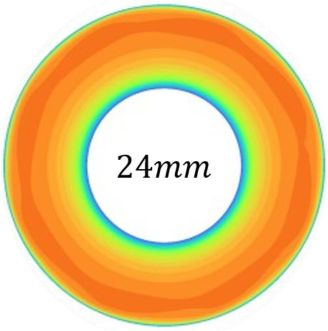	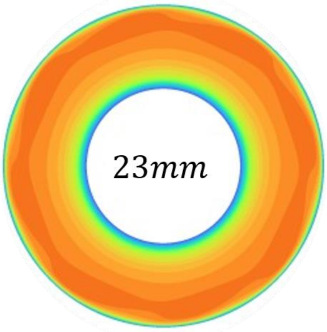	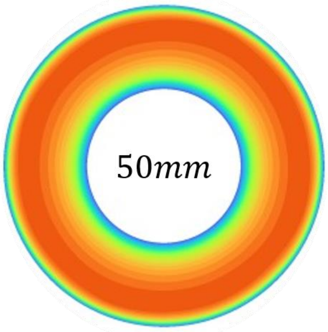
Free Swirling Zone	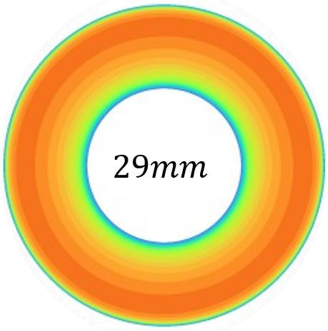	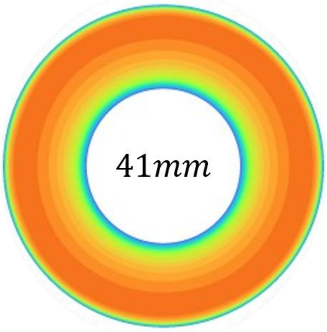	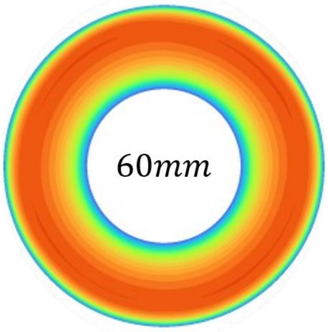

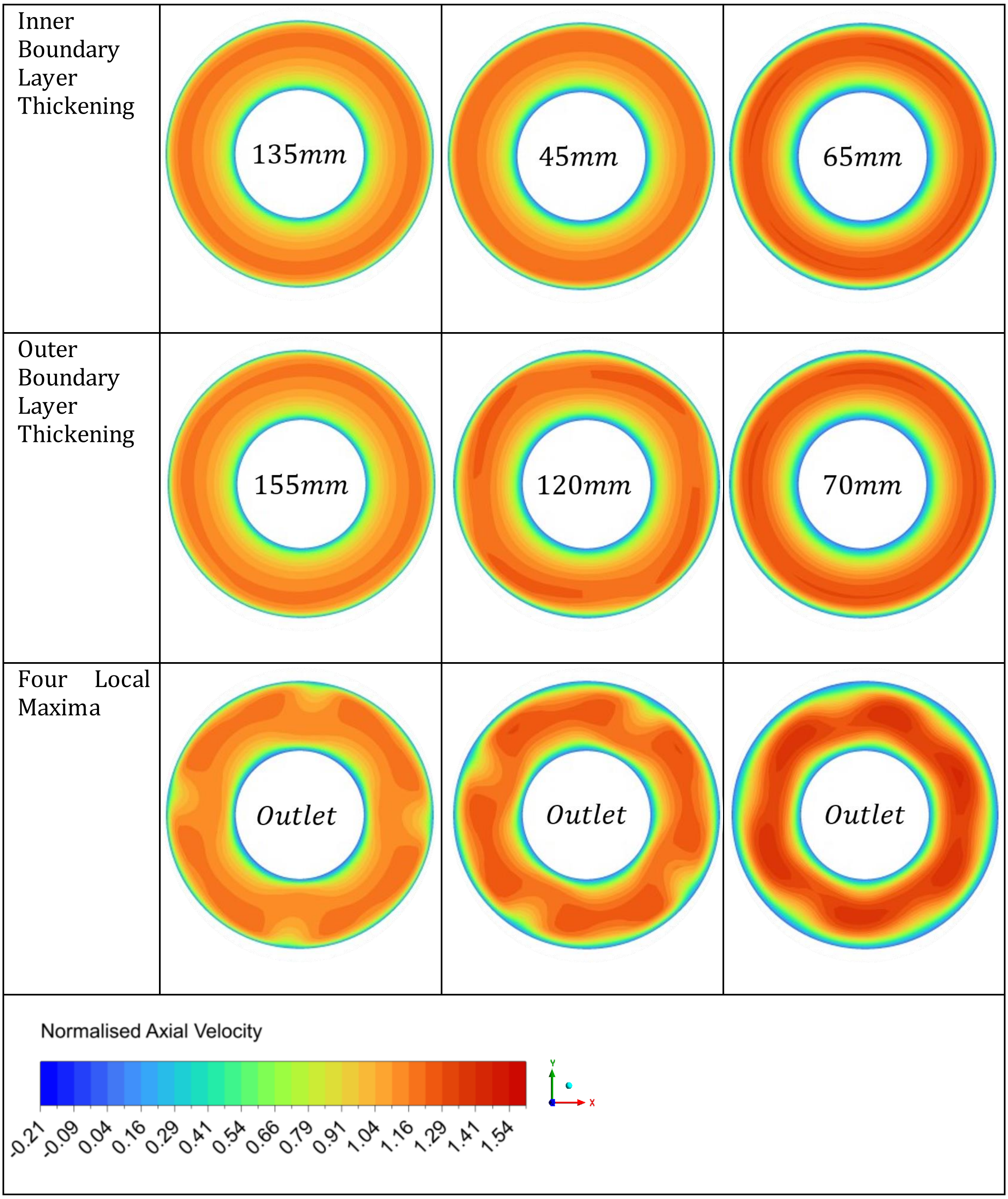

Figure 5.60: Heated cross-sectional contours of the normalised axial component in the case of SSC30.

Zones	4000	2000	1000
Beginning of Jet Impingement Effect	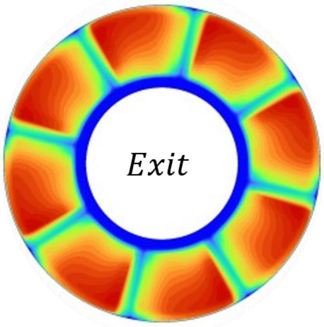	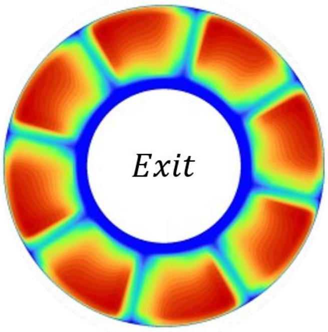	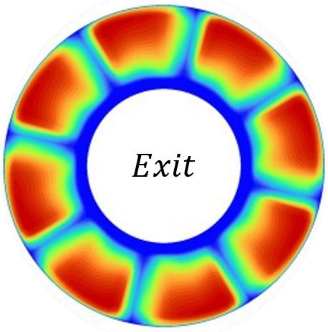
Thickening of the Inner Boundary Layers	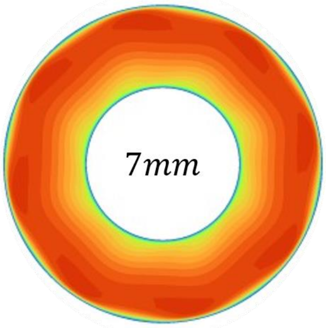	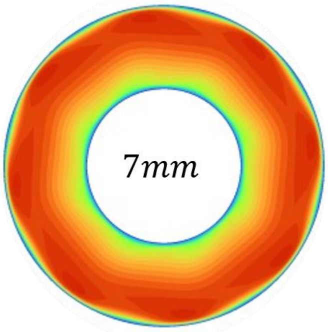	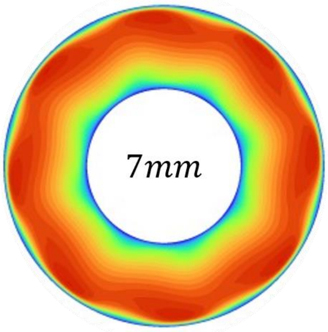
Uniform Distribution	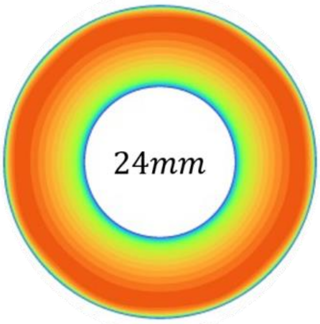	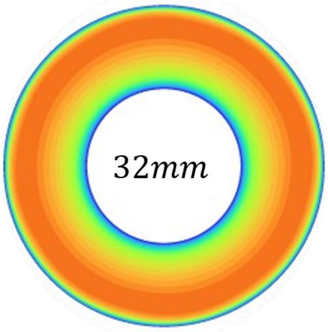	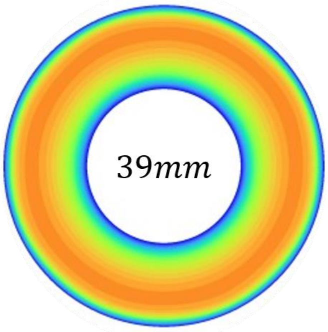
Swirl Free Flow	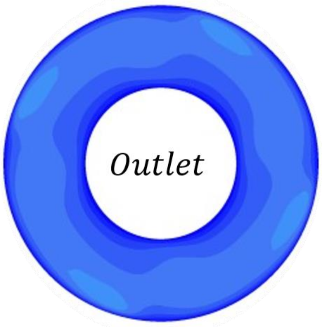	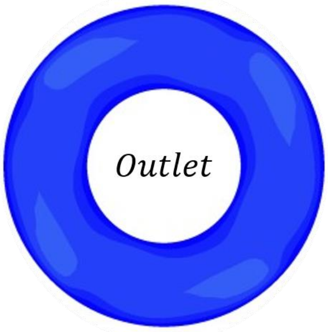	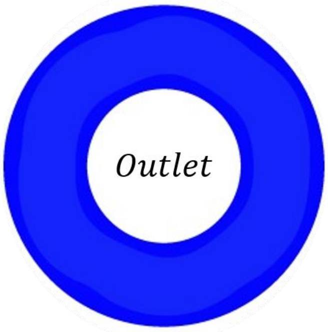

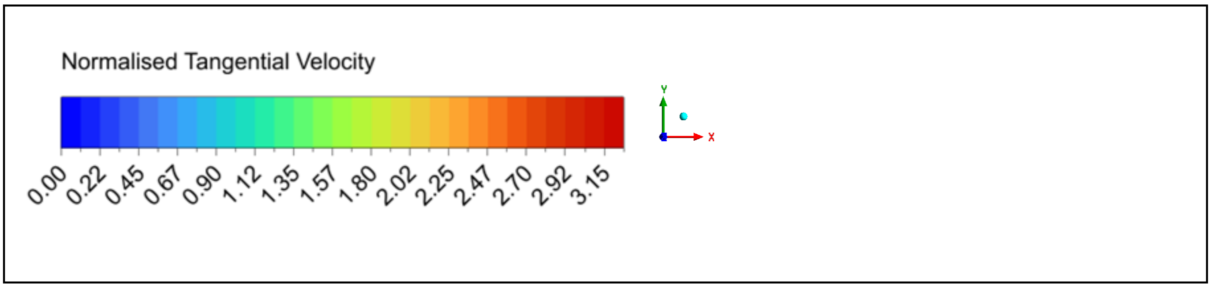

Figure 5.61: Heated cross-sectional contours of the normalised tangential component in the case of $SSC30$.

5.2.5.4 Swirl Angle Effect

Reducing the swirl angle decreased the swirl intensity at which the swirling flow exits the swirler. The results showed that the reduction in the swirl angle resulted in a shorter swirl decay cycle. Figure 5.62 shows that only two stages out of seven observed in the case of $SSC30$ were observed for $SSC60$ over the span of 950 mm when Re was 1000. The jet impingement effect was observed to dissipate at 695 mm ($\tilde{Z} = 75\%$) from the exit of the swirler. Development of the free swirling region took place, which continued until the outlet. However, from the results of the tangential component, it was deduced that the flow structure matching the free swirling zone in the case of $SSC30$, is the hydrodynamic development of the flow. In other words, the second stage that the results presented was of a nearly axial flow, as the tangential component nearly achieved complete decay ($\leq 10\%$) of the inlet velocity, demonstrating the terminal end of the swirl decay cycle.

As expected, increasing the inlet Reynolds number to 2000 and 4000 resulted in this second stage of the swirling cycle (i.e., complete decay) being pushed further downstream by 33% and 29%, respectively. This is typically the distinction between laminar and turbulent flows, where the development of the axial profile occurs sooner in the latter. At the outlet, in the case of $Re = 4000$, the axial component showed a more uniform development than that of $Re = 2000$. At higher Re, the inertial forces are stronger compared to the viscous forces. This helps overcome the viscous damping effect, promoting a more regular development of the normalised axial component. At lower Re, the stronger viscous forces may suppress instabilities in the flow but can also lead to thicker boundary layers near the walls. These effects, combined with the weaker swirl intensity compared to $SSC30$, led to the scenario where the axial flow encounters less disruption from secondary flows and viscous effects, resulting in the axial profile developing more regularly in the case of $SSC60\_4000$ compared to $SSC60\_2000$. Further support for these observations was provided by the results of the tangential component shown in Figure 5.63. It was seen that, even though the tangential component was higher at the specified locations, a more diffused structure was observed at $Re = 4000$, which was also reflected in the axial component.

Similar stages of the swirling cycle were observed in the case of the heated $SSC60$. Figure 5.64 and Figure 5.65 show the results of the normalised axial and tangential components, respectively. The distinguishable difference with the addition of heat was the significantly quicker development of the axial component. In the case of laminar swirling flow (i.e., $Re = 1000$), the jet effect dissipated 33% sooner than in the unheated case. Another situation showcasing the difference between turbulent and laminar axial component developments were the cases of $Re =$ 2000 and 4000, where the axial component developed quickly when $Re = 4000$ (at 685 mm) than that of $Re = 2000$ (at 700 mm).

Zones	4000	2000	1000
Start of Jet Effect	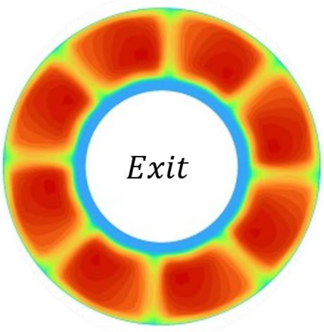	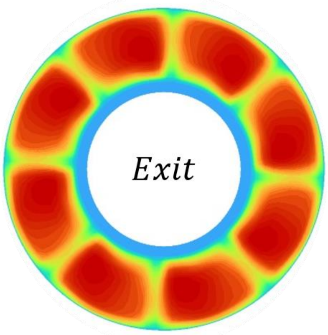	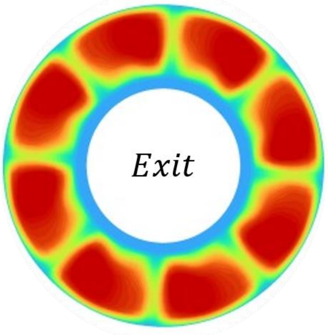
End of Jet Effect	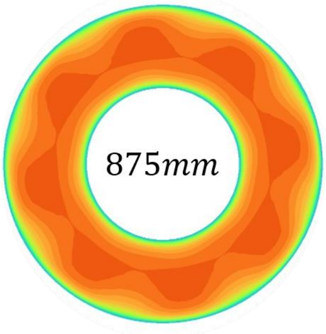	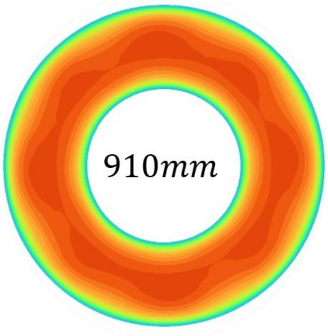	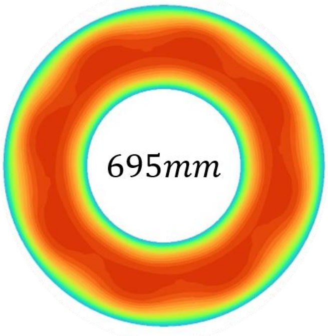
-	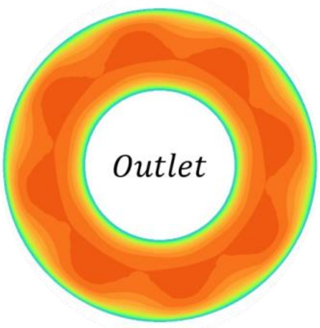	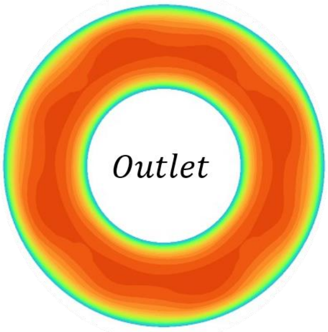	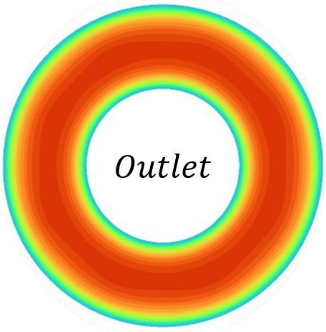
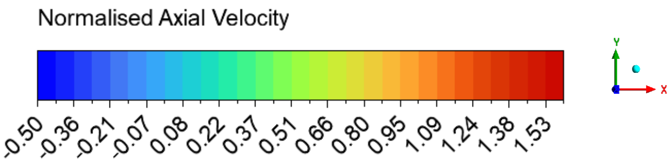			

Figure 5.62: Unheated cross-sectional contours of the normalised axial component in the case of SSC60.

Zones	4000	2000	1000
Start of Jet Effect	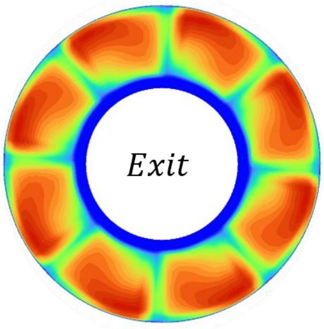	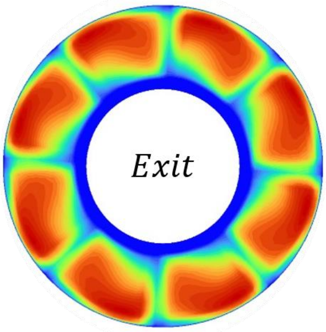	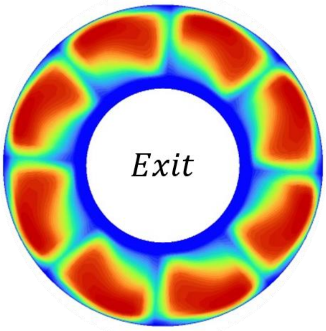
End of Jet Effect	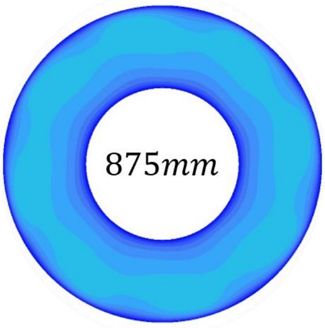	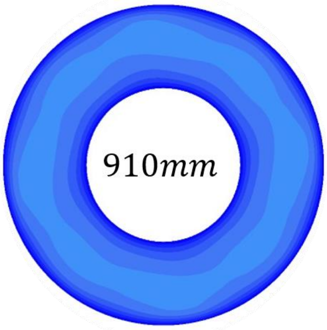	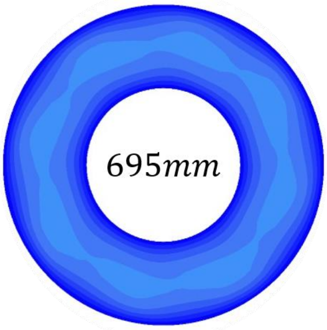
-	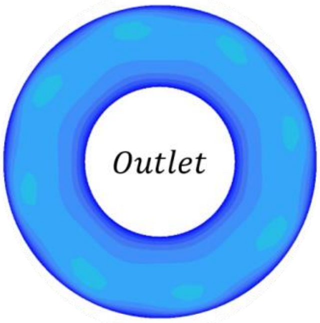	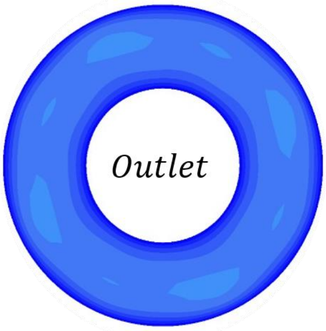	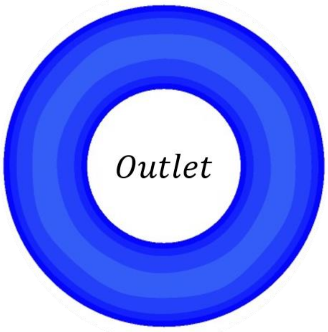

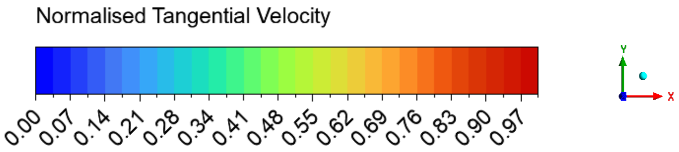

Figure 5.63: Unheated cross-sectional contours of the normalised tangential component in the case of SSC60.

Zones	4000	2000	1000
Start of Jet Effect	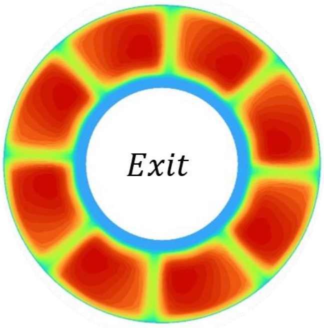	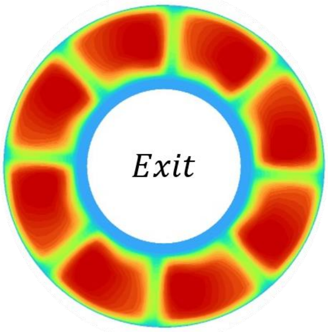	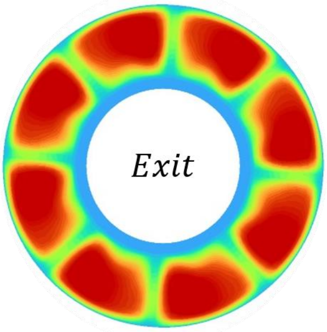
End of Jet Effect	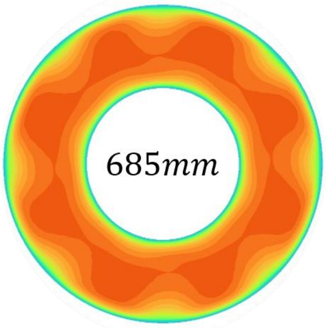	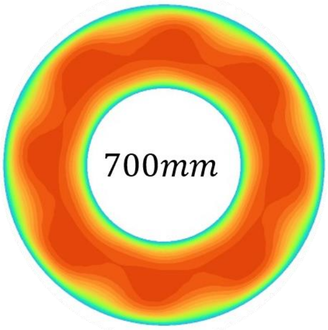	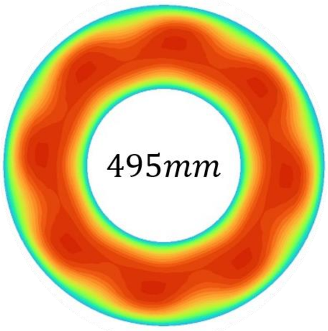
-	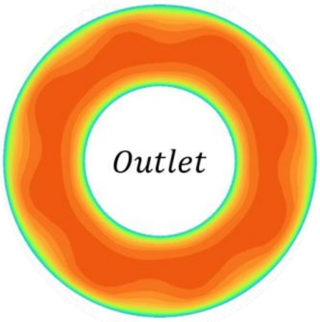	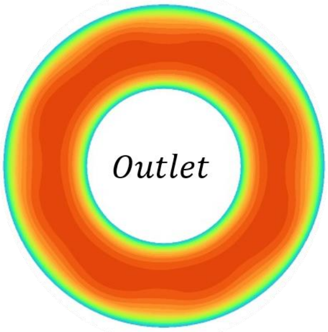	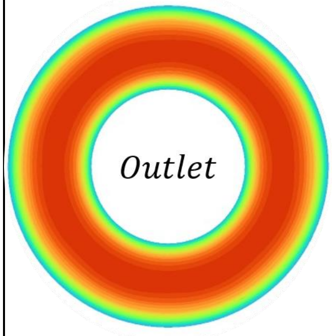
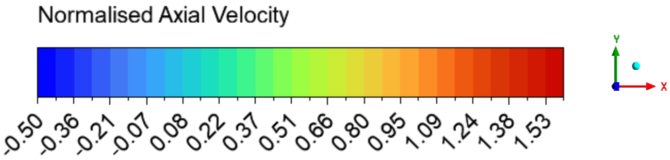			

Figure 5.64: Heated cross-sectional contours of the normalised axial component in the case of SSC60.

Zones	4000	2000	1000
Start of Jet Effect	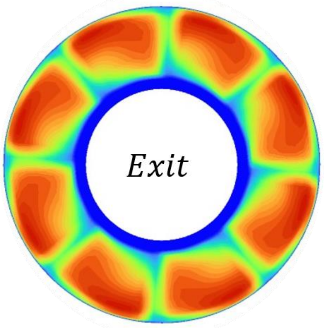	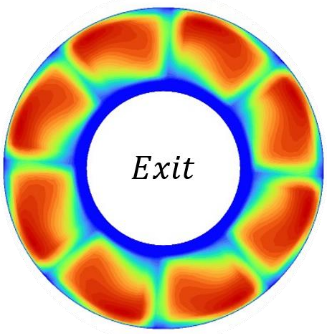	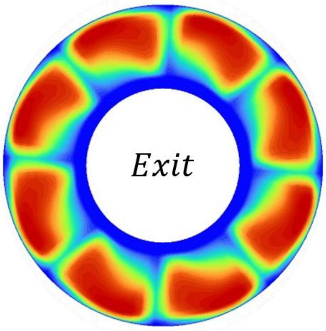
End of Jet Effect	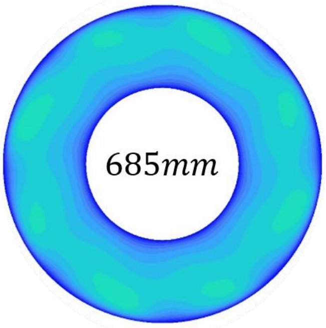	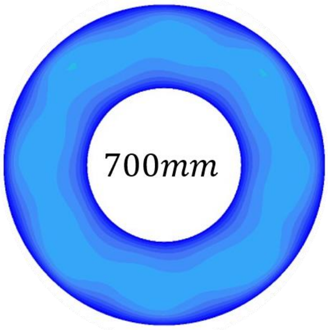	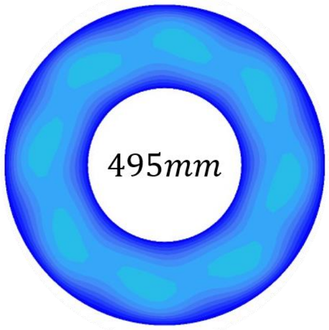
-	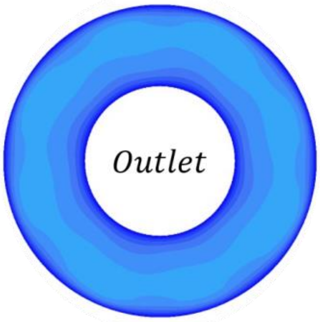	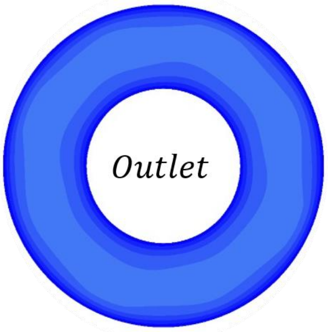	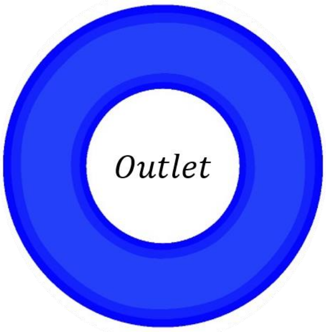
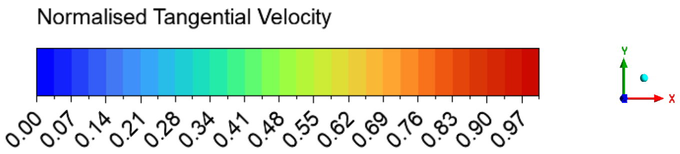			

*Figure 5.65: Heated cross-sectional contours of the normalised tangential component in the case of SSC*60.

5.2.6 Swirl Number

5.2.6.1 Unheated Swirl Number

After discussing the isolated behaviour of each velocity component, it is essential to study their combined effect. The swirl number is the parameter that quantifies this combined effect and provides researchers with a tool to measure the swirl intensity of the swirling flow. Since the cases of SSC consist of swirlers placed at the inlet of the annulus, producing swirl decaying flow, it is essential to define the intensity of the swirl flow at different locations downstream to correlate the influence of the swirl number against various parameters, including the heat transfer coefficient and friction factor. The swirl number has been defined in Section 4.2.3 above and was calculated using Eq. (4.7). Using the cross-sectional mass flow-averaged velocity components at several axial locations, the axial variation of the swirl number was calculated and is presented in Figure 5.66.

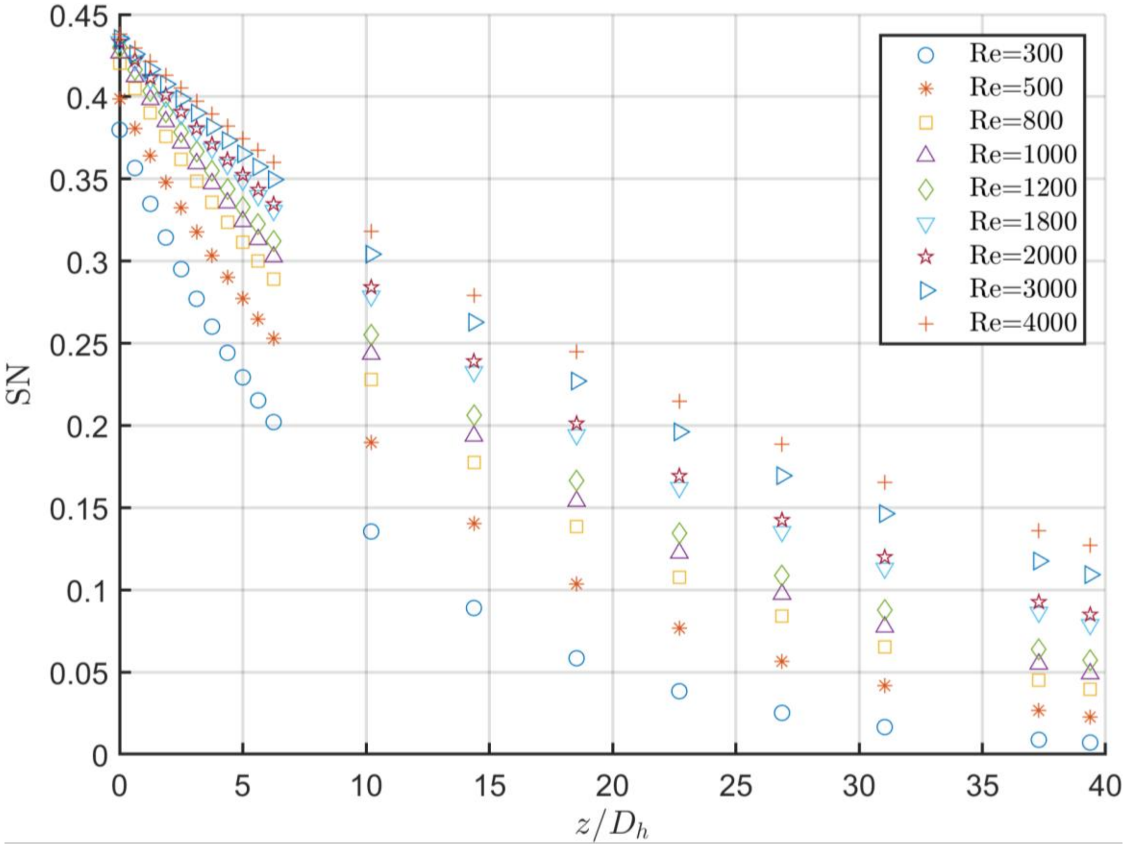

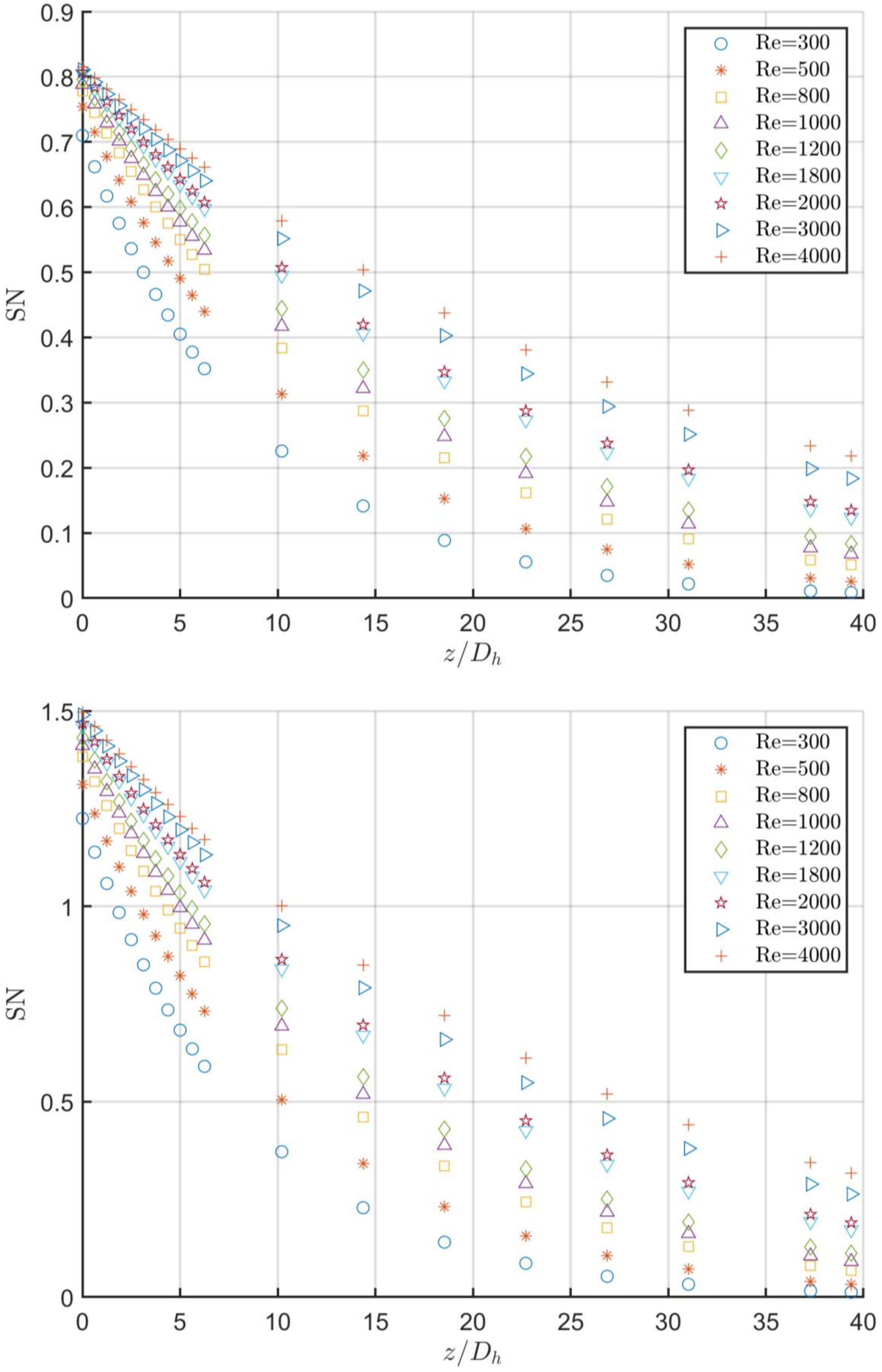

Figure 5.66: Unheated swirl number downstream for SSC60 (top), SSC45 (middle) and SSC30 (bottom).

The figure shows the swirl number produced by different combinations of swirl angle and Reynolds number. Observing the results from the plots, the swirl intensity decreases exponentially downstream. This agrees with the previous results of the velocity profiles, where the tangential component generated by the swirler vanes decayed as the flow progressed downstream. This decay occurs due to the viscous effects between fluid particles, which act as brakes on the tangential motion. When decay is complete, the flow becomes purely axial while continuing to develop hydrodynamically.

As expected, increasing Re resulted in higher swirl numbers, as shown in Figure 5.67. For $SSC60$, increasing Re from 1000 to 2000 caused the swirl number to rise. At the swirler exit, there was a modest 2% increase, which grew by 54% by the annulus outlet. Further increasing Re to 4000 showed diminished returns, only 1% initial growth at the exit, reaching a maximum 15% increase downstream.

Similar trends appeared for other angles. $SSC45$ showed increases from 2% to 66% when Re doubled to 2000, with further doubling yielding 17% maximum gain. $SSC30$ followed this pattern with 70% and 18% maximum increments at $Re = 2000$ and 4000, respectively.

Reducing θ_{sw} increased initial swirl intensity at the swirler exit. Figure 5.68 reveals despite different starting intensities, swirl numbers decay to similar values at the same downstream locations when Re is constant. This demonstrates that decay location is independent of swirl angle for a given Re.

The convergence occurs because higher angles experience faster decay rates, offsetting their initial intensity advantage. Lines A and B in the figure visually track where different angle plots converge for each Re, clearly illustrating this phenomenon.

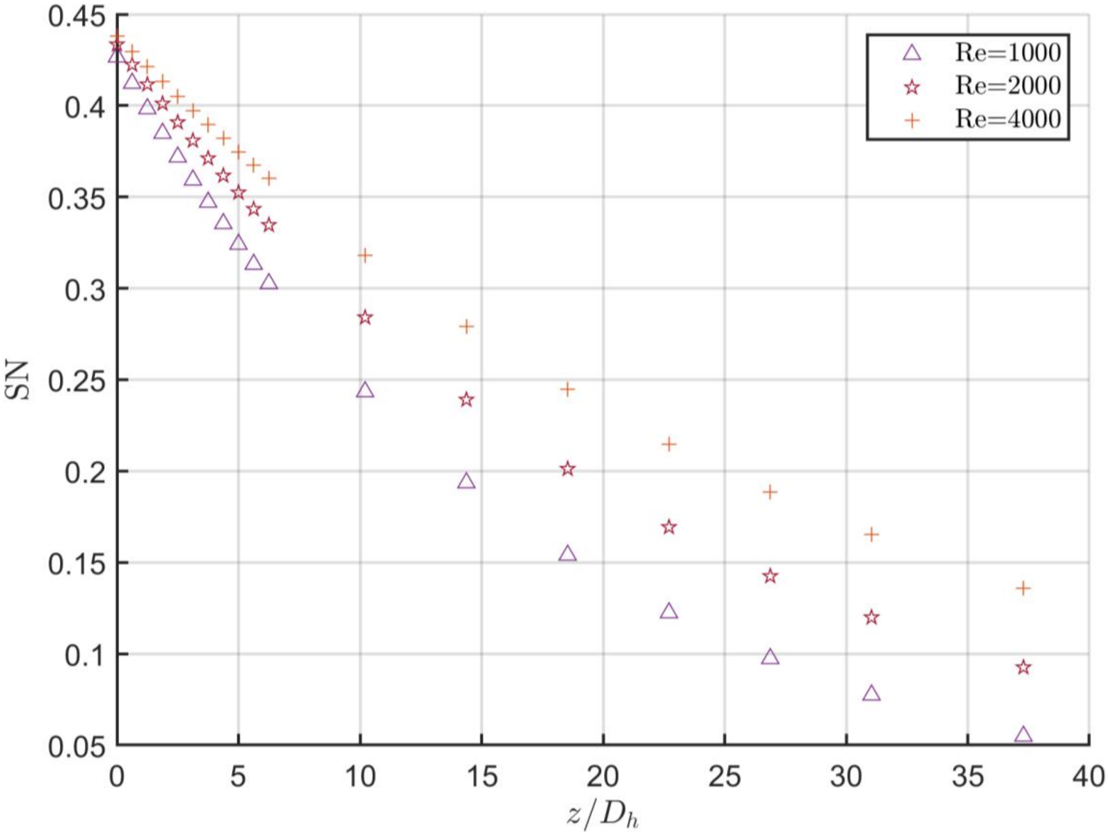
0.45
0.4
0.35
0.3
0.25
0.2
0.15
0.1
0.05
SN
0
5
10
15
20
25
30
35
40
z/D_h
Re=1000
Re=2000
Re=4000

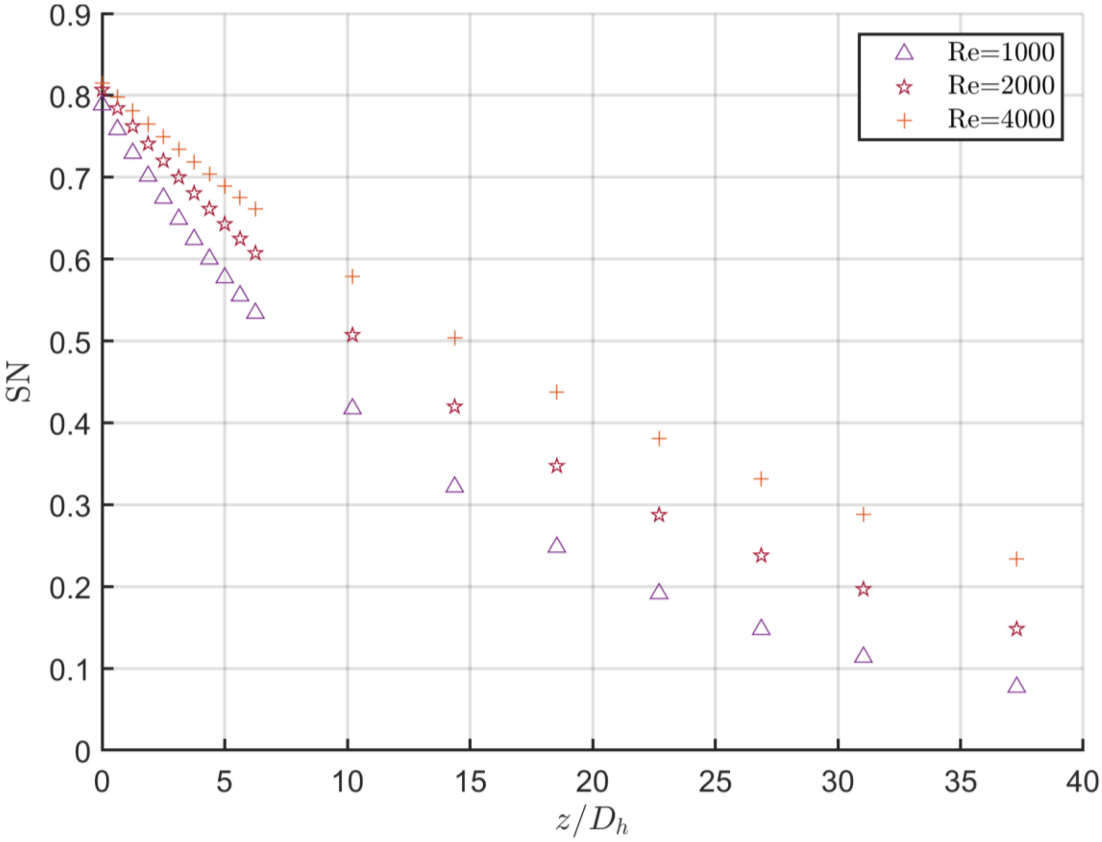
0.9
0.8
0.7
0.6
0.5
0.4
0.3
0.2
0.1
0
SN
0
5
10
15
20
25
30
35
40
z/D_h
Re=1000
Re=2000
Re=4000

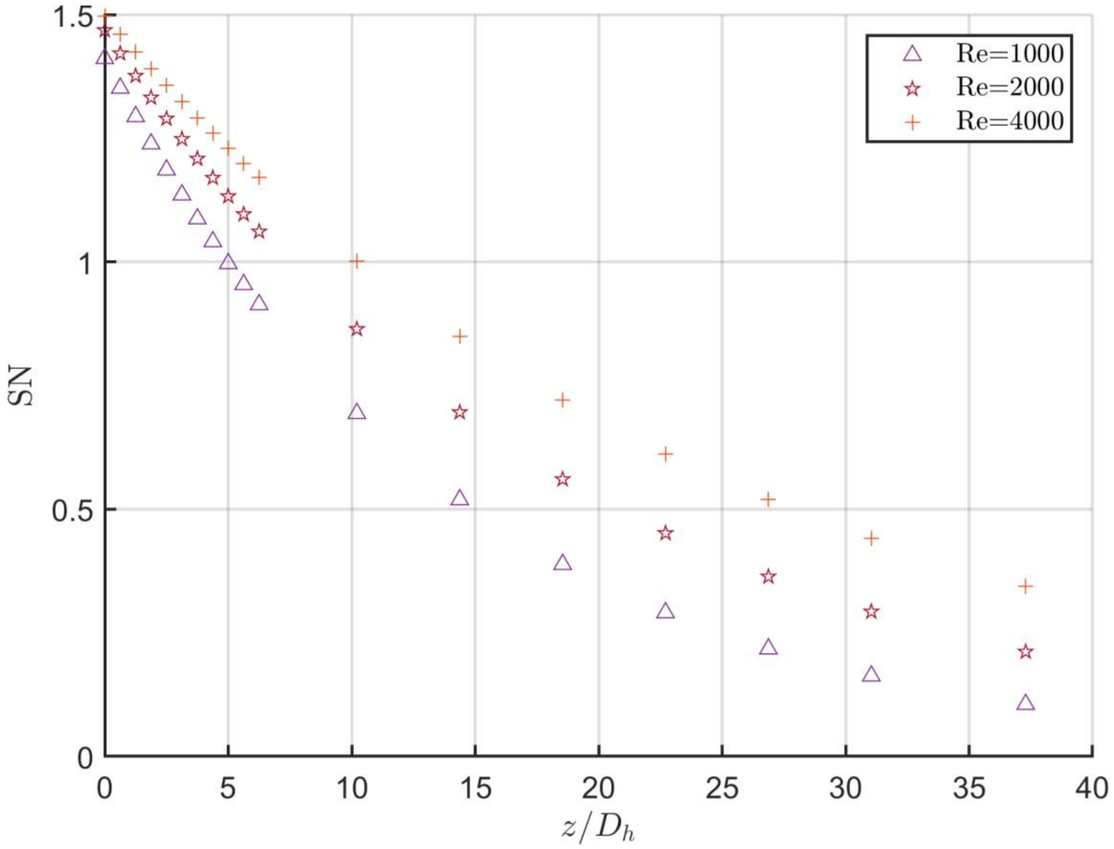

Figure 5.67: Comparison of swirl number when scaling Reynolds number with respect to each swirl angle in the case of the unheated annulus. SSC60 (top), SSC45 (middle) and SSC30 (bottom).

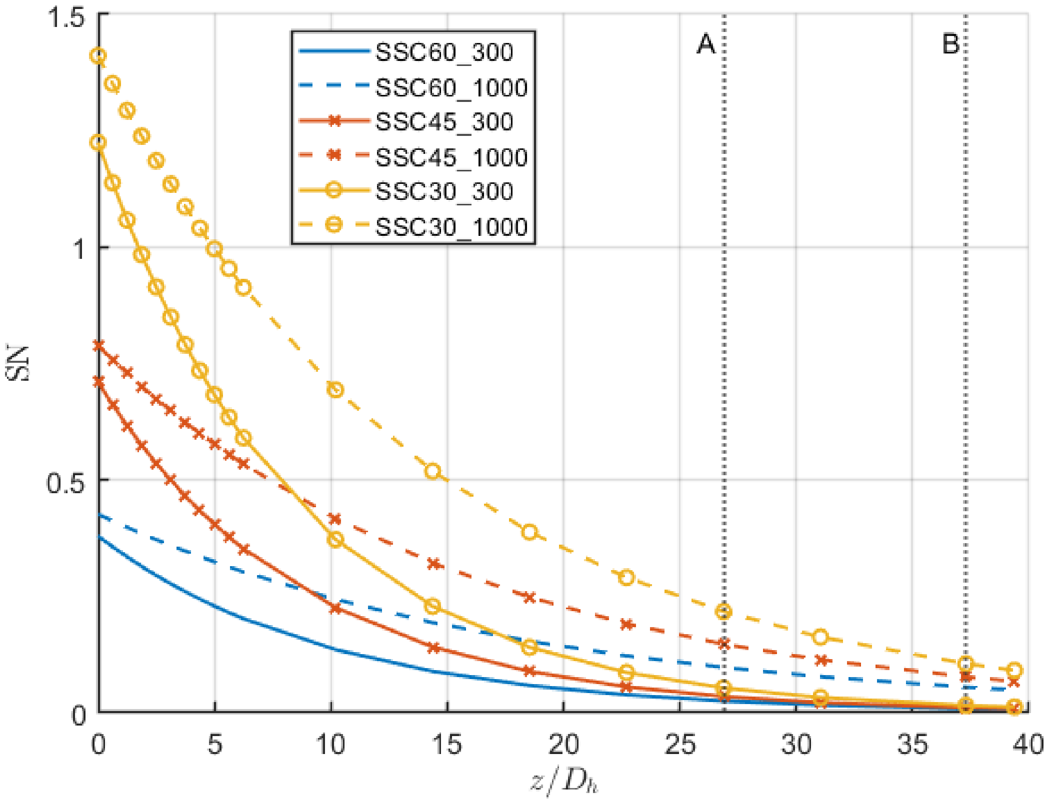

Figure 5.68: Comparison of unheated swirl number produced by the three swirlers when Re=300 and 1000.

From the swirl number results, the following equations listed in Table 5.1 were derived using the generalised reduced gradient [150] method offered by a commercial data-analysing software (Microsoft Excel) to optimise the lines of best fit. It is apparent from the aforementioned plots that the functions are in the format:

$$SN = SN_0 e^{-\beta \frac{z}{D_h}} \tag{5.3}$$

SN_0 and β are coefficients defining the initial swirl number and decay rate at each combination of Re and θ_{sw}, respectively. z/D_h is used to define the dimensionless axial location of the flow, to remain consistent with the function suggested by Seeno et al. [151], Halsey [152], Li et. al. [153], Reader-Harris [154], and Steenbergen et. al. [57]. SN_0 was observed to increase with decreasing θ_{sw} indicating a stronger initial swirl. β decreases with increasing Re for all three SSCs, which implies a slower decay of SN. From the table, it was interesting to note that SN_0 remained constant (at 0.4 to 1 d. p.) at all Re values in the case of $SSC60$. This suggests that the initial swirl generated is independent of Re within the investigated range. A slightly similar observation was seen in the case of $SSC45$ for $Re \geq 500$ and $SSC30$ for $Re \geq 1800$. Add, as Re increased, the coefficients became more consistent for all swirl angles. This suggests a possible convergence of the swirl number at higher Re values. A reasonable method to calculate these values was to use the functions developed by $SSC30$. The selected angle was based on the delayed convergence of this configuration compared to the rest. Table 5.2 shows the calculated values of the normalised axial location at which the swirl number has completely decayed to 0.001. In the table, it can be seen that defining the axial location based on $SSC30$ was suitable, where the SN of both $SSC60$ and $SSC45$ was relatively equivalent to 10^{-3}. From the function, it can be deduced that the SN is not binary, where it can be evaluated at zero due to inherent flow characteristics. It can only decrease to minimal values, but no cut-off value can be set. Therefore, for every application, the designers set their assumptions where the value of the swirl number no longer has an effect on the performance or the output.

Table 5.1: Unheated swirl number decay functions at different swirl angles and Reynolds numbers.

Re	θ_{sw}		
	60°	45°	30°
300	$0.380e^{-0.101\frac{z}{D_h}}$	$0.710e^{-0.112\frac{z}{D_h}}$	$1.225e^{-0.117\frac{z}{D_h}}$
500	$0.399e^{-0.073\frac{z}{D_h}}$	$0.754e^{-0.086\frac{z}{D_h}}$	$1.312e^{-0.094\frac{z}{D_h}}$
800	$0.420e^{-0.060\frac{z}{D_h}}$	$0.778e^{-0.069\frac{z}{D_h}}$	$1.383e^{-0.076\frac{z}{D_h}}$
1000	$0.427e^{-0.055\frac{z}{D_h}}$	$0.788e^{-0.062\frac{z}{D_h}}$	$1.411e^{-0.070\frac{z}{D_h}}$
1200	$0.430e^{-0.051\frac{z}{D_h}}$	$0.796e^{-0.057\frac{z}{D_h}}$	$1.431e^{-0.065\frac{z}{D_h}}$
1800	$0.433e^{-0.043\frac{z}{D_h}}$	$0.805e^{-0.048\frac{z}{D_h}}$	$1.462e^{-0.054\frac{z}{D_h}}$
2000	$0.433e^{-0.041\frac{z}{D_h}}$	$0.807e^{-0.046\frac{z}{D_h}}$	$1.468e^{-0.052\frac{z}{D_h}}$
3000	$0.435e^{-0.035\frac{z}{D_h}}$	$0.811e^{-0.038\frac{z}{D_h}}$	$1.490e^{-0.044\frac{z}{D_h}}$
4000	$0.438e^{-0.031\frac{z}{D_h}}$	$0.815e^{-0.034\frac{z}{D_h}}$	$1.497e^{-0.039\frac{z}{D_h}}$

Table 5.2: List of locations where $SN = 0.01$ for all three swirl angles at constant inlet Re.

Re	300	500	800	1000	1200	1800	2000	3000	4000
$\left(\frac{z}{D_h}\right)_{SSC30}$	60.9	57.1	72.2	81.8	88.1	110.3	115.7	138.7	153.6
SN_{SSC60}	0.0008	0.0015	0.0014	0.0013	0.0013	0.0013	0.0012	0.0012	0.0012
SN_{SSC45}	0.0008	0.0010	0.0011	0.0011	0.0013	0.0013	0.0013	0.0015	0.0016

5.2.6.2 Heated Swirl Number

The effect of heat transfer across the inner wall of the annulus resulted in the heated SN functions listed in Table 5.3. In comparison to the unheated functions, it was found that β achieved higher values across all cases. This indicated a faster rate of decay of the swirl number downstream from the swirlers. This variation is the outcome of several factors discussed in Section 5.2.5.3. The initial swirl number remained nearly constant for all Reynolds numbers. Nevertheless, Figure 5.69 showed a decrease in the swirl number when heat was introduced, averaging 22% and 11% for $SSC30\_300$ and $SSC30\_1000$ and 25% and 6% for $SSC60\_300$ and $SSC60\_1000$, when compared to their unheated cases, respectively. The decreased swirl number can be related to the reduced viscosity, which allows the flow to increase its velocity near the walls. This, in turn, results in a faster axial component, reducing the calculated swirl number and hence increasing the rate of decay, as the full decay of swirling flow is primarily affected by the Reynolds number.

Similar to the unheated case, the full decay of the swirling flow takes place at relatively the same axial location, and a trend of convergence was observed with increasing Reynolds number.

Table 5.3: Heated swirl number decay functions at different swirl angles and Reynolds numbers.

Re	θ_{sw}		
	60°	45°	30°
300	$0.400e^{-0.133\frac{z}{D_h}}$	$0.693e^{-0.130\frac{z}{D_h}}$	$1.184e^{-0.132\frac{z}{D_h}}$
500	$0.405e^{-0.087\frac{z}{D_h}}$	$0.747e^{-0.095\frac{z}{D_h}}$	$1.281e^{-0.102\frac{z}{D_h}}$
800	$0.428e^{-0.069\frac{z}{D_h}}$	$0.781e^{-0.076\frac{z}{D_h}}$	$1.357e^{-0.085\frac{z}{D_h}}$
1000	$0.438e^{-0.063\frac{z}{D_h}}$	$0.792e^{-0.068\frac{z}{D_h}}$	$1.389e^{-0.077\frac{z}{D_h}}$
1200	$0.444e^{-0.059\frac{z}{D_h}}$	$0.801e^{-0.063\frac{z}{D_h}}$	$1.410e^{-0.072\frac{z}{D_h}}$
1800	$0.449e^{-0.050\frac{z}{D_h}}$	$0.818e^{-0.052\frac{z}{D_h}}$	$1.449e^{-0.060\frac{z}{D_h}}$
2000	$0.449e^{-0.048\frac{z}{D_h}}$	$0.821e^{-0.049\frac{z}{D_h}}$	$1.457e^{-0.057\frac{z}{D_h}}$
3000	$0.449e^{-0.040\frac{z}{D_h}}$	$0.831e^{-0.041\frac{z}{D_h}}$	$1.481e^{-0.048\frac{z}{D_h}}$
4000	$0.452e^{-0.036\frac{z}{D_h}}$	$0.837e^{-0.036\frac{z}{D_h}}$	$1.490e^{-0.043\frac{z}{D_h}}$

In summary, the exponential function accurately describes the decaying behaviour of the induced swirl flow downstream in the annulus. The decay rate has been shown to be influenced by both Re and θ_{sw}. Furthermore, the addition of heat to the annulus affected both the initial swirl number and the decay rate, but the complete decay of the swirling flow is independent of both swirl angle and heat transfer effects.

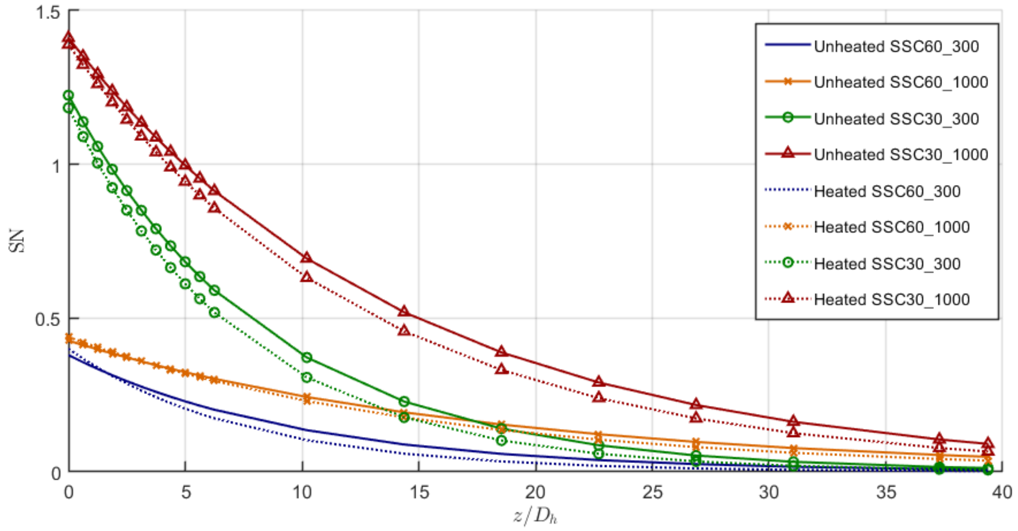

Figure 5.69: Comparison between unheated and heated swirl numbers.

5.2.6.3 Decay Rate Correlation

As discussed earlier in the literature (section 2.3), the rate of decay has been a major parameter of discussion. Although not the only parameter contributing to the decay of the swirl number generated at the exit of the swirlers [51], this parameter has been proven to be the most effective in providing a reasonable predictive model for the decaying behaviour of the swirl flow generated. As per the definition of the decay rate [55], a correlation of the rate of decay is to be defined in terms of f.

For the current augmentation method investigated, the relationship between β and f is presented in Figure 5.70. Similar to the relationship found in the literature, a linear relationship can be observed. The function for each of the $SSC60$, $SSC45$ and $SSC30$ was $0.38f$, $0.41f$, and $0.39f$ in the unheated case, and $0.40f$, $0.39f$, and $0.38f$ in the heated case. The average correlation was found to be:

$$\beta = (0.39 \pm 0.02)f \tag{5.4}$$

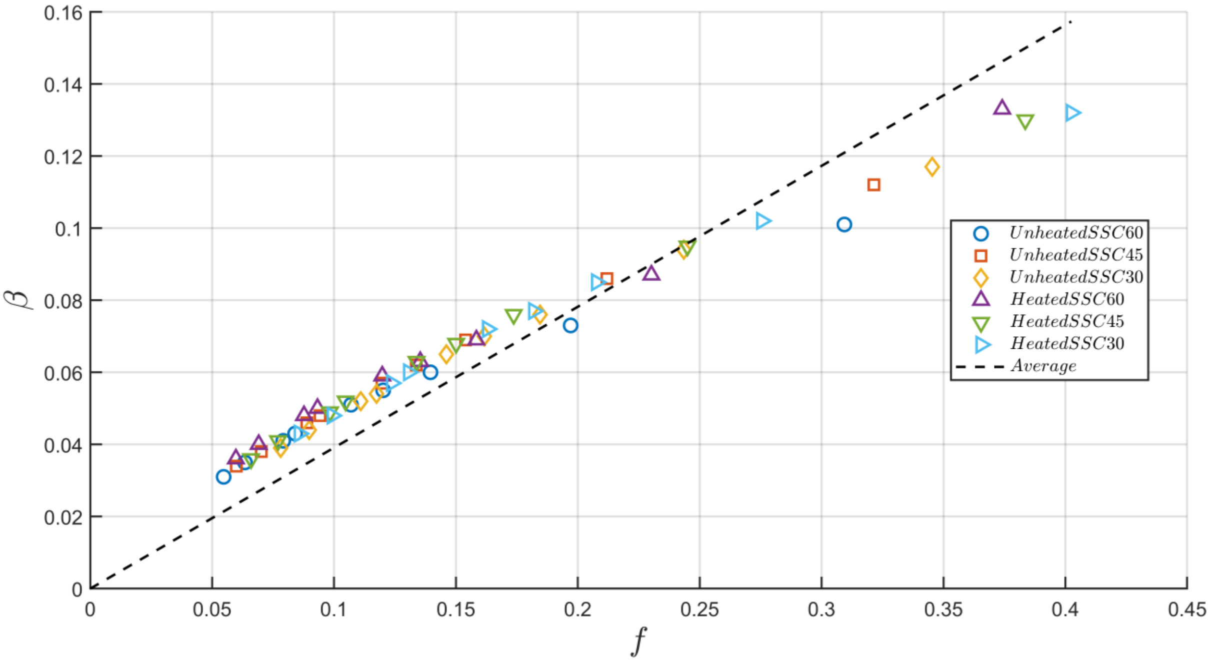

Figure 5.70: Variation of rate of decay of swirl number with friction for all swirl angles under unheated and heated annuli.

5.2.6.4 Swirl Number Effect on Temperature

To observe the variation of the normalised temperature of the cold flow as the swirl number decays, temperature contours are presented in Figure 5.71. The normalised temperature was calculated using:

$$\tilde{T} = \frac{T - T_{a,inlet}}{T_m - T_{a,inlet}} \tag{5.5}$$

T_m and $T_{a,min}$ refer to the maximum and minimum evaluated in the annular domain, respectively. his equation takes into account the different maximum temperatures achieved at different inlet Reynolds numbers and swirl angles. Having such a denominator was deemed better than having $(T_{h,inlet} - T_{c,inlet})$, as a smaller denominator would provide better sensitivity to present any changes in temperature around the cross-section. It was observed that at the exit of the swirler, a non-uniform distribution of temperature near the inner wall was evident due to the presence of recirculation zones attached to the walls of the swirlers. 5 mm downstream, the recirculation zones had dissipated, and the temperature was regularly distributed circumferentially. It should be noted that this is at the peak of the swirl number decay rate. Slow and regular growth of the thermal boundary layer was observed until 295 mm. Then, cyclic thickening of the boundary layers was observed as the decay rate decreased, and the annular free stream temperature began to heat up. By 535 mm, the temperature rise had reached the outer wall of the annulus, resulting in an overall rise of 4% – 5% in the free stream temperature radially inwards (4% being at the outer wall). At 545 mm, another cyclic increase in the thermal boundary layer thickness was observed. Non-uniformity of the temperature distribution was directly observed. Finally, another increase in the free stream temperature took over the annular region at a range of 7% – 10% radially inwards. Downstream, less temperature was retained, with a more rapid growth of the boundary layer. This is justified by two primary factors: the decreasing decay rate of the swirl number as the flow turned more axial, and the annular flow approaching the heat source at the inlet of the hot domain. At a higher rate of decay, the temperature retention lasted for a longer distance. As the rate of decay decreased downstream, temperature retention also decreased, indicating a faster rate of thermal boundary layer growth.

The effect of the Reynolds number can be observed in Figure 5.72. A reduction in the Reynolds number resulted in a more apparent non-uniform distribution around the inner wall of the annulus at the exit of the swirler. The recirculation zone had a more noticeable effect compared to when Re was 4000. This relates back to the breakdown of the recirculation zone discussed previously in Section 5.2.2.2. The effect of the recirculation zone did not seem to exist beyond $5mm$ for all cases. Similarly, the temperature then showed a uniform distribution. A uniform expansion started at 5 mm. The non-uniform cyclic growth of the boundary layer commenced 68% and 81% earlier in the cases of $Re = 2000$ and 1000, respectively, when compared to 4000. A full rise in the free stream temperature was observed at 545 mm and 665 mm, of about $4\% - 6\%$ radially inwards. It was observed that the rise in free stream temperature was more uniform in turbulent flow. As the flow became more laminar, the temperature distribution became more rapid in the radial direction. Concurrently, the increase in free stream temperature was found to have commenced earlier as the thermal boundary layers grew uniformly outward. The temperature rise achieved as the annular flow approached the hot inlet was higher than that when Re was 4000.

A reduction in Re was reflected in the turbulence intensity in the flow, and while the θ_{sw} was constant, the swirl intensity was also reduced. This led to lower turbulence and a reduced radial pressure gradient [155] in the flow, resulting in less mixing. This, in turn, increased water retention in a single annular region, resulting in less diffusion of heat throughout the annular domain, causing less temperature retention throughout the fluid downstream from the swirler. This was primarily caused by the weaker swirling intensity, which had a much higher rate of decay (of 30%), which led to less resistance to the rise of the free stream temperature in the annulus, producing a more rapid temperature gradient.

In Figure 5.73, $SSC60$ was observed to be exposed to a higher level of temperature near the inner wall of the annulus compared to $SSC45$ and $SSC30$ (by about 10% and 19%, respectively). Additionally, thickening of the boundary layers took place in more regions circumferentially, indicating weaker resistance to thermal growth at weaker swirling intensity due to less mixing. At $z/D_h = 12.5$, $SSC30$ showed an irregularity in the growth of its cross-sectional boundary layers. This was suggested to be the combined effect of two factors: 1) The resistance to thermal increment was still maintained in some regions, as swirl intensity is relatively higher than at other angles at the same Re. 2) The higher rate of decay resulted in a significant pressure gradient, causing irregular growth in the free stream temperatures. Nevertheless, this resistance was observed to continue downstream until the outlet of the annulus. Meanwhile, $SSC60$ presented similar behaviour in thermal boundary growth to that of a plain annulus. It should be noted that the swirling flow demonstrated its resistance in the direction of increasing temperature in the tube (i.e., approaching the heat source in the $DPHE$).

The growth of the boundary layers was observed to commence slightly further downstream (at $z/D_h = 16.7$ instead of 12.5) for $SSC30$ and $SSC45$ as Re was doubled, as shown in Figure 5.74. However, $SSC60$ seemed to remain unaffected in terms of thermal growth structure. Yet, the temperature near the inner wall decreased as Re increased for all angles. This is a reasonable deduction due to the relatively insignificant decrease in the decay rate. Furthermore, the thermal boundary layers grew faster for $SSC30$, then $SSC45$, followed by $SSC60$, suggesting weaker resistance for higher swirling intensity. However, this was due to the higher rate of decay because, as SN converged for all angles, the resistance was observed to be still higher at the outlet.

Similar behaviours were observed at $Re = 4000$ in Figure 5.75. An interesting behaviour was presented by $SSC45$, with an irregularity observed in the development of the boundary layers. Since this was not seen at lower Re (i.e., weaker swirl intensities), it was suggested that the intensity achieved at $Re = 4000$ was high enough to show significant resistance to the development of the boundary layers, adopting a similar behaviour to that observed in $SSC30$ when Re was 1000. The development remained consistent for $SSC60$ for the range investigated. However, it is reasonable to predict that at a certain Re, the swirl intensity would be high enough to demonstrate this irregularity, showing significant resistance to thermal development.

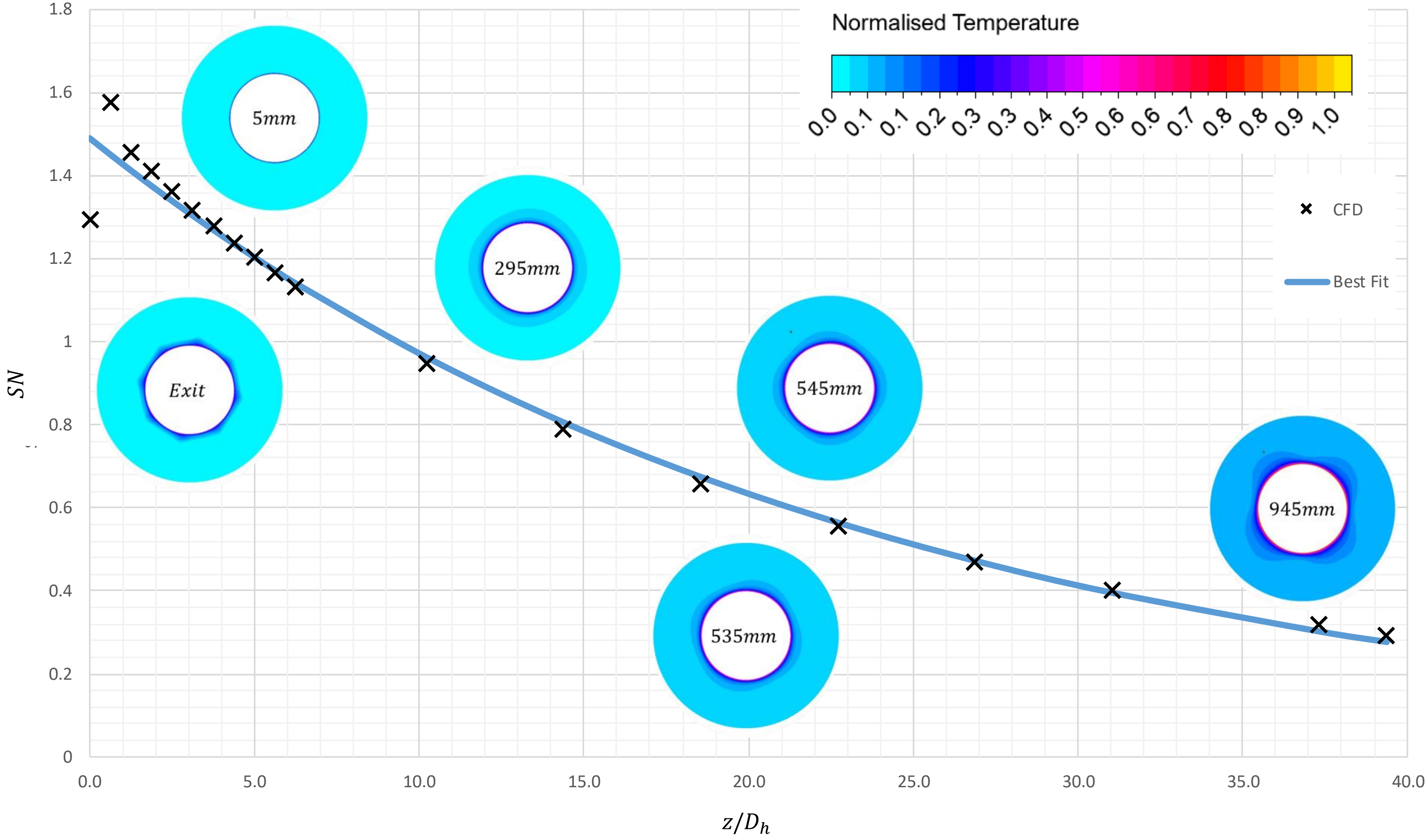

Figure 5.71: Swirl number calculated results (marked with a cross) and best fitted curve and normalised temperature contours.

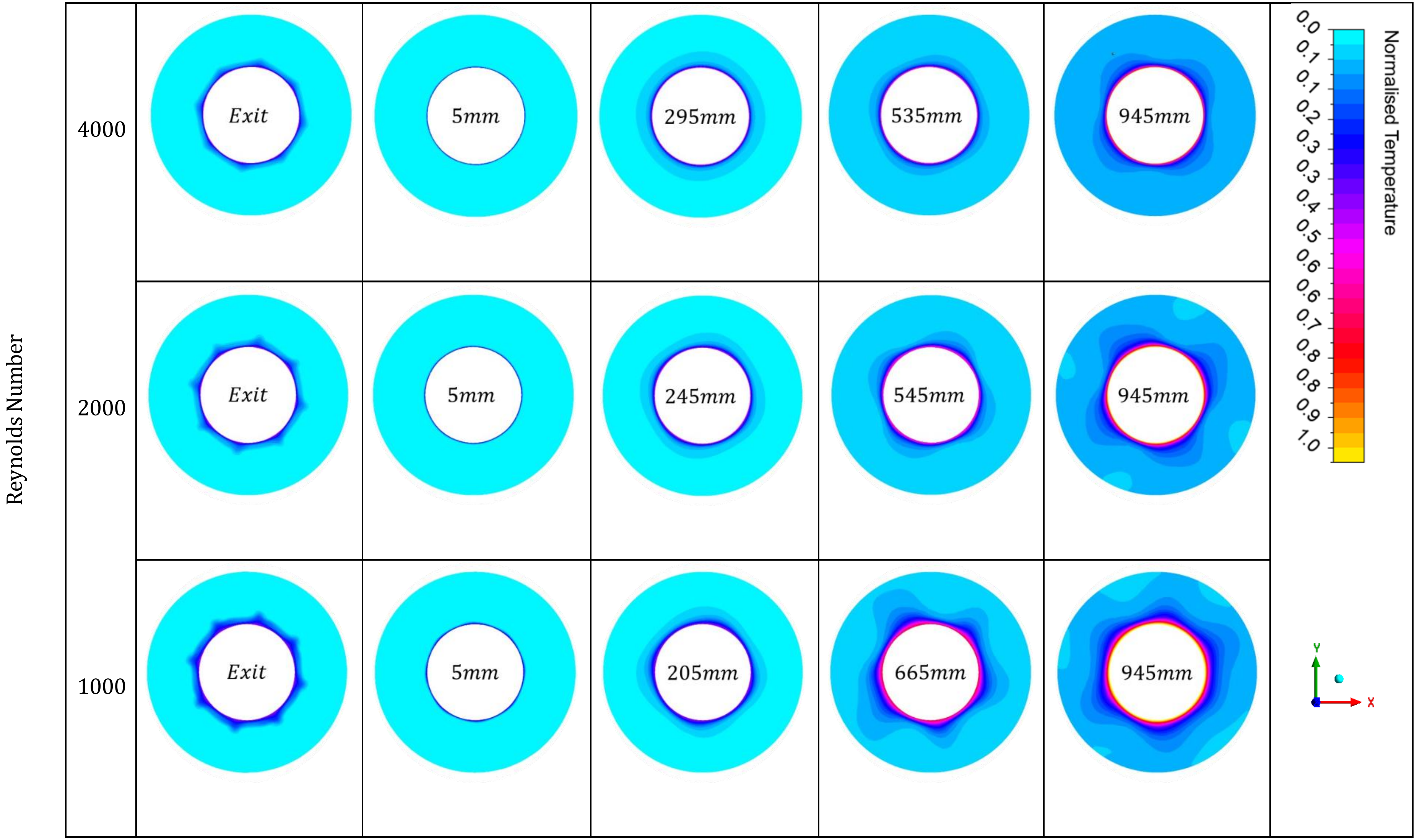

Figure 5.72: Cross-sectional contours of normalised temperature in the case of $SSC30$ when $Re = 1000, 2000$ and 4000.

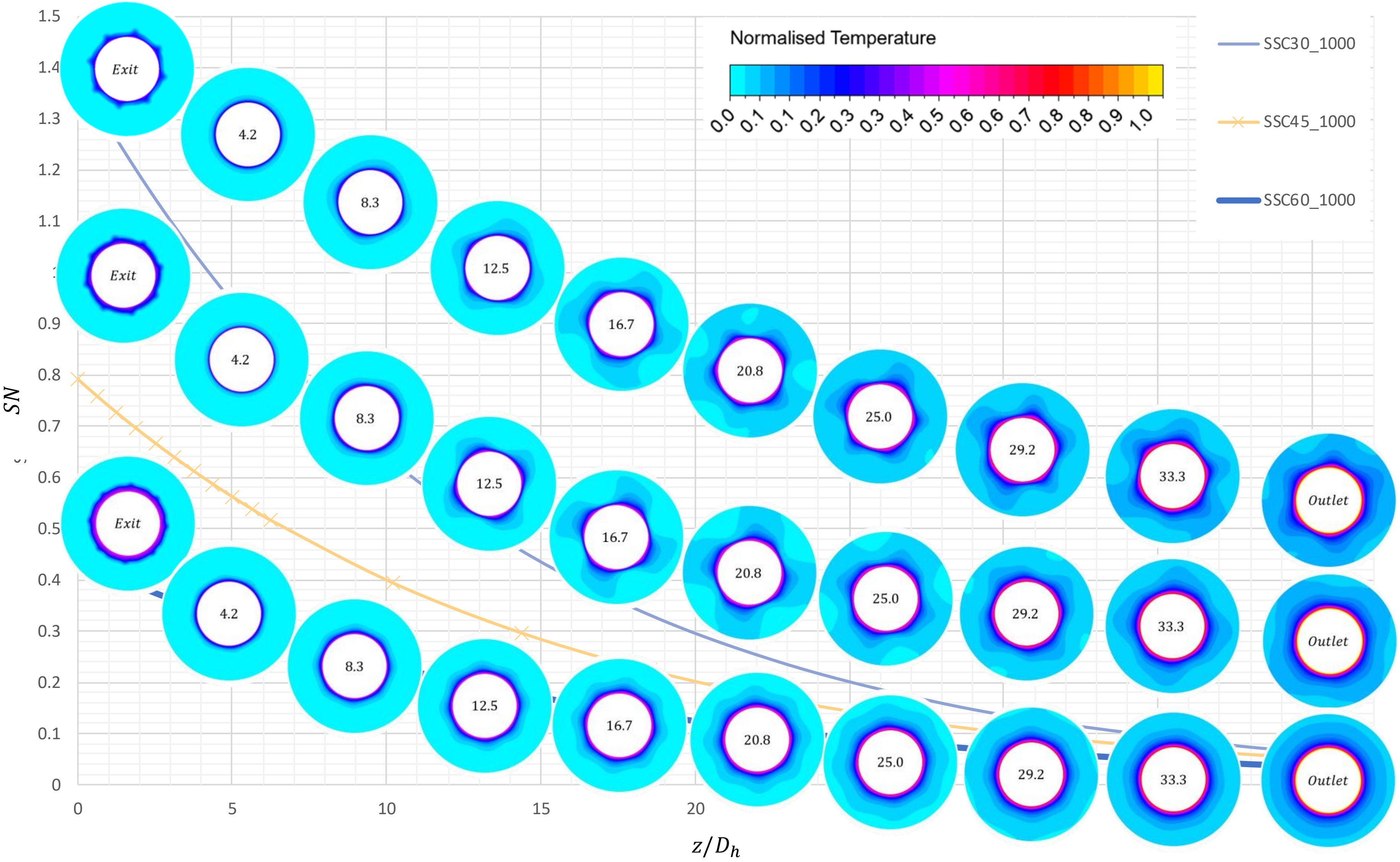

Figure 5.73: Variation of cross-sectional temperature distribution for three swirl angles at $Re = 1000$

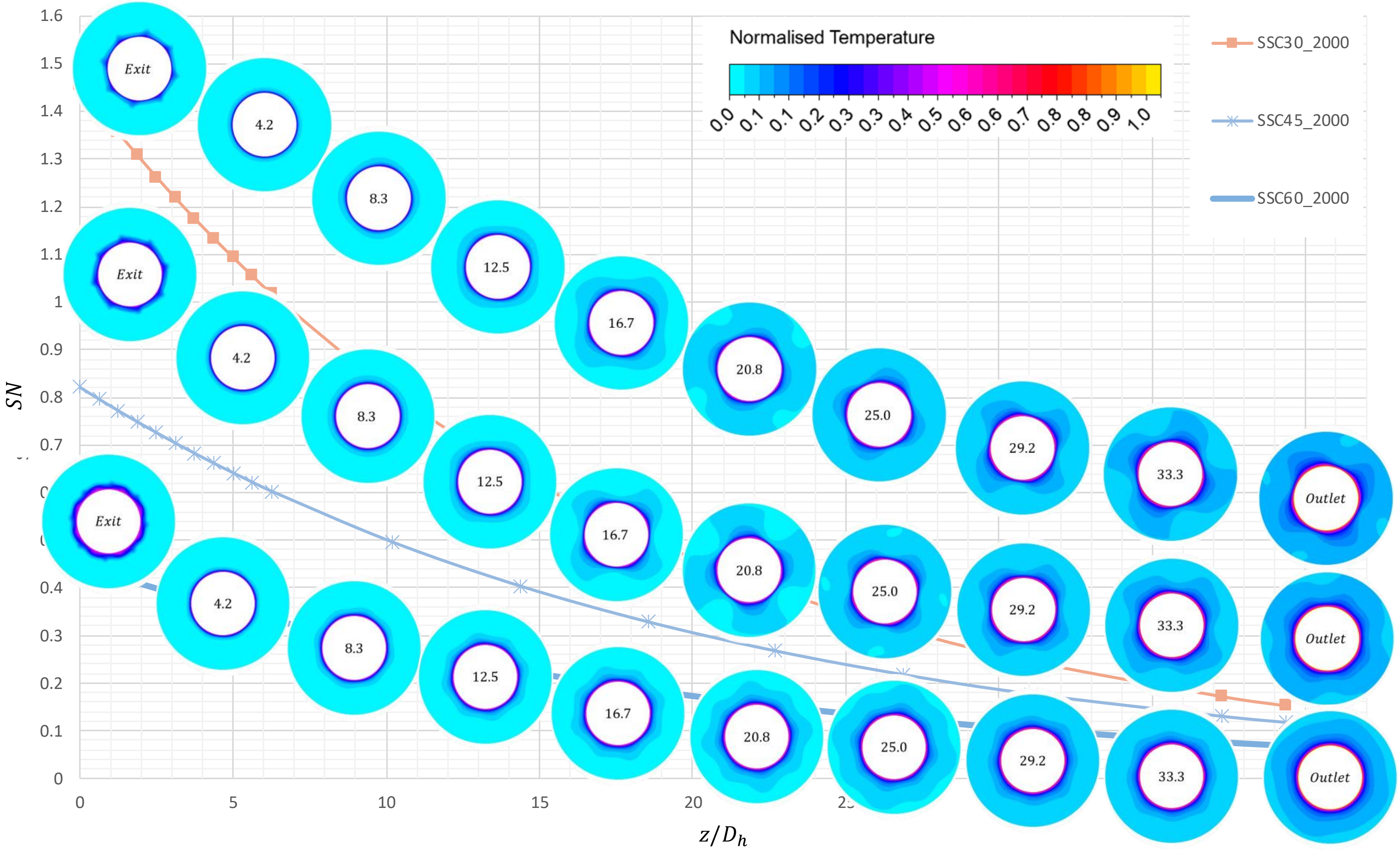

Figure 5.74: Variation of cross-sectional temperature distribution for three swirl angles at $Re = 2000$

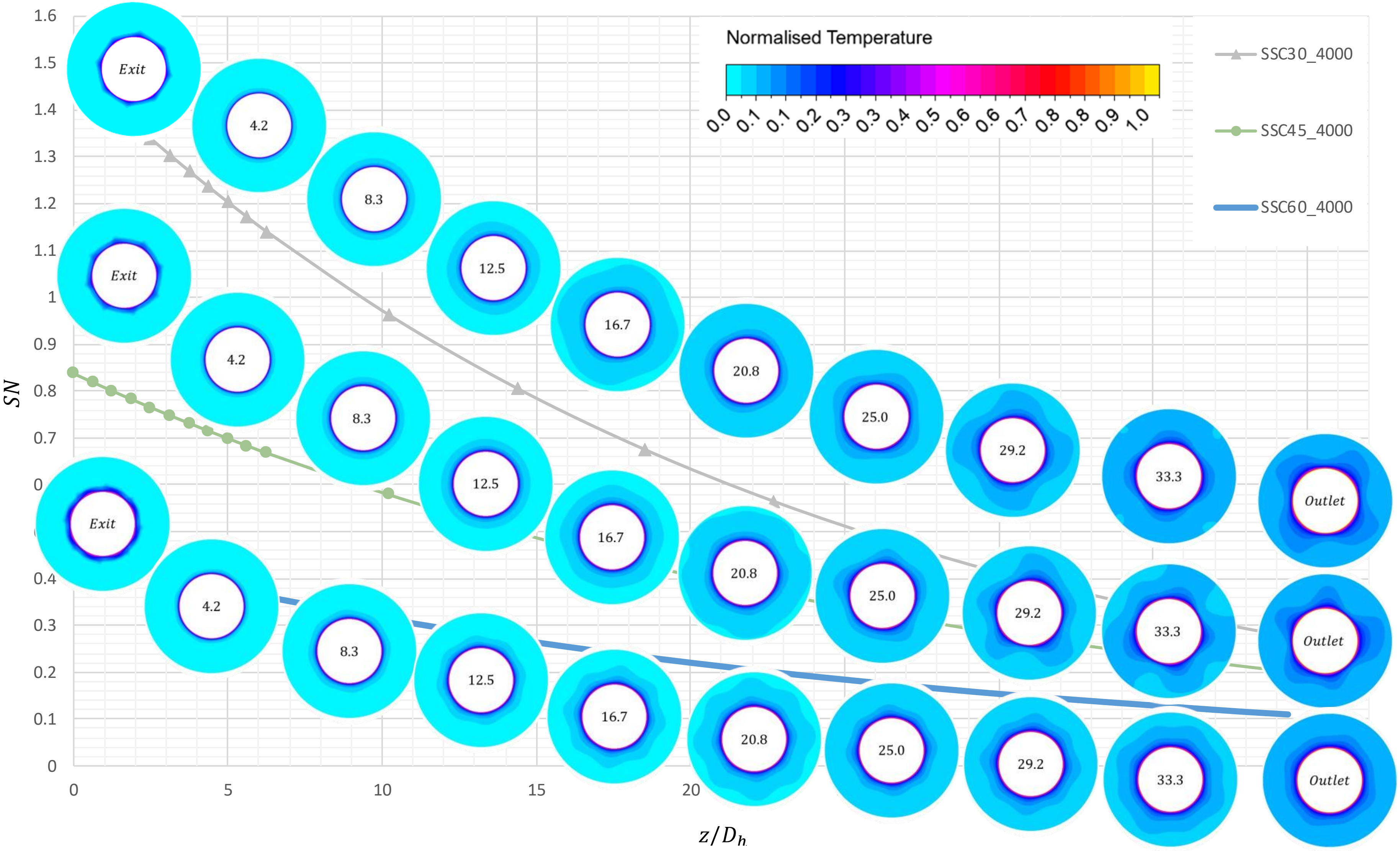

Figure 5.75: Variation of cross-sectional temperature distribution for three swirl angles at $Re = 4000$

5.3 Performance Evaluation of Single Swirling Configuration

To analyse the performance of the different configurations designed, evaluation of global parameters namely, pressure drop and rate of heat transfer, was conducted. These values were evaluated in terms of friction factor and Nusselt number from Eqs. (3.36) and (3.5) which represent the loss and gain in the heat exchanger, respectively.

5.3.1 Friction factor

To begin the analysis, the friction factors of the unheated $DPHE$s were plotted in Figure 5.76. It was observed that f decreases with increasing Re. In comparison to the plain $DPHE$, the SSCsachieved higher friction factors. These increments were measured to be from about $1.00-1.67$, $1.01-1.87$, and $1.09-2.33$ for $SSC60$, 45, and 30, respectively. The swirling flow is expected to increase the pressure drop when compared to an axial flow. This is mainly due to the induced tangential component, which allows the fluid to travel a longer path. This results in a centrifugal force that pushes the fluid towards the outer wall, and the increased contact with the walls of the annulus results in increased frictional losses. Furthermore, a non-uniform velocity distribution radially creates a thicker and more turbulent boundary layer, resulting in a further pressure drop. These findings were in agreement with all the literature that was found. Further details regarding annular variation of pressure were discussed by Solnordal et al.[156] and Barakat et al. [157]. It can be noticed that at $Re = 300$, the friction factor in $SSC60$ was evaluated to be slightly lower than that of the plain $DPHE$. However, this slight variation of 2.56% was attributed to the numerical error caused by the difference in the models used (laminar and RNG models) at low Re, which was neglected, and the difference was assumed to be unity, similar to that found in the case of the other angles.

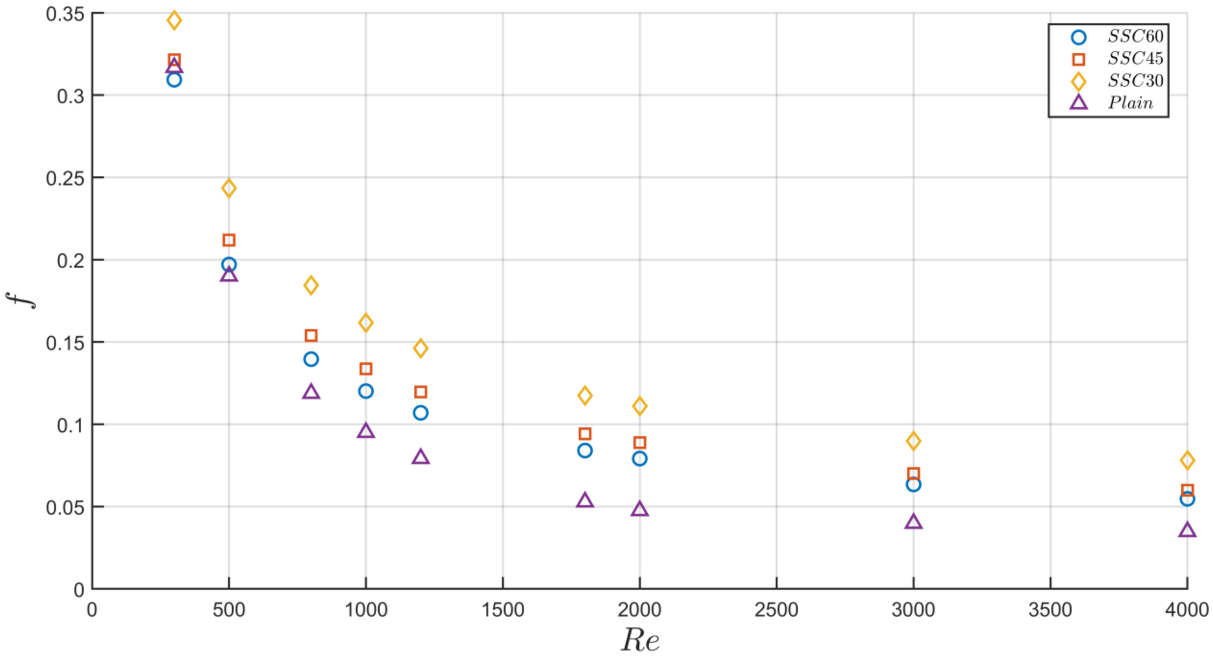

Figure 5.76: Friction factor plot against Reynolds number for the three swirlers under the unheated condition. The three swirlers were compared to the plain DPHE.

When hot water is pumped through the concentric tube, forced convection affects the friction factor in the annulus. The variation of the heated friction factor can be seen in Figure 5.77. Similar to the unheated case, the addition of swirlers at the inlet increased the friction factor by $1-1.59$, $1-1.78$, and $1-2.27$ with respect to the plain $DPHE$ for the cases of $SSC60$, $SSC45$, and $SSC30$, respectively. It should be noted that the increment in the heated case was observed to be lower than in the unheated case, due to the increase caused by the heating effect in the plain $DPHE$. This can be recalled from section 5.2.6.

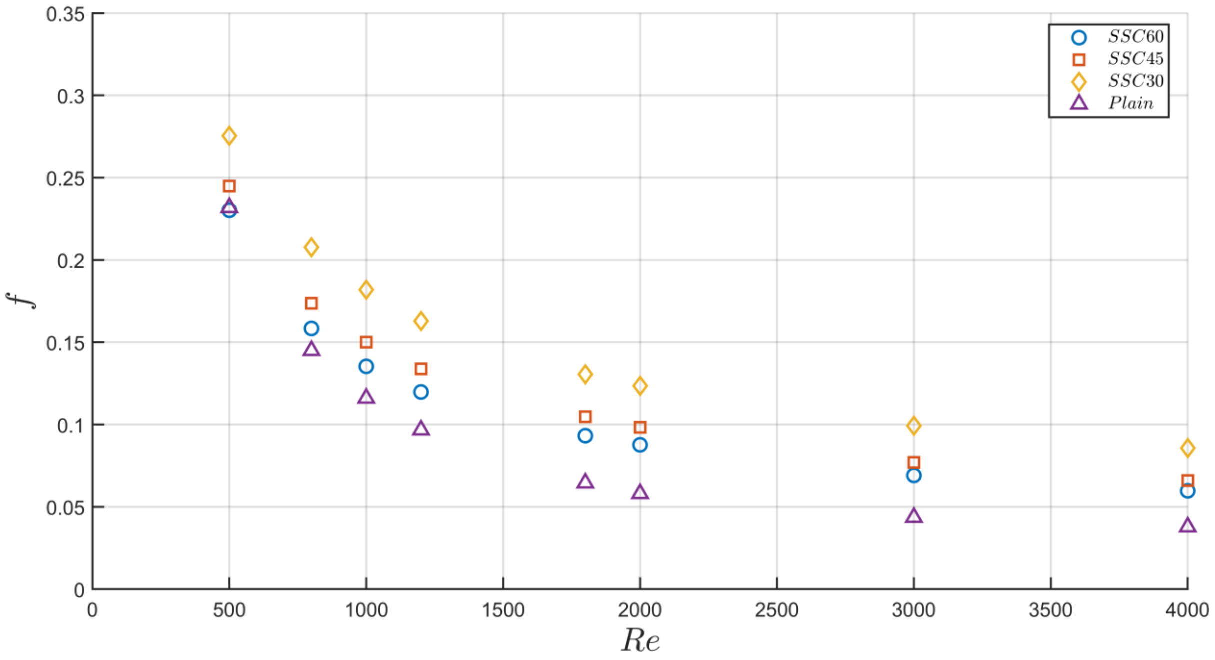

Figure 5.77: Friction factor plot against Reynolds number for the three swirlers under the heated condition. The three swirlers were compared to the plain DPHE.

A comparison between the heated and the unheated effects was plotted in Figure 5.78. The variations of the ratio of augmented to plain friction factors (f/f_0) with increasing Re are presented. With regards to the unheated cases, it can be seen that the ratio increased with increasing Re until $Re = 3000$ and 4000, where the ratio seemed to decrease slightly from 1.67, 1.87, and 2.33 to 1.57, 1.72, and 2.24 for $SSC60$, 45, and 30, respectively. This was less significant in the heated cases, where the friction factor ratio increased with increasing Re but was found to be nearly constant when the ratios at $Re = 3000$ and 4000 were compared. Comparing the unheated to the heated cases, it was shown that the ratio achieved higher values in the unheated cases than in the heated ones. The increment reached a maximum of 10% among all angles at $Re = 1800$ and 2000. In more turbulent flows, there was no difference between the cases in the ratio.

The friction factor ratios did not show it, but for each swirler, the heated friction factor was found to be higher than its corresponding unheated one. The increment was caused by viscous heating effects. The increased temperature of the particles near the inner wall of the annulus resulted in reduced viscosity. This reduction implied that the shear stress between adjacent particles close to the wall was reduced, consequently increasing the resultant velocity. As the axial velocity remained constant, the gain in velocity was added to the tangential component of the swirling flow. This resulted in greater centrifugal forces acting towards the outer wall of the annulus, producing the profiles shown in Figure 5.50- Figure 5.54, causing more contact with the outer wall, increasing shear stresses in the adjacent particles, and, in turn, the pressure.

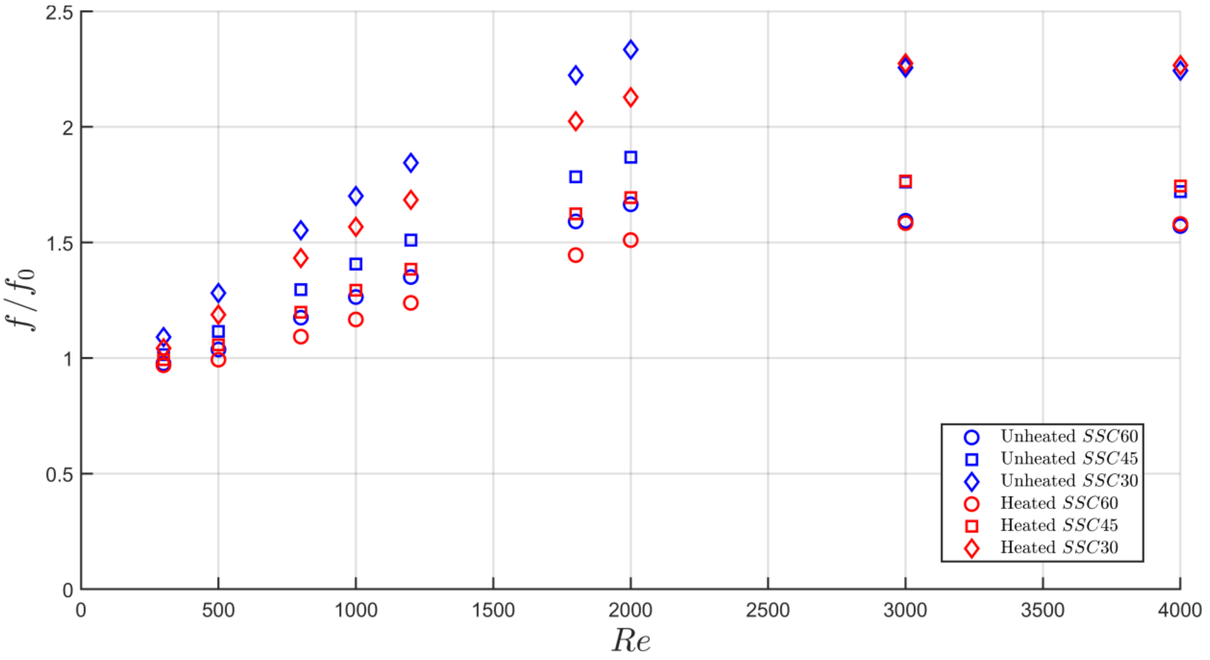

Figure 5.78: Comparison between heated and unheated friction factor ratios.

5.3.2 Nusselt Number

The Nusselt number was evaluated to represent the dimensionless heat transfer coefficient obtained in each case. Figure 5.79 presents the local variation of Nusselt number for all the angles and Reynolds numbers. A common behaviour observed in all cases was that Nu_l initially increased before decaying to a constant value. Peaks of the Nusselt number were achieved in the range $0.2 \leq z/D \leq 0.4$ in the laminar regime ($Re \leq 1200$), then earlier at nearly 0.16 in the turbulent regime ($Re \geq 1800$). As swirling intensity increased, the peaks were achieved at an earlier location, which decreased with increasing Re from $0.33 - 0.16$ and $0.30 - 0.13$ for $SSC45$ and $SSC30$, respectively. A higher decay rate was observed for the turbulent flows. This was due to the high molecular conduction achieved in laminar flow. The peaks achieved were found to be located within the impingement jet zones discussed in Section 5.2.6.4.

The decay of Nu_l was seen to follow a similar behaviour to that of the local SN, suggesting a proportional relationship between the decay rates of Nu_l and the decaying tangential momentum of the swirling flow. Similar to SN, Nu_l also increased with increasing Re. Nevertheless, this was found to be a more sensitive factor in the swirling annular flow studied by Chen B. et al. [46]. This presented a major distinction between having a heat source of limited length at the annular inlet, in contrast to the counterflow arrangement of the $DPHE$ currently under investigation. Another difference was identified: $SSC60$ and $SSC45$ showed an initial decay at the exit of the swirlers in the referred research, while in the current investigation, for all cases, Nu_l grew to a maximum before decaying non-linearly. It is noteworthy to mention that in the referred research, the standard $K - \epsilon$ model was selected as the turbulence model, which might have been a factor contributing to the differences in local behaviour. A comparison between the angles in the laminar ($Re = 1000$) and turbulent ($Re = 4000$) regimes was shown in Figure 5.80. It was observed that the lower the swirl angle, the higher the maximum Nu_l achieved, and consequently, the faster the decay rate. Additionally, like SN, the value of Nu converged at similar values at the same Re, independent of θ_{sw}. This increment was found to be up to nearly 5 times that achieved by $SSC30$ in the turbulent regime when compared to the predicted annular turbulent Nu by Dittus-Boelter [106]. The correlation returned 32 at $Re = 4000$. It was found that with the current heat transfer augmentation, Nu exceeded the correlation in the decaying region for all angles, even in the laminar regime for a brief length $(z/D < 0.38)$ in the annulus. The value decayed and was retained at 1.3 times that in the asymptotic region.

The local results have set the stage for the global behaviour of Nu. A presentation of its evaluation with increasing Re is presented in Figure 5.81. As expected, decreasing θ_{sw} resulted in a higher Nu. This is due to the higher swirling intensity, which disrupted the thermal boundary layers more significantly and resulted in a delay in the re-establishment of the boundary layers when compared to higher θ_{sw}. Simultaneously, a continuous increase in the difference between $SSC30$ and the other angles was observed, where Nu increased in the range of $1.03 - 1.10$ and $1.03 - 1.18$ when compared to $SSC45$ and $SSC60$, respectively. The comparison between these angles and the plain $DPHE$ was better presented in Figure 5.82, showing the variation of Nu/Nu_0 with Re for the three angles. It was observed that in the laminar region of the plain $DPHE$. Nu/Nu_0 achieved by the swirlers continuously grew with increasing Re, reaching a maximum of 2.04. However, when the ratio was evaluated at the turbulent level, it was seen that this increment was reduced to 1.29. This was the result of the turbulent plain DPHE achieving a much higher Nu as the flow entered a more turbulent regime.

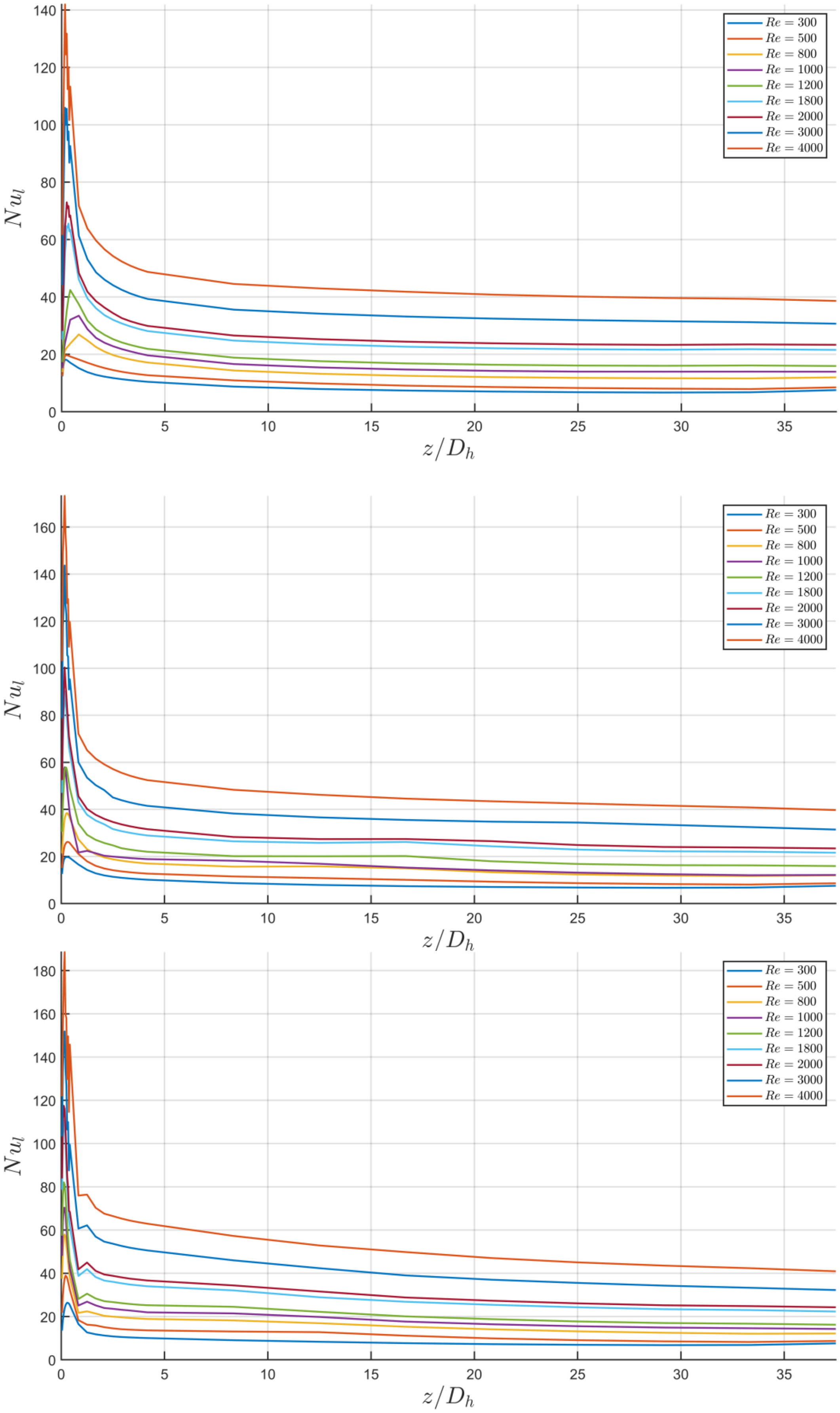

Figure 5.79: Variation of local Nusselt number along the axial length of the inner wall of the annulus at various Reynolds numbers for SSC60, SSC45 and SSC30 (top to bottom).

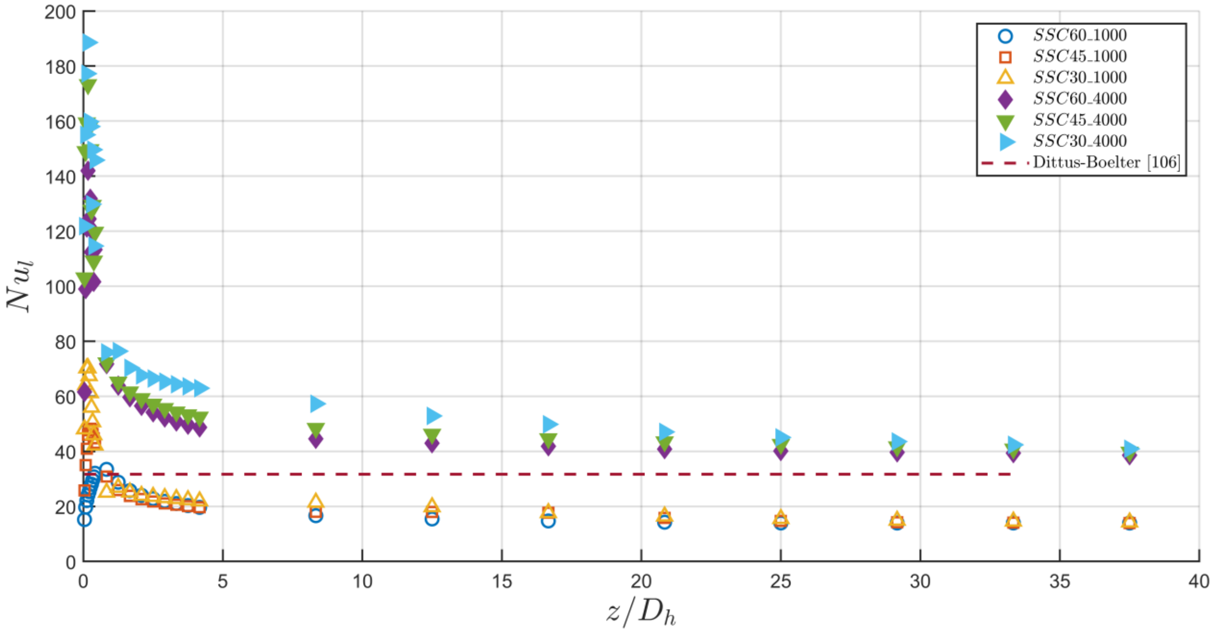

Figure 5.80: Local Nusselt number variation along the inner wall for different swirl angles at $Re = 1000$ *and* 4000.

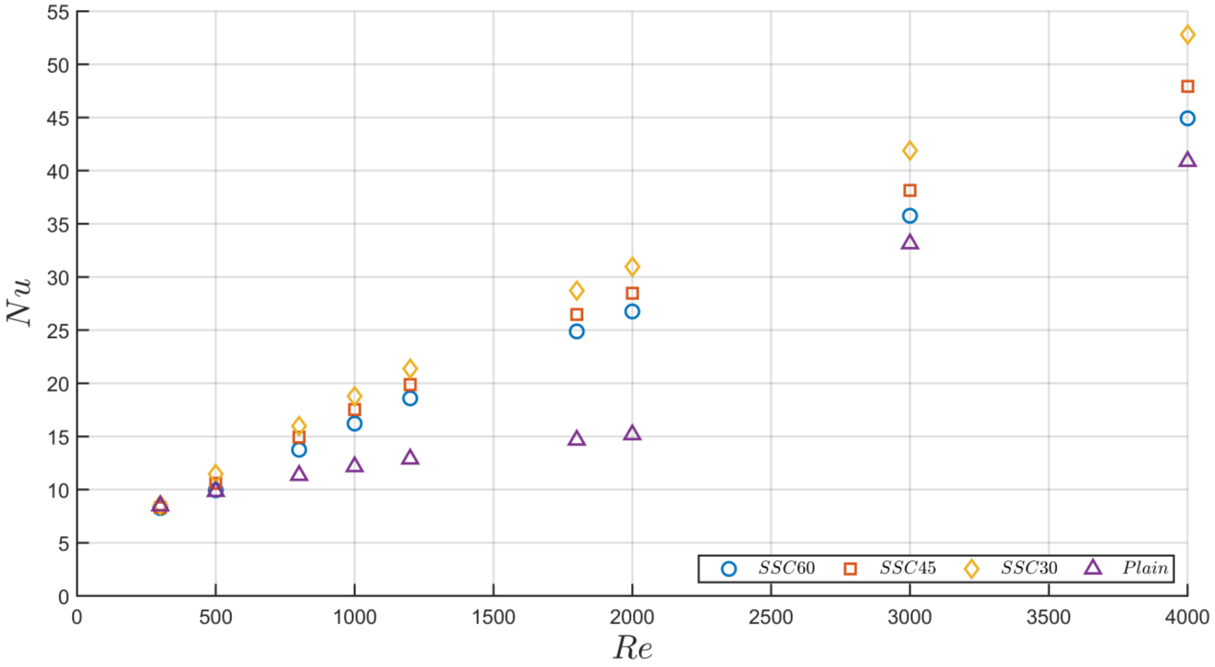

Figure 5.81: Average Nusselt number variation with increasing Reynolds number for all swirl angles.

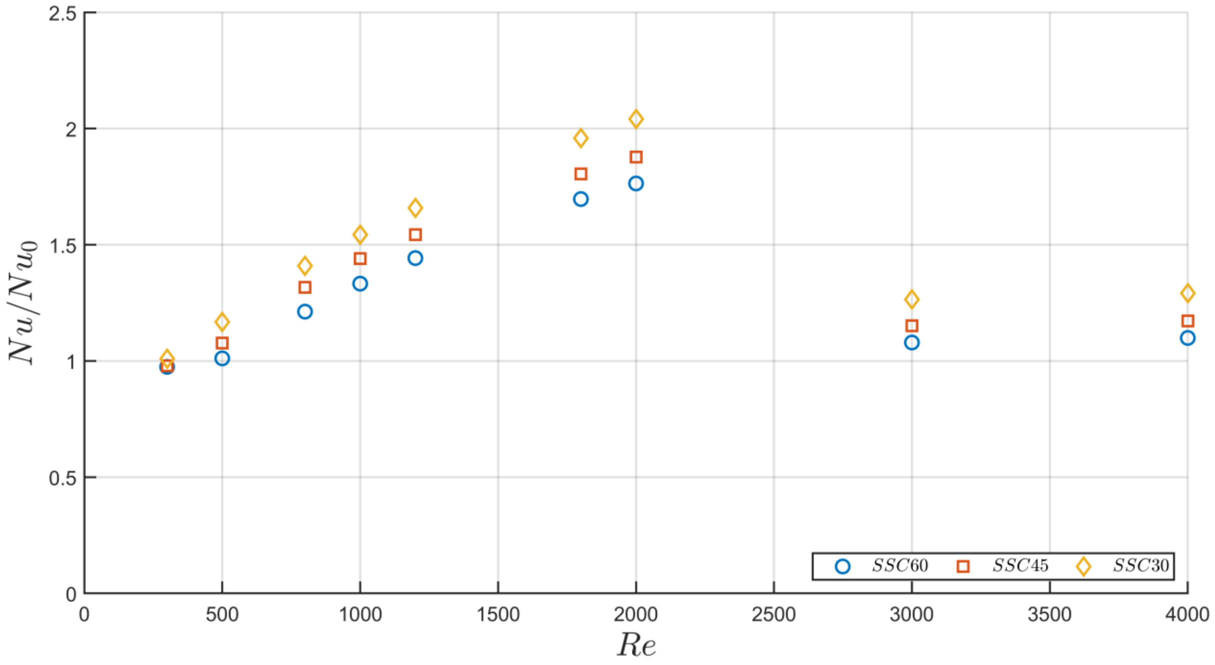

Figure 5.82: Comparison of the Nu ratio (numerical to plain Nusselt numbers) between all swirl angles.

5.3.3 Performance Enhancement Criteria

The results of the Nusselt number and friction factor discussed earlier are now combined to determine the performance of the mechanical augmentation introduced by inserting the swirlers under the current operating conditions and material properties. Figure 5.83 shows the results obtained after evaluating the performance enhancement criteria using Eq.(3.42), with increasing Re for all the swirl angles. The results showed that the PEC of all the swirlers was greater than unity in the laminar region of the plain $DPHE$. The results ranged from nearly $1.00 - 1.53$, $1.00 - 1.57$, and $1.00 - 1.59$ for $SSC60$, $SSC45$, and $SSC30$, respectively. Furthermore, the performance was reduced to nearly unity once more for all three angles at both $Re = 3000$ and 4000, when the flow in the plain $DPHE$ accounted for turbulence in the flow. This demonstrated superior performance of the swirlers in the laminar regime in comparison, but they did not maintain the same impact in low-turbulence flows. Nevertheless, it should be noted that the operating conditions under which the $SSCs$ was operating did not significantly contribute towards heat transfer (low ΔT) or the induction of amplified swirl intensities (low inlet Re). The swirlers were investigated with minimal environmental intrusion to test their true strength.

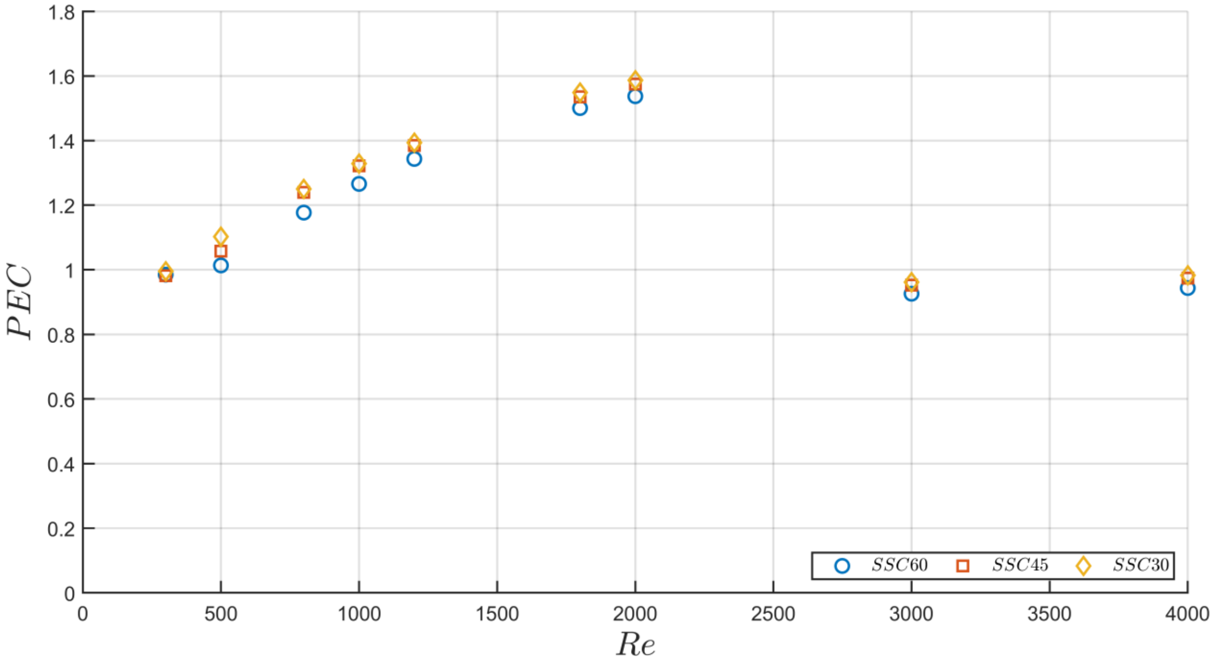

Figure 5.83: Performance enhancement criteria for all three swirl angles against Reynolds number.

5.4 Performance Evaluation of Full Swirling Configuration

It is now time to use the functions described in Table 5.3. Using these functions, the Decay Percentage (DP) parameter, defined earlier in Section 4.2.5 is applied. The steps were listed in the definition, so this section will focus on presenting a practical example before presenting the results. It should be noted that the description of the cases will be summarised by presenting them in the following format: $FSCAA\_BBBB$, where AA is the selected DP and $BBBB$ is the inlet Reynolds number.

The following example will consider $FSC70\_1000$, which means that this case focuses on the full assembly of the swirlers with a spacing between them that corresponds to the length from the exit of the swirler in the SSCs where 70% of each of their maximum swirl numbers was achieved at an inlet Reynolds number of 1000. From the definition in the aforementioned section, steps 1 to 3 were achieved in Section 5.2.6. In step 4, the selected DP is 70% and Re is 1000. These values were substituted into the following functions:

$$SSC60\_1000: SN = 0.438e^{-0.063\frac{z}{D_h}}$$

$$SSC45\_1000: SN = 0.792e^{-0.068\frac{z}{D_h}}$$

$$SSC30\_1000: SN = 1.389e^{-0.077\frac{z}{D_h}}$$

Recall that SN_0 in Eq.(5.3) is also the maximum SN achieved; hence, the general function of DP is defined as:

$$DP = \frac{SN}{SN_0} \times 100 \tag{5.6}$$

Therefore, the axial location of the selected DP is:

$$z = \frac{D_h}{\beta} \ln\left(\frac{1}{DP}\right) \tag{5.7}$$

For $FSC70\_1000$, the spacings required by the swirlers are 136 mm, 125 mm, and 111 mm for $SSC60$, 45, and 30, respectively. This leads to a sum of 372 mm. Taking into account the length of the swirlers (50 mm each), the total length of $FSC70\_1000$ is evaluated to be 522 mm. Table 5.4

shows the heat transfer surface lengths of the FSCs designed after evaluating the length of the required DP downstream from every swirler. The CAD assembly is shown in Figure 5.84. As shown in the figure, the mesh followed a similar style to that performed in the SSC to ensure an accurate and fair comparison between both configurations.

Table 5.4: List of the heat transfer surface lengths (in mm) of the FSCs depending on their inlet Reynolds number.

Re	$FSC50$	L_{FSC50}/L_0	$FSC70$	L_{FSC70}/L_0
300	379	40%	295	31%
500	529	56%	373	39%
800	657	69%	439	46%
1000	722	76%	472	50%
1200	772	81%	503	53%
1800	934	98%	580	61%
2000	976	103%	600	63%
3000	1163	122%	699	74%
4000	1312	138%	775	82%

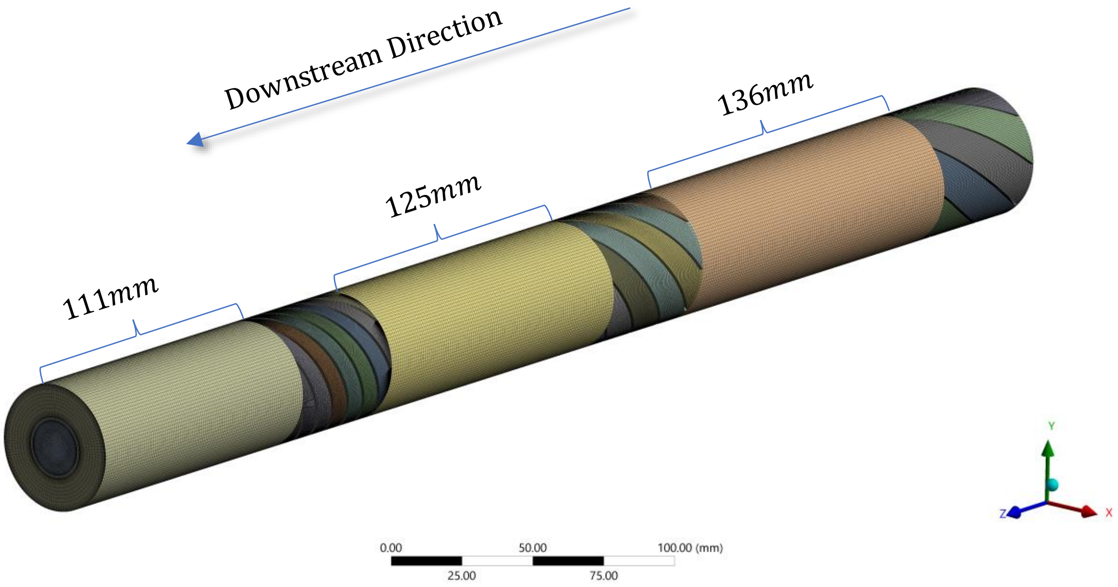

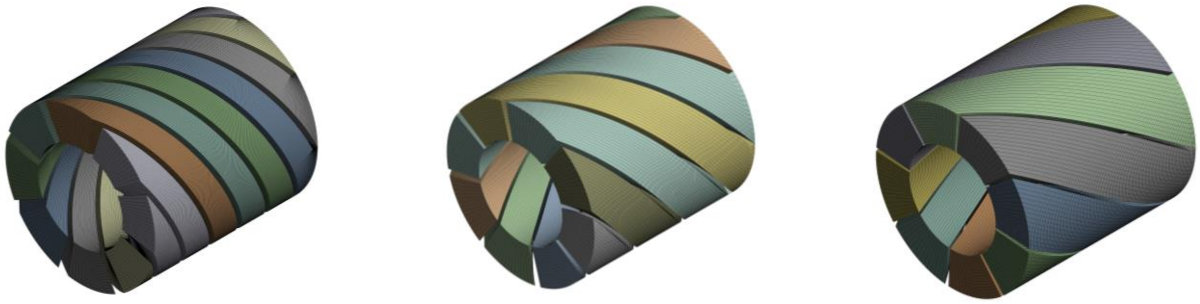

Figure 5.84: Computer-aided design and mesh of the full swirling configuration (Top). The fluid domain inside the swirlers: 30°, 45° *and* 60° *(Bottom Left to Right).*

This assembly was then imported into the solver (FLUENT CFD) to solve the CFD codes and evaluate the heat transfer coefficient and pressure drop obtained using the current design. The flow of water in the annulus can be seen in Figure 5.85. The behaviour of the swirling fluid exiting the first swirler (60°), which then decayed to 70% of the maximum swirl number achieved at $Re = 1000$, was the point at which the fluid enters the second swirler (45°). Then, with the guiding vanes of the swirler, the flow is adjusted to follow the new swirling angle with which it exited the swirler, achieving a new swirl number maximum. This process is repeated until the flow exits the third swirler and the swirl number has decayed to 70% at the outlet of the annulus. This led to the FSCs being designed with different lengths, depending on the sum of the lengths at which the swirl number achieves the desired DP for every inlet Reynolds number investigated. The results obtained are then used to evaluate the PEC and compare them to observe the impact of applying this augmentation method in $DPHE$s.

5.4.1 Nusselt Number

In this investigation, the FSCs were compared to the plain $DPHE$ (of 0.95 m in length), to which the SSCs were also compared. First, the heat transfer coefficients were represented by the Nusselt number and were plotted in Figure 5.86. As shown earlier in the case of SSCs, the thermal boundary layers are disrupted at the exit of each swirler. The boundary layers were then observed to attempt to reform and develop as the intensity of the swirling flow decayed. Assembling the swirlers together in the FSC provides the advantage that the flow is not allowed to decay completely before the swirlers cause the swirl number to spike up repeatedly, resulting in a simultaneous spike in the local Nusselt number. In the figure, it was shown that both FSCs achieved a higher heat transfer coefficient than the plain $DPHE$. Furthermore, $FSC70$ achieved the highest performance thermally. It consistently presented a dominating performance compared to that achieved by $FSC50$, ranging from $1.15 - 1.18$ times. The reason was that, as the thermal boundary layers were disrupted in both configurations, $DP = 70$ provided a shorter distance for the swirling intensity to decay and the thermal boundary layers to regain their developed shape. Instead, the thermal boundary layers were briefly excited once more, sooner than when DP was 50. The ratio of Nu of the FSCs to the plain $DPHE$ is shown in Figure 5.87. At low Re $(300 - 500)$, the increments were found to remain constant, indicating independence from the Reynolds number. Moreover, increasing Re produced a growing increment up to 2000 (laminar plain $DPHE$). Similar to the SSCs, the increment remained higher than unity but dropped significantly for $Re = 3000$ and 4000 at a nearly constant increment of 1.2 and 1.4 for $FSC50$ and 70, respectively.

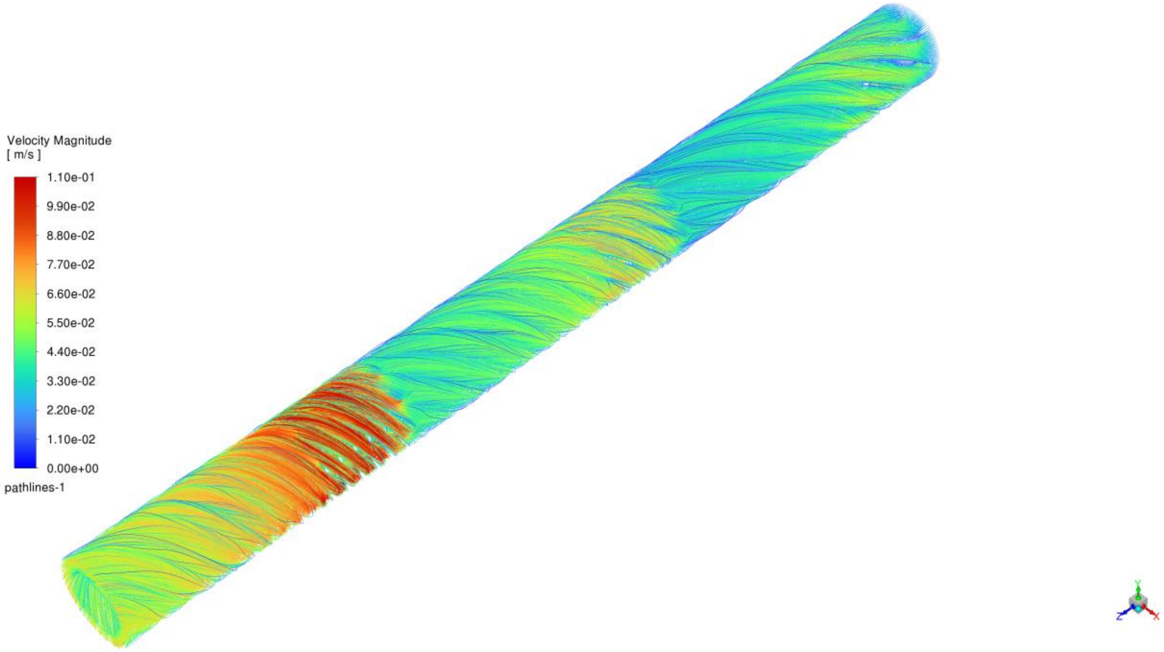

Figure 5.85: Streamlines of heated water flow in the annular domain of FSC70_1000.

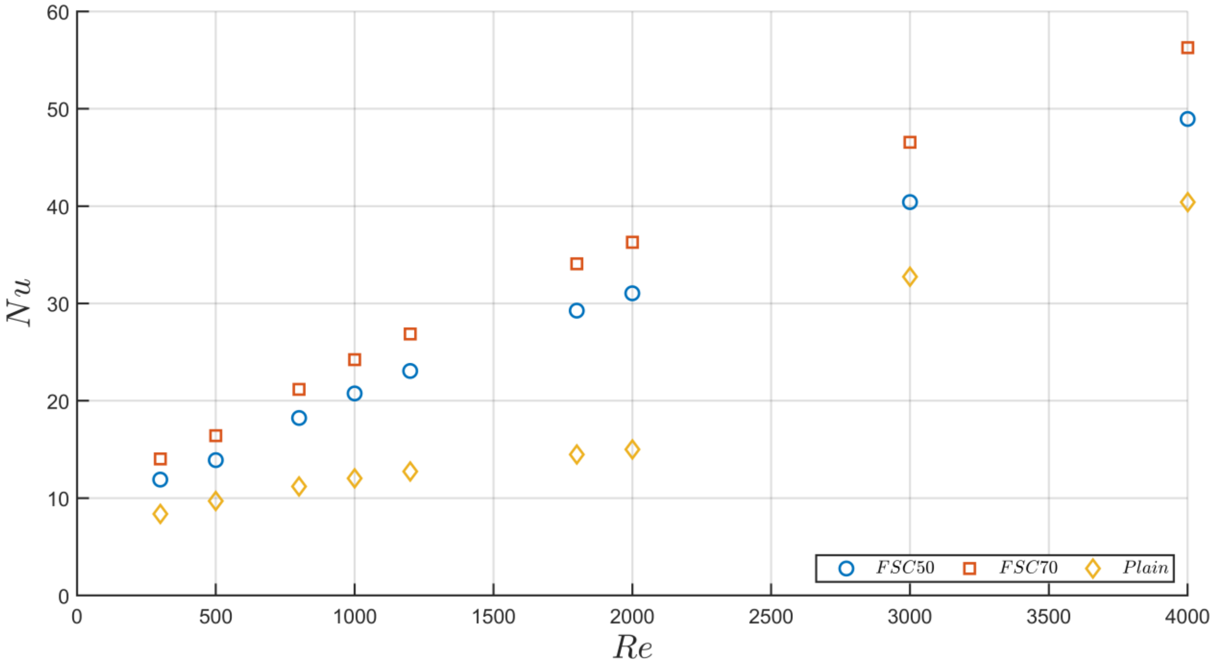

Figure 5.86: Comparison between the Nusselt number variations with increasing Reynolds number for $FSC50$, $FSC70$ and plain $DPHEs$.

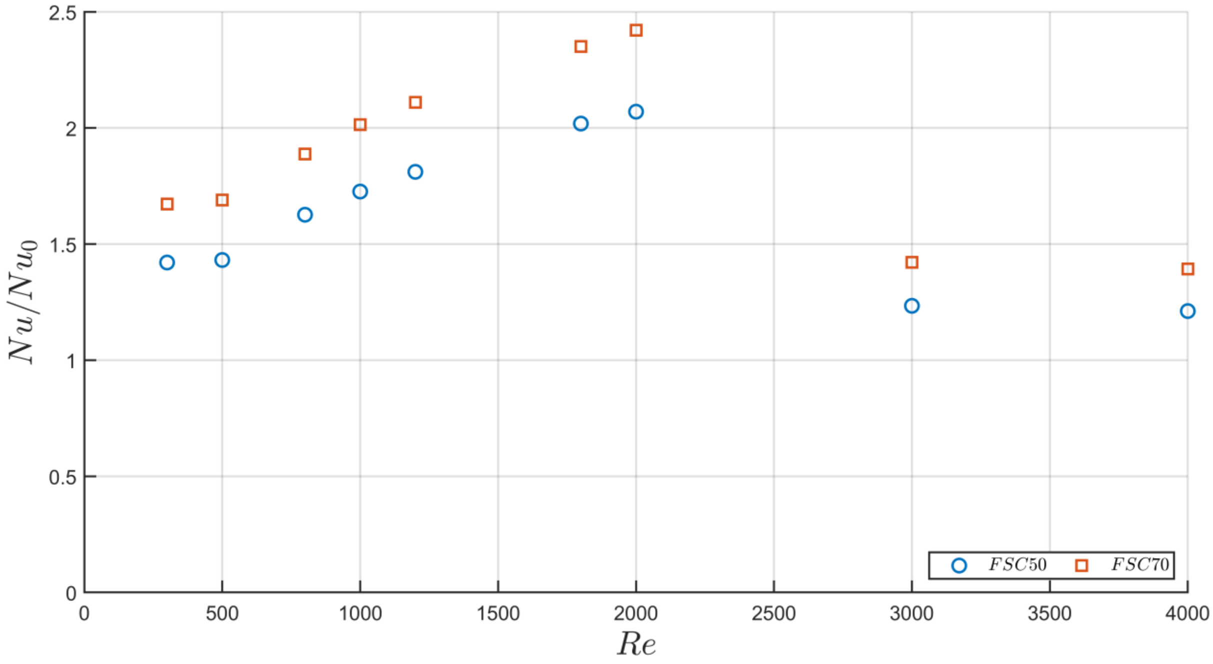

Figure 5.87: Nusselt number ratio of the $FSCs$ to the plain $DPHE$ with increasing Reynolds number.

5.4.2 Friction factor

Figure 5.88 presents the friction factors achieved by the FSCs designs in both configurations, along with a comparison to the plain $DPHE$. It was found that the friction factor achieved by $FSC70$ at Re=300 was much higher than both $FSC50$ and the plain $DPHE$s. This was expected, as $FSC70$ produces relatively more turbulence. The friction factor increment was found to remain nearly constant at 1.75 for the entire range of Re. Figure 5.89 demonstrates the friction factor ratio of FSC to the plain $DPHE$. Similar behaviour to the Nu ratio was observed, with the ratio showing Re-independence when $Re = 300 - 500$ and $3000 - 4000$. The ratio increased in the range of $9 - 13$ and $15 - 23$ for $FSC50$ and 70, respectively.

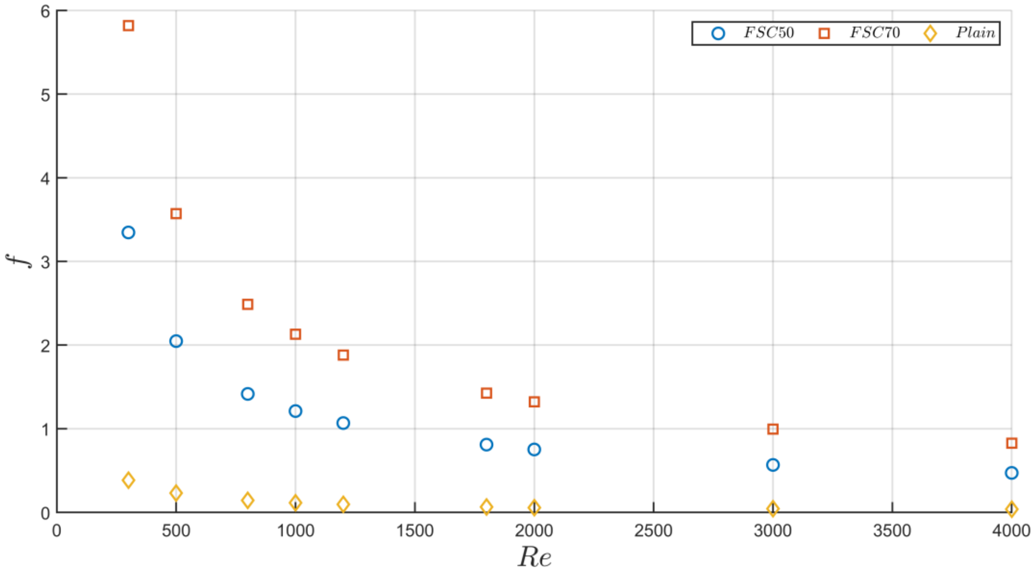

Figure 5.88: Friction factor variation in $FSC50$ and 70 and plain $DPHE$ with increasing Reynolds number.

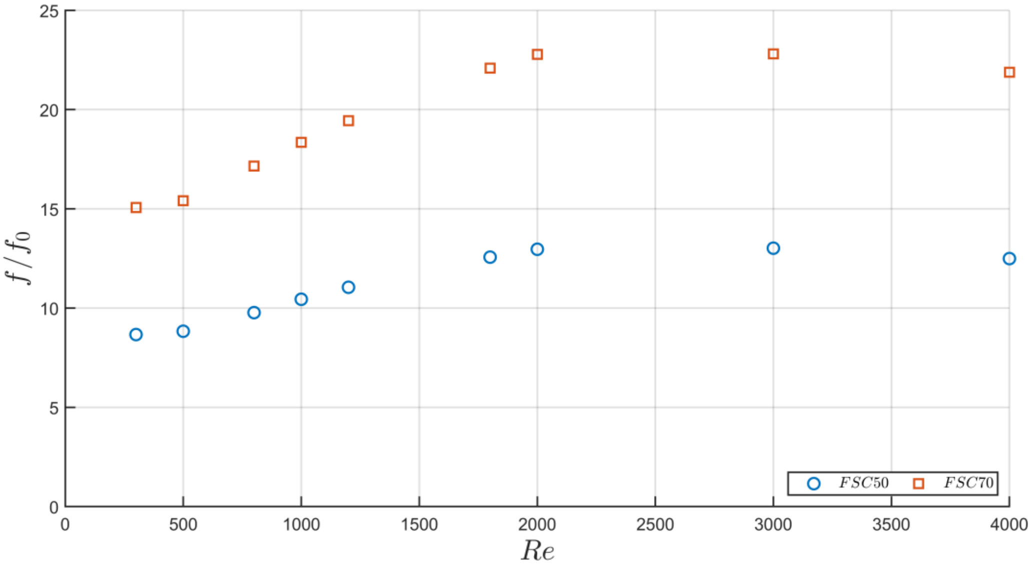

Figure 5.89: Friction factor ratio of the FSCs to the plain $DPHE$ with increasing Reynolds number.

5.4.3 Performance Enhancement Criteria

After observing the hydrodynamic and thermal performances of the heat exchangers, The PEC was again used to evaluate their overall performance. It was found, as shown in Figure 5.90, that with the current geometrical design, operating conditions, and working fluid properties, the performance of the FSCs was inefficient when compared to a $DPHE$ of $0.95m$. This inefficiency was mainly attributed to the friction factor induced by the blockage resulting from the placement of two swirlers inside the flow. In addition, the size ratio, shown in Table 5.4 of the newly developed FSC and plain $DPHE$ shows the significant advantage of size reduction achieved by $FSCs$. This reduction can be translated financially into much desired savings in industrial applications.

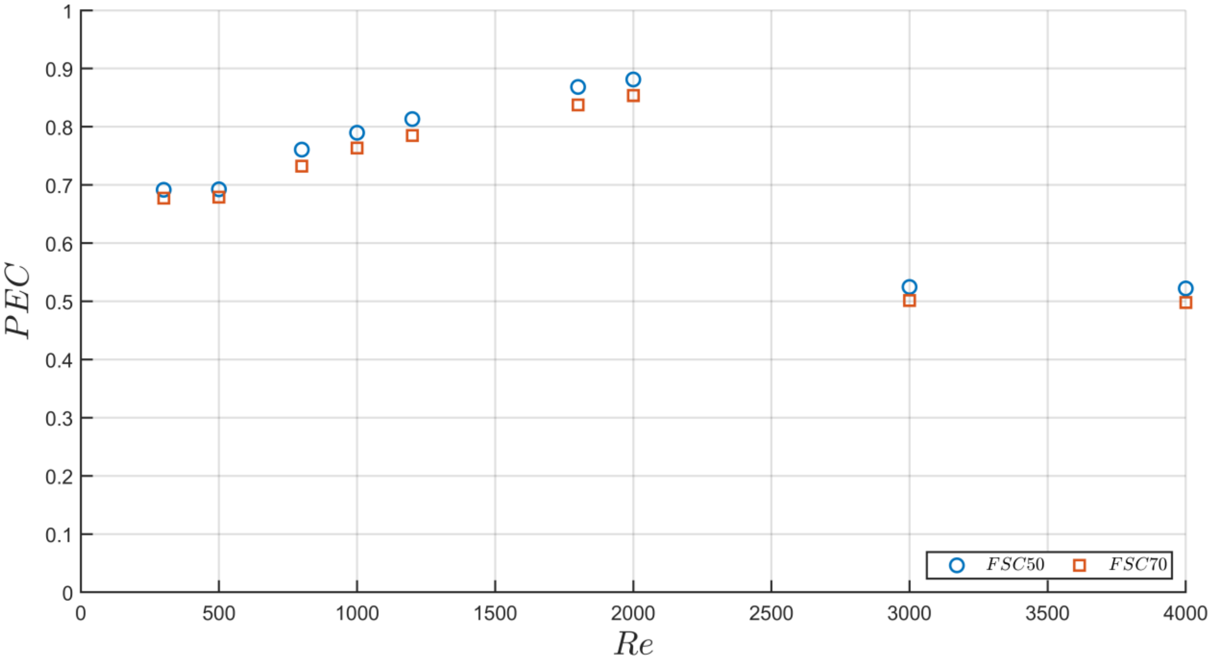

Figure 5.90: Performance enhancement criteria of the $FSC50$ and 70.

The findings of this study offer actionable insights for industrial heat exchanger design, particularly in optimising performance through swirl enhancement. One key consideration is swirl angle selection. The SSC30 configuration delivers the highest thermal performance, with heat transfer gains ranging from $139\% - 242\%$. However, this comes at the cost of a $25\% - 40\%$ increase in friction factor, making it ideal for compact systems such as aerospace heat exchangers, where spatial constraints outweigh pumping energy concerns. In contrast, SSC60 offers a more balanced approach, reducing friction penalties by $30\% - 50\%$ while sill achieving $70\% - 80\%$ thermal gains. This makes it well-suited for large-scale energy systems, such as refinery heat recovery units, where pressure drop significantly impacts operational expenses.

Reynolds number optimisation also plays a critical role in swirl implementation. Laminar regimes show the greatest benefit from swirl augmentation, with performance enhancement coefficients between 1.53 and 1.59. These results support the retrofitting of low-flow systems, such as direct heating networks, where flow rates are inherently limited. For turbulent flows, the SSC45 configuration promotes faster flow uniformity, up to 40% quicker, reducing vibration risks in sensitive applications like nuclear reactor cooling systems.

In terms of configuration implementation, the Full Swirling Configuration design enables up to 69% size reduction through strategic swirler spacing. This directly addresses compactness requirements in automotive and aircraft thermal management systems. Additionally, decay percentage control offers real-time adaptability by allowing selective swirler activation in variable-load environments, such as chemical batch reactors. This dynamics control maintains optimal Nusselt number to friction factor ratios during throughput fluctuations, ensuring consistent thermal performance without excessive pressure penalties.

Together, these results provide a validated framework for deploying swirl-enhanced double-pipe heat exchangers across diverse energy systems. By balancing efficiency, compactness, and operational flexibility, while mitigating friction-related drawbacks, the study supports targeted design strategies for next-generation thermal systems.

Chapter 6: Conclusion and Future Recommendations

The research methods developed in this thesis were aimed at achieving the research objectives listed in Chapter 1. The conclusions for each objective are as follows:

First Objective

"Analyse the detailed variations of the velocity and temperature profiles in annular swirl decaying flow with and without heat effects, varying Reynolds number and swirl angle."

This was achieved through two methods: a breakdown of the flow profiles and cross-sectional results using contours describing the swirl flow decay cycle. These methods directly addressed the first objective by quantifying how Re, θ_{sw}, and heating alter velocity and temperature distributions, though RANS limitations in capturing low-Re transitions should be noted.

Regarding the profile investigation, both unheated and heated cases were tested. For the heated case, one scenario involved equal flow rates for the hot and cold fluids, while another involved a constant hot fluid flow rate and an increasing cold fluid flow rate. From these three investigations, the following conclusions were drawn:

1. Axial and tangential velocity components showed a significant outward bias in the first section for all cases. This bias increased with increasing swirl angle and decreased with increasing Reynolds number. As turbulence increased, the profile adopted a turbulent form with a naturally reduced boundary layer thickness, damping the effect of Reynolds number on the profiles.

2. Oscillations, velocity fluctuations during decay recovery, of the profile peaks were commonly observed in both axial and tangential components. This phenomenon was amplified in the third section of the annulus where swirl intensity was significantly weakened due to tangential component decay. It was a byproduct of the recovery system initiated by viscous forces countering the swirl flow effects to stabilise the tangential motion into axial flow. These oscillations were more apparent with increasing Reynolds number and decreasing swirl angles.
3. Recirculation zones, reverse-flow regions identified via $u_z = 0$ isosurfaces, caused by the swirler walls were detected as negative values in the axial profile. They were tracked and observed using iso-surfaces representing the dividing surface engulfing the zones. They were categorised as central and vane wall regions downstream, and convex and concave walls upstream of the swirlers. Increasing the sharpness of the swirling angle led to the development of zones in additional regions.
4. The central region was of particular interest as it extended into the flow beyond the swirler and attached to the inner wall of the annulus. The other zones can be utilised in further research regarding swirler geometry optimisation. The central region reached maximum axial and radial ranges in the laminar regime, while it decreased to a constant value in the turbulent regime. More turbulent flows resulted in shorter recirculation zones due to the dominating inertial forces, resulting in thinner boundary layers. Increasing the swirl angle had a higher impact on the axial range of the zone, especially in the laminar regime. A maximum increase of 250% was achieved by $SSC60$ when $Re = 800$ for the unheated annulus. With heat addition, this maximum was also found at $Re = 1000$. The thickness of the central region showed a direct relationship to its length in the case of $SSC60$. However, maximum thickness was achieved by $SSC30$ at Re=300, demonstrating complete segregation between the two parameters.

5. Due to the varying behaviours of the profiles in both axial and tangential directions along with the recirculation zones, it was suspected that the critical Reynolds number, transition between flow regimes, lies between 1200 and 1800 for all angles.
6. Thermal boundary layers were found to reach a thinning as low as $\tilde{r} = 9\%$ for $SSC30$ in the turbulent regime, as opposed to 15% in the laminar regime. As the swirl angle increased, the maximum thinning of the boundary layers reached 20% in the turbulent region. Moreover, the thickness development was higher (up to 81% compared to 71%) at sharper angles as the swirl flow decayed. It was also concluded that sharper angles and higher Reynolds numbers maintained the thinning effects for a longer range through the annulus, providing better conditions for heat transfer. This was also observed in the heated case with equivalent flow rates in both fluids compared to keeping the hot fluid constant.
7. A comparison between heated and unheated profiles showed that thermal effects influenced the bias of the axial and tangential profile peaks. The thermal bias in both components was observed towards the heat source (i.e. the inner wall) in the annulus. At some axial locations where oscillations occurred, the peaks deviated in opposite directions, generating a damping effect on the oscillations and providing early indications of a slightly accelerated swirl decay.

With regards to the mapped results of the contours, the following results were drawn:

1. The velocity contours identified regions of high-speed concentration at various axial locations in the annulus. The behaviour of these regions was different for each of the velocity components as they diffused radially to fill the annular space downstream.
2. A swirl decay cycle was noticed as an emerging trend among the $SSCs$. For each of the components, these stages were:

Axial	**Tangential**
❖ Start of jet effect (initial high-velocity confinement)	❖ Start of jet effect
❖ Local maxima columns	❖ Inner boundary layer thickening
❖ End of jet effect	❖ End of jet effect
❖ Free swirling zone (undisturbed rotational flow)	❖ Swirl free flow
❖ Inner boundary layer thickening	
❖ Outer boundary layer thickening	
❖ Four local maxima	

3. Increasing Reynolds number resulted in delaying these stages further downstream, yet they still occurred.
4. Increasing swirl angle led to a significantly shorter swirl decay cycle. The only two stages that took place were the start and end of the jet effect in both components, indicating rapid flow development in the annulus.
5. In the heated annulus, the effect of Reynolds number extended the jet effect further downstream while the thickening of the boundary layers occurred earlier. This resulted in earlier flow development, driven by thermal expansion force. Increasing the swirl angle showed similar effect to that in the unheated annulus.

Second Objective

"To model the relationship between the decay rate of the swirl number and the friction factor. Compare the model under heated and unheated conditions."

1. To model the decay of the swirl number downstream, a regression method was adopted to develop a model for each angle at each inlet Reynolds number. As Reynolds number increased for each angle, higher initial swirl numbers and lower decay rates were observed.
2. At the same Reynolds number, decreasing swirl angles resulted in higher initial swirl numbers but also larger decay rates. This condition led to the convergence of the decaying swirl numbers for all angles, intersecting their profiles as the swirl component fully decayed. This case demonstrated the independence of the complete decay location from the Reynolds number.
3. A model of the decay rate in terms of the friction factor was developed with an acceptable level of confidence for the range of $0.4 \leq SN \leq 1.5$ for liquid water in the annulus using the current swirler geometry. This model contributes to the existing database of decay rate models, expanding the range of applications. This achieves the second objective by providing a friction-decay correlation applicable to industrial double pipe heat exchangers across $0.4 \leq SN \leq 1.5$ but requiring further verification for extreme flow regimes.
4. As predicted by the profile results, the heated profiles exhibited a slightly faster decay for the same angle and Reynolds number. Additionally, the heated condition had no discernible effect on the decay rate model, further generalizing its applicability.

Third Objective

"Investigate the effect of maintaining a minimal percentage of the maximum swirl number achieved by each swirler throughout the entire test section on the thermal performance of the double pipe heat exchanger."

1. Regarding the performance of the swirlers, it was found that the friction factor increased with increasing swirl angle. In comparison to the plain annulus, the highest increase was reached by the unheated $SSC30$ at $Re = 2000$. In the turbulent regime, the increment in friction factor remained constant.
2. The local Nusselt number was found to be a function in the form: $f\left(Re, \theta_{sw}, \frac{z}{D_h}\right)$. It peaked near the exit of the swirler as a consequence of the thinning of the thermal boundary layers. The thinner the boundary layers achieved, the higher the peak. The longer the range of the thinning effect, the larger the overall enhancement in comparison to the theoretical correlation. At a quarter of the Reynolds number, the local values briefly surpassed the correlation at $Re = 4000$ during the peak. At $Re = 4000$, all SSCs surpassed the correlation for the entire length, including the asymptotic region. Maximum enhancements reached 5.9, 5.4 and 4.4 times that of the correlation for $SSC30$, $SSC45$ and $SSC60$, respectively.
3. The average Nusselt number increased as both the Reynolds number and swirl angle increased. Maximum enhancement was of 2.04 times for $SSC30$ at $Re = 2000$. The enhancement was lower and constant at higher Reynolds numbers.
4. PEC was found to be follow the trend of the ratios of both the friction factor and the Nusselt number achieving a maximum of 1.53, 1.57 and 1.59 for $SSC60$, $SSC45$ and $SSC30$, respectively.
5. Using the Decay Percentage, novel parameter defining allowable swirl loss, the full swirling configuration was assembled. The results showed an adverse PEC of the FSCs assembled at $DP = 50\%$ and 70%. PEC increased with decreasing DP for $Re \leq 2000$,

achieving a maximum of 0.88 and 0.85 for $FSC50$ and $FSC70$, respectively at $Re = 2000$. This inefficiency was mainly attributed to the friction factor induced by the blockage resulting from placing two swirlers inside the flow.

6. The main advantage of the FSC can be appreciated in the amount of heat transfer achieved for the same operating conditions and fluid properties, along with the significant reduction in the heat exchanger size. A maximum of about 250% enhancement was achieved by $FSC70$ at Re=2000, as shown in Figure 5.87. This configuration was 63% of the original size of the plain $DPHE$. Modifying the swirl generator would improve the friction factor and in turn increase the PEC, but the Nusselt number achieved was shown to be directly influenced by the swirl number. This will be reflected by the decay percentage considered during the design stage of the FSC using any geometry of swirl generators. This fulfils the third objective by demonstrating DP-controlled configurations improving thermal performance, though current designs show adverse PEC at high friction factors due to swirler blockage effects.

Finally, the introduction of the novel parameter, Decay Percentage, will pave the way for a new branch of passive methods utilised by future researchers, as it will allow for a great degree of control over the expected performance of the heat exchanger. The concept of using discontinuous swirlers has proven significantly advantageous over continuous swirlers in terms of pressure drop within the flow. It is believed that the current trial-and-error approach to optimising the spacing between swirlers can be replaced with a more targeted approach based on swirl intensity earlier in the design stage. While DP enables unprecedented control of swirl decay, its current implementation requires CFD-derived SN functions. Future work should develop analytical DP predictors and test manufacturable swirler geometries to overcome blockage-induced friction penalties. This will aid in achieving the desired performance with a significant reduction in the size of the heat exchangers (automotive cooling), saving pumping power (refinery heat recovery), space (aerospace thermal management) and significant costs on an industrial scale.

Future Recommendations

Recommendations for future work that can build upon the current work are listed as follows:

1) Review machine learning methods (e.g., genetic algorithms, neural networks) that can be used to optimise the geometry of the swirlers to minimise flow obstruction. Then, use the most appropriate method to design better swirlers with optimised dimensions. Develop a machine learning model that can be generalised for use by other researchers. Investigate more configurations to train and diversify the use of this model.
2) Apply this model to the FSC to define the optimal configuration required for the best thermal performance. Investigate the possibility of deducing an optimal decay percentage for each swirl angle and Reynolds number. This parameter critically balances heat transfer gains and pressure penalties, enabling customised thermal performance tuning for dynamics industrial loads.
3) Assess boundary layer accuracy using free stream velocity and shear stress gradients. Derive a formulation linking maximum swirl number and Reynolds number under both heated and unheated swirling flow conditions to improve prediction accuracy of heat transfer coefficients in swirl-augmented systems.
4) Run transient simulations, though computationally intensive, to investigate the development of the recirculation zones and instabilities missed by steady-state simulations to identify vortex shedding frequencies that could compromise structural integrity in high-vibration environments like aircraft thermal management.
5) Run tests for a larger range of temperature gradients between cold and hot flows observed in nuclear reactor cooldown cycles and chemical batch processing.
6) Investigate and compare the results of reversing the assembly of the FSCs, where the swirler of 30° is placed at the inlet, increasing the swirl angle to 60° which may enhance thermal uniformity in compact heat recovery systems.
7) Explore swirl decay control in combustion and fluidized-bed reactors, where managing rotational momentum influences reaction efficiency and emission profiles.

Sustainable Development Goals (SDGs)

This research directly supports Sustainable Development Goal 7 (Affordable and Clean Energy) [158] and Goal 9 (Industry, Innovation and Infrastructure) [159] by enhancing the thermal efficiency of heat exchangers through optimised swirling flow configurations. Swirl-induced augmentation of convective heat transfer significantly improves energy utilisation in industrial systems, reducing fuel consumption and operational costs.

By refining swirl decay control, particularly in combustion and fluidized-bed reactors, this work promotes cleaner and more efficient thermal processes. These improvements are critical for industries transitioning to low-carbon technologies, aligning with SDG 7.3 which aims to double the global rate of improvement in energy efficiency by 2030 [158]. Additionally, swirl-enhanced designs can reduce NOx emissions in combustion systems [160], contributing to cleaner air and improved environmental performance. Integrating advanced flow control strategies into reactor and exchanger design exemplifies technological innovation in infrastructure, supporting SDG 9's focus on sustainable industrialisation and resilient systems [161]. Key applications include:

- Waste heat recovery systems in power plants and manufacturing facilities
- High-efficiency boilers and gas turbines with reduced emissions.
- Process intensification in chemical reactors for lower energy footprints

Future work will assess the lifecycle environmental and economic impacts of swirl optimisation, including energy savings over operational lifetimes, evaluating emission reductions, and exploring integration into circular economy frameworks. These efforts aim to align technical outcomes with SDG indicators, such as:

- SDG 7.3 [158]: Doubling the global rate of improvement in energy efficiency
- SDG 9.4 [159]: Upgrading infrastructure and retrofitting industries to make them sustainable.

By aligning engineering innovation with global sustainability metrics, this research reinforces the role of fluid dynamics and thermal design in addressing climate and energy challenges.

Bibliography

[1] A. Hosseinian and A. H. Meghdadi Isfahani, "Experimental study of heat transfer enhancement due to the surface vibrations in a flexible double pipe heat exchanger," *Heat and Mass Transfer/Waerme- und Stoffuebertragung*, vol. 54, no. 4, pp. 1113–1120, 2018, doi: 10.1007/s00231-017-2213-2.

[2] Z. Feng, X. Luo, J. Zhang, J. Xiao, and W. Yuan, "Effects of electric field on flow boiling heat transfer in a vertical minichannel heat sink," *Int J Heat Mass Transf*, vol. 124, pp. 726–741, 2018, doi: 10.1016/j.ijheatmasstransfer.2018.03.067.

[3] M. Goharkhah, A. Salarian, M. Ashjaee, and M. Shahabadi, "Convective heat transfer characteristics of magnetite nanofluid under the influence of constant and alternating magnetic field," *Powder Technol*, vol. 274, pp. 258–267, 2015, doi: 10.1016/j.powtec.2015.01.031.

[4] B. Yang, T. Gao, J. Gong, and J. Li, "Numerical investigation on flow and heat transfer of pulsating flow in various ribbed channels," *Appl Therm Eng*, vol. 145, no. January, pp. 576–589, Dec. 2018, doi: 10.1016/j.applthermaleng.2018.09.041.

[5] K. Navickaitė, M. Penzel, C. R. H. Bahl, and K. Engelbrecht, "Performance Assessment of Double Corrugated Tubes in a Tube-In-Shell Heat Exchanger," *Energies (Basel)*, vol. 14, no. 5, p. 1343, 2021, doi: 10.3390/en14051343.

[6] R. Tiwari, R. S. Andhare, A. Shooshtari, and M. Ohadi, "Development of an additive manufacturing-enabled compact manifold microchannel heat exchanger," *Appl Therm Eng*, vol. 147, no. October 2018, pp. 781–788, 2019, doi: 10.1016/j.applthermaleng.2018.10.122.

[7] D. K. Kim, "Comparison of optimal thermal performances of finned tube annuli with various fin shapes," *Int J Heat Mass Transf*, vol. 175, p. 121402, 2021, doi: 10.1016/j.ijheatmasstransfer.2021.121402.

[8] M. Sheikholeslami, M. Gorji-Bandpy, and D. D. Ganji, "Experimental study on turbulent flow and heat transfer in an air to water heat exchanger using perforated circular-ring," *Exp Therm Fluid Sci*, vol. 70, pp. 185–195, 2016, doi: 10.1016/j.expthermflusci.2015.09.002.

[9] M. Sheikholeslami, M. Gorji-Bandpy, and D. D. Ganji, "Effect of discontinuous helical turbulators on heat transfer characteristics of double pipe water to air heat exchanger," *Energy Convers Manag*, vol. 118, pp. 75–87, 2016, doi: 10.1016/j.enconman.2016.03.080.

[10] S. Sivalakshmi, M. Raja, and G. Gowtham, "Effect of helical fins on the performance of a double pipe heat exchanger," *Mater Today Proc*, vol. 43, pp. 1128–1131, 2020, doi: 10.1016/j.matpr.2020.08.563.

[11] C. Thianpong, P. Eiamsa-ard, K. Wongcharee, and S. Eiamsa-ard, "Compound heat transfer enhancement of a dimpled tube with a twisted tape swirl generator," 2009. doi: 10.1016/j.icheatmasstransfer.2009.03.026.

[12] N. Targui and H. Kahalerras, "Analysis of a double pipe heat exchanger performance by use of porous baffles and pulsating flow," *Energy Convers Manag*, vol. 76, pp. 43–54, 2013, doi: 10.1016/j.enconman.2013.07.022.

[13] T. Alam and M. H. Kim, "A comprehensive review on single phase heat transfer enhancement techniques in heat exchanger applications," *Renewable and Sustainable Energy Reviews*, vol. 81, no. June 2017, pp. 813–839, 2018, doi: 10.1016/j.rser.2017.08.060.

[14] M. Omidi, M. Farhadi, and M. Jafari, "A comprehensive review on double pipe heat exchangers," *Appl Therm Eng*, vol. 110, pp. 1075–1090, 2017, doi: 10.1016/j.applthermaleng.2016.09.027.

[15] M. H. Mousa, N. Miljkovic, and K. Nawaz, "Review of heat transfer enhancement techniques for single phase flows," *Renewable and Sustainable Energy Reviews*, vol. 137, no. December 2020, p. 110566, 2021, doi: 10.1016/j.rser.2020.110566.

[16] J. P. Richter, *The notebooks of Leonardo da Vinci*, vol. 2. Courier Corporation, 1970.

[17] T. P. Grazulis, *The tornado: nature's ultimate windstorm*. University of Oklahoma Press, 2001.

[18] M. Jakob, *Heat Transfer*, no. v. 1. in Heat Transfer. Wiley, 1949. [Online]. Available: https://books.google.com.eg/books?id=owgkAAAAMAAJ

[19] L. Moody, "Friction Factor for Pipe Flow," *Trans. ASME*, vol. 66, Jan. 1944.

[20] C. J. Stairmand, "The design and performance of cyclone separators," *Trans. Inst. Chem. Engrs.*, vol. 29, pp. 356–362, 1951.

[21] R. M. Manglik and A. E. Bergles, "Heat Transfer and Pressure Drop Correlations for Twisted-Tape Inserts in Isothermal Tubes: Part I—Laminar Flows," *J Heat Transfer*, vol. 115, no. 4, pp. 881–889, Nov. 1993, doi: 10.1115/1.2911383.

[22] R. M. Manglik and A. E. Bergles, "Heat transfer and pressure drop correlations for twisted-tape inserts in isothermal tubes: Part II—transition and turbulent flows," *J Heat Transfer*, vol. 115, no. 4, pp. 890–896, Nov. 1993, doi: 10.1115/1.2911384.

[23] S. W. HONG and A. E. BERGLES, "Augmentation of Laminar Flow Heat Transfer in Tubes By Means of Twisted-Tape Inserts.," *Trans. a.S.M.E., Ser. C, J. Heat Transfer*, vol. 98, no. 2 (MAY, 1976), pp. 251–256, 1976.

[24] S. Eiamsa-Ard, P. Somkleang, C. Nuntadusit, and C. Thianpong, "Heat transfer enhancement in tube by inserting uniform/non-uniform twisted-tapes with alternate axes: Effect of rotated-axis length," *Appl Therm Eng*, vol. 54, no. 1, pp. 289–309, 2013, doi: 10.1016/j.applthermaleng.2013.01.041.

[25] B. V Patel, R. M. Sarviya, and S. P. S. Rajput, "Experimental study of thermal characteristics of alternatively twisted swirl generator tape in a heat exchanger tube," *Energy Sources, Part A: Recovery, Utilization, and Environmental Effects*, vol. 44, no. 4, pp. 9603–9619, Dec. 2022, doi: 10.1080/15567036.2022.2134520.

[26] P. Murugesan, K. Mayilsamy, and S. Suresh, "Turbulent heat transfer and pressure drop in tube fitted with square-cut twisted tape," *Chin J Chem Eng*, vol. 18, no. 4, pp. 609–617, 2010, doi: 10.1016/S1004-9541(10)60264-9.

[27] S. Tamna, Y. Kaewkohkiat, S. Skullong, and P. Promvonge, "Heat transfer enhancement in tubular heat exchanger with double V-ribbed twisted-tapes," *Case Studies in Thermal Engineering*, vol. 7, pp. 14–24, 2016, doi: 10.1016/j.csite.2016.01.002.

[28] A. García, J. P. Solano, P. G. Vicente, and A. Viedma, “Enhancement of laminar and transitional flow heat transfer in tubes by means of wire coil inserts,” *Int J Heat Mass Transf*, vol. 50, no. 15–16, pp. 3176–3189, 2007, doi: 10.1016/j.ijheatmasstransfer.2007.01.015.

[29] P. Naphon, “Effect of coil-wire insert on heat transfer enhancement and pressure drop of the horizontal concentric tubes,” *International Communications in Heat and Mass Transfer*, vol. 33, no. 6, pp. 753–763, 2006, doi: 10.1016/j.icheatmasstransfer.2006.01.020.

[30] J. Y. San, W. C. Huang, and C. A. Chen, “Experimental investigation on heat transfer and fluid friction correlations for circular tubes with coiled-wire inserts,” *International Communications in Heat and Mass Transfer*, vol. 65, pp. 8–14, 2015, doi: 10.1016/j.icheatmasstransfer.2015.04.008.

[31] S. Eiamsa-ard, K. Wongcharee, and S. Sripattanapipat, “3-D Numerical simulation of swirling flow and convective heat transfer in a circular tube induced by means of loose-fit twisted tapes,” *International Communications in Heat and Mass Transfer*, vol. 36, no. 9, pp. 947–955, Nov. 2009, doi: 10.1016/j.icheatmasstransfer.2009.06.014.

[32] H. Sadighi Dizaji, S. Jafarmadar, and M. Hashemian, “The effect of flow, thermodynamic and geometrical characteristics on exergy loss in shell and coiled tube heat exchangers,” *Energy*, vol. 91, pp. 678–684, Nov. 2015, doi: 10.1016/j.energy.2015.08.084.

[33] S. Chourasia, A. Kumar, and B. K. Ahirwar, “Numerical study of fluid flow and heat transfer in a circular tube with Trapezoidal-cut twisted tape inserts,” *J Therm Anal Calorim*, 2024, doi: 10.1007/s10973-024-13389-w.

[34] A. Hasanpour, M. Farhadi, and K. Sedighi, “Experimental heat transfer and pressure drop study on typical, perforated, V-cut and U-cut twisted tapes in a helically corrugated heat exchanger,” *International Communications in Heat and Mass Transfer*, vol. 71, pp. 126–136, 2016, doi: 10.1016/j.icheatmasstransfer.2015.12.032.

[35] T. Lee, Y. T. Guahk, N. Kim, H. Lee, and M. J. Lee, “Stability and emission characteristics of ammonia-air flames in a lean-lean fuel staging tangential injection combustor,” *Combust Flame*, vol. 248, Feb. 2023, doi: 10.1016/j.combustflame.2022.112593.

[36] C. I. Staschus and R. A. Frederick, “An overview of combustion instabilities and rocket engine injector design,” in *52nd AIAA/SAE/ASEE Joint Propulsion Conference, 2016*, American Institute of Aeronautics and Astronautics Inc, AIAA, 2016. doi: 10.2514/6.2016-4724.

[37] N. Syred and J. M. Bekr, “Combustion in Swirling Flows: A FReview,” 1974.

[38] M. Zhao, T. Ye, C. Cao, T. Zhou, and M. Zhu, “Study of sonic injection from circular injector into a supersonic cross-flow using large eddy simulation,” *Int J Hydrogen Energy*, vol. 41, no. 39, pp. 17657–17669, Oct. 2016, doi: 10.1016/j.ijhydene.2016.07.018.

[39] F. N. M. Elwekeel and A. M. M. Abdala, “Numerical Analysis of the Heat Transfer Performance of the Absorber Tube of a Parabolic Trough Solar Collector Using the Swirling Flow Technique,” *Case Studies in Thermal Engineering*, p. 104801, 2024.

[40] A. Durmuş, “Heat transfer and exergy loss in a concentric heat exchanger with snail entrance,” *International Communications in Heat and Mass Transfer*, vol. 29, no. 3, pp. 303–312, 2002, doi: 10.1016/S0735-1933(02)00320-2.

[41] E. Kavak Akpinar, Y. Bicer, C. Yildiz, and D. Pehlivan, "Heat transfer enhancements in a concentric double pipe exchanger equipped with swirl elements," 2004. doi: 10.1016/S0735-1933(04)00072-7.

[42] B. Chen, K. Ho, F. G. F. Qin, R. Jiang, Y. A. Abakr, and A. Chan, "Validation and Visualization of Decaying Vortex Flow in an Annulus," *Energy Procedia*, vol. 75, pp. 3098–3104, 2015, doi: 10.1016/j.egypro.2015.07.640.

[43] B. Chen, K. Ho, Y. A. Abakr, and A. Chan, "Fluid dynamics and heat transfer investigations of swirling decaying flow in an annular pipe Part 1: Review, problem description, verification and validation," *Int J Heat Mass Transf*, vol. 97, pp. 1029–1043, Jun. 2016, doi: 10.1016/j.ijheatmasstransfer.2015.07.129.

[44] B. Chen, K. Ho, Y. A. Abakr, and A. Chan, "Fluid dynamics and heat transfer investigations of swirling decaying flow in an annular pipe Part 2: Fluid flow," *Int J Heat Mass Transf*, vol. 97, pp. 1012–1028, Jun. 2016, doi: 10.1016/j.ijheatmasstransfer.2016.01.069.

[45] B. Chen, F. G. F. Qin, Y. Shao, H. Xiao, S. Huang, and K. Ho, "The development of swirling decaying laminar flow in an annular pipe," *E3S Web of Conferences*, vol. 51, pp. 1–4, 2018, doi: 10.1051/e3sconf/20185103001.

[46] B. Chen, K. Ho, H. Xiao, Y. A. Abakr, and A. Chan, "The effects of swirling decaying flow towards pipe entry length and heat transfer in an annular pipe," *Int J Heat Mass Transf*, vol. 123, pp. 668–677, Aug. 2018, doi: 10.1016/j.ijheatmasstransfer.2017.12.160.

[47] D. of M. Engineering. Stanford University. Kays, W. M., United States., Office of Naval Research., "Numerical solutions for laminar flow heat transfer in circular tubes.," 1953.

[48] R. K. Shah and M. S. Bhatti, "'Laminar convective heat transfer in ducts,' in Handbook of single -phase conective heat transfer," *Handbook of single-phase convective heat transfer*, vol. 3, 1987.

[49] M. Jafari, M. Farhadi, and K. Sedighi, "Thermal performance enhancement in a heat exchanging tube via a four-lobe swirl generator: An experimental and numerical approach," *Appl Therm Eng*, vol. 124, pp. 883–896, Sep. 2017, doi: 10.1016/j.applthermaleng.2017.06.095.

[50] M. Jafari, M. Farhadi, and K. Sedighi, "An experimental study on the effects of a new swirl generator on thermal performance of a circular tube," *International Communications in Heat and Mass Transfer*, vol. 87, no. August, pp. 277–287, 2017, doi: 10.1016/j.icheatmasstransfer.2017.07.016.

[51] D. W. Baker, "Decay of swirling, turbulent flow of incompressible fluids in long pipes," *Ph. D., Thesis*, 1967.

[52] Y. SENOO and T. NAGATA, "Swirl Flow in Long Pipes with Different Roughness," *Bulletin of JSME*, vol. 15, no. 90, pp. 1514–1521, 1972, doi: 10.1299/jsme1958.15.1514.

[53] F. Kreith and O. K. Sonju, "The decay of a turbulent swirl in a pipe," *J Fluid Mech*, vol. 22, no. 2, pp. 257–271, 1965, doi: 10.1017/S0022112065000733.

[54] C. J. Scott, "A Series Solution for Decay of Swirl in an Annulus," *J Appl Mech*, vol. 39, no. 1, pp. 289–290, Mar. 1972, doi: 10.1115/1.3422635.

[55] O. Kitoh, "Experimental study of turbulent swirling flow in a straight pipe," *J Fluid Mech*, vol. 225, pp. 445–479, 1991, doi: 10.1017/S0022112091002124.

[56] M. J. Reader-Harris, "The decay of swirl in a pipe," 1994.

[57] W. Steenbergen and J. Voskamp, "The rate of decay of swirl in turbulent pipe flow," 1998.

[58] H. J. Sheen, W. J. Chen, S. Y. Jeng, and T. L. Huang, "Correlation of Swirl Number for a Radial-Type Swirl Generator," *Exp Therm Fluid Sci*, vol. 12, no. 4, pp. 444–451, 1996, doi: 10.1016/0894-1777(95)00135-2.

[59] A. F. Najafi, S. M. Mousavian, and K. Amini, "Numerical investigations on swirl intensity decay rate for turbulent swirling flow in a fixed pipe," *Int J Mech Sci*, vol. 53, no. 10, pp. 801–811, Oct. 2011, doi: 10.1016/j.ijmecsci.2011.06.011.

[60] M. Cavazzuti and M. A. Corticelli, "Convective heat transfer of turbulent decaying swirled flows in concentric annular pipes," *Appl Therm Eng*, vol. 120, pp. 517–529, 2017, doi: 10.1016/j.applthermaleng.2017.04.015.

[61] T. Yan, J. Qu, X. Sun, Y. Chen, Q. Hu, and W. Li, "Numerical evaluation on the decaying swirling flow in a multi-lobed swirl generator," *Engineering Applications of Computational Fluid Mechanics*, vol. 14, no. 1, pp. 1198–1214, Jan. 2020, doi: 10.1080/19942060.2020.1816494.

[62] F. Seibold, P. Ligrani, and B. Weigand, "Flow and heat transfer in swirl tubes — A review," May 15, 2022, *Elsevier Ltd*. doi: 10.1016/j.ijheatmasstransfer.2021.122455.

[63] C. R. Hedlund, G. P. Student M Ligrani Professor, and H. B. Moon Principal Engineer Glezer, "Heat Transfer and Flow Phenomena in a Swirl Chamber Simulating Turbine Blade Internal Cooling," 1999. [Online]. Available: http://www.asme.org/about-asme/terms-of-use

[64] B. Kobiela, *Wärmeübertragung in einer Zyklonkühlkammer einer Gasturbinenschaufel*. Verlag Dr. Hut, 2014.

[65] P. Novotny, "Stability of swirl tube flow," 2019.

[66] F. Kreith and D. Margolis, "Heat transfer and friction in turbulent vortex flow," *Applied Scientific Research*, vol. 8, no. 1, pp. 457–473, 1959, doi: 10.1007/BF00411769.

[67] M. Bruschewski, *New Insights Into the Swirling Flow in Turbine Blade Cooling Models Obtained Via Magnetic Resonance Velocimetry*. Shaker Verlag, 2017.

[68] S. K. Saha, A. Dutta, and S. K. Dhal, "Friction and heat transfer characteristics of laminar swirl flow through a circular tube fitted with regularly spaced twisted-tape elements," *Int J Heat Mass Transf*, vol. 44, no. 22, pp. 4211–4223, Nov. 2001, doi: 10.1016/S0017-9310(01)00077-1.

[69] M. A. Rahman, "The influence of geometrical and operational parameters on thermofluid performance of discontinuous colonial self-swirl-inducing baffle plate in a tubular heat exchanger," *Heat Transfer*, vol. 53, no. 2, pp. 328–345, Mar. 2024, doi: 10.1002/htj.22956.

[70] Z. Esmaeili, S. M. Vahidhosseini, and S. Rashidi, "A novel design of double pipe heat exchanger with innovative turbulator inside the shell-side space," *International Communications in Heat and Mass Transfer*, vol. 155, Jun. 2024, doi: 10.1016/j.icheatmasstransfer.2024.107523.

[71] S. Kumar, P. Dinesha, A. Narayanan, and R. Nanda, “Effect of hemispherical turbulators in a double-pipe heat exchanger for heat transfer augmentation,” *Journal of Turbulence*, vol. 21, no. 3, pp. 166–185, 2020, doi: 10.1080/14685248.2020.1742344.

[72] S. Yadav and S. K. Sahu, “Heat transfer augmentation in double pipe water to air counter flow heat exchanger with helical surface disc turbulators,” *Chemical Engineering and Processing - Process Intensification*, vol. 135, no. October 2018, pp. 120–132, 2019, doi: 10.1016/j.cep.2018.11.018.

[73] W. Duangthongsuk and S. Wongwises, “An experimental investigation of the heat transfer and pressure drop characteristics of a circular tube fitted with rotating turbine-type swirl generators,” *Exp Therm Fluid Sci*, vol. 45, pp. 8–15, 2013, doi: 10.1016/j.expthermflusci.2012.09.009.

[74] W. Duangthongsuk and S. Wongwises, “Comparison of the heat transfer performance and friction characteristics between fixed and rotating turbine-type swirl generators fitted in a small circular tube,” *Exp Therm Fluid Sci*, vol. 50, pp. 222–228, Oct. 2013, doi: 10.1016/j.expthermflusci.2013.04.007.

[75] A. Bartwal, A. Gautam, M. Kumar, C. K. Mangrulkar, and S. Chamoli, “Thermal performance intensification of a circular heat exchanger tube integrated with compound circular ring–metal wire net inserts,” *Chemical Engineering and Processing: Process Intensification*, vol. 124, no. December 2017, pp. 50–70, 2018, doi: 10.1016/j.cep.2017.12.002.

[76] S. K. Saha and A. Dutta, “Thermohydraulic study of laminar swirl flow through a circular tube fitted with twisted tapes,” *J Heat Transfer*, vol. 123, no. 3, pp. 417–427, Jun. 2001, doi: 10.1115/1.1370500.

[77] P. Sivashanmugam and S. Suresh, “Experimental studies on heat transfer and friction factor characteristics of turbulent flow through a circular tube fitted with regularly spaced helical screw-tape inserts,” *Appl Therm Eng*, vol. 27, no. 8–9, pp. 1311–1319, 2007, doi: 10.1016/j.applthermaleng.2006.10.035.

[78] W. Yang *et al.*, “Innovative design for thermoelectric power generation: Two-stage thermoelectric generator with variable twist ratio twisted tapes optimizing maximum output,” *Appl Energy*, vol. 363, Jun. 2024, doi: 10.1016/j.apenergy.2024.123047.

[79] S. A. Orszagt, “Analytical theories of turbulence,” 1970.

[80] L. H. Hodges, W. Reichelderfer, J. E. Caskey, and E. Volume, “DEPARTMENT OF COMMERCE MONTHLY WEATHER REVIEW GENERAL CIRCULATION EXPERIMENTS WITH THE PRIMITIVE EQUATIONS I. THE BASIC EXPERIMENT* 100 MONTHLY WEATHER REVIEW CONTENTS,” 1963.

[81] G. E. P. Box and K. B. Wilson, “On the Experimental Attainment of Optimum Conditions,” *Journal of the Royal Statistical Society: Series B (Methodological)*, vol. 13, no. 1, pp. 1–38, Jan. 1951, doi: 10.1111/j.2517-6161.1951.tb00067.x.

[82] M. R. Shakeel and E. M. A. Mokheimer, “Swirl flow in annular geometry with varying cross-section,” *Engineering Applications of Computational Fluid Mechanics*, vol. 16, no. 1, pp. 1154–1172, 2022, doi: 10.1080/19942060.2022.2076744.

[83] B. E. Launder and D. B. Spalding, “The numerical computation of turbulent flows,” *Comput Methods Appl Mech Eng*, vol. 3, no. 2, pp. 269–289, 1974, doi: 10.1016/0045-7825(74)90029-2.

[84] V. Yakhot and S. A. Orszag, “Renormalization group analysis of turbulence. I. Basic theory,” *J Sci Comput*, vol. 1, no. 1, pp. 3–51, 1986, doi: 10.1007/BF01061452.

[85] T.-H. Shih, W. W. Liou, A. Shabbir, Z. Yang, and J. Zhu, “A new k-ϵ eddy viscosity model for high reynolds number turbulent flows,” *Comput Fluids*, vol. 24, no. 3, pp. 227–238, Mar. 1995, doi: 10.1016/0045-7930(94)00032-T.

[86] F. R. Menter, “Two-equation eddy-viscosity turbulence models for engineering applications,” *AIAA Journal*, vol. 32, no. 8, pp. 1598–1605, 1994, doi: 10.2514/3.12149.

[87] A. M. Jawarneh, “Heat Transfer Enhancement in Swirl Annulus Flows.”

[88] A. Rahman, F. Ernesto, R. Corredor, M. Bizhani, and E. Kuru, “A CFD SIMULATION OF NEAR WALL TURBULENT FLOW IN CONCENTRIC ANNULUS,” 2013. [Online]. Available: http://asmedigitalcollection.asme.org/OMAE/proceedings-pdf/OMAE2013/55416/V007T08A068/4431635/v007t08a068-omae2013-11211.pdf

[89] T. Parra, R. Perez, M. A. Rodriguez, F. Castro, R. Z. Szasz, and A. Gutkowski, “Numerical Simulation of Swirling Flows - Heat Transfer Enhancement,” *J Fluid Flow Heat Mass Transf*, no. January, 2015, doi: 10.11159/jffhmt.2015.001.

[90] X. Xiong, M. A. Rahman, and Y. Zhang, “RANS Based Computational Fluid Dynamics Simulation of Fully Developed Turbulent Newtonian Flow in Concentric Annuli,” *Journal of Fluids Engineering, Transactions of the ASME*, vol. 138, no. 9, Sep. 2016, doi: 10.1115/1.4033314.

[91] L. Xu, J. Lan, Y. Ma, J. Gao, and Y. Li, “Numerical study on heat transfer by swirling impinging jets issuing from a screw-thread nozzle,” *Int J Heat Mass Transf*, vol. 115, pp. 232–237, 2017, doi: 10.1016/j.ijheatmasstransfer.2017.07.053.

[92] C. Luo, K. W. Song, and T. Tagawa, “Heat transfer enhancement of a double pipe heat exchanger by Co-Twisting oval pipes with unequal twist pitches,” *Case Studies in Thermal Engineering*, vol. 28, Dec. 2021, doi: 10.1016/j.csite.2021.101411.

[93] M. Hangi, A. Rahbari, and W. Lipiński, “Design improvement of compact double-pipe heat exchangers equipped with tube-side helical insert and annulus-side helical strip: Hydrothermal and exergy analyses,” *Appl Therm Eng*, vol. 190, May 2021, doi: 10.1016/j.applthermaleng.2021.116805.

[94] A. El Maakoul, M. El Metoui, A. Ben Abdellah, S. Saadeddine, and M. Meziane, “Numerical investigation of thermohydraulic performance of air to water double-pipe heat exchanger with helical fins,” *Appl Therm Eng*, vol. 127, pp. 127–139, 2017, doi: 10.1016/j.applthermaleng.2017.08.024.

[95] C. Liu *et al.*, “Experimental and numerical study on flow field characteristics of a combustion chamber with double-stage counter-rotating swirlers,” *International Communications in Heat and Mass Transfer*, vol. 151, p. 107245, Feb. 2024, doi: 10.1016/j.icheatmasstransfer.2024.107245.

[96] G. F. C. Rogers and Y. R. Mayhew, *Thermodynamic and Transport Properties of Fluids*, Fifth. Oxford, UK: Blackwell Publishing, 1995.

[97] W. M. Kays, M. E. Crawford, and B. Weigand, *Convective Heat and Mass Transfer*. Boston: McGraw-Hill Higher, 2005. [Online]. Available: https://nusearch.nottingham.edu.my/primo-explore/fulldisplay?docid=44NOTMY_ALMA2117822420005562&context=L&vid=44NOTMY&lang=en_US&search_scope=44NOTMY_COMPLETE&adaptor=Local Search Engine&tab=44notmy_complete&query=any,contains,Convective heat and mass tra

[98] R. K. Shah and A. L. London, "Discussion—An Overview for the Designer and the Applied Mathematician," in *Laminar Flow Forced Convection in Ducts*, Elsevier, 1978, pp. 385–420. doi: 10.1016/B978-0-12-020051-1.50022-X.

[99] V. Gnielinski, "Heat transfer coefficients for turbulent flow in concentric annular ducts," *Heat Transfer Engineering*, vol. 30, no. 6, pp. 431–436, May 2009, doi: 10.1080/01457630802528661.

[100] F. P. Incorpera and D. P. De Witt, *Fundamentals of Heat and Mass Transfer*, Third Edit. Singapore, 1976.

[101] W. M. Rohsenow, J. P. (James P.) Hartnett, and Y. I. Cho, *Handbook of heat transfer*. McGraw-Hill, 1998.

[102] J. Dirker, "HEAT TRANSFER COEFFICIENTS IN CONCENTRIC ANNULI," 2002.

[103] K. Hirbodi, M. Yaghoubi, and D. M. Warsinger, "New Nusselt number correlations for developing and fully developed laminar flows in concentric circular annular ducts," *International Communications in Heat and Mass Transfer*, vol. 134, May 2022, doi: 10.1016/j.icheatmasstransfer.2022.105936.

[104] R. H. S. Winterton, "Where did the Dittus and Boelter equation come from?," Elswier Science Ltd, 1998.

[105] G. A. HAWKINS, "Heat Transmission. William H. McAdams. McGraw-Hill, New York-London, ed. 3, 1954. xiv + 532 pp. Illus. $8.50," *Science (1979)*, vol. 120, no. 3128, pp. 984–984, Dec. 1954, doi: 10.1126/science.120.3128.984.

[106] F. W. Dittus and L. M. K. Boelter, "Heat transfer in automobile radiators of the tubular type," *International Communications in Heat and Mass Transfer*, vol. 12, no. 1, pp. 3–22, Jan. 1985, doi: 10.1016/0735-1933(85)90003-X.

[107] A. S. Foust and G. A. Christian, "Non-boiling heat transfer coefficients in annuli," *American Institute of Chemical Engineers*, vol. 36, pp. 541–554, 1940.

[108] C. C. Monrad, "Heat transfer by convection in annular spaces," *Trans. AIChE*, vol. 38, pp. 593–611, 1942.

[109] E. S. Davis and N. York, "Heat Transfer and Pressure Drop in Annuli," 1943. [Online]. Available: http://tribology.asmedigitalcollection.asme.org/fluidsengineering/article-pdf/65/7/755/6964779/755_1.pdf

[110] J. H. Wiegand, "Discussion on Annular Heat Transfer Coeffcients for Turbulent Flow," *AIChE*, vol. 41, pp. 147–153, 1945.

[111] R. P. Stein and W. Begell, "Heat transfer to water in turbulent flow in internally heated annuli," *AIChE Journal*, vol. 4, no. 2, pp. 127–131, 1958, doi: 10.1002/aic.690040203.

[112] W. M. Kays and E. Y. Leung, “Heat transfer in annular passages—hydrodynamically developed turbulent flow with arbitrarily prescribed heat flux,” *Int J Heat Mass Transf*, vol. 6, no. 7, pp. 537–557, 1963, doi: https://doi.org/10.1016/0017-9310(63)90012-7.

[113] B. S. Petukhov and L. I. Roizen, “Generalized relationships for heat transfer in turbulent flow of gas in tubes of annular section,” *Teplofizika vysokikh temperatur*, vol. 2, no. 1, pp. 78–81, 1964.

[114] R. B. Crookston, R. R. Rothfus, and R. I. Kermode, “Turbulent heat transfer in annuli with small cores,” *Int J Heat Mass Transf*, vol. 11, no. 3, pp. 415–426, Mar. 1968, doi: 10.1016/0017-9310(68)90086-0.

[115] H. Martin and M. Nilles, “Radiale Wärmeleitung in durchströmten Schüttungsrohren,” *Chemie Ingenieur Technik*, vol. 65, no. 12, pp. 1468–1477, Dec. 1993, doi: 10.1002/cite.330651206.

[116] V. Gnielinski, “Ein neues Berechnungsverfahren für die Wärmeübertragung im Übergangsbereich zwischen laminarer und turbulenter Rohrströmung,” *Forsch Ingenieurwes*, vol. 61, no. 9, pp. 240–248, Sep. 1995, doi: 10.1007/BF02607964.

[117] J. Dirker, H. Van Der Vyver, and J. P. Meyer, “Convection heat transfer in concentric annuli,” *Experimental Heat Transfer*, vol. 17, no. 1, pp. 19–29, 2004, doi: 10.1080/08916150490246528.

[118] V. Gnielinski, “Berechnung des Druckverlustes in Glatten Konzentrischen Ringspalten bei Ausgebildeter Laminarer und Turbulenter Isothermer Strömung,” *Chem Ing Tech*, vol. 79, no. 1–2, pp. 91–95, Jan. 2007, doi: 10.1002/cite.200600126.

[119] B. S. Petukhov and V. V Kirillov, “On heat exchange at turbulent flow of liquid in pipes,” *Teploenergetika*, vol. 4, no. 4, pp. 63–68, 1958.

[120] M. Bernardi, V. Silveira Jr., V. R. N. Telis, A. L. Gabas, and J. Telis-Romero, “Forced convection to laminar flow of liquid egg yolk in circular and annular ducts,” *Brazilian Journal of Chemical Engineering*, vol. 26, no. 2, pp. 287–298, Jun. 2009, doi: 10.1590/S0104-66322009000200006.

[121] H. Abou-Ziyan, R. Ameen, and K. Elsayed, “Fluid flow and convection heat transfer in concentric and eccentric cylindrical annuli of different radii ratios for Taylor-Couette-Poiseuille flow,” *Advances in Mechanical Engineering*, vol. 13, no. 8, 2021, doi: 10.1177/16878140211040731.

[122] H. Darcy, *Recherches Experimentales Relatives Aux Mouvements de l’Eau Dans Tuyauz*. Paris: Mallet-Bachelier, 1857.

[123] O. C. Jones and J. C. M. Leung, “An improvement in the calculation of turbulent friction in smooth concentric annuli.,” vol. 103, no. December 1981, 1979.

[124] R. L. Webb and E. R. G. Eckert, “Application of rough surfaces to heat exchanger design,” *Int J Heat Mass Transf*, vol. 15, no. 9, pp. 1647–1658, 1972, doi: 10.1016/0017-9310(72)90095-6.

[125] R. Karwa, C. Sharma, and N. Karwa, “Performance Evaluation Criterion at Equal Pumping Power for Enhanced Performance Heat Transfer Surfaces,” vol. 2013, no. 1, 2013, doi: http://dx.doi.org/10.1155/2013/370823.

[126] O. Reynolds, “An Experimental Investigation of the Circumstances Which Determine Whether the Motion of Water Shall Be Direct or Sinuous, and of the Law of Resistance in Parallel Channels,” 1883.

[127] F. M. White, *Fluid mechanics (seventh ed.).*, Seventh. New York: McGraw-Hill, 2009.

[128] M. Ahmadvand, A. F. Najafi, and S. Shahidinejad, “An experimental study and CFD analysis towards heat transfer and fluid flow characteristics of decaying swirl pipe flow generated by axial vanes,” *Meccanica*, vol. 45, no. 1, pp. 111–129, 2010, doi: 10.1007/s11012-009-9228-9.

[129] N. A. Chigier and J. M. Beér, “Velocity and static-pressure distributions in swirling air jets issuing from annular and divergent nozzles,” *Journal of Fluids Engineering, Transactions of the ASME*, vol. 86, no. 4, pp. 788–796, 1964, doi: 10.1115/1.3655954.

[130] N. Kerr and D. Fraser, “Swirl part 1: Effect on axisymmetrical turbulent jets,” *J. Inst. Fuel*, vol. 38, no. 299, p. 519, 1965.

[131] B. M. Vaziri and A. Shahsavand, “Optimal Selection of Supersonic Separators Inlet Velocity Components via Maximization of Swirl Strength and Centrifugal Acceleration,” *Separation Science and Technology (Philadelphia)*, vol. 50, no. 5, pp. 752–759, Mar. 2015, doi: 10.1080/01496395.2014.958782.

[132] M. Cavazzuti and M. A. Corticelli, “Convective heat transfer of turbulent decaying swirled flows in concentric annular pipes,” *Appl Therm Eng*, vol. 120, pp. 517–529, 2017, doi: 10.1016/j.applthermaleng.2017.04.015.

[133] T. Jianping Gu Weizao Shen Jiarui Liu Wenyan, “An Investigation of the Swirling Flow and Heat Transfer in a Duct,” 1992.

[134] Y. Wang and V. Yang, “Central recirculation zones and instability waves in internal swirling flows with an annular entry,” *Physics of Fluids*, vol. 30, no. 1, Jan. 2018, doi: 10.1063/1.5000967.

[135] M. Percin, M. Vanierschot, and B. W. van Oudheusden, “Analysis of the pressure fields in a swirling annular jet flow,” *Exp Fluids*, vol. 58, no. 12, Dec. 2017, doi: 10.1007/s00348-017-2446-3.

[136] T. F. Ayinde, “A generalized relationship for swirl decay in laminar,” *Sciences-New York*, vol. 35, no. April, pp. 129–137, 2010.

[137] G. Vignat, D. Durox, and S. Candel, “The suitability of different swirl number definitions for describing swirl flows: Accurate, common and (over-) simplified formulations,” Mar. 01, 2022, *Elsevier Ltd*. doi: 10.1016/j.pecs.2021.100969.

[138] “Ansys Fluent Theory Guide,” 2022. [Online]. Available: http://www.ansys.com

[139] M. O. Deville, *An Introduction to the Mechanics of Incompressible Fluids*. Cham: Springer International Publishing, 2022. doi: 10.1007/978-3-031-04683-4.

[140] ANSYS Inc., *ANSYS Fluent Meshing User ' s Guide*, vol. 15317, no. July. 2021.

[141] S. A. Orszag, V. Yakhot, W. S. Flannery, and F. Boysan, “Renormalization group modeling and turbulence simulations,” in *Near-wall turbulent flows*, Elsevier; , 1993, p. 1031. [Online]. Available: https://www.tib.eu/de/suchen/id/BLCP%3ACN003216810

[142] A. Salama, "Velocity profile representation for fully developed turbulent flows in pipes: A modified power law," *Fluids*, vol. 6, no. 10, Oct. 2021, doi: 10.3390/fluids6100369.

[143] M. García-Villalba, A. G. Kidanemariam, and M. Uhlmann, "DNS of vertical plane channel flow with finite-size particles: Voronoi analysis, acceleration statistics and particle-conditioned averaging," *International Journal of Multiphase Flow*, vol. 46, pp. 54–74, Nov. 2012, doi: 10.1016/j.ijmultiphaseflow.2012.05.007.

[144] P. Schlatter and R. Örlü, "Assessment of direct numerical simulation data of turbulent boundary layers," *J Fluid Mech*, vol. 659, pp. 116–126, 2010, doi: 10.1017/S0022112010003113.

[145] S.-E. Kim and F. Boysan, "Application of CFD to environmental flows," *Journal of Wind Engineering and Industrial Aerodynamics*, vol. 81, no. 1–3, pp. 145–158, May 1999, doi: 10.1016/S0167-6105(99)00013-6.

[146] E. H. Song, K. B. Lee, and S. H. Rhi, "Thermal and flow simulation of concentric annular heat pipe with symmetric or asymmetric condenser," *Energies (Basel)*, vol. 14, no. 11, Jun. 2021, doi: 10.3390/en14113333.

[147] Y. Xu, G. S. He, V. Kulkarni, and J. J. Wang, "Experimental investigation of influence of Reynolds number on synthetic jet vortex rings impinging onto a solid wall," *Exp Fluids*, vol. 58, no. 1, Jan. 2017, doi: 10.1007/s00348-016-2287-5.

[148] Y. Yang, D. S.-K. Ting, and S. Ray, "Nusselt number-turbulent strain rate relationship: Forced convection of a flat surface downstream of a pair of side-by-side rectangular strips," *Exp Therm Fluid Sci*, vol. 128, no. 8, p. 110437, Oct. 2021, doi: 10.1016/j.expthermflusci.2021.110437.

[149] M. Rahimi-Esbo, Y. Vazifeshenas, A. K. Asboei, R. Mohammadyari, and Vandana, "Numerical simulation of twisted tapes fitted in circular tube consisting of alternate axes and regularly spaced tapes," *Acta Scientiarum - Technology*, vol. 40, 2018, doi: 10.4025/actascitechnol.v40i1.37348.

[150] S. Maleki, "Excel Solver Online Help." Accessed: Apr. 20, 2024. [Online]. Available: https://www.solver.com/excel-solver-online-help

[151] Y. SENOO and T. NAGATA, "Swirl Flow in Long Pipes with Different Roughness," *Bulletin of JSME*, vol. 15, no. 90, pp. 1514–1521, 1972, doi: 10.1299/jsme1958.15.1514.

[152] D M Halsey, "Flowmeters in swirling flows," *J Phys E*, vol. 20, no. 10, pp. 1294–1294, Oct. 1987, doi: 10.1088/0022-3735/20/10/537.

[153] H. Li and Y. Tomita, "Characteristics of Swirling Flow in a Circular Pipe," *J Fluids Eng*, vol. 116, no. 2, pp. 370–373, Jun. 1994, doi: 10.1115/1.2910283.

[154] M. J. Reader-Harris, "The decay of swirl in a pipe," *Int J Heat Fluid Flow*, vol. 15, no. 3, pp. 212–217, Jun. 1994, doi: 10.1016/0142-727X(94)90040-X.

[155] O. M. Oyewola, A. S. Akinwonmi, O. O. Ajide, and T. O. A. Salau, "Effect of Swirl on Temperature Decay Function in Straight Blade Liquid Fuel Swirl Burner," *International Journal of Heat and Technology*, vol. 40, no. 2, pp. 527–534, Apr. 2022, doi: 10.18280/ijht.400220.

[156] C. B. Solnordal, N. B. Gray, and G. K. Williams, "An experimental study of fluid through a heated annulus flow and heat transfer in decaying swirl," Springer Verlag, 1994.

[157] S. Barakat, H. Wang, T. Jin, W. Tao, and G. Wang, "Isothermal swirling flow characteristics and pressure drop analysis of a novel double swirl burner," *AIP Adv*, vol. 11, no. 3, Mar. 2021, doi: 10.1063/5.0041361.

[158] United Nations, "SDG 7 Policy Briefs 2021: Ensuring access to affordable, reliable, sustainable and modern energy for all," 2021. [Online]. Available: https://sustainabledevelopment.un.org/contact

[159] UNESCO, "SDG 9: Industry, innovation & infrastructure – Policy brief," UNESDOC Digital Library. Accessed: Aug. 08, 2025. [Online]. Available: https://www.unesco.org/reports/science/2021/sites/default/files/medias/fichiers/2022/08/USR21_policy-brief_SDG-9.pdf

[160] A. Alghafis, "Performance Enhanced In Reduction Of No x Emissions Using Swirl In A Combustion Procedure," 2023.

[161] S. Küfeoğlu, *Emerging Technologies: Value Creation for Sustainable Development*. 2022. doi: 10.1007/978-3-031-07127-0_9.

[162] T. Bali and B. A. Sarac, "Experimental investigation of decaying swirl flow through a circular pipe for binary combination of vortex generators," *International Communications in Heat and Mass Transfer*, vol. 53, pp. 174–179, 2014, doi: 10.1016/j.icheatmasstransfer.2014.02.030.

[163] M. Wannassi and F. Monnoyer, "Numerical simulation of the flow through the blades of a swirl generator," *Appl Math Model*, vol. 40, no. 2, pp. 1247–1259, 2016, doi: 10.1016/j.apm.2015.07.018.

[164] H. Wang, Y. Yang, B. Yang, Y. Tang, and W. Jing, "Analysis of stability and internal flow mechanisms in spiral annular flow with different swirlers," *Exp Therm Fluid Sci*, vol. 158, Oct. 2024, doi: 10.1016/j.expthermflusci.2024.111263.

Appendix A

Derivation of the Performance Enhancement Criterion

The performance enhancement criterion is derived by equating the pumping power of the plain and augmented tubes:

$$(\dot{V}\Delta P)_0 = (\dot{V}\Delta P)_{aug} \tag{A.1}$$

$\dot{V}$ represents the volumetric flow rate:

$$\dot{V} = \frac{\dot{m}}{\rho} \tag{A.2}$$

ΔP is the pressure drop recalled from Eq. (3.36).

Expressing Re in terms of $\dot{m}$:

$$Re = \frac{\rho u_{avg} D_{hd}}{\mu} = \frac{u_{avg} D_{hd}}{\nu} = \frac{4\dot{V}}{\pi D_{hd}\nu} = \frac{4\dot{m}}{\pi D_{hd}\mu} \tag{A.3}$$

Where ν is the kinematic viscosity. Substituting $\dot{V}$ and ΔP into Eq. A.1 yields:

$$\left(\frac{\dot{m}}{\rho}\left(f\left(\frac{L}{D}\right)\left(\frac{\rho u^2}{2}\right)\right)\right)_0 = \left(\frac{\dot{m}}{\rho}\left(f\left(\frac{L}{D}\right)\left(\frac{\rho u^2}{2}\right)\right)\right)_{aug} \tag{A.4}$$

Expressing $\dot{m}$ and u in terms of Re, the equation becomes:

$$\left(\frac{Re\mu\pi D}{4\rho}\left(f\left(\frac{L}{D}\right)\left(\frac{\rho}{2}\right)\left(\frac{Re\mu}{\rho D}\right)^2\right)\right)_0 = \left(\frac{Re\mu\pi D}{4\rho}\left(f\left(\frac{L}{D}\right)\left(\frac{\rho}{2}\right)\left(\frac{Re\mu}{\rho D}\right)^2\right)\right)_{aug} \tag{A.5}$$

Reorganising the equation:

$$\left(f.Re^3\left(\cancel{\frac{\mu^3\rho\pi D}{8\rho^3 D^3}}\right)\right)_0 = \left(f.Re^3\left(\cancel{\frac{\mu^3\rho\pi D}{8\rho^3 D^3}}\right)\right)_{aug} \tag{A.6}$$

Leading to the simplified form:

$$(f.Re^3)_0 = (f.Re^3)_{aug} \tag{A.7}$$

$$(f^{1/3}.Re)_0 = (f^{1/3}.Re)_{aug} \tag{A.8}$$

$$\frac{Re_0}{Re_{aug}} = \left(\frac{{f_{aug}}^{\frac{1}{3}}}{{f_0}^{\frac{1}{3}}}\right) \tag{A.9}$$

The Nusselt number general form:

$$Nu = C \cdot Re^m \cdot Pr^n \tag{A.10}$$

where C, m and n are constants. This allows expressing the thermal enhancement factor (η) as:

$$\eta = \left.\frac{h_{aug}}{h_0}\right|_{pp} = \left.\frac{Nu_{aug}}{Nu_0}\right|_{pp} = \frac{C_{aug}}{C_0}\left(\frac{Re_{aug}}{Re_0}\right)^m \tag{A.11}$$

Substituting Eq. A.9 and assuming $C_{aug} \approx C_0$:

$$\eta = \left(\frac{f_0}{f_{aug}}\right)^{m/3} \tag{A.12}$$

For $m = 1$ (isolating friction effects), the final performance enhancement criterion form is:

$$\eta = \frac{Nu_{aug}/Nu_0}{(f_{aug}/f_0)^{1/3}} \tag{A.13}$$

Appendix B

Detail Drawings of the Swirlers

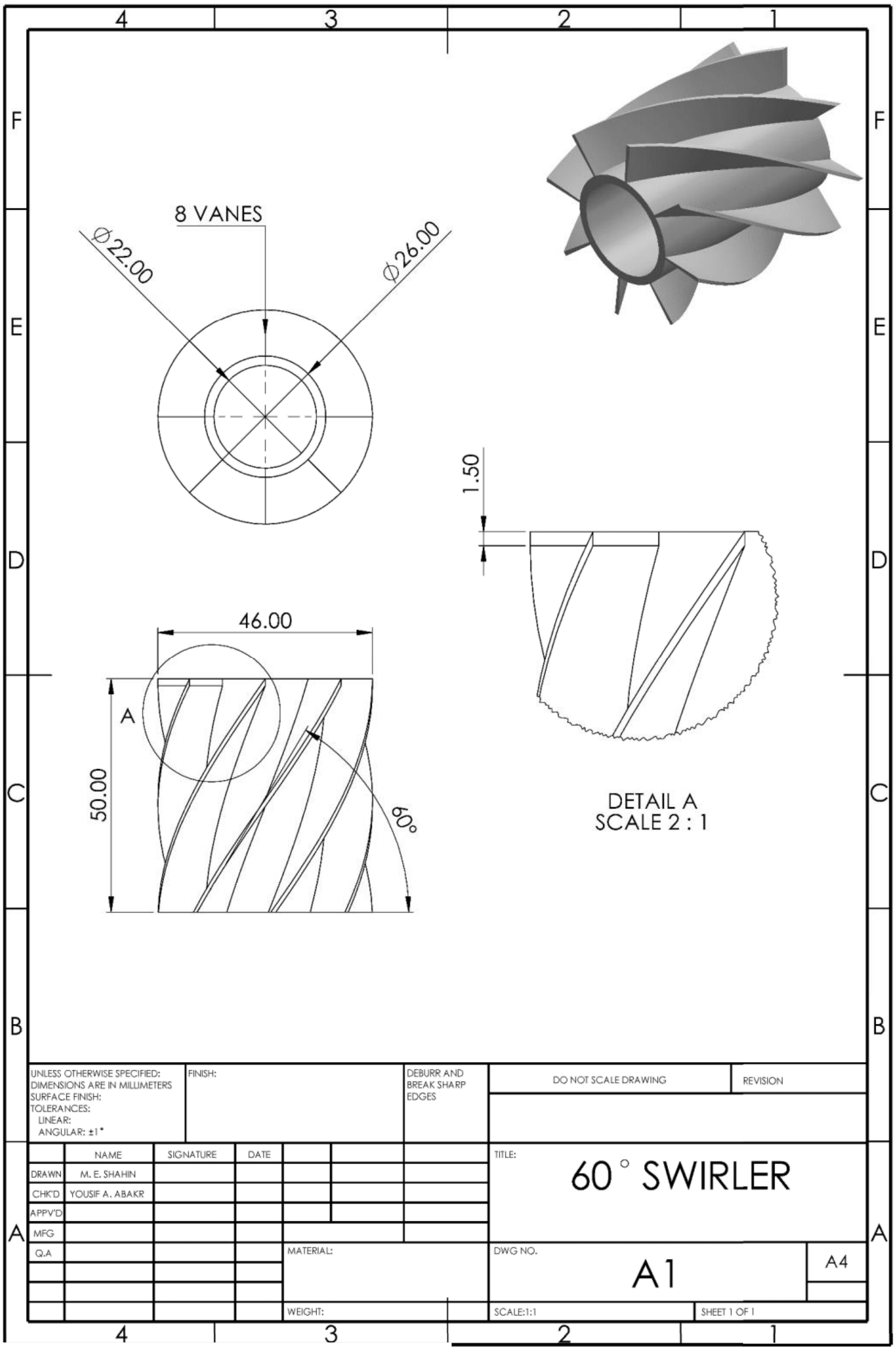

Figure B.1 Computer aided design detail drawing of the 60° swirler.

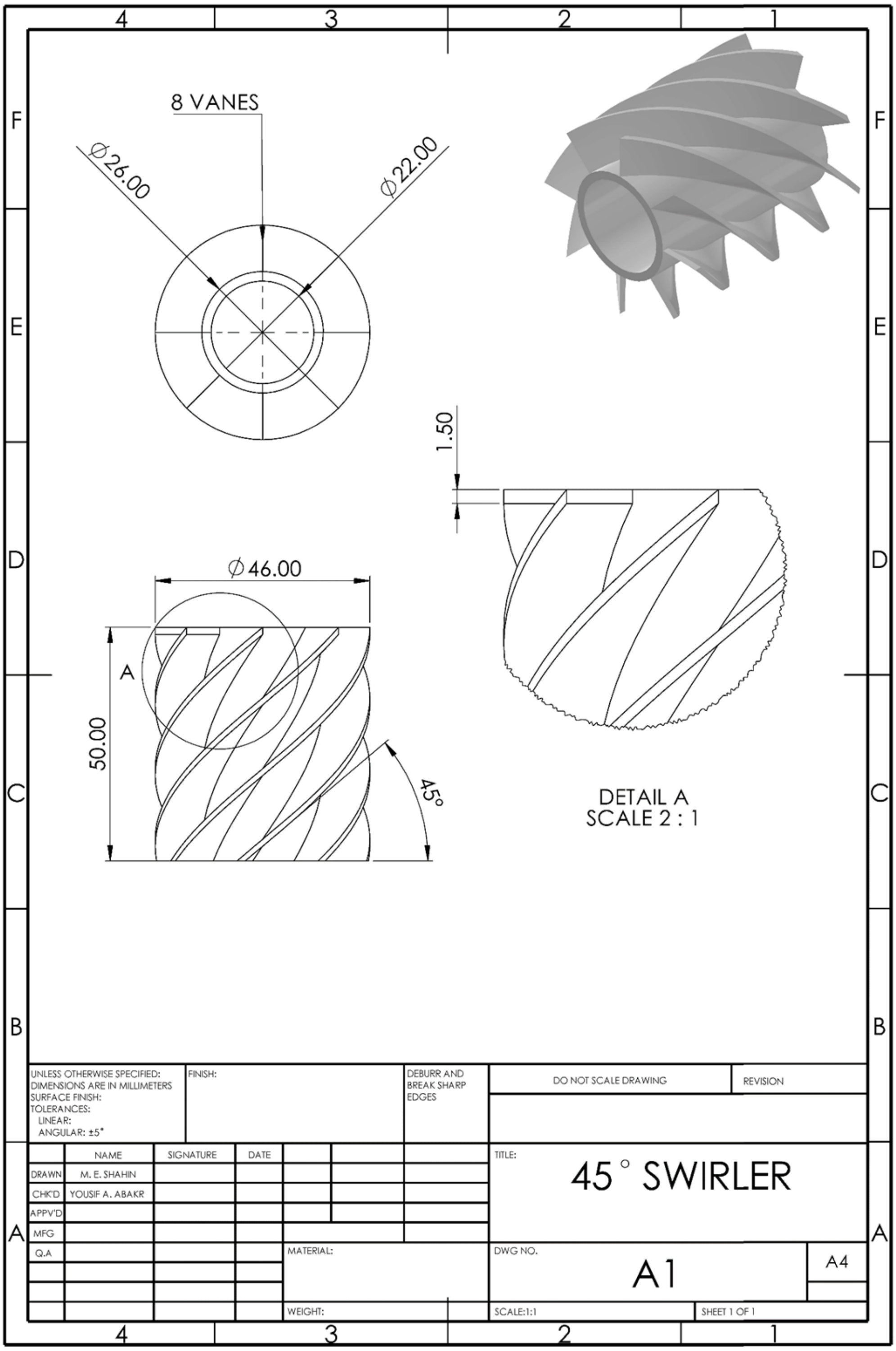

Figure B.2: Computer aided design detail drawing of the 45° swirler.

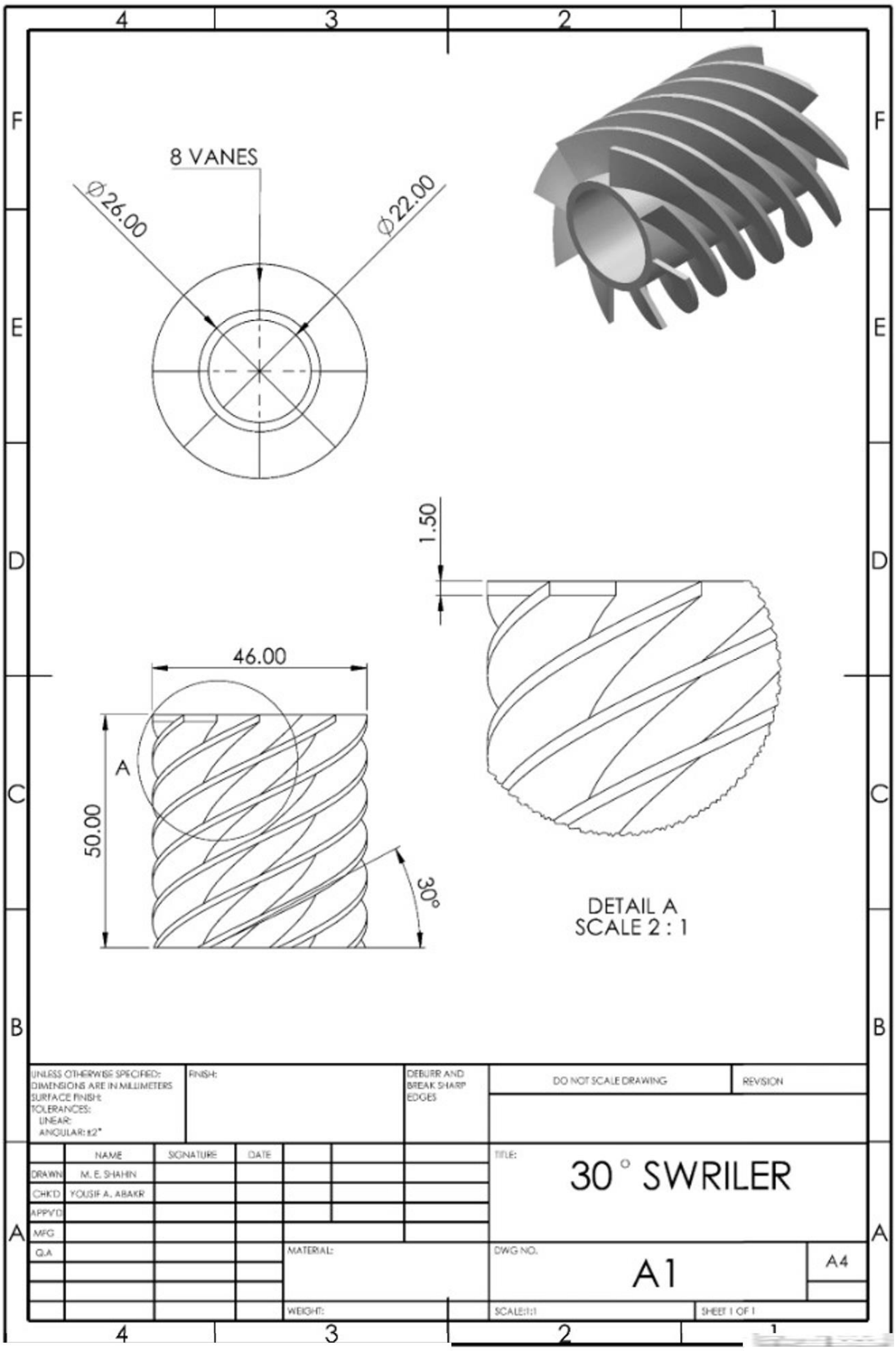

Figure B.3 Computer aided design detail drawing of the 60° *swirler.*